Flow-gamis : Interaction de structures pliées et coupées avec un écoulement

Tom Marzin

INSTITUT POLYTECHNIQUE DE PARIS

NNT : 2023IPPAX024

Thèse de doctorat

Flow-gamis: Interaction of folds and cuts with a flow

Thèse de doctorat de l'Institut Polytechnique de Paris
préparée à l'École Polytechnique

École doctorale n°626 École doctorale de l'Institut Polytechnique de Paris (EDIPP)
Spécialité de doctorat : Mécanique des fluides et des solides, acoustique

Thèse présentée et soutenue à Palaiseau, le 24/03/2023, par

TOM MARZIN

Composition du Jury :

Marcelo Dias Associate Professor, The University of Edinburgh - School of Engineering	Rapporteur
Frederick Gosselin Professeur, École Polytechnique de Montréal - Laboratory for Multiscale Mechanics	Rapporteur
Basile Audoly Professeur, École Polytechnique - Laboratoire de mécanique des solides	Président du jury
Stéphane Douady Directeur de recherche, Université Paris Diderot - Laboratoire Matière et Systèmes complexes	Examinateur
Frédéric Lechenault Chargé de recherche, Ecole normale supérieure - Laboratoire de Physique	Examinateur
Karen Mulleners Assistant professor, École Polytechnique Fédérale de Lausanne - Unsteady flow diagnostics laboratory	Examinateur
Emmanuel de Langre Professeur, École Polytechnique - LadHyX	Directeur de thèse
Sophie Ramananarivo Assistant professor, École Polytechnique - LadHyX	Co-directrice de thèse
Joël Marthelot Chargé de recherche, Université Aix-Marseille- IUSTI	Invité

Flow-gamis: Interaction of folds and cuts with a flow

Tom Marzin - LadHyX

Merci !

Je tiens en premier lieu à adresser mes remerciements aux membres du Jury. Merci Marcelo Dias et Frederick Gosselin pour votre relecture minutieuse de mon manuscrit et d'avoir mis en avant mes travaux aux travers de vos remarques pertinentes. Merci à Karen Ann Mullerners, Frédéric Lechenault et Stephane Douady de leurs expertises et leurs intérêts pour mes recherches qui émanaient de leurs questions lors de la soutenance. Merci à Basile Audoly d'avoir présider ce jury et gérer le débat scientifique qui a suivi la soutenance.

Pfiou... Voilà un grand chapitre de ma vie écrit, et je n'y serai jamais parvenue sans l'aide d'un bon nombre de personnes que je souhaite remercier dès à présent.

Commençons par le début, 1998, école primaire de Notre Dame de la Clarté à Combrit, mes premières années d'études à l'école ont été à l'origine de tout ce qui suivra et l'ensemble du corps enseignant, Brigitte, Laurence, Véronique et Gaelle, merci à mes quatre maîtresses ! Une multitude de professeurs se sont ensuite succéder et je les remercie tous et toutes. J'ai une pensée particulière pour mon professeur de mathématique Mr Royant qui m'a le premier donné le goût des sciences et la rigueur nécessaire à mon futur métier. Les années de Prépa suivent ensuite et encore une fois, l'équipe pédagogique est au rendez-vous, merci Mr Queffelec et Mr Daré pour leurs passions qui par capillarité ont alimenté la mienne.

Je souhaite ensuite bien évidement remercier le LadHyX, permanents ou non je tenais à tous vous remercier pour ces 4 années avec vous. Depuis la salle info jusqu'au plus grand bureau des doctorants, des discussions sur la route du Magnan au fond du Grand Canyon, ce laboratoire a été la structure adéquate pour faire me faire grandir scientifiquement. Je tiens tout particulièrement à remercier quelques personnes qui ont rendu mon quotidien au travail si agréable...

Je commencerai par mes collègues doctorants arrivés la même année que moi, Pierre le spécialiste des frites double cuisson, merci d'avoir partagé ce premier bureau et les premiers de mois de thèse ensemble, au plaisir de lire tes futurs papiers de grand chercheur Belge. Charlie et Antoine D., deux "grands" sportifs chacun à leurs manières qui ont fait vivre le préfa... Avec l'aide non-négligeable de B^3 et Juliette. Un grand merci à ces deux personnes pour leur accueil au LadHyX pour l'ensemble des discussions et expériences partagées, l'enseignement pour l'une la fête de l'Huma pour l'autre.

Parmi les plus "jeunes", je pense à PA, qui est l'instigateur de la vie au labo, je ne te connaissais pas avant la conf à Phoenix et tu es devenu un ami précieux, merci pour toute l'aide que tu m'as apportée ! Merci à mes trois voisins : merci général Quentin pour les discussions polémologiques et stratégiques, Merci Monseigneur R. Grivet, pour vos discussions d'esthète. Thanks Chris for all your advices about the US, I hope to see you soon as a future PI. Merci à la team FSI: Antoine T., Rishabh et Agathe pour votre bonne humeur et votre curiosité qui ont beaucoup inspiré mes travaux, hâte de voir les prochains projets ! Merci également à Ursy et Olivier. Merci aux nouveau préfa, Alice, Thomas et Hector, vous perpétrez la tradition de la bonne humeur et de la belle science ! Également un clin d'œil aux doctorants du bâtiment 65, Clara, Sarah, Ambre, Hassane et Claire.

Un grand merci aux post-doc également Slider Huang, Mathilde, Valentin et Wladimir pour tous vos conseils et vos encouragements en fin de rédaction. Un gran agradecimiento a mi compañero de lucha Daniel el loco (y el coco) el sonrisa de LadHyX.

Parmi les permanents, je tenais à remercier Lutz et Christophe C. pour leurs actions en tant que directeurs. Blaise pour les ref musicales, les séminaires et les conseils en tout genre. Camille Caro pour leurs gentillesses et leurs confiances pour les missions d'enseignements. Merci à Christophe J. pour ces moments passés en dehors du labo et des sentiers battus de l'Arizona. Capitaine Arezki et Pascal pour les supers week ends de voile, un plaisir d'avoir fait partie de votre équipage !

Merci à Caroline Frot, Dani et Antoine Garcia pour leurs coups de mains précieux et conseils avisés.

Merci à tous les étudiants stagiaires que j'ai eu la chance de côtoyer lors de ces 3 ans. Merci Kerian, Judith, Nicolas, Bernardo et Edouard pour vos travaux et l'intérêt que vous avez porté aux sujets. Merci également aux étudiants de l'X que j'ai pu encadrer et qui par leurs curiosités scientifiques m'ont permis de prendre du recul sur mon travail de recherche.

Enfin un grand merci à mes deux superviseurs. Merci Emmanuel pour ta patience, ta sagesse et ton recul sur mon travail. Merci d'y voir toujours les bons côtés, et de me faire sans arrêt regarder en arrière, constater le chemin parcouru. Merci pour tous tes conseils toujours bien illustrés d'une référence bien choisie. Au plaisir de te recroiser dans les bois pour écouter le brame du cerf ! Profite bien de ta retraite et encore un grand bravo pour l'ensemble de ta carrière.

La meilleure pour la fin, merci Sophie, sans toi et ton sourire cette thèse n'aurait jamais vu le jour. Ce sourire qui ne te lâche jamais et qui fait de chaque expérience peu concluante un pas en avant. Cet optimisme qui te caractérise si bien et qui m'a beaucoup apporté au quotidien. Tu as été présente à tous les niveaux lors de ces 3 dernières années et je te remercie infiniment de ta confiance. Merci de m'avoir transmis ta passion pour ce métier, tu m'as fait grandir en tant que chercheur et je t'en serais toujours reconnaissant. Ce fut un honneur d'être ton premier thésard et j'espère de tout cœur pouvoir continuer à travailler avec toi dans le futur.

Merci au FAST, le premier labo qui m'a initié à la recherche. Merci Harold et Adama pour leur confiance et de m'avoir convaincu de persévérer dans la mécanique des fluides.

Merci aux Marseillais Joël, Victor, Ignacio et Simon qui m'ont accueilli à l'IUSTI et fait découvrir la mécanique du solide lors d'un bel été sudiste.

Merci aux Mecawet du PMMH qui m'ont accueilli dans leur super labo pour des longues journées Instron, en particulier un grand merci à Benoit pour tes astuces et conseils qui ont marqué cette thèse et mon futur.

Je tenais aussi à remercier mes nouveaux compagnons américains qui m'ont permis de me sentir immédiatement chez moi dans mon nouveau labo : PT (c'est le s), Trevor, Christopher, Lauren, Abby, Barath et Yuchen, et les quatre Français qui ne me font pas oublier mon pays (et l'X) Julien, Néo (merci à vous deux pour le squat canapé), Thomas (...et gang!) et Romain.

Merci à tous mes proches, qui m'ont aidé à écrire ce chapitre de vie, chacun à leur manière. Tout d'abord mes parents qui ont toujours été d'un soutien sans faille, vous avez toujours cru en moi, toujours voulu que je me dépasse dans mes études, voilà l'école est finie, mais vous êtes toujours là, merci pour votre amour et votre présence, même si je ne le dis pas souvent, je vous aime très fort.

Merci à mes amis : inspecteur Thomas qui depuis la maternelle me suit et reste présent 25 ans après. Jérémy le mec le plus drôle de France (même si la France n'est pas encore prête), merci Robin pour tes anecdotes et nos longues balades dominicales qui ont été le soupir de ma partition. Merci les voisins Jeoffrey, Marie, Gaëlle et Bonnard (team Blinis) pour les soirées, pour votre bonne humeur et nos discussions jusqu'au bout de la nuit. Merci Axel pour ta sympathie pour les pintes de bière à Marseille comme à Paris. Merci à Pedro pour tes analyses footballistiques, toujours précises et passionnées. Merci à ma pote Sophie pour ces debriefings au téléphone, qui apaisent après de longues journées de rédaction.

Merci les Diabolos ! La plus grande équipe de soft (à mes yeux), vous allez me manquer les amis ! Merci pour ces weeks ends tournois, pour ces manches de défense toujours trop longues et d'attaque toujours trop courtes... Je reviendrai des USA plus fort !

Merci Manon, pour toutes ces années passées à tes côtés, pour nos soirées, nos week-ends, nos voyages, pour tous ces beaux moments ensemble, même si les choses ne finissent pas comme nous le souhaitions, tu restes et resteras une personne très importante pour moi, merci Let pour tout et veille bien sur nos petits chats, vous me manquez déjà...

Merci aux chats qui par leurs ronrons sont toujours aussi mignons, Holly (zipette), Skittles, Maoki, Gwendu, Jimmy et Indiana !

Contents

INTRODUCTION

0.1 Flow-induced deformation of flexible structures

A flexible system is able to bend without breaking when external forces are applied. This type of deformation occurs under any type of loading, including from a surrounding fluid. Flexible components have however long been overlooked by industry in favor of rigid ones, especially in sectors such as aeronautics, turbines, and civil engineering. In such fields, flexible systems may not seem suitable as they are deformable, or prone to instabilities and vibrations caused by flows. Nevertheless, compliance is well established in the plant and animal world.

0.1.1 Welcome to the plant life

Flexibility plays a major role in the adaptation of species to their environment. For example, a tree must be able to survive in harsh external conditions such as strong winds, storms, and drought. A rigid or fixed structure would make it difficult for the plant to survive.

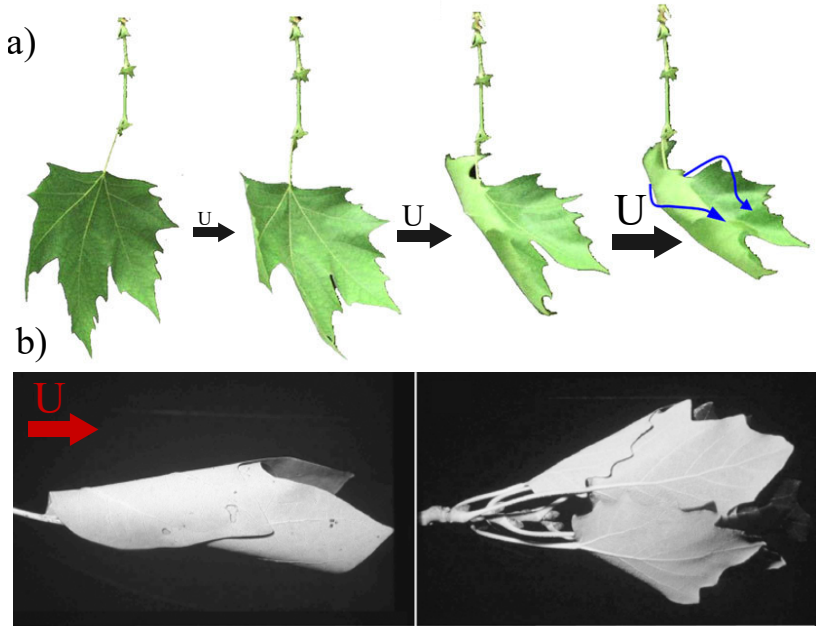

Figure 1: a) A tree leaf bends in the wind and adapts its shape to the flow velocity [1].b) Several examples of leaves exposed to the wind at 20 m/s from [2]

To withstand these extreme conditions, trees have developed a passive strategy that takes advantage of the flexibility of their leaves. When exposed to winds, the leaves bend and adapt their shape to the surrounding fluid flow. These deformations must be somewhat reversible so that in the absence of wind, the leaves return to a flat surface to capture incident light rays. To understand this shape change, S. Vogel initiated a set of experimental measurements of deformations induced by a flow around a single leaf or a cluster of leaves attached to a branch (see Fig1b) [3, 4, 2]. More than shape-shifting, the study also focused on the drag force F_d, which is defined as the fluid force component directed along the incoming flow, and its evolution as a function of wind velocity U. The study compared these measurements to those of a rigid system, which experiences a quadratic law $F_d \sim U^2$, and found that the deformation of the plant is accompanied by a process of drag reduction. This phenomenon is captured through a scalar $\mathcal{V}$, called the Vogel exponent, which expresses the drag evolution with a weaker power law: $F_d \sim U^{2+\mathcal{V}}$. More details on this point will be provided in the next section. Numerous studies have followed, classifying plant species according to their flexibility and drag reduction capabilities [5, 6, 7, 1]. Some of them, such as the tulip tree or the red marble leaf (see the first picture in Fig1), are able to roll up into

a cone shape when in flow, and exhibit a streamlined shape that enhances its drag reduction process [4]. The challenge for the plant is therefore to have foliage that is sufficiently rigid to ensure a large surface area exposed to the sun, while also being highly flexible to adapt passively to changing weather conditions. A quick discussion of another bio-strategy is presented in the interlude n^o1.

All these phenomena are collectively referred to as reconfiguration. It is the process by which flexible structures change their shape and adapt to external fluid loading. This strategy is particularly interesting to exploit because it is passive and governed by structural properties. Drag is also a force component that we generally seek to minimize. For rigid systems, one of the few ways to achieve this is to actively change the body shape, which is not a sustainable response to fluctuating environments.

Interlude n^o1 : Le Chêne et le roseau - some doubts about the moral of the story

In his fable, Jean de La Fontaine illustrates his morals through the dialogue between a small reed and a large, arrogant oak. When the wind rises, the reed "bends but does not break," while the rigid and pretentious tree is uprooted, demonstrating the importance of humility and avoiding pretense (see Fig a below). However, La Fontaine did not know that trees can also resist violent storms, not only through the flexibility of their foliage, as discussed earlier but also through a process called anemomorphosis. In areas with high exposure to wind gusts, trees grow in an orientation that aligns with the prevailing wind direction. As illustrated in figure b), the shape of the trunk and branch network aligns with the surrounding fluid, reducing the overall forces generated by the fluid and thus the bending moment on the trunk. By orienting their growth, trees provide an additional response to chronic weathering [8].
Note that other strategies are possible, such as stronger rooting or more robust trunks, but in any case, the oak has the tools to compete with the reed, contrary to what La Fontaine thought.

a) 

b) 

0.1.2 Shape-shifting for functionality

Aside from drag reduction effects, flow-induced deformation has inspired other fields of research with applied perspectives. For example, in micro-channels, flexible valves can passively deform in response to the moving fluid and regulate the flow throughout the circuit. In this vein, Gomez et al. [9] placed a buckled blade in an axial flow, and when a critical load was reached, the arch snapped to its other state which increased the channel section (see Fig2). Alternatively, Brandenbourger et al. [10] studied the coupling between elasticity, geometry, and fluid in a flexible valve network inspired by the lymphatic system, seeking to understand the role of each parameter in regulating biological flows.

We can also mention studies on flapping flight where flexibility plays a predominant role for insects. Passive deformation of the wings increases the effective amplitude of flapping and

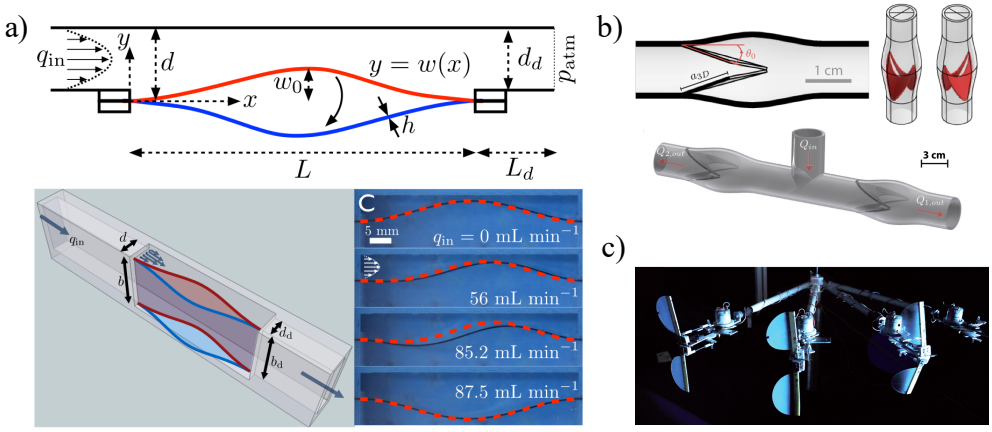

Figure 2: a) A thin bent plate placed in an axial flow snaps to its other stable state when the fluid loading increases, resulting in a wider micro-channel section locally [9]. b) Experimental reduced model that mimics the lymphatic flexible valves [10]. c) Robotic flapping insect with flexible wings, which improve its flight performances [11].

reorients the fluid forces in the direction of propulsion, thus improving propulsive performances [11]. Finally, the flexibility of slender structures such as ropes/cables in flows can lead to vibrating motions induced by vortex detachment [12]. One application is to extract energy from such vibrations and manipulate the elastic properties to enhance efficiency.

These examples demonstrate the advantages of flexibility for systems operating in fluid environments, where flow-induced deformation can be utilized as a self-protection strategy or to perform a specific function. However, for the structure to fulfill its function, it must deform in the appropriate way. Therefore, it is crucial to understand the fluid-elastic mechanisms behind this deformation and identify ways to control it.

0.2 An hydro-elastic fight

The systems presented above have complex shapes, with localized stiffnesses along the veins of leaves or insect wings. To better understand the interaction of such deformable surfaces with a flow, a series of investigations have been conducted on model systems with simpler and controlled geometry and stiffness.

0.2.1 An overview of the boxing ring

Building on Vogel's findings, Alben et al. [13, 14] first investigated the case of a flexible filament placed in a soap film flow and were able to describe their experiments using a two-dimensional fluid-elastic model. They established a link between shapes and drag evolution, as well as a scaling of drag with flow velocity for this purely two-dimensional configuration. Schouveiler et al. [15] and Gosselin et al. [16] then examined the case of a thin disk cut along one radius and or several radii, respectively. Figure 3a and b show the deformation that becomes more pronounced with increasing flow speed. By changing the dimensions and stiffness of the systems, it was shown that the flow-induced deformation (and the resulting drag reduction) is the result of a balance between structural stiffness and fluid forces, as further discussed in the following section.

Comparing these two disk-like systems illustrates that another factor must be considered: the geometry. Indeed, the ribbons forming the disk with multiple cuts bend like cantilevered beams (Fig3a), while the disk cut along only one radius rolls into a cone (Fig3b). The morphologies reached in the flow are thus quite different depending on the initial geometry considered. These differences are also reflected in the respective drag laws of the two systems,

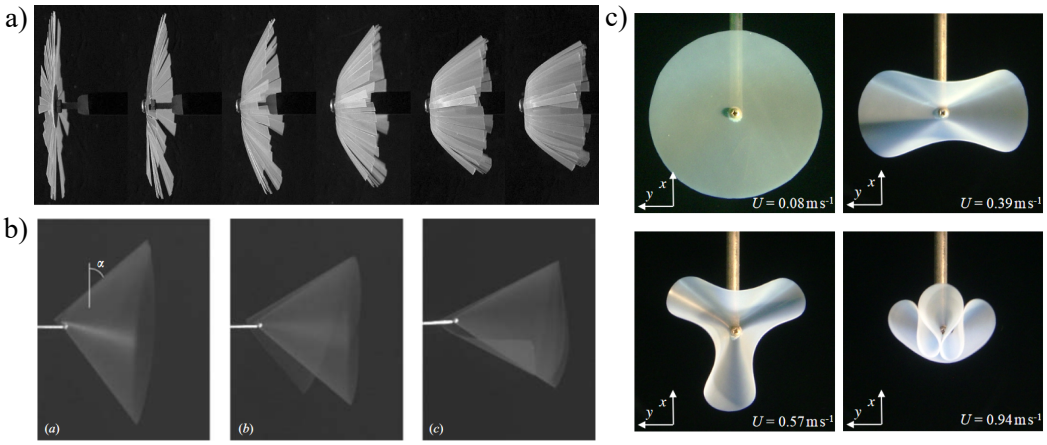

Figure 3: Flow-induced deformation of, a) a disk cut along several radii [16], b) a disk cut along a single radius [15], c) an uncut disk [17].

associated to different Vogel exponents (see interlude n^o3). A last striking example of the importance of geometrical properties is given by a disk (again!) without any cuts (see Fig3c). It deforms into draped shapes that have more and more lobes as the flow speed increases. The sudden transition from one shape to another is related to a change in the configuration that minimizes the energy of the system (including both the fluid and elastic contribution) [17].

These three examples demonstrate the diversity of shapes and drag laws that can be achieved through simple geometrical changes. Let us now delve a little deeper into the elasto-fluid competition mentioned above.

Interlude n^o2 : Thin sheets prefer bending

Slender structures are very deformable and prone to instabilites (such as buckling), which generally result from bending deformation. But why does it bend instead of a stretch? Why is it difficult to extend a sheet of paper?
To understand this, we consider the energies associated to the two modes of deformation of a sheet (see figure below): the energy of stretching E_s, and the energy of bending E_b which scale as [18]:

$$E_s \sim EWt\varepsilon^2 \qquad E_b \sim EWt^3\gamma^2$$

where E is the Young's modulus of the sheet (typically $1-4$GPa for paper), W its width, t its thickness, ε the in plane elongation and γ the curvature. The ratio of the two energies scales as: $E_b/E_s \sim t^2(\gamma/\varepsilon)^2$. For a slender sheet with $t \ll 1$, this ratio is small and it is therefore far easier to bend it than to stretch it.

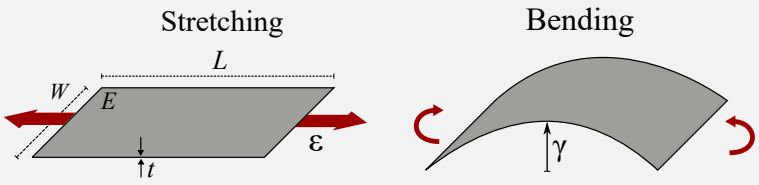

0.2.2 The first fighter: elasticity of the slender body

We consider slender structures, which are defined as having one of its dimensions being negligible compared to the others. This is the case with the tree leaves mentioned earlier, which have a smaller thickness compared to their width or length, regardless of their shape.

In most cases discussed here, it will also be the thickness that is the smallest dimension. It greatly affects the mechanical response, notably giving significant flexibility compared to bulkier materials. Slender structures like paper sheets exhibit a preferred mode of deformation. Due to its small thickness, it is much easier to bend a sheet than to lengthen it. As discussed in the interlude $n^o 2$, bending has a lower energetic cost than stretching, which explains why all previous examples bend when subjected to a flow. The forces generated by the fluid are then counteracted by the bending moment of the slender system considered.

This bending moment can be expressed as a linear function of the imposed curvature: $T = EI\gamma$, where EI is the bending stiffness. The latter takes into account both the geometry of the object with the quadratic moment $I = Wt^3/12$ (with t the thickness and W the width), and the nature of the material through the Young's modulus E. Note that this linear dependence is based on the assumption of low deformation [19] and must be corrected if shear forces are present [20].

0.2.3 The opponent: fluid loading

The flow behavior of the surrounding fluid can be described by the Reynolds number $Re = UR/\nu$ that compares inertia to viscous forces, with U the flow velocity, R a characteristic linear dimension, and ν the kinematic viscosity. In the experiments discussed above (and in our experiments), Re can be as large as 10^5, indicating that we are in an inertial regime and that viscosity can be neglected (except in the turbulent wake formed downstream). The flow then exerts normal dynamic pressure forces on the object, and the net force can be broken down into a drag component in the direction of the flow and a lift component perpendicular to it. For a solid object with a fixed shape, the drag writes as $F_d = 1/2 C_d S \rho U^2$, with S the reference area (that is often the projected frontal area) and C_d a dimensionless drag coefficient that depends on the shape of the object and quantifies its resistance in a fluid flow. The curve with a solid line in Fig4d, which corresponds to the drag force on a rigid plate, illustrates such quadratic U^2 evolution.

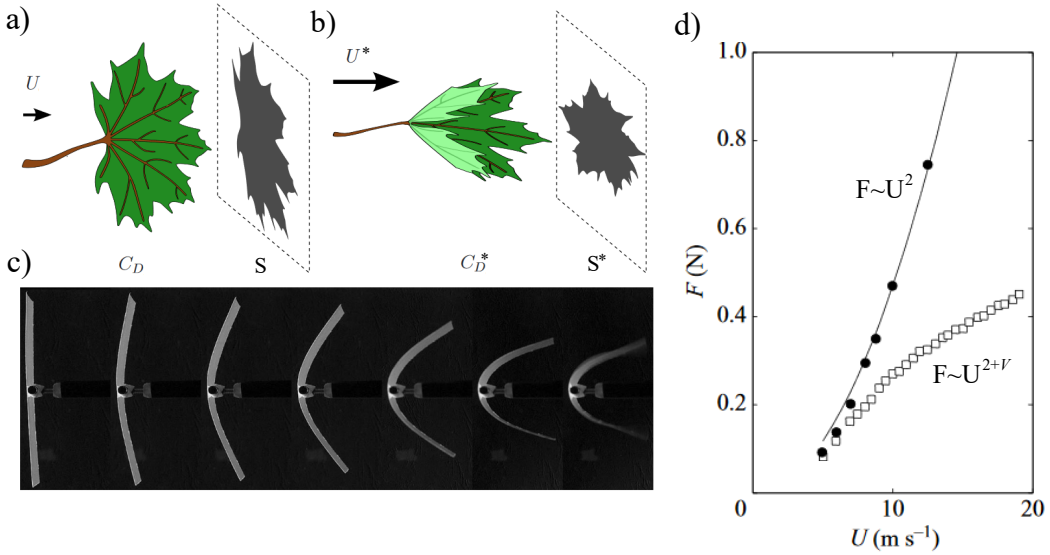

Figure 4: a-b) Schematic illustrating the drag reduction mechanisms through reconfiguration, adapted from [21] and showing a tree leaf in a flow with a) low and b) high velocity. Drag is impacted by the reduction of the frontal area $S^* < S$, shape streamlining $C_d^* < C_d$ and a change in the effective velocity U^* for confined configurations. c) Deformation of a flexible rectangular plate in a flow of increasing speed U. d) Evolution of the drag force with U for such flexible plate (hollow markers), compared to the drag on a rigid plate (black line) [16].

The quadratic relationship between drag and velocity is well-verified for rigid, bluff bodies. However, if the system is flexible, things become more complex. As discussed in the context

of plants, the shape-shifting caused by fluid loading can reduce the relative frontal area S relative to the flow, and the slender body can align along the flow direction with a more streamlined shape with lower C_d. Additionally, if the flexible system is porous or in a confined flow, shape-dependent blockage may also change the effective flow speed around the object. These drag reduction mechanisms are illustrated in Fig4a-b for a leaf, and in Fig4c for a simpler flexible plate [16]. As the flow velocity increases, the plate bends, which drastically reduces its frontal area and leads to a more streamlined shape. The impact on drag is shown in Fig4d. At low speeds, the flexible specimen (hollow squares) exhibits a similar drag as the rigid plate (solid circles), but as the fluid load increases, the shape reconfiguration significantly reduces the drag compared to the rigid case. The drag no longer follows a quadratic behavior, but a power law with a lower exponent characterized by the Vogel coefficient $\mathcal{V} \approx -2/3$. Note that $\mathcal{V}$ can be determined through dimensional analysis in the asymptotic regime of large deformation, as presented in interlude n^o3. Importantly, this power law is a function of shape: a cone that rolls up or a filament does not reduce drag in the same way, and different Vogel exponents are observed.

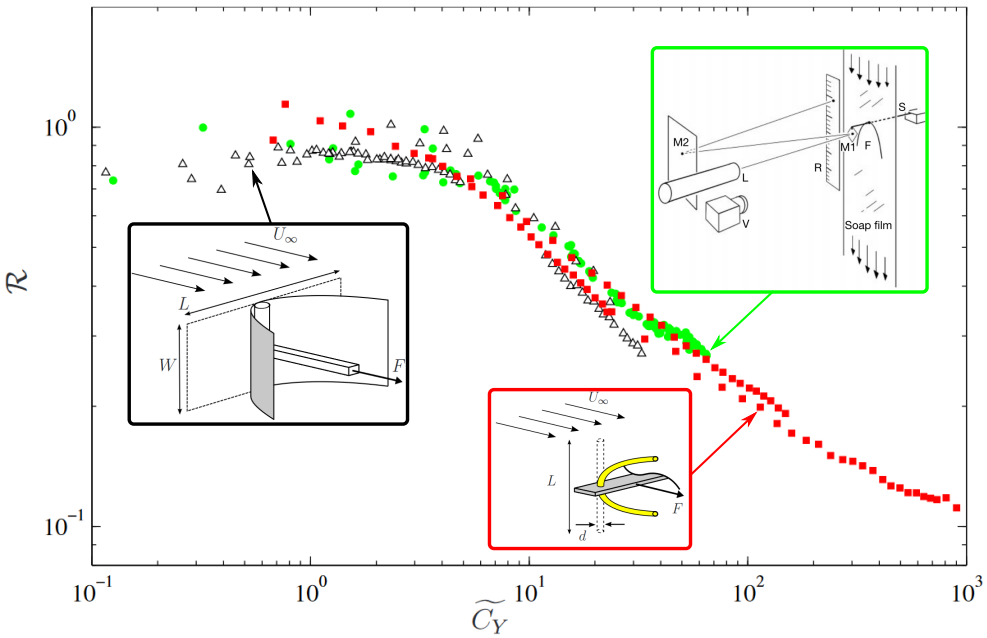

Figure 5: Reconfiguration number $\mathcal{R}$ for three different slender flexible systems:: rectangular plates of varying size and stiffness, flexible filament (both from [21]); short fibers tested in soap film flow by Alben et al. [13]. All are replotted as a function of Cauchy number.

0.2.4 The referee: the Cauchy number

To arbitrate the competition between these two fighters, we typically introduce a number that balances the typical fluid loading on the structure and the elastic restoring forces. This is the role of the dimensionless Cauchy number, C_y. In the case of the thin strip discussed above, it is defined as the ratio of the dynamic pressure force and the bending rigidity of the plate:

$$C_y = \frac{\text{fluid loading}}{\text{elastic restoring force}} = \frac{\rho U^2 W L^2}{EI} \tag{1}$$

To illustrate the significance of this number in fluid-elastic processes, drag measurements for deformable objects (plates, filaments and fibers) with varying stiffness can be replotted in a dimensionless form as a function of C_y (instead of U). In addition to the Cauchy number,

Gosselin et al. introduced the reconfiguration number $\mathcal{R} = F_d/F_{d,r}$, which compares the drag of the flexible devices F_d to that of a rigid one with the same geometry $F_{d,r}$ [16, 21, 13]. We will use this dimensionless quantity as well in our study to characterize the effect of deformability on drag. As shown in Fig5, the data collapse onto a single curve. Behaviors are indeed determined by the competition between elasticity and fluid forces, which is captured by the Cauchy number. Fig5 also shows a transition between two drag regimes. At low C_y, when the fluid load is small compared to the structural rigidity, the plate or fibers barely deform and their drag forces are similar to that of a rigid object (i.e. $\mathcal{R} \sim 1$). For large C_y, the reconfiguration of the deformable system reduces drag, and $\mathcal{R}$ decreases. In the asymptotic regime of large deformation, it appears to decrease with a constant logarithmic slope, yielding a new scaling of drag with flow speed, which is discussed in interlude n^o3.

For the flexible plate, the structural response is determined by the bending stiffness, as flexion is the preferred mode of deformation. However, as we will see in this thesis, if another mode is involved, the denominator of the Cauchy number will be modified to take into account the new nature of the deformation. Note also that this number does not reflect any notion of temporality. All the studies on reconfiguration presented so far have been performed in a stationary regime, and our future experiments and models will also be in a purely static framework.

Interlude n^o3 : Drag force on flexible plates $F_d \sim U^?$

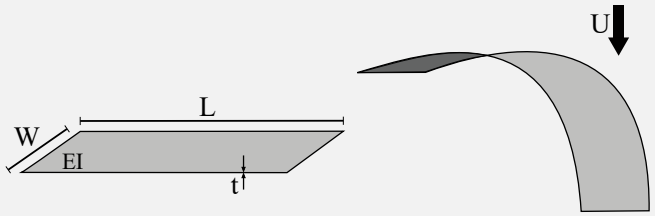

Gosselin et al. [16] show that we can recover the scaling of the drag force F_d with flow speed U through simple dimensional analysis, in the asymptotic case of large deformation. They consider a flexible rectangular plate with length L, width W, and bending stiffness $B = EI$; it is immersed in a fluid with density ρ and flow velocity U (see left figure below). In the case of large deformation, the length L is no longer relevant as the plate aligns with the flow and only the portion close to the support bears drag forces (see the right figure below). The physical problem is then reduced to four quantities (and three dimensions): B [N.m], U [m.s^{-1}], ρ [kg.m^{-3}], and the drag per unit with (for this two-dimensional problem) F_d/W [N.m^{-1}]. The Vaschy-Buckingham theorem then states that the problem can be described using only one dimensionless number:

$$\frac{F_d}{W(EI)^{1/3}\rho^{2/3}U^{4/3}}$$

It gives a scaling of the drag force with flow velocity $F \sim U^{4/3}$ (that is $\mathcal{V} = -2/3$), which is in agreement with experimental measurements. Using a similar approach, one can obtain $F_d \sim U$ ($\mathcal{V} = -1$) for a disk cut along several radii, and $F_d \sim U^{2/3}$ ($\mathcal{V} = -4/3$) for a disk with a single cut that rolls up into a cone [16, 15].

0.2.5 New levers to tune shapes and forces in a fluid flow

At this point, we conclude that deformable structures have the advantage of passively adapting their shape to an external fluid load. This reconfiguration offers a powerful means of regulating fluid loading on the structure. It can notably reduce drag force to avoid damage or rupture in strong winds or currents. Deformations can also fulfill a function, such as flexible valves, enhancement of aerodynamic performance with deformable wings, or energy extraction. However, to operate as desired, the structure must deform in the appropriate

way. Therefore, it is important to understand the fluid-elastic underlying mechanisms and find ways to control them.

So far, most of the experimental and modeling studies in the literature have focused on the interaction with fluids of continuously flexible slender structures, such as beams or plates, which are particularly prone to deformation. Different behaviors have been obtained by changing the stiffness that resists deformation or the geometry of the object, with a rectangular plate behaving differently than a disk, for example. In this PhD, we seek to expand the range of accessible behaviors through a shift from the traditional approach. We explore a new framework for the design of components exposed to flows, by adding a set of folds or slits to thin surfaces. This is the technique of origami and kirigami, which is presented in the following section. While it was initially an art, it has since emerged as a promising engineering solution to fabricate structures with complex three-dimensional deformation modes and to obtain interesting and predictable mechanical properties. For us, it represents a new lever to tune deformation and forces in a fluid flow.

0.3 Ori- and Kiri-gami: new levers from Japanese art

0.3.1 A brief history of ancient paper art

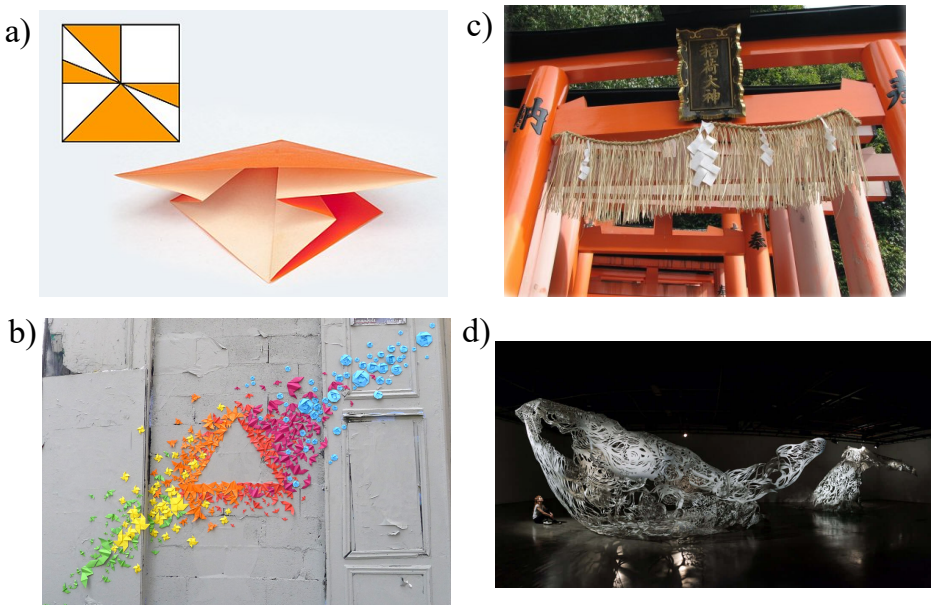

Figure 6: a) Schematic illustration of Kawasaki's theorem: It states that a one-vertex pattern is flat-foldable if and only if alternatingly adding and subtracting the angles of consecutive folds around the vertex gives zero .b) Origami street art from Mademoiselle Maurice. c) Origami and kirigami are also used for Shinto ceremonies. d) Giant whale sculpture made of cut paper, done by Nahoko Kojima.

Contrary to popular belief, the origin of cutting and folding paper comes from China, where the art of jianzhi was practiced. Archaeological evidence from the 6th century shows that it was mainly used for religious purposes. Although other materials like tissue or leather were also used, the paper was preferred for its ease of manipulation. This art then spread to Japan, where it developed into two distinct techniques: origami and kirigami. Both involve creating complex 3D shapes by placing creases or cuts on thin materials.

Since their introduction in Japan around the 7th-8th century, origami and kirigami have evolved from being used in Shinto religious ceremonies (Fig6c) to becoming art forms and creative leisure activities. The main goal is to create harmonious geometric shapes or shapes

inspired by animals or plants, such as the crane, which gave rise to a famous Japanese legend (see the cover picture of chapter 6) or the work of street artist Mademoiselle Maurice, who covers streets walls with her colored foldings (Fig6b). Although origami is more famous in popular culture, kirigami is becoming increasingly popular. It involves applying a specific arrangement of cuts to a sheet to create three-dimensional forms. One impressive example is the giant kirigami whale designed by artist Nahoko Kojima (see Fig6d).

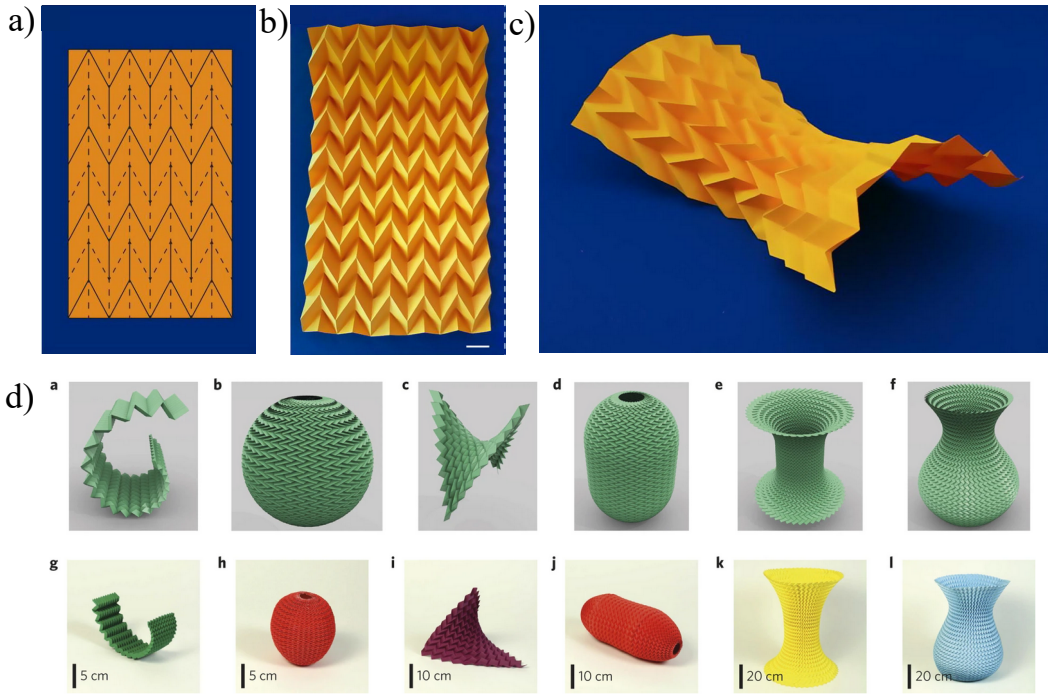

Figure 7: a) The Miura-Ori pattern, which consists of multiple folded chevrons, allows for a flat and inextensible sheet to form a saddle-shape with a non-zero Gaussian curve (from [22]). b) Generalized Miura-ori tessellations can be used to fit arbitrarily complex curved surfaces [23].

More than just artistic methods, origami and kirigami have also inspired the scientific world, as in the field of Mathematics with the Kawasaki and Meakawa theorems [24] (Fig6a). It is also becoming increasingly important in the Engineering and Mechanics field, and in Engineering and mechanics. The presence of these creases or cuts on an initially flat surface creates a set of mechanical and morphing properties that will be described in the following sections.

0.3.2 Shape morphing and new kinematics

Let us begin by discussing origami, a technique that involves folding a flat sheet along predefined lines that form the crease pattern. This pattern conditions the three-dimensional morphing, with the folds acting as hinges around which the facets rotate. In our study, we will furthermore make the "rigid facet approximation" that simplifies kinematics. It assumes that facets are inflexible and that deformation only occurs along the folds. A significant body of research then studied the relationship between shape change and folding patterns.

The interesting feature of the origami method for our current problem is its ability to undergo extreme shape changes. A thin plate with a large surface area can be folded into a very compact object, which is used in the storage or robust deployment of airbags [29] and solar panels/sails [30] (see Fig9a and c). Studies have also sought to use the origami method for shape morphing, such as reaching a targeted surface with arbitrarily complex curvatures, as shown in Fig7b [23]. Another interesting example is the saddle shape of Fig7a [22], which has a non-zero gaussian curvature that cannot be achieved by bending a

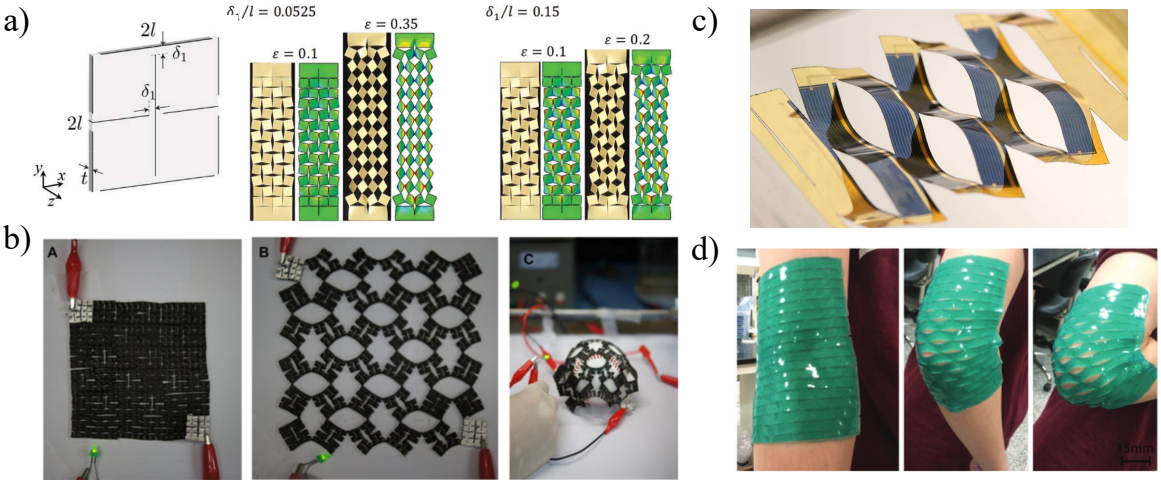

Figure 8: a) Perpendicular slit pattern that allows for local rotation of the uncut parts, resulting in bi-axial expansion of the sheet [25]. b) A flat sheet can be transformed to conform to a baseball ball, changing its Gaussian curvature [26]. c) Parallel and staggered slit pattern, which extends through the out-of-plane buckling of uncut parts. The tilted geometry can be used for the creation of solar panels that can track the sun's trajectory through simple sheet traction [27]. d) Kirigami can be used to conform to moving supports, such as elbows or knees, for applications as medical patches [28].

flat and inextensible sheet, as imposed by the "theorema egregium" (Gauss theorem) for isometric deformations. In brief, the strengths of the origami method are that it allows for large and complex three-dimensional deformations, which are also programmable through the crease pattern. Those significant shape changes will be interesting for the interaction with a flow, where variations of the frontal area and streamlining greatly affect the drag forces, as discussed earlier.

For the kirigami method, cuts replace folds. The network of slits allows for the sheet to extend through the opening of the slits, as shown in Fig8. We remind, as discussed in interlude n^o2, that a slender structure prefers to bend rather than stretch, energetically speaking. Here, at first glance, kirigami sheets seem to refute this statement, but this extensional capacity is "effective" only. To understand this point, let us take a closer look at the local mechanisms that make this super-extensibility possible through the examples of two famous cutting patterns.

The first pattern shown in Fig8a divides the sheet into a set of polygons connected at their ends by ligaments. When an external axial tension is applied, the polygons rotate by flexing the ligaments which act as hinges, resulting in a bi-axial extension of the kirigami sheet. This pattern allows the sheet to conform to sphere morphologies, such as a baseball ball (Fig8b), with positive Gauss curvature, which cannot be achieved with an inextensible, uncut sheet. This square pattern has already inspired applications to increase shoe friction [31] and for soft robotics locomotion [32].

The second pattern, which is the focus of this thesis, consists of an array of parallel and staggered slits. Upon stretching, the elementary blades formed by the uncut portions of the sheet buckle out of the plane and further bend, forming a three-dimensional meso-texture. This meso-texture will prove important in our study. It has also been exploited by Lamoureux et al. [27], to design solar panels with inclined elements that can follow the course of the sun over a day through simple sheet extension (Fig8c). The kirigami morphing ability has also been used for medical patches (Fig8d), which better conform to moving curved surfaces like elbows and knees [28] or even electronic probes to analyze high-fast motions in baseball (see Fig9b). As with origami, the kirigami technique allows for

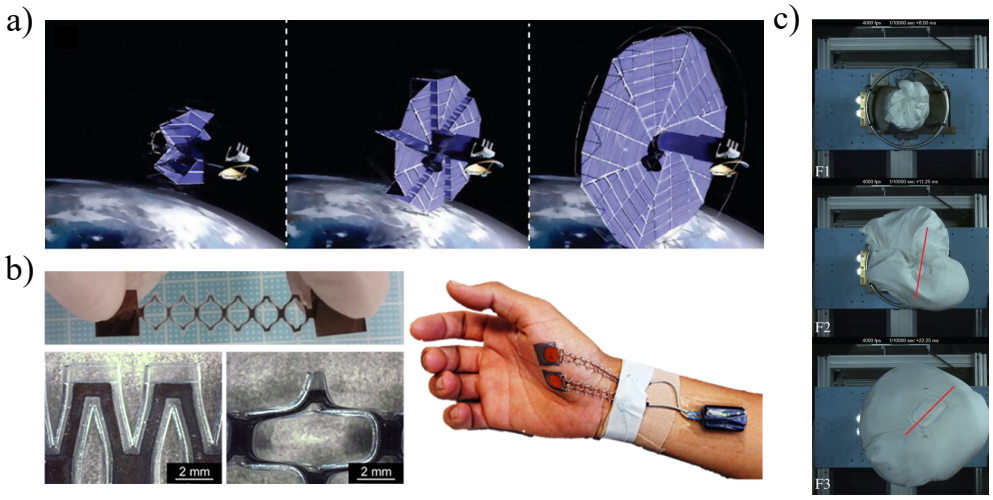

Figure 9: a) Deployment of an origami solar sail from a compact shape to a large surface to capture the sun's rays, using a pattern inspired by the famous Miura Ori fold [30]. b) An extensible electronic probe based on a kirigami network of slits allows for the analysis of rapid human movements, such as those made during baseball pitching [33]. c) The origami method can be used for robust inflation of a pre-folded airbag, while allowing for compact storage of the device [29].

arbitrarily complex shape-morphing, which can be controlled through the cutting parameters [26, 34].

The examples of origami and kirigami tessellations presented here illustrate the close link between the elementary pattern and global deformation. This relationship also impacts mechanical properties. These structures hold many surprises in store!

0.3.3 The cornucopia of mechanical properties

Although many studies on origami and kirigami focused on the kinematics of deformation and the geometrical relations imposed by the pattern, it has also sparked interest in mechanics. These structures have the interesting feature that they derive their mechanical properties from the cut/fold pattern, rather than the constitutive sheet used to make them. As such, they have been described as meta-sheet, a subset of mechanical meta-material. More concretely, the interest lies in being able to engineer mechanical properties by tuning the pattern of cuts or folds. We will now illustrate some examples of unusual mechanical behaviors obtained.

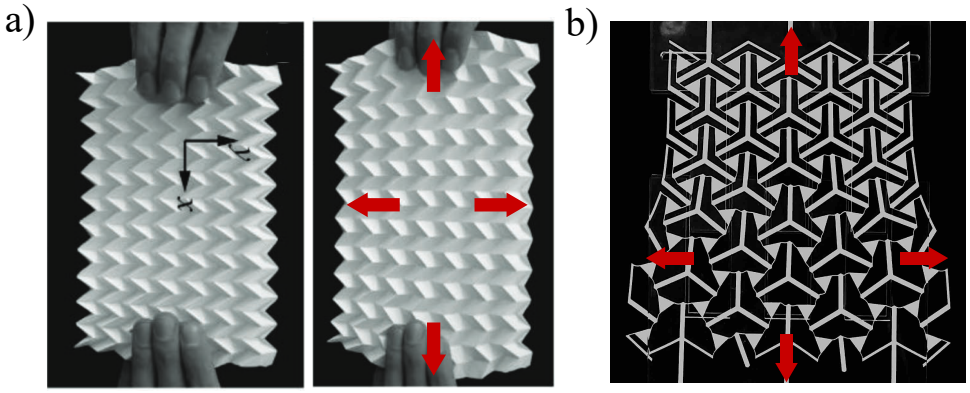

Figure 10: a) The Miura-ori pattern induces an auxetic behavior: pulling along the axial direction lead to the extension in the transverse direction [30]. b) Bi-stable and auxetic kirigami pattern: during a tensile test the bi-axial expansion of the sheet propagates from the bottom edge (fixed) to the top one (moving) [35].

Folding brings out interesting mechanical properties such as auxetism: the Miura-ori sheet of Fig10a extends in the transverse direction when stretched (see Fig10a), as opposed to regular materials that tend to shrink [36]. Folded structures are also able to support significant loads while remaining ligthweight. This rigidity can be selective, with flexible modes of deformation and stiff ones, for which deformation would require stretching or shear of the constitutive sheet. It has been envisioned to design adaptive origami wheels for robots, which can easily expand and still operate in extreme conditions [37]. Another interesting feature of origami is multistability [38, 39, 40]. It notably allows foldable structures to be stable in both their compact and deployed states. An example is the origami tube Fig11b, where each elementary cell is bi-stable, and the whole tube can thus be locked in its folded and deployed state. This type of system is of particular interest for developing new medical stent technology that needs to be compacted during surgery and deployed once in place [41]. Multistability also allows for rapid and large shape changes to minor changes in the external stimuli, such as a flow with increasing velocity as explored in our work.

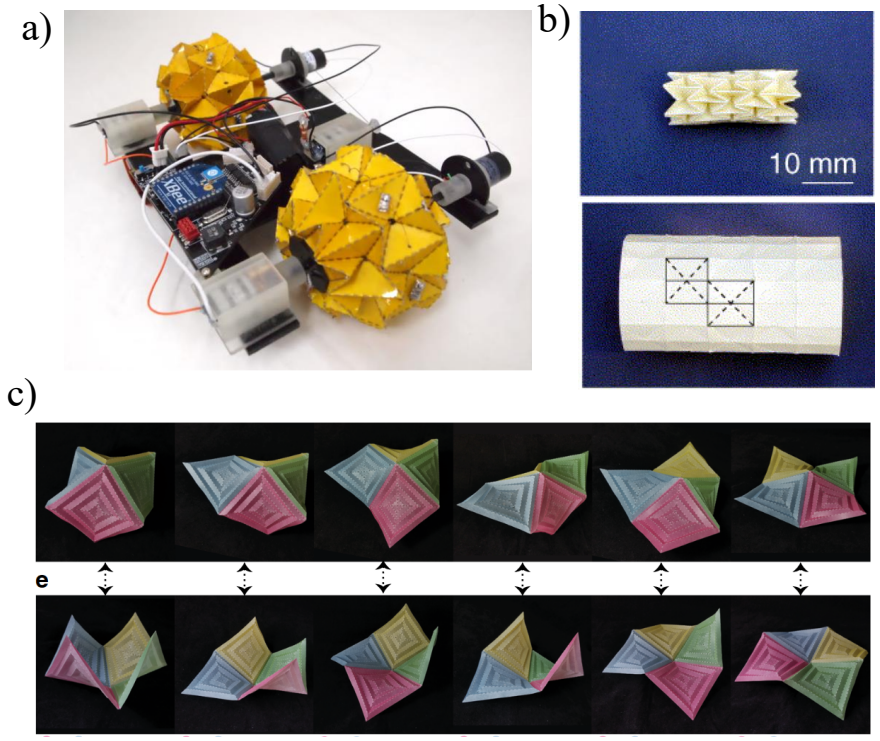

Figure 11: a) Deformable robot wheels: an actuator changes the wheel shape and adapts it to the ground condition [37]. b) Auxetic origami tube, which expands radially when extended longitudinally. Both the folded and unfolded states are stable, making this structure a suitable candidate for the next generation of stents. [41]. c) Multi-stable origami tessellation made of four hypar origami units, which have twelve different stable configurations [39].

Cuts in kirigami sheets can produce interesting mechanical behaviors such as auxetic properties and multi-stability. It is the case of the pattern of Fig10b: it extends in the direction perpendicular to the uniaxial loading, and its cutting cells are bistable, which notably leads to non-uniform deployment [35]. However, one of the most prominent feature of kirigami sheet is their extreme stretchability discussed earlier, which comes from the large bending of slender elements in the parallel-cut pattern of Fig8c. This has raised interest for flexible electronics as shown in Fig12c. The electronic component can extend without actually stretching (and breaking) the conductive material, preserving the electrical circuit [42]. Because of the large deformation and elastic instabilities, kirigami sheets can have very non-linear stress-strain curves (see Fig12a, [25]). The mechanical response can be modified significantly through the cutting pattern, as illustrated by the two curves in Fig12a that

correspond to different slit lengths. Several studies have investigated the relationship between the arrangement of cuts and mechanical properties, to achieve "engineered elasticity" [43, 44, 45, 46, 25]. High stiffness states were also reported when kirigami sheets deform plastically upon stretching, as shown on Fig12b, [47].

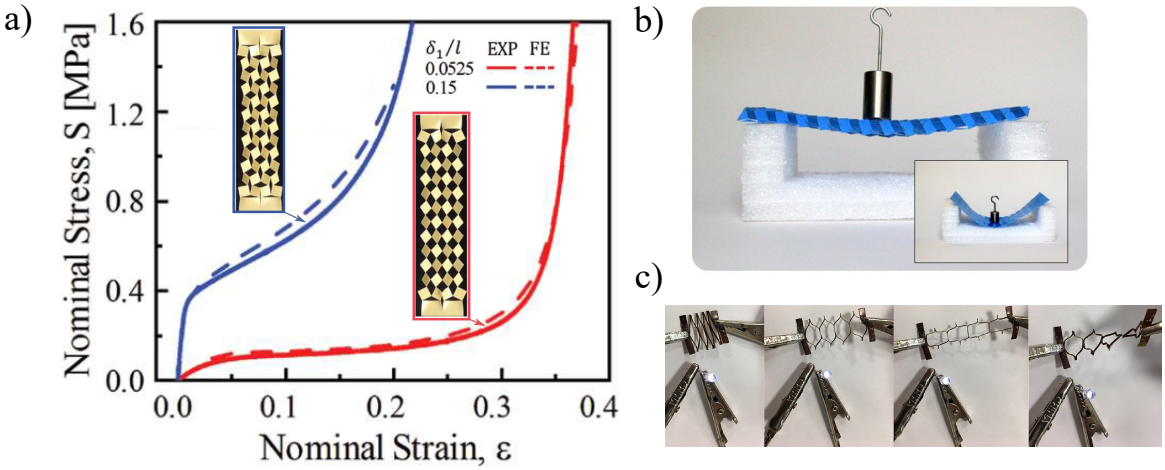

Figure 12: a) Stress-strain curves from two kirigami sheets with different cutting parameters, which leads to two distinct responses [25]. b) A plastically deformed sheet has a higher bending stiffness than the flat cut sheet (inset) [47]. c) Flexible and extensible electronic component [42].

Origami and kirigami methods have proved to be promising for mechanics and engineering. The addition of slits/folds allowsto overcome certain limitations of regular sheets (that only deforms isometrically with constant gaussian curvature for example) and to design customized kinematics and mechanical behaviors. Note that mechanical studies have investigated the response of origami and kirigami sheets to only a few types of loading, typically applying in-plane uniaxial traction to characterize stress-strain relationships. In the following, we briefly discuss how these systems respond to other types of external solicitation, and what will be the specific characteristics of loading from a fluid flow.

0.4 Towards responsive origami/kirigami structures

One of the ongoing challenges in the field of origami and kirigami structures is to actuate them or make them responsive to changes in their environment (which is a fluid environment for us). To achieve this, it is necessary to be able to program their mechanical response to specific external stimuli. Previous investigations have mainly focused on axial tensile loading to understand the mechanical response of these structures. In the following, we will present other types of loading to which kirigami and origami have been subjected.

0.4.1 Different types of loading

Meta-structures can be actuated using shape-memory alloys (SMA) that have the ability to return to their initial shape at a given temperature. It has been used for the deployment or compacting of an origami stent, by simply varying the external temperature (Fig13a, [41]). Fig13b shows another example of a thermally-actuated structure, with the kirigami opening according to the ambient temperature [48]. By introducing a folded reflective substructure inside the pores, the authors were able to passively tune the structure's reflection capacity according to external thermal conditions.

A commonly used method of actuation in soft robotics is through the use of pneumatic networks or pouches. By pressurizing these embedded systems, it is possible to actuate an

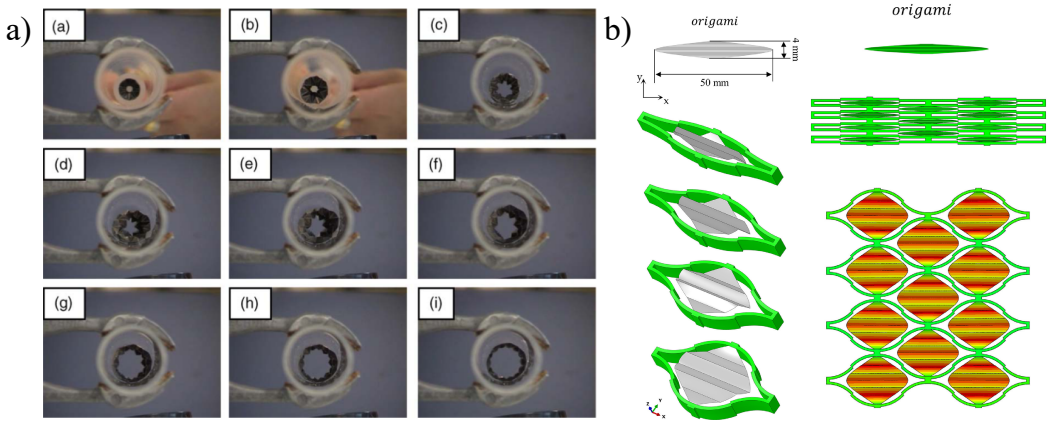

Figure 13: a) Tubular origami stent expanding once the external temperature is above 319 K [41]. b) Progressive deployment of kirigami reflector actuated thermally [48].

arm or enable locomotion. One of the challenges is to control the deformation of inflatable structures. To this end, kirigami has been explored, introducing a cutting pattern within an inflatable stretchable membrane [49]. Upon pressurization, a cylinder can then deform into a hook (Fig14). Pneumatic actuation has also been used to deploy origami cellular structures, using a pressurized air pouch enclosed inside. The non-trivial interaction between the internal fluid volume and the global deformation of the structure can result in an unusual negative stiffness, which could be exploited for energy absorption purposes [50].

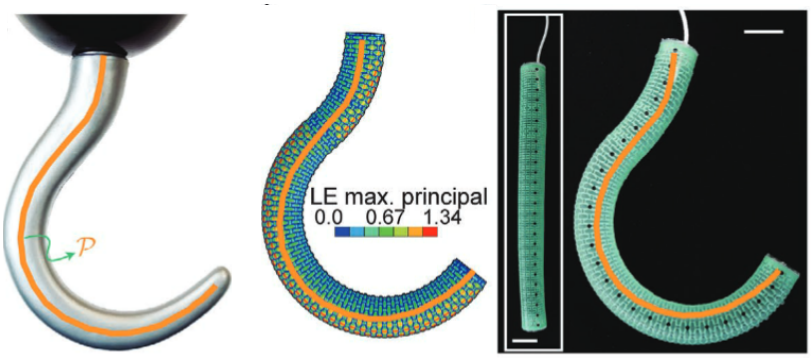

Figure 14: Inflatables with programmable shapes, made of a kirigami sheet embedded in an elastomeric membrane. Once pressurized, it deforms into a hook [49].

The above examples show the rich range of responses of origami and kirigami sheets to fluid loading, which has the specificity of depending on the shape. However, fluid is mainly used as a way to transmit uniform pressure forces, and no use has been made of its motion in these studies so far. In the following, we will discuss a few studies that have subjected origami and kirigami designs to flows. Note, however, that these studies focus exclusively on rigid structures that are fixed in a given configuration and thus have no fluid-elastic coupling.

0.4.2 Cuts in flows

There are limited studies on kirigami structures in the presence of fluid flow. The two existing ones primarily use the kirigami technique as a way to produce a surface with a three-dimensional texture that will manipulate flows. The sheet is frozen in the desired configuration. The first study presents a kirigami fog-collector [51]. The local geometry impacts the flow, creating vortices that improve aerosol capture while allowing the fluid to pass through the structure (Fig15a). The second study covers an aircraft wing with

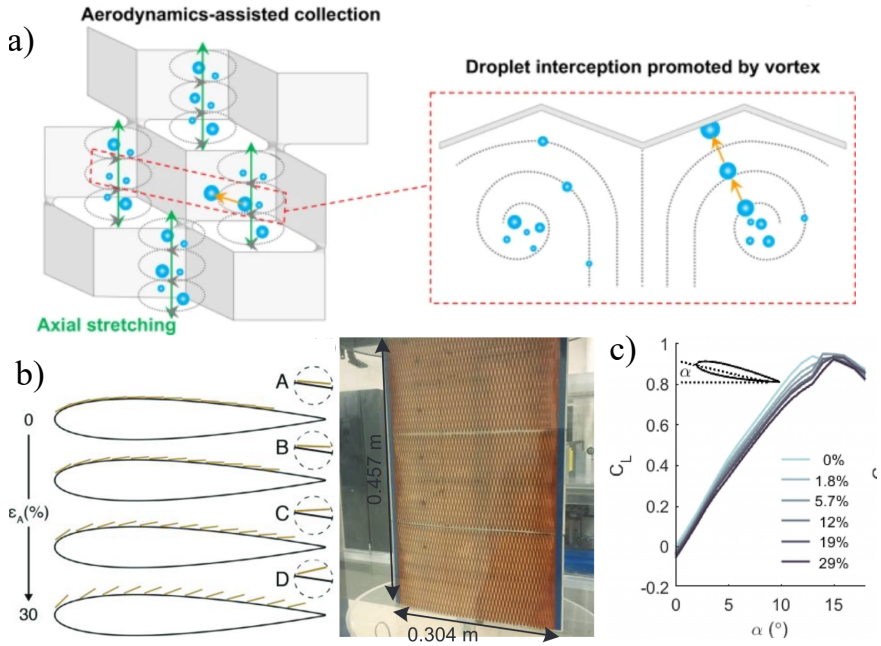

Figure 15: a) Kirigami fog collector; the 3D meso-texture forms vortices that trap the droplets and increase the capture efficiency [51]. b) Kirigami patches placed over a wing in various states of extension. c) The associated roughness shifts the stall angle [52].

a kirigami sheet to create a surface roughness that will affect the fluid boundary layer (Fig15b,[52]). This roughness can be modified through the sheet extension, which shifts the critical angle of attack at which the wing stalls and delay the phenomena (that is when the lift coefficient suddenly drops, 15c).

Importantly, both of these studies focus on fixed, rigid structures, and do not explore the possibility of allowing the kirigami sheet to deform in response to the flow. We aim to investigate this aspect. As for the (uncut) flexible plates of the literature, it will involve a coupling between the dynamic of the fluid and that of the deformable object. Forces exerted by the fluid will depend on the structure deformation, which in turn will affect the fluid flow. However, for kirigami structures, deformation involves a significant opening of the sheet, forming pores that allow fluid to pass through. As mentioned before, the size and geometry of those pore change with the sheet elongation, which will affect local fluid forces. We aim to study this poro-elastic system and how to control the shapes and forces that result from this interaction.

0.4.3 Folds in flows

Origami structures have also been little studied in the field of fluid-structure interaction. To our knowledge, only two studies investigated the aerodynamics of folded structures. In one study, the authors measure drag force and visualize wake patterns for a fixed configuration of a Miura-ori unit (Fig16a) to determine which configuration generates the least drag [53]. They relate the generation of vortices induced by the folded shape to the decrease of forces. In a more active situation (controlled by an external user), the work of Cozmei et al. (2020) investigates the use of two folding patterns as surface controllers [54]. By actively changing the folding state, they can modify the frontal area exposed to the fluid and, as a result, the drag force. They demonstrate that by adjusting the configuration of creases, they can achieve a targeted force for a given flow. This work suggests that changing the configuration of a folded structure alters its aerodynamic properties and that large shape shifts can lead to significant variations in fluid loads.

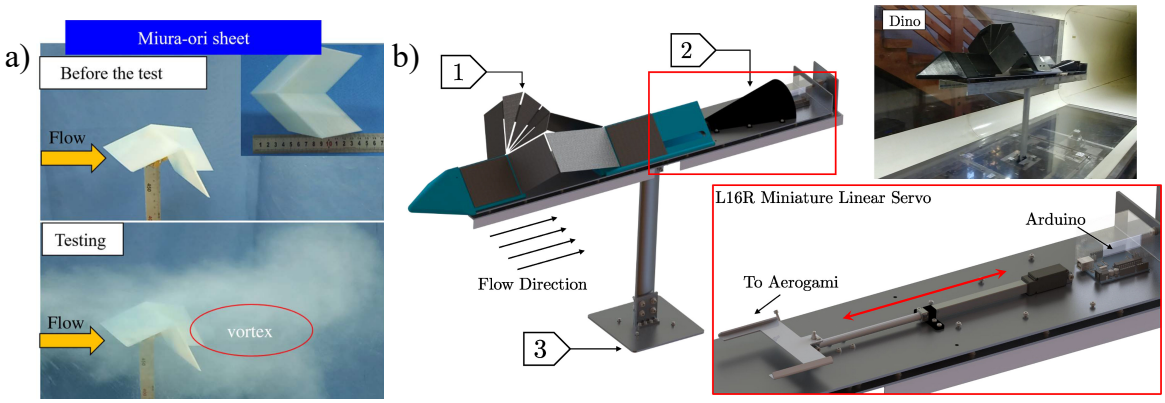

Figure 16: a) Flow around a Miura ori cell, [53]. b) An origami unit (1) can be deployed/compacted by a linear actuator connected to an Arduino and load sensor (2) [54]

Here, we are interested in studying deformable origami structures (as opposed to ones with a fixed configuration) that passively adapt their shape to the fluid environment. Given the large shape changes induced by the folding kinematics, we also expect new evolution of drag with flow speed that will depend on the pattern features. Similar to the way three leaves blow away in the wind, it is time to let the (meta)-structure be free.

0.5 Thesis outlines

In this thesis, we seek to answer the following question: **Can we use origami and kirigami techniques to tune the deformation of sheets in a flow, and the resulting drag forces?** To this end, we have to understand how folds and cuts impact the interaction with a fluid flow. It departs from the traditional framework of fluid/structure interaction in two ways. First, it involves unusual modes of deformations and mechanical properties. Second, the interaction of the small-scale structure with flows can impact local fluid forces and thus the deformation and dynamics at the larger scale. We investigated those aspects with an approach combining experiments in water or wind tunnels and theoretical models. We also adopted a bottom-up approach, starting with simple kirigami and origami geometries to understand the underlying mechanisms, and then expanding to more complex ones to probe the potential of the kirigami and origami methods.

This thesis is divided into two parts. The first part (chapters 1 to 4) focuses on deformations in a flow, and the second one (chapters 5 and 6) on the corresponding evolution of drag forces. The content of each chapter is introduced in the following.

In the first part, we investigate the use of the kirigami technique to control deformations caused by fluid flow, focusing on patterns with parallel and staggered slits. In **chapter 1**, we investigate the response of a uniform kirigami sheet in a water flow (the pattern is the same throughout the sheet). We characterize the deformation for different cutting parameters to understand the effects of these cuts on the fluid-structure interaction and compare the experimental results to a theoretical model that helps to explain the underlying mechanisms. We show that the cutting pattern controls both the elastic restoring forces that oppose the external fluid loading and the shape of the pores during the opening kinematics. The pore geometry leads to unexpected asymmetric deformations despite the symmetry of the initial pattern.

The next two chapters investigate the effect of varying the pattern spatially (as opposed to the uniform pattern used in chapter 1), starting with kirigami specimens with two different zones. In **chapter 2**, we prescribe the direction of rotation of the local meso-texture and vary it along the sheet. It impacts the orientation of local fluid forces and the resulting

macroscopic shape. In **chapter 3**, we change the cutting pattern along the sheet, creating a non-uniform stiffness. Both of these spatial variations expand the range of possible shapes. Interestingly, since the direction of rotation of the elementary cells is defined relative to the flow, we show that the same non-uniform specimen can produce different deformations depending on the direction of the fluid passing through it. In the shorter **chapter 4**, we conclude the first part of the thesis by exploring potential ways to implement the inverse shape morphing problem, which consists in determining the cutting pattern that would create a desired shape in a given flow.

The second part of the thesis focuses on the impact of deformations on fluid drag forces. In **chapter 5**, we show that the deformation and opening of kirigami sheets reduce their drag, compared to that of a rigid structure. We analyze the evolution of drag with flow speed for uniform specimens with different cutting parameters and relate it to the effective stiffness of the sheet. Measurements on non-uniform specimens also yield interesting results: since the same specimen can produce two different shapes, it also results in two different evaluations of drag with flow speed.

Finally, **chapter 6** studies the impact of folds (instead of slites) on the reconfiguration process and the resulting drag. We focus on an elementary origami unit, the "waterbomb base", which is selected for its ability to fold from a flat disk into a very compact configuration. Drag measurements in an air flow show that these significant shape changes further enhance the mechanisms of drag reduction, to the extent that drag no longer increases with flow speed in regimes of large deformation. We characterize the origami behavior while changing its parameters such as the stiffness and arrangement of folds, and show that it allows us to tune the evolution of drag and in particular the value of the upper limit that it reaches.

Each chapter begins with a brief overview of the main content and key objectives and concludes with a summary of the main results. Throughout this thesis, you will find interludes, identified by a colored box and a number, which provide additional information or anecdotes related to our study. These interludes are not essential to understanding the main text and can be skipped for a quick read. Let us start the journey.

PART I

INTRODUCING CUTS TO CONTROL SHAPES IN A FLOW

1

Uniform kirigami pattern: a complex interaction with flow

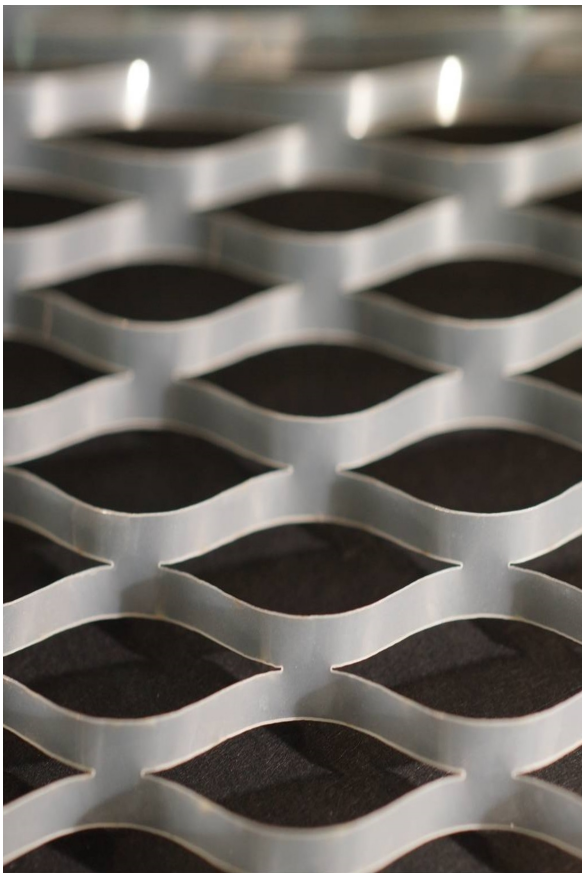

The purpose of this chapter is to characterize the influence of slits on the interaction of a thin sheet with a fluid flow. We begin by analyzing a uniform pattern of parallel cuts and investigate the relationship between the spatial arrangement of the slits and the deformation in a water flow. It reveals intriguing behaviors such as asymmetric deformation despite a symmetric cutting pattern. We also develop a simplified model to understand the underlying fluid-elastic mechanisms.

1.1 Kirigami pattern with parallel slits

Kirigami art is created by adding cuts to a flat sheet to create complex shapes. To study the interaction between a kirigami sheet and the surrounding flow, we focus on one specific tessellation that consists of a periodically spaced and staggered network of slits, as shown in Fig1.1. This cutting pattern is both simple enough for a representative experimental study and rich enough to exhibit original mechanical and structural properties that have been little explored in the field of fluid-structure interaction. Before submerging our kirigami sheets in water, let us have a quick look at the existing literature on this pattern.

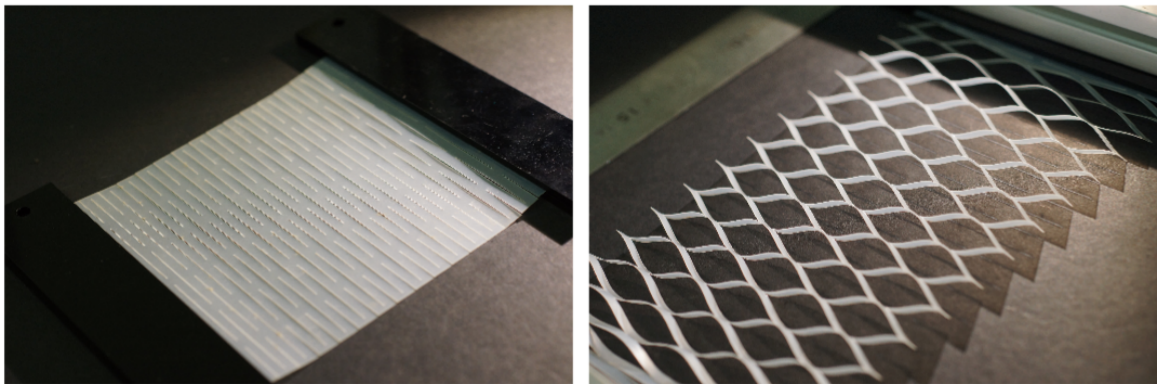

Figure 1.1: Kirigami with an array of parallel and staggered slits makes it highly stretchable.

1.1.1 Large stretchability

The addition of an array of parallel and staggered slits is not of particular artistic interest but it is one of the kirigami patterns that has been extensively studied in mechanics and engineering. Many fundamental works have notably focused on the particular mechanical response of this pattern. As discussed in the introduction, the addition of those slits transforms an initially inextensible sheet into a highly stretchable structure. I encourage the reader to test this with the kirigami sheet provided with the manuscript. Upon traction, the sheet can reach three to four times its initial length,[45]. This extensibility is not due to the stretching of the sheet itself but results from the large local bending of the uncut parts (see Fig1.1). Indeed, the slits divide the sheet into a set of slender plate elements that buckle out-of-plane when tension is applied in the direction perpendicular to the slits. The collective rotation and bending of those elementary plates allow for the global stretching of the entire structure. Such extensibility is interesting for us as it will result in large deformations in a flow, and thus significant fluid-structure couplings.

1.1.2 Three-dimensional meso-texture

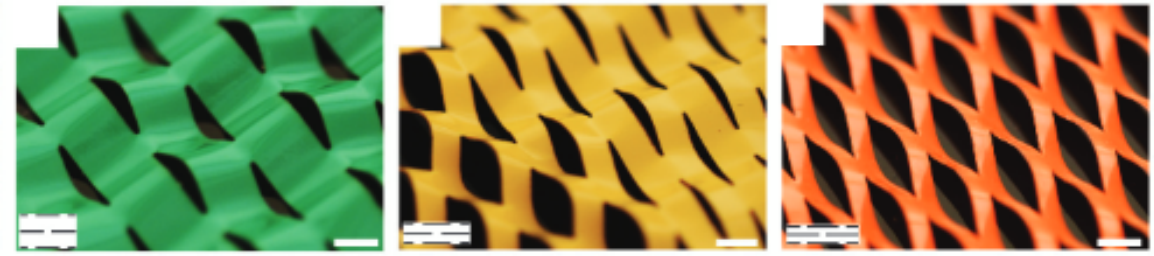

Figure 1.2: Three buckling modes depending on the cutting parameters and producing different types of meso-texture [55].

As discussed in the introduction, a three-dimensional texture forms on the kirigami sheet as it stretches, with elementary blades that become increasingly tilted with elongation and openings that widen. As we will see later, this 3D local texture will play a key role in the interaction with a fluid flow.

The local deformation and the tilting direction of the blades can differ depending on the cutting pattern. The pattern attached to the manuscript has narrow blades that rotate in the same direction as the structure is stretched (as on the cover photo of the chapter). However, this is not necessarily the case and other behaviors can be observed for different cutting parameters. As we will discuss in detail when describing our fabrication method, the cutting parameters for this tessellation can be reduced to only three quantities: the length of the slits L_s, and the gap between cuts d_y and between rows of cuts d_x (see Fig1.3b). By changing the latter, Yang et al. (2018) showed that different bending modes could be selected and other meso-structures can form [55]. As illustrated by Fig1.2, the authors distinguish two main modes: the first one is a symmetric bending with the rotation of the blades in alternate directions, which is particularly observable for larger gap values d_x (green sheet) compared to the slit length L_s. The second one (orange sheet) is an asymmetric mode where the cells rotate in the same direction. They also identify a third parameter range where both modes coexist (yellow sheet). In our work, we will restrict our parameters to the pure asymmetric mode which presents the most flexible behavior.

The cutting parameters play a key role in not only the local deformation of the sheet but also its mechanical properties, as discussed in the introduction. The pattern can be adjusted to produce a predictable and robust change in the mechanical properties of the sheet. As discussed in the introduction, deformations in flow depend on the structural resistance of the object. In the following section, we will thus describe the fabrication of the kirigami sheet and its mechanical characterization.

1.2 Manufacturing and mechanical properties

1.2.1 Cutting parameters

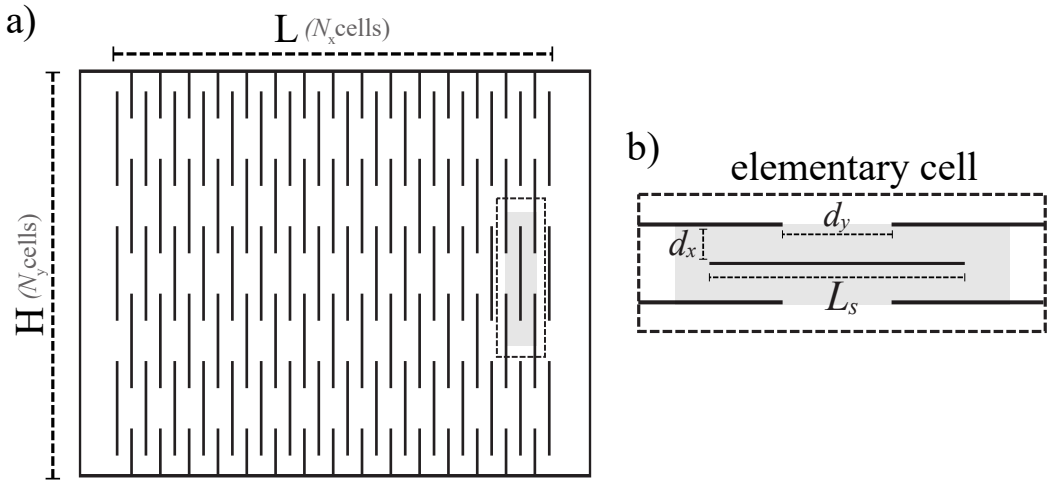

Figure 1.3: a) Schematic of the kirigami sheet with length L and height H, corresponding respectively to N_x and N_y unit cells (the latter is shown in grey). b) Zoomed view showing the cutting parameters: slits length L_s, and spacings d_x and d_y.

We consider a rectangular Mylar sheet with dimensions of length $L = 12$cm, width $H = 10.7$cm, and thickness $t = 100\mu$m that is small compared to L and H. More details on the choice of Mylar material and the cutting techniques (laser-cutter) are provided below. The

slit pattern consists of the periodic repetition of a unit cell shown in grey in Fig1.3a-b. It is characterized by three parameters: the slit length L_s, the spacing between the row of slits d_x, and the spacing between slits within a row d_y. The unit cell is repeated N_x times along the sheet length L and N_y times along its height H. The different dimensions are thus related by:

$$L = 2N_x d_x \quad \text{and} \quad H = N_y(L_s + d_y) \tag{1.1}$$

These relations couple the dimensions of the cells and their number, reducing the parameter space (for example, one cannot vary d_x without also varying N_x, etc.). Additionally, in order to preserve the asymmetric bending mode (tilting of the blades in the same direction) as described in [55] and earlier, we ensure that $L_s > 3d_y$.

We manufactured nineteen specimens, divided into three series, where we systematically varied each parameter while keeping the others fixed, as indicated in the following tables:

- Serie with varying L_s: d_x = 3.8mm, d_y= 4.4mm -

L_s (mm)	17.2	19.6	22.6	26.5	31.3	38.4	49.1

- Serie with varying d_x: L_s = 31.6mm, d_y= 4.4mm -

d_x (mm)	1.9	2.1	2.3	2.7	3.1	4.7	6.3	9.4

- Serie with varying d_y: L_s = 31.6mm, d_x= 3.8mm -

d_y (mm)	1.7	5.6	10.6	17.8

1.2.2 Mylar sheet

Let us briefly summarize the specifications for our choice of material: our experiments are performed in water, so the materials must be waterproof with a density close to that of water to limit any gravity or buoyancy effects (see interlude n^o5). Additionally, our kirigami sheets will undergo large deformations, so we need to prevent plasticity. The literature offers a variety of usable materials for kirigami fabrication, ranging from classical paper sheets [43] to polymeric materials (PDMS) [56], and various types of plastic ones [45, 44, 55]. In light of our application, we have chosen a PolyEthylene Terephthalate (PET) film with thickness $t = 100\mu$m. This material is widely used for its thermoforming properties in the food industry. Our mylar sheets are cut from a roll and usually have a slight pre-curvature. To remove it, they are placed in an oven at 75° for about 1 hour and pressed by a weight. The sheets come out flat and ready to be cut!

1.2.3 Laser-cutting slits

All cuts are made using a laser cutting machine. The pattern is first generated by a custom Matlab program that integrates all the parameters and constraints (Eq1.1). It is then loaded onto a drawing software (Inkscape or Coreldraw) that serves as the interface between the drawing and the cutting machine. We mainly performed our cuts using two models of the EPILOG laser cutter machine: the Mini Helix 50W and the Fusion Pro 36 with parameters specific to our materials and their thickness.

The use of a laser cutter is more reproducible and quicker than traditional hand-cutting done in art. This tool also allows us to easily change the pattern. The final rendering of a hand-cut or laser-cut slit is also different, with the edges of the slits being sharper in the first case and the slits thinner, as shown in Fig1.4a-b. The slightly rounded cut edges, obtained with laser cutting, also prevent the localization of stress under tension and potential tears [20]. The width of the slits is however greater in the case of the laser (Fig1.4b). The laser

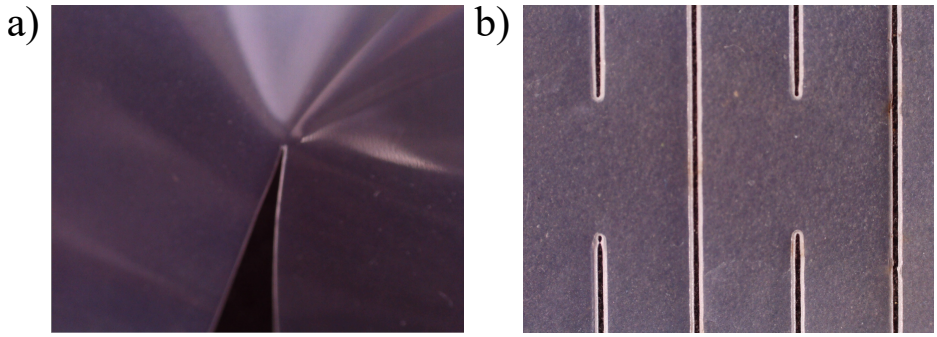

Figure 1.4: Zoomed views of slits on a mylar sheet (thickness $t = 100\mu$m). The cuts have been performed: a) by hand, and b) by a laser cutter machine.

beam strikes the sheet at the waist, whose width depends on the model and the laser cutting parameters (speed and power). After optimizing the latter, we arrive at a width of about $0.2 - 0.5$mm, which does not appear to influence the kinematics of opening or mechanical behavior.

1.2.4 Force-displacement curve

To characterize the mechanical response of a kirigami, we conduct tensile tests, measuring the force required to stretch a kirigami sheet (Fig1.5b). The sheet is clamped at its two edges and we use an Instron 5865 equipped with a 200N force cell (model 2525-816) to simultaneously record the displacement and the associated tensile forces, at a low imposed velocity of 0.2mm/s, ensuring quasi-static deformation.

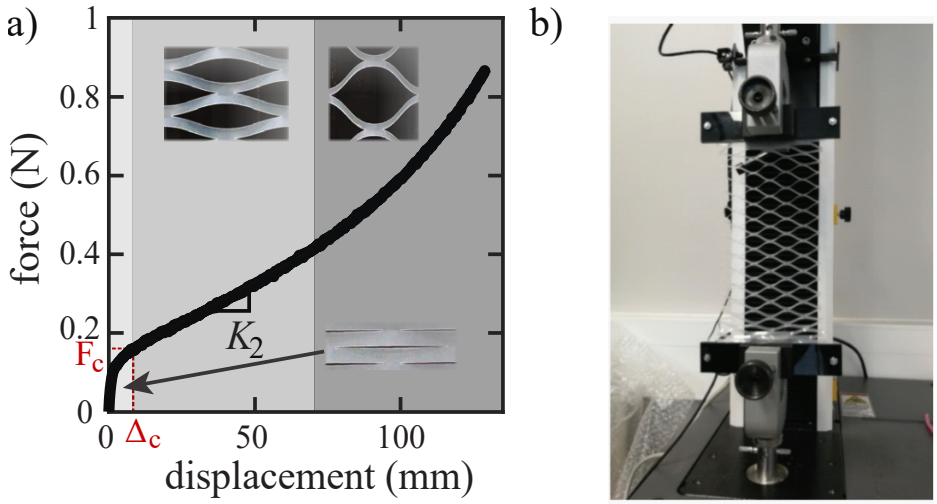

Figure 1.5: a) The typical force-displacement curve for a kirigami sheet with the cutting parameters $(L_s, d_x, d_y) = (31.6, 4.7, 3.8)$mm. b) Picture of a tensile test.

The test is manually stopped before rupture, all residual plastic deformations can then be removed by using Mylar's thermoformable property (one hour in an oven at $75 - 80°$C). Fig1.5a shows a typical force-displacement curve. We observe a highly nonlinear behavior, which is consistent with what is reported in the literature [43, 57, 45, 56, 58]. This curve can be divided into three regimes (denoted by different gray levels):

1. **Regime 1: In-plane deformation :** The kirigami sheet deforms in the tensile plane, and the curve presents a linear force-displacement relationship characterized by an effective stiffness K_1.

2. **Regime 2: Out-of-plane deformation :** Past a critical displacement Δ_c (associated with a critical force F_c), we observe a significant softening of the structure that corresponds to the transition from in-plane to out-of-plane deformation induced by buckling. This linear regime is valid over a large range of displacement and can be characterized by an effective stiffness K_2. Our structures in water mostly operate within this regime.

3. **Regime 3: Limit of deformation** The kirigami sheet then finally hardens as it further expands, with deformation focusing at the extremities of the cuts.

As discussed in the introduction, an advantage of the kirigami technique is that the mechanical properties are mainly controlled by the cutting pattern, making it easy to tune them through the slit arrangement. In the following, we will identify the relationship between the cutting parameters and the properties of the sheet. We will specifically focus on the first two regimes, which are characterized by their respective effective stiffness. In our fluid-structure problem, K_2 will prove to be the relevant stiffness, as deformation will mainly occur within the intermediate regime. However, we will also use K_1 at the end of this chapter to estimate the effect of mechanical non-linearities. Therefore, we will discuss both K_1 and K_2 in the next section.

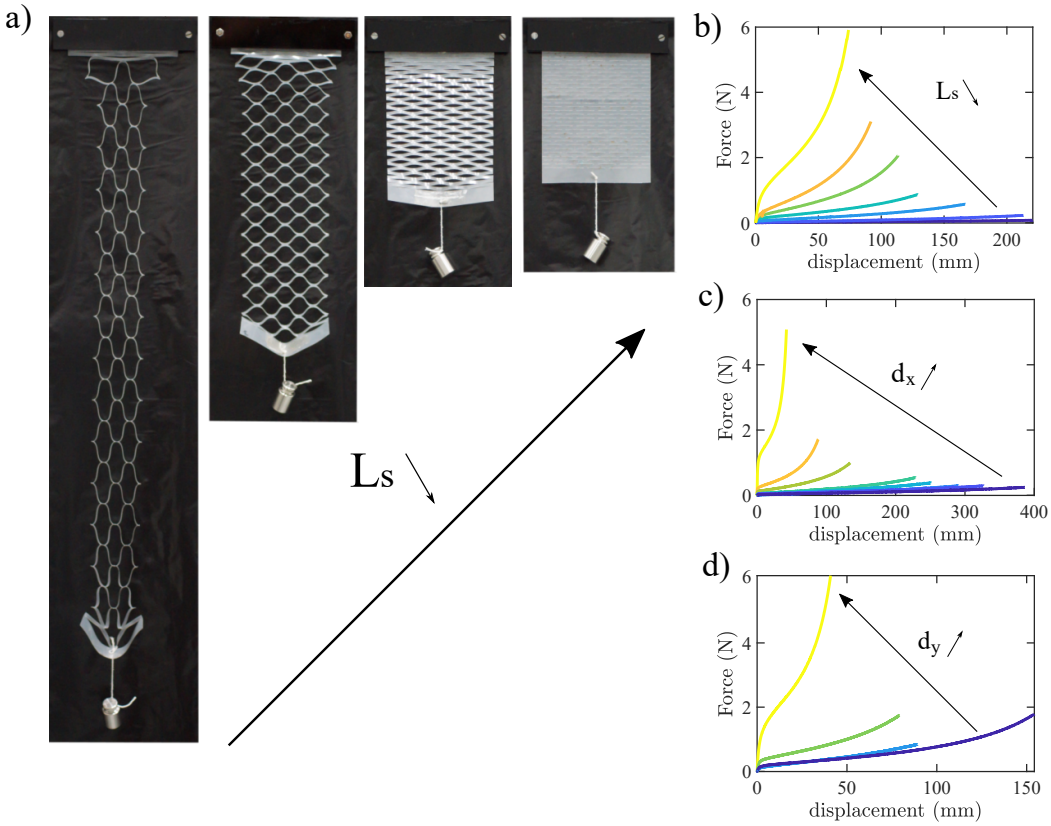

Figure 1.6: a) Illustrative test: four specimens with different slit lengths exhibit distinct deformation amplitudes when subjected to the same load (mass of 50g). Quantitative measurements of the cutting parameters in the three series detailed in the tables above: b) L_s, c) d_x, and d). We perform mechanical characterization through uniaxial tensile tests, using an Instron 5865 with a load cell 2525-816. The color gradient represents an increasing order of stiffness (K_2).

1.2.5 Engineered elasticity

All nineteen specimens with varying cut parameters were subjected to tensile tests. Before discussing the results, let us focus on an illustrative example shown in Fig1.6a. Four kirigami

sheets with different slit lengths L_s are subjected to the same load applied by a hanging mass of $50g$. Increasing L_s yields significantly larger deformations for a given load, showing that the mechanical properties can be greatly varied through small changes in the cutting parameters. Now, let us return to the tensile machine tests and be more quantitative.

The force-displacement curves are displayed in Fig1.6b-c-d, for each variation of parameters (namely, L_s, d_x, and d_y). The color scale ranges from blue to yellow corresponding to an increasing effective rigidity, the impact of each characteristic length is suggested by an arrow in the graph. We see that increasing d_x or d_y results in stiffer specimens (Fig1.6c-d), and increasing L_s produces more flexible specimens Fig1.6b. Here "rigid" refers to the effective stiffness coefficients $K_{1,2}$, that we are going to detail.

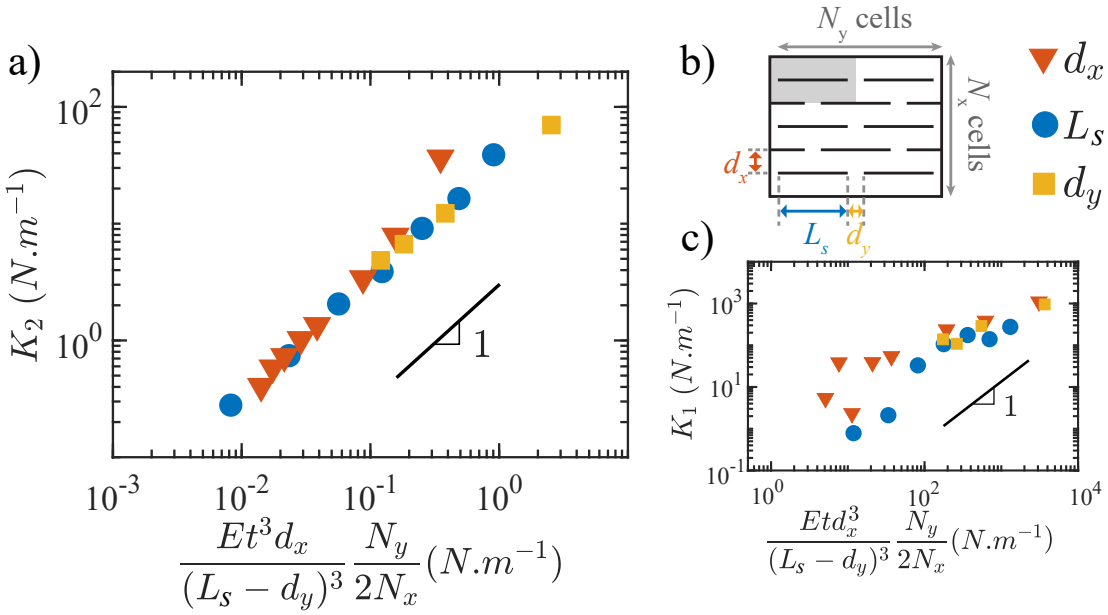

Figure 1.7: a) Effective stiffness K_2 measured in the intermediate linear regime (and K_1 measured in the first regime, in the inset), and compared to the predicted scaling of Eq1.2. b) Schematics showing the cutting parameters.

We determine the effective stiffness K_1 and K_2 through linear fits on the force-displacement curve in each regime. These coefficients vary significantly with the cutting pattern. The effects of each parameter on mechanical properties can be understood through a reasoning in terms of equivalent springs, as proposed in previous studies [43, 57, 45, 58]. In these models, a kirigami sheet is considered as a collection of slender plates that bend and act as springs arranged in series (along the $y-$ axis in Fig1.3a) and in parallel (along the $x-$ axis). The spring-like stiffness of a beam relates the force applied to the resulting deflection, and it is determined by its dimensions (length L, width W, and thickness t_b) and its Young modulus E [43]: Et_b^3W/L^3.

In practice, changing the cutting parameters means changing the dimensions of the individual beams. The first and second regimes, which correspond to in-plane bending and out-of-plane bending (with rotation), must be distinguished. In the first regime, the set of parameters (L, W, t_b) is mapped to $(L_s - d_y, t, d_x)$, and the stiffness of a beam scales as $Etd_x^3(L_s - d_y)^3$ [59]. In the second regime, the mapping is $(L, W, t_b) \rightarrow (L_s - d_y, d_x, t)$, and the beam stiffness scales as $Ed_xt^3/(L_s - d_y)^3$. The combined stiffness of all springs (N_y springs in series, and $2N_x$ in parallel) gives the stiffness of the entire sheet in each regime:

$$K_1 \sim \frac{Etd_x^3}{(L_s - d_y)^3}\frac{N_y}{2N_x} \quad \text{and} \quad K_2 \sim \frac{Ed_xt^3}{(L_s - d_y)^3}\frac{N_y}{2N_x} \tag{1.2}$$

Fig1.7a compares our measurements for K_2 to the predictions of Eq1.2 (and K_1 in the inset). In these graphs, each dot represents one specimen, with marker shapes (and colors) differentiating the variation of each cutting parameter as explained in Fig1.7b (for example, blue circles correspond to kirigami sheets with varying L_s). We find a good agreement: K_2 scales as predicted by Eq.1.2 with a numerical coefficient of 30, consistent with previous studies [43, 45, 58]. This coefficient is determined by the shape and boundary conditions of the constitutive beams and is discussed in interlude n^o4. The logarithmic scale shows a variation of K_2 by more than two orders of magnitude in the range of cutting parameters covered. Kirigami technique thus provides a valuable tool for predictable and largely tunable elasticity. The stiffness K_1 also shows reasonable agreement with the scaling (Fig1.7c), although with a larger dispersion. This is due to the fact that the slope in this first regime is experimentally more difficult to measure as it covers a very small displacement range (see Fig1.5a and Fig1.6b-c-d).

Interlude n^o4: Numerical coefficient for the stiffness scaling law

To determine the prefactor for K_1 and K_2, we need to further examine the bending plate analogy. Following the approach of Shyu et al (2015) for the second deformations regime, we consider the deformation of cells to be similar to that of four small cantilever beams with free-clamped boundary conditions (see the picture a and schematic b) [58]. A clamped-clamped beam with length l and bending stiffness EI, subjected to a load at its free end, produces a deflection of $\delta_{1,\text{beam}} = (4Fl^3)/(EI)$. By substituting the parameters of the kirigami unit cell and inverting the expression, one deduces the force for a single beam.

$$F_{1\,\text{beam}} = \frac{16Et^3d_x}{(L_s - d_y)^3}\delta_{1\,\text{beam}}$$

The displacement of an entire cell is therefore expressed as $\delta = 4\delta_{1,\text{beam}}$. Similarly, the force is $F = 4F_{1,\text{beam}}$. The cells are connected in series and parallel, so the global formulation for effective stiffness in the second regime is finally obtained by multiplying by the periodicity factor $N_y/2N_x$

$$K_2 = 32\frac{N_y}{2N_x}\frac{Et^3d_x}{(L_s - d_y)^3}$$

Hwang et al. (2018) proposed a similar approach for the first regime[45], they find a prefactor of around 16 for clamped-clamped boundary conditions.

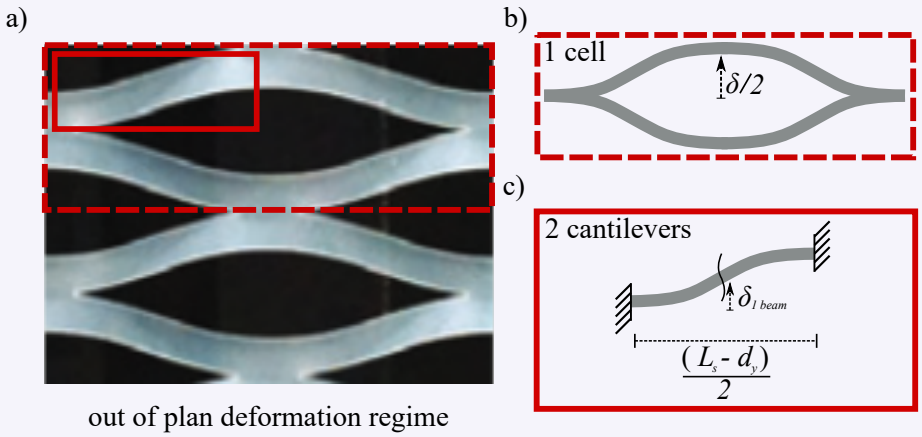

1.2.6 Evolution of the local geometry with elongation

The stretching discussed earlier occurs through a significant opening up of the material. In this thesis, we refer to the small-scale openings in the kirigami structure as "pores," as they allow fluid to pass through. These pores become larger with sheet elongation and change shape as the elementary beams become increasingly tilted and spaced apart. A relationship between the rotation angle θ of these beams relative to the sheet centerline and the elongation ε can be derived through simple geometry arguments [27]. Fig1.8b shows a side view of two neighboring cells of width $2d_x$ (see cell definition in Fig.1.3). Upon stretching, the blades tilt at an angle θ and the distance between cells becomes d. These lengths and angles are related by $\cos\theta = 2d_x/d$, and the elongation ε is defined as $d = 2d_x(1+\varepsilon)$. We thus obtain:

$$\cos\theta = \frac{1}{1+\varepsilon} \tag{1.3}$$

Note that this relationship does not depend on the blade size d_x, meaning that the tilting motion is purely geometric and independent of cutting parameters. The validity of Eq1.3 can be experimentally confirmed by taking pictures of kirigami sheets during elongation and measuring the ratio of void to total surface, which corresponds to a porosity $\Phi = (d - d')/d$ with $d' = 2d_x\cos\theta$ being the blade projection in the observation plane (as shown in Fig.1.8b). This can be rewritten as a function of elongation:

$$\Phi = \frac{(1+\varepsilon)^2 - 1}{(1+\varepsilon)^2} \tag{1.4}$$

All the kirigami patterns were subjected to a simple controlled displacement test, and porosity is measured through image analysis (typical snapshots can be seen in the inset of Fig1.8a). After a binary thresholding process (as shown in Fig1.8c), Φ was calculated by counting the black pixels relative to the total image size. The results are shown in Fig.1.8a (with markers representing each family of parameters) and compared to Eq1.4 (dashed black line). The two show good agreement, supporting the relationship between elongation and cell geometry evolution.

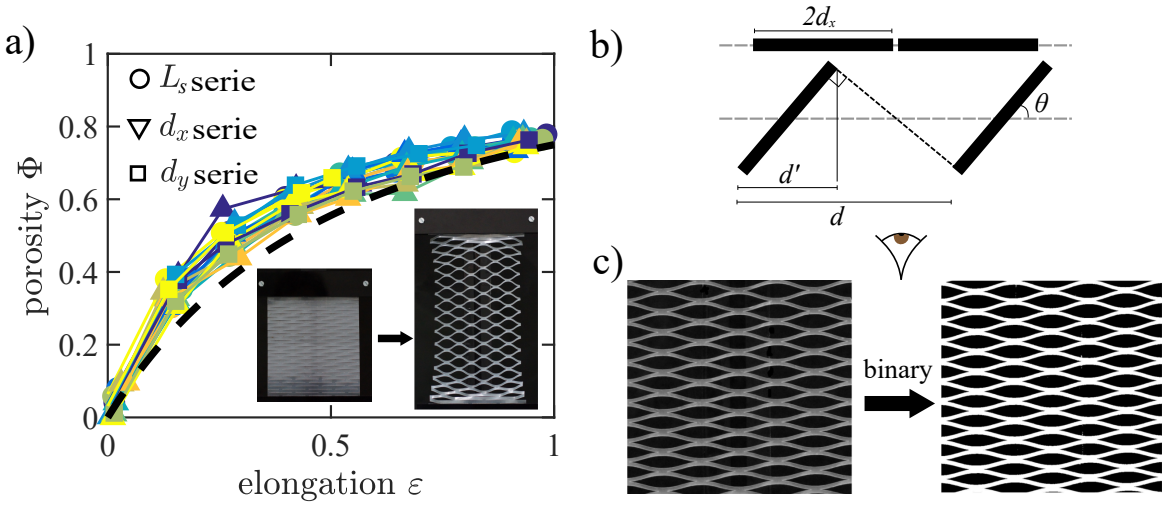

Figure 1.8: a) The evolution of porosity is plotted against elongation (experiments shown with markers and the dashed black line represents eq.1.4). b) Schematic of cutting cells rotating out-of-plane at an angle θ upon stretching. c) Thresholding process from a raw picture to a binary one, with pores corresponding to black pixels.

Although the stiffness and non-linear mechanical properties of the kirigami sheets are closely tied to the cutting pattern, the pore opening kinematics is the same for all. The rotation of

the elementary cells out of the plane is purely a geometrical process and cannot be modified without changing the nature of the paving. Now that the mechanical behavior has been characterized, it's (high) time to immerse the kirigami sheets in water.

1.3 Flow-induced deformation of a uniform kirigami sheet

1.3.1 Experimental set up

We conducted experiments in a closed circuit water tunnel, as depicted in Fig1.9a. A pump placed below the test section drives the water flow, which is measured by an integrated mechanical flow meter. The pump generates flow rates ranging from 40 to 300 LPM (liter per minute), with increments of 20 LPM. The flow enters the test section (dashed red rectangle in Fig1.9a) after passing through a converging section. The test section measures 15×15 cm, resulting in typical speeds between 3-22 cm/s.

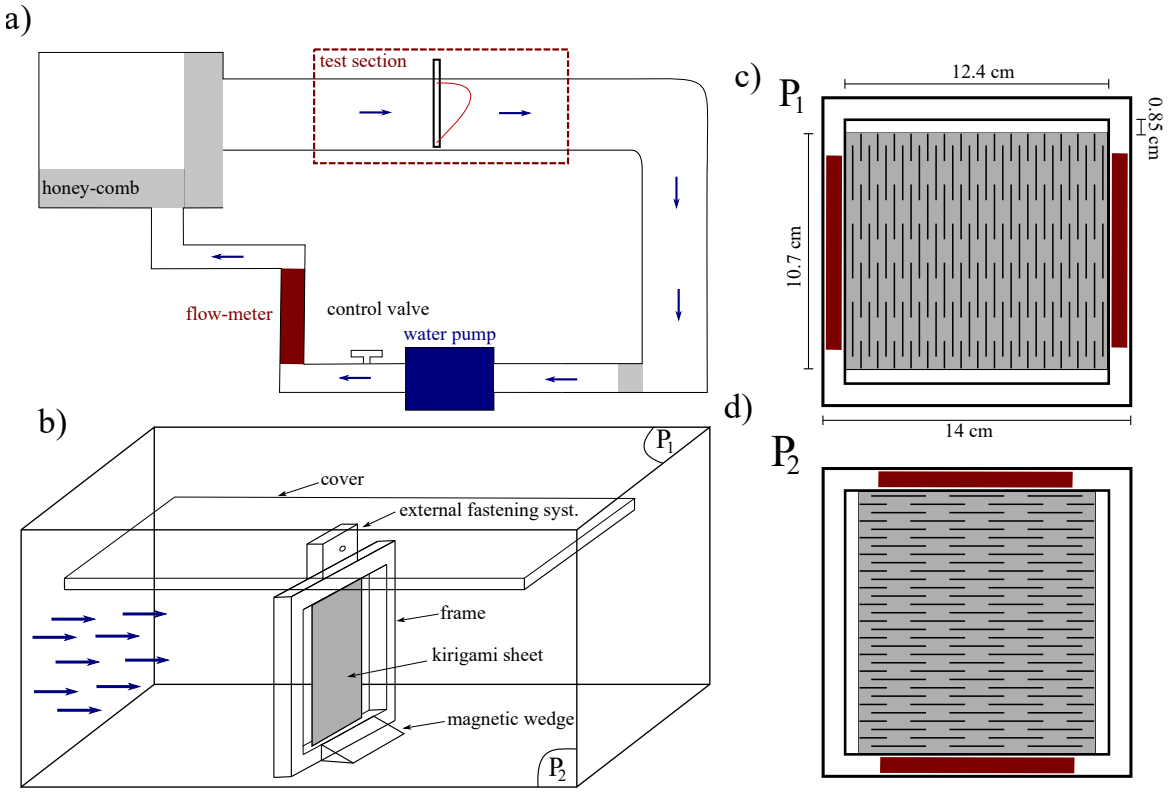

Figure 1.9: Schematic view of a) The water tunnel setup with its recirculating flow, b) The test section with the clamped kirigami sheet, and c-d) The two ways for fixing the kirigami sheet in the frame and their dimensions. The two red rectangles illustrate adhesive strips that improve the fixation of the kirigami sheet.

As shown in Fig. 1.9b, the test section consists of three fixed walls with the top side being a free surface. In our experiments, the top is always kept closed with a custom-designed Plexiglas cover that has a slot to secure the frame holding the specimens. The kirigami sheet is clamped at its two edges to the frame by sandwiching it between two Plexiglas plates that are screwed together and further secured with double-sided tape. The dimensions of the frame are shown in Fig1.9c. Note that the height of the kirigami sheet H is slightly smaller than that of the inner frame H_f, leaving clearance between the frame and the sheet. To prevent bending of the frame due to fluid forces, a magnet wedge is placed on the bottom wall of the channel for a second point of support; no frame deformation is thus observed. The kirigami can be clamped either horizontally as is the case in this chapter (Fig1.9c), or

vertically as will be the case in the following chapters to facilitate visualizations (Fig1.9d). The two configurations yield the same behavior indicating a negligible effect of gravity (see interlude n^o5 as well). The deformation of the sheet is captured by a camera that is positioned far enough to avoid distortions.

Interlude n^o5 : Effects of gravity (and buoyancy)

The structure deforms due to fluid forces generated by the flow. However, another force, gravity, is also present. In all our experiments and modeling, we neglect gravity, assuming that the forces associated with the flow are greater. To test this assumption, we can calculate the magnitude of each force (per unit length): fluid force scale as $\rho_w U^2 H$ (for our range of Reynolds number, given below) and gravity + buoyancy forces give $(\rho_m - \rho_w)gHt$, respectively. Where ρ_w and $\rho_m = 1.38 g/cm^3$ are the density of water and Mylar respectively, and g is the gravitational acceleration. With a mass per unit length of approximately $\rho_m Ht \approx 14$ g/m and a flow velocity $U = 0.15$ m/s (mid-range value for our set-up), we find that the gravity and buoyancy effects are approximately 60 times weaker than the fluid force.

In this setup, blockage effects are substantial as the frame and kirigami sheet take up nearly 90% of the test section when it's undeformed. The impact on the flow will be considered in the theoretical modeling later, but for the experimental results presented in the following, the flow speed U will correspond to the flow passing through the empty frame. It is determined by flow rate conservation and results in speeds between 4 and 32 cm/s.

The kirigami sheet quickly reaches its equilibrium deformed shape when subjected to a flow, and no noticeable vibrations have been observed. Before discussing the first experimental results, we will briefly introduce the image processing and analysis performed to quantify the deformation of a kirigami sheet in flow.

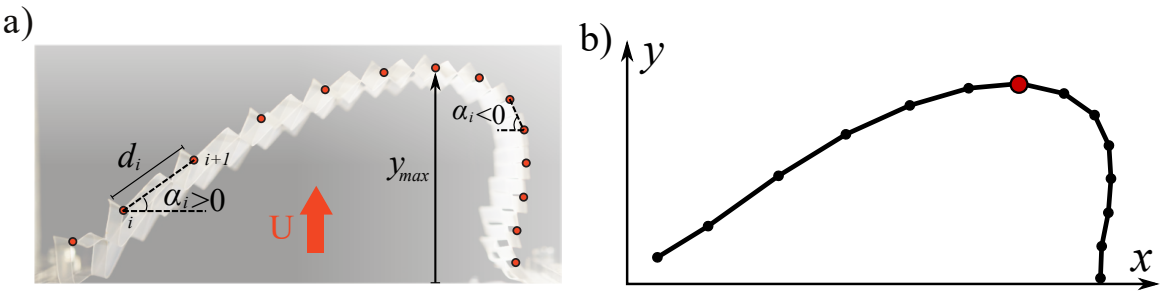

Figure 1.10: a) Typical shape profile extraction from top-view pictures, with orange dots locating the center of elementary cutting cells (on the top row). y_{max} is the amplitude of the deformation and d_i the distance between cell i and $i+1$. b) Corresponding deformation profile, the amplitude y_{max} is highlighted by a red point.

1.3.2 Image analysis and shape extraction

Due to our choice of cutting pattern and boundary conditions, the deformation of the kirigami sheet in a flow is invariant along its height. As a result, we can determine its shape through a single snapshot (see Fig1.10a). We then track the position of each unit cell by manually marking their centers using the ImageJ software (shown as dots in Fig.1.10a). This tedious method was later improved and fully automated (more details in Chapter 2). We obtain a set of points (x_i, y_i), where $i \in [1, N_x]$ is the cell number, which gives us the global deformation profile (as shown in Fig1.10b). To describe the deformation, we define several quantities, the simplest of which is the deformation amplitude, $y_{max} = \max(y_i)$, marked by a red point in Fig1.10b. While focusing on the amplitude is a straightforward

way to characterize deformations, it does not provide any information on the local scale. We can also extract two other quantities:

1. **Local elongation** $\varepsilon_i = \frac{d_i - 2d_x}{2d_x}$, with $d_i = \sqrt{(x_{i+1} - x_i)^2 + (y_{i+1} - y_i)^2}$ the distance between the *i-th* and the *i+1-th* cells, which is compared to the distance at rest $2d_x$. Note that we can estimate the cells tilting inclination from this measurement using the geometric relation in Eq1.3 (more details are given in the interlude n^o6).

2. **Local profile inclination**: $\alpha_i = \text{atan}\left(\frac{y_{i+1} - y_i}{x_{i+1} - x_i}\right)$. For a value of 0, the sheet is perpendicular to the flow, and for $\pi/2$ it is parallel to it. This variable is algebraic and can be either positive or negative (see sign convention in Fig1.10a).

1.3.3 Typical behavior: an asymmetric expansion

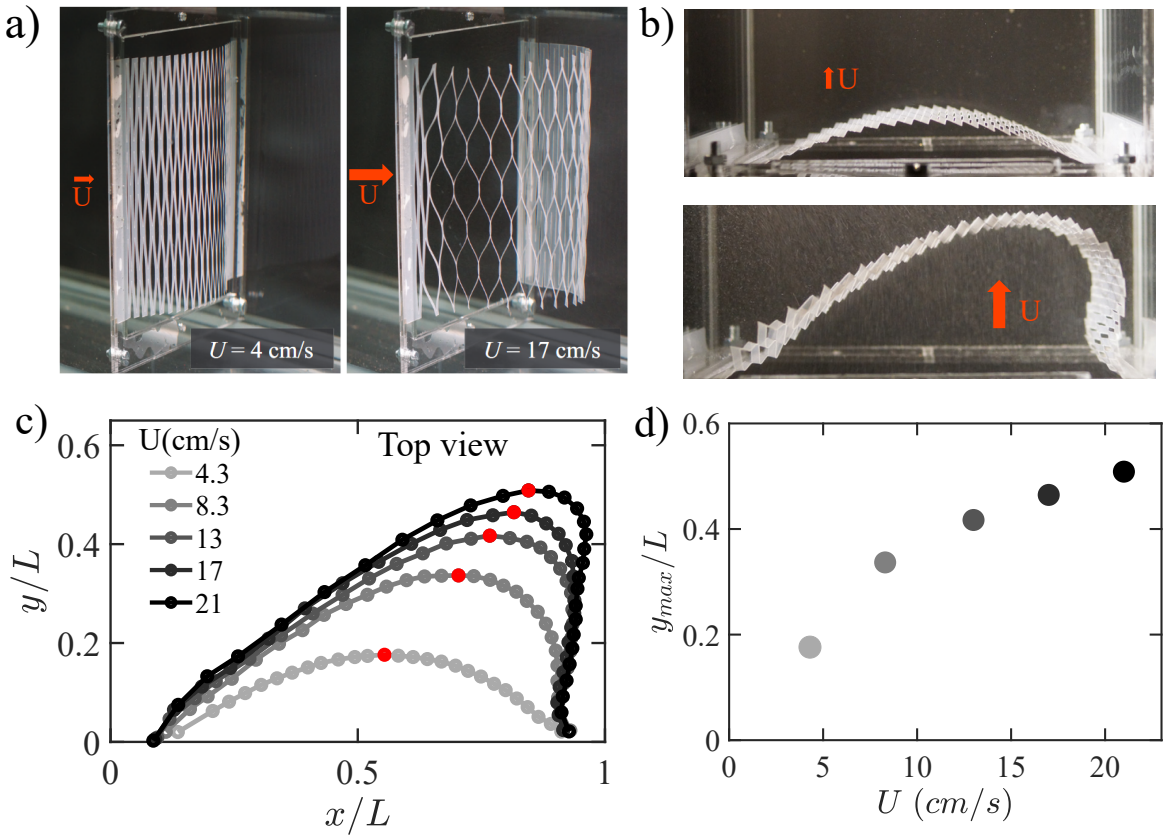

Figure 1.11: a) Deployment of a kirigami sheet in the water flow for a typical specimen (L_s = 3.16 cm, d_x = 1.9 mm, d_y = 4.4 mm, N_x=30 and N_y=3). b) Top-view pictures. c) Typical shape profiles of the sheet (of length L), when increasing the flow speed U (dots locate the cutting cells, see Fig1.10a-b). d) Dimensionless amplitude y_{max}/L as a function of U.

Fig1.11a-b show the typical deformation of a kirigami sheet in the water flow. As we gradually increase the flow speed, the sheet stretches, opening pores that let the fluid through. The two-dimensional profiles (from a top view) are displayed in Fig1.11c, with the grayscale indicating flow velocity U. It shows a significant expansion of the kirigami specimen, which tends to slow down as the sheet becomes more and more porous. This expansion can be quantified through the simple observable y_{max} (deformation amplitude), plotted as a function of U in Fig1.11d.

An important observation is that the profile is asymmetric with a lobe facing right, despite the cutting pattern's symmetry. This interesting feature is due to the three-dimensional

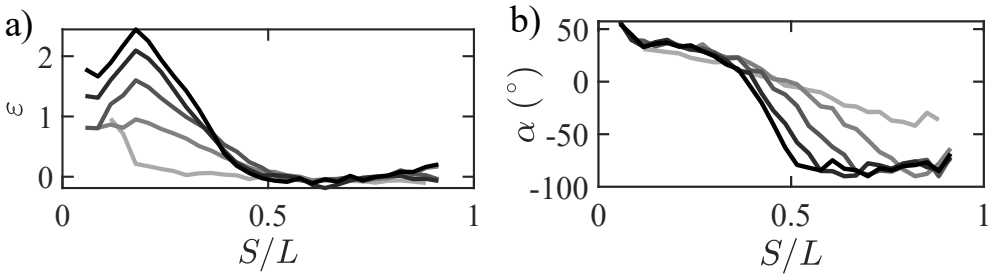

Figure 1.12: a) Local elongation and b) profile angle, along the curvilinear coordinate S (defined in the unstrained reference configuration), for the kirigami specimen of Fig1.11. The light-gray to black color scale corresponds to increasing velocities, which are the same as in Fig1.11c-d.

geometry of stretched pores, which will be discussed in further detail later. The asymmetry of the shape profile can also be seen at the local scale in Fig1.12. Fig1.12a displays the local elongation versus the curvilinear coordinate S along the sheet, defined in the unstressed reference configuration. It shows that half of the original sheet gradually elongates (for $S \leqslant 0.5$), while the other half remains fairly unstretched. As shown in Fig1.12b, this undeformed portion tends to align with the flow direction ($\alpha \sim -90^o$).

In the following paragraph, we will present the evolution of these same variables but for three patterns whose cells width differ, we thus apprehend the effect of a local geometry change on the response in a flow.

Interlude n^o6: Cells tilting and elongation : $\theta(\varepsilon)$

As previously stated, the rotation angle of the elementary beams θ is linked to the local elongation ε through Eq1.3. This connection was confirmed experimentally for kirigami sheets under uniaxial loading (and stretching in a plane) through the porosity measurement (see Fig1.8). We can show that the same holds true for a kirigami sheet deformed out-of-plane and in a water flow, as shown in the figure below. The figure below shows the elongation ε and angle θ measured in our flow experiments. It shows good agreement with Eq1.3.

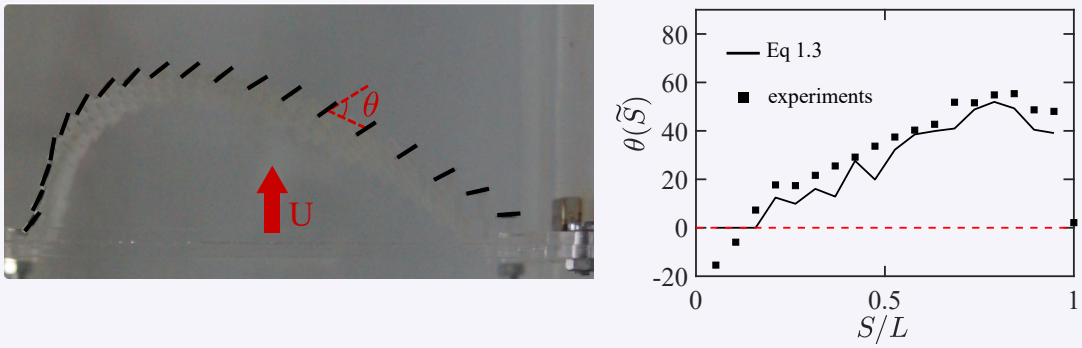

Except for the sign changes of θ that may occur near the clamping point, which can result in a slight bending of the whole sheet, as shown in the attached picture.

1.3.4 Parametric study and Cauchy number

To evaluate the impact of the slit pattern on flow-induced deformation, experiments are performed in the water tunnel for all kirigami specimens. As an illustration, Fig1.13a-b-c display the profiles for three sheets with different slit row spacings d_x, along with the corresponding evolution of deformation amplitude y_{max}/L versus flow velocity U in Fig1.13d. All specimens gradually expand, with a growth of y_{max} with U that gradually slows down, and

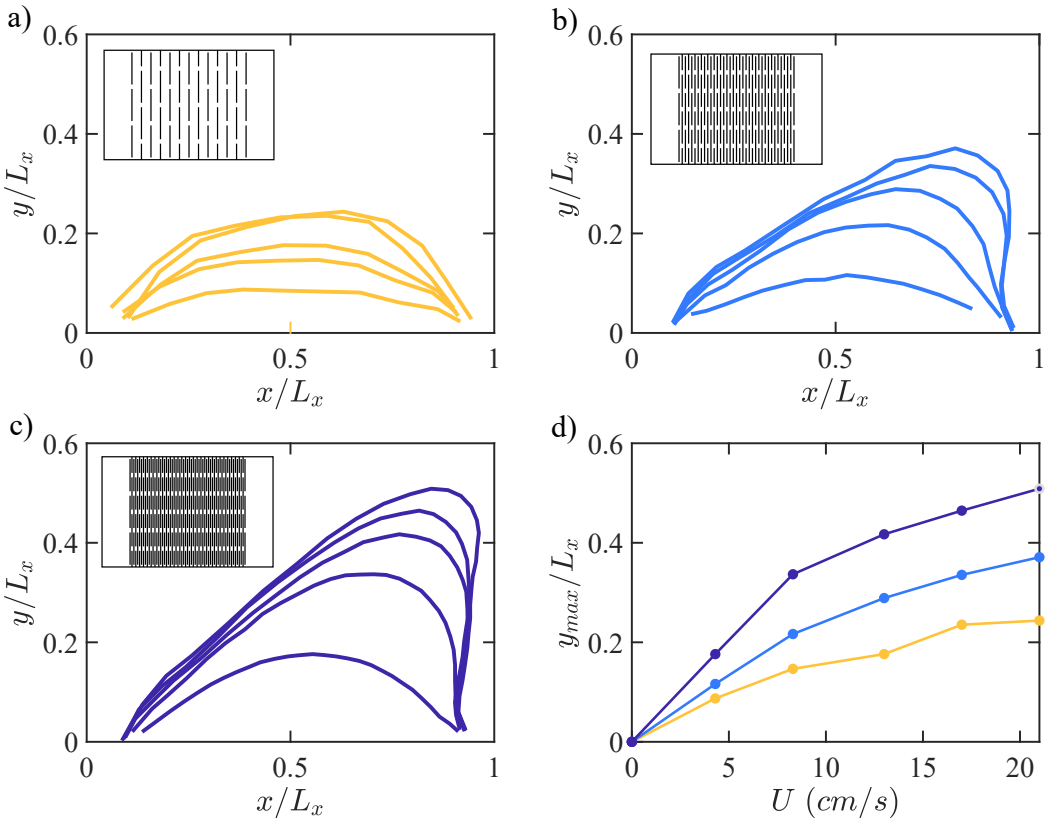

Figure 1.13: Shape profiles for an increasing flow speed (same range than for Fig1.11c) for three patterns from the d_x series: a) d_x = 9.4 mm (N_x = 6), b) d_x = 2.7 mm (N_x = 18, c) d_x = 1.9 mm (N_x = 30). d) Corresponding evolution of the deformation amplitude y_{max}/L as a function of incoming velocity U

with increasingly asymmetric profiles. However, deformation is less pronounced for larger d_x at a given U. This result seems intuitive based on the earlier mechanical characterization, which showed that increasing d_x leads to stiffer sheets.

Alternatively, instead of presenting the evolution of deformation with U for a specific sheet, we show in Fig1.14a the evolution of shapes at a fixed velocity U for sheets with different stiffness. The colors distinguish samples with different d_x, with blue representing soft sheets and yellow representing stiffer ones. As previously observed, reducing stiffness leads to larger expansion. More interestingly, the similar profile evolution in Fig1.13c and Fig1.14a indicates that changing the flow speed is equivalent to changing sheet stiffness.

Amplitudes for all parametric series are presented in Fig1.14b-c-d as a function of flow velocity U. Each curve corresponds to a specimen with a color gradient defined based on the stiffness evolution (with blue corresponding to a soft sheet, and yellow to stiffer sheets). It is observed that smaller d_x and d_y result in larger deformation (Fig1.14b-c), and conversely decreasing L_s reduces the deformation. This order of the curves is similar to that of force-displacement graphs, and the softer the sheet, the greater its deformation

A natural step is then to define a Cauchy number C_y, in line with previous studies and as presented in the introduction. It compares the fluid loading per unit length $\rho U^2 H$ to the sheet effective stiffness K_2:

$$C_y = \frac{\rho U^2 H}{K_2} \tag{1.5}$$

Fig1.15 shows the evolution of the deformation amplitudes for all kirigami specimens (the three parametric series with varying L_s, d_x and d_y). Data collapse onto a single curve over

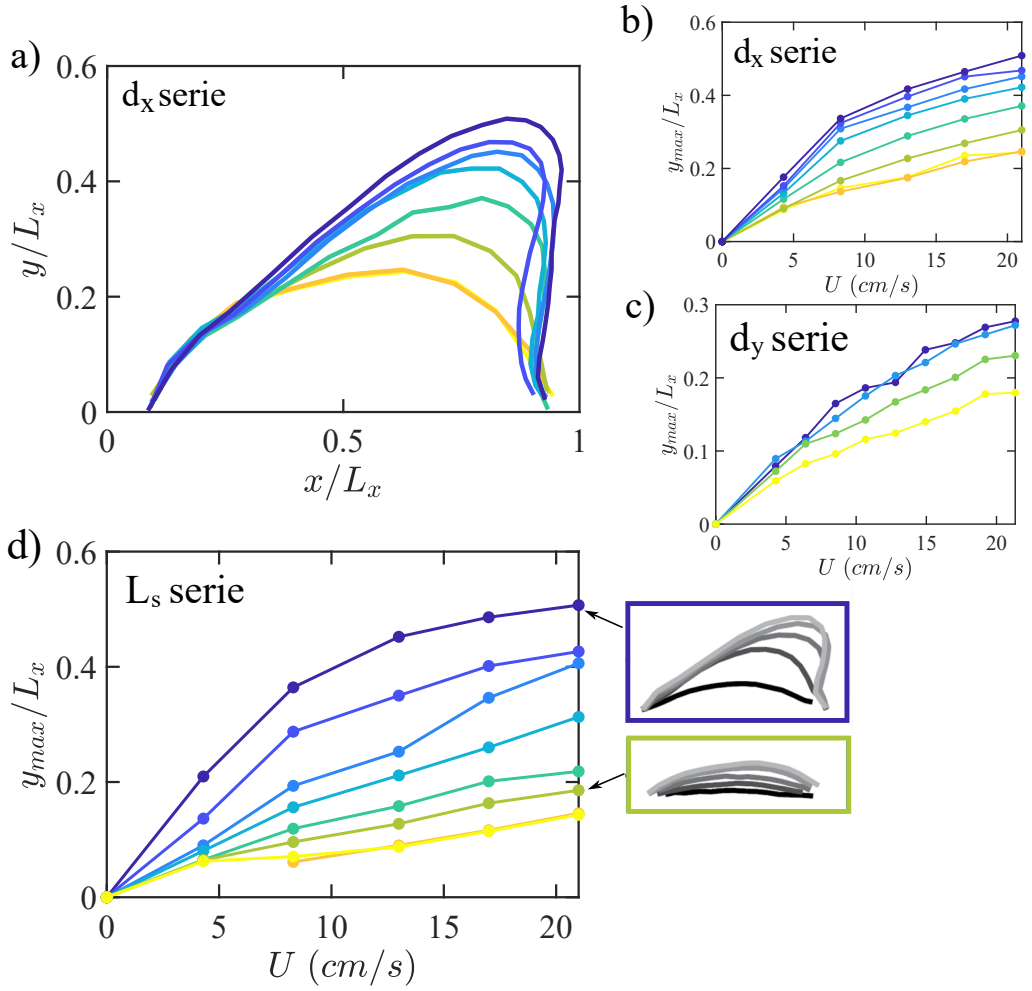

Figure 1.14: a) Deformation profile of kirigami sheets with different parameter d_x, in a flow with fixed speed $U = 21$ cm/s (maximum speed of the range explored). Dark blue corresponds to the smallest d_x (flexible sheet) in the parametric series (see series table), and yellow to the largest d_x (stiffer sheet). Amplitudes of deformations for all 19 cutting patterns, classified according to their series b) d_x, c) d_y and d) L_s as a function of velocity U. For the last graph, two deformation shapes are provided.

four orders of magnitude of C_y. It shows that the behavior of the kirigami sheets is indeed governed by the balance between fluid loading and the elastic resistance of the sheet, which is captured by this elasto-hydrodynamic Cauchy number. It also corroborates that stiffness K_2 is the relevant mechanical parameter in our study and that deformation is dominated by pure stretching in the intermediate mechanical regime.

While the Cauchy number provides key insight into the amplitude of the deformation, it does not account for its asymmetry. We discuss this point in the next section.

1.3.5 Origin of the shape asymmetry

As mentioned earlier, one has to look at the small-scale structure of the kirigami sheet to understand the asymmetric deformation. The deformed elementary cells are analogous to blades (highlighted in black in Fig1.16), which are tilted relative to the direction of the incoming flow. Those inclined blades are subjected to both drag and lift forces. It results in a local fluid loading on the sheet that not only has a normal component, but also a transverse one. The latter induces local tension, consistently deflecting the profile to one side.

Note that cut units should a priori collectively buckle up or down indiscriminately, but our

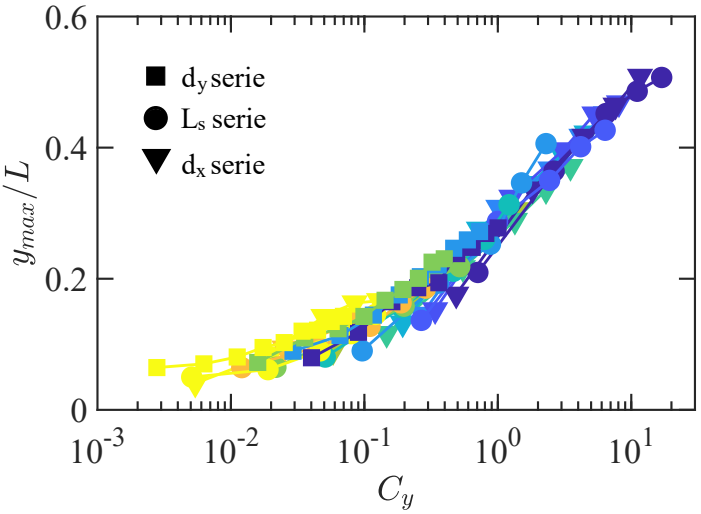

Figure 1.15: Deformation amplitudes as a function of the Cauchy number C_y (see Eq1.5) for all 19 cutting patterns. Color gradients differentiate specimens within each parametric series, denoted by symbols.

laser cutting fabrication seems to bias towards a preferred tilting orientation. The latter can however be reversed by flipping the specimen upside down in the water tunnel. The sheet then spontaneously deforms into the left-right mirror image (see the inset of Fig1.16 and the interlude n^o7).

1.4 Theoretical modeling

To improve our understanding of the complex interaction between fluid flow, the poro-elastic kirigami sheet, and its changing mesostructure, we are seeking a theoretical model that describes the macroscopic response. We will now outline the key components of the model, and then compare its predictions with experimental results.

The literature presents various ways to theoretically describe flow-induced deformations [13, 16, 60, 61, 17]. The basic idea behind those approaches is that static equilibrium shapes result from the balance between the external fluid loading and the internal mechanical forces. The complexity arises from the feedback of the structural deformation on the surrounding flow, which in turn affects the fluid forces. For our kirigami structures, we will follow a similar approach, but first, let us highlight the unique features present here.

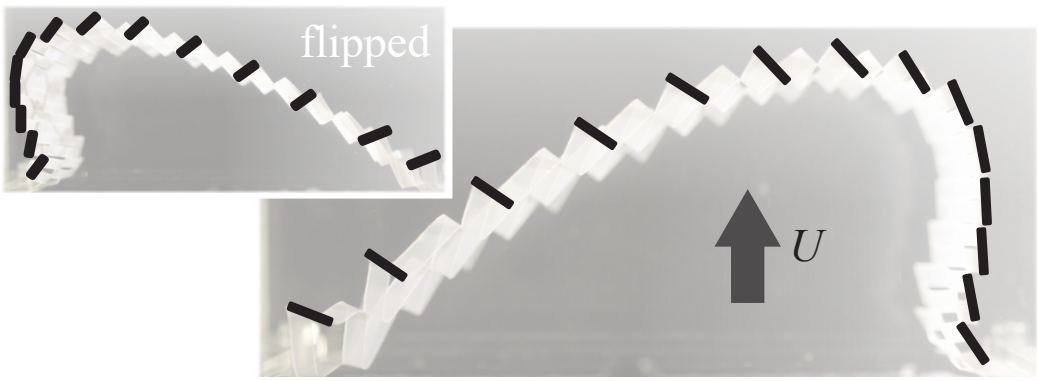

Figure 1.16: The tilting of buckled cut units (outlined in black) induces tangential fluid forces, resulting in asymmetric profiles prescribed by the buckling direction (reversed in the inset).

The first distinction lies in the mode of deformation. While previous studies primarily

examine deformations in bending or torsion [13, 16, 60, 61, 15, 17], kirigami structures undergo stretching. Secondly, the sheets are porous, and the shape and size of the pores change along the sheet based on local elongation. It affects local interstitial flows and fluid velocity. Furthermore, the three-dimensional pore morphology generates tangential forces, whereas previous studies typically consider only normal pressure forces. These factors demonstrate the complexity of the fluid-structure coupling that governs the deformation of kirigami sheets in flow. We aim to capture these key components and their impact on deformation with a simplified model.

1.4.1 Continuous description of the sheet

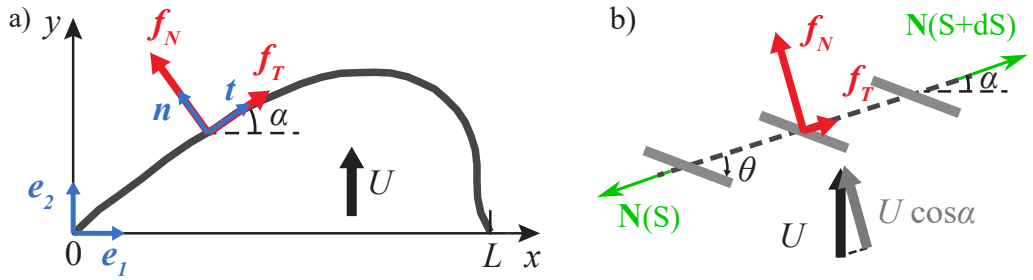

Figure 1.17: a) Modeling of the kirigami sheet as a continuous membrane subjected to distributed fluid forces f_N and f_T. b) Local fluid loading depends on the orientation α of the membrane relative to the flow, and the internal mesostructure of tilted surface elements with angle θ

Inspired by previous work on porous flexible structures such as fishing nets [62], we choose a continuous description with net properties instead of describing each cell individually. This approach reduces computational complexity and has been proven efficient [62, 61, 63, 64], even if it describes less accurately the details at a local scale. The kirigami sheet is described as an equivalent membrane with length L, fixed at its extremities. It is subjected to an external fluid loading $\mathbf{f}(S)$ defined per unit length of the reference un-stretched configuration, parameterized by curvilinear coordinate S (see Figure 1.17a). This is balanced by local internal membrane tension $N(S)$, resulting in local force balance:

$$(N\mathbf{t})'(S) + \mathbf{f}(S) = 0 \tag{1.6}$$

where the notation $'$ denotes the spatial derivative with respect to S. The unit vector $\mathbf{t}$ tangential to the profile is expressed as $\mathbf{t} = \cos\alpha(S)\mathbf{e_1} + \sin\alpha(S)\mathbf{e_2}$, with $\alpha(S)$ the angle of the membrane relative to the undeformed configuration (see Fig1.17a). Finally, the fixed-fixed boundary conditions at each end:

$$\begin{cases} x(0) = 0 \quad x(L) = L = \int_0^L (1 + \varepsilon(S))cos(\alpha(S))dS \\ y(0) = 0 \quad y(L) = 0 = \int_0^L (1 + \varepsilon(S))sin(\alpha(S))dS \end{cases} \tag{1.7}$$

To complete the models, two ingredients are still needed: a constitutive law connecting internal forces to deformations and an expression for the external fluid loadings.

Based on experimental observations, we choose an elastic constitutive law linking the tension force N to the elongation ε: $N(S) = K_2 L\varepsilon(S)$. As previously stated, and discussed further, the deformations induced by the flow are mainly in the linear second mechanical regime. Fig1.18a shows the force-extension curve for a typical kirigami sheet with the second mechanical regime (characterized by K_2) shaded in gray. This same area is shown in

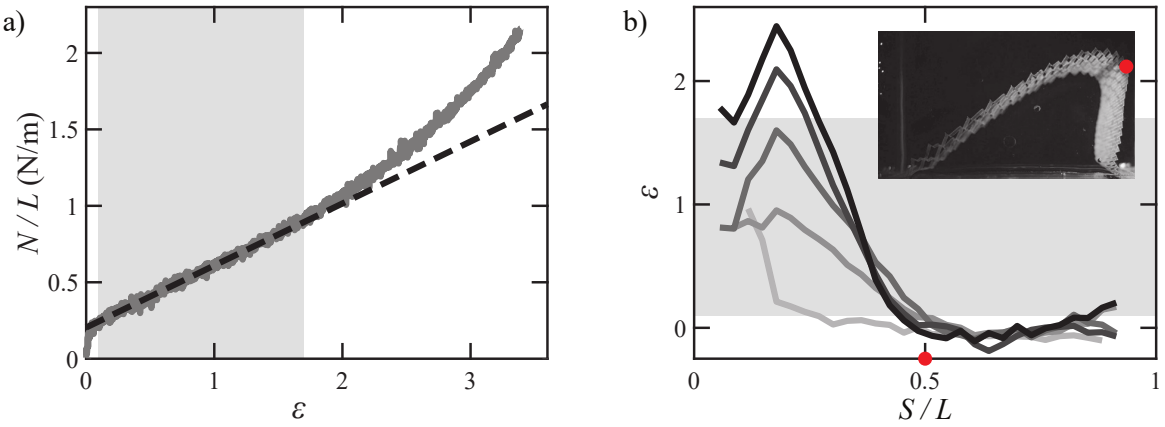

Figure 1.18: a) Tensile force per unit length N/L as a function of elongation ε. The grey zone delineates the second mechanical regime of deformation. b) Local flow-induced elongation along the curvilinear coordinate S for this kirigami specimen, for increasing Cauchy number (denoted by the greyscale). Inset : The limit between the extended and non-extended regions at $S/L = 0.5$ is indicated by the red dot on the experimental picture.

Fig1.18b, which shows local elongation along the kirigami length for increasing speeds (following the gray scale color). We observe that for each curve (each velocity), the first half is mainly in the second regime, while the other half remains almost unstretched and would belong to the first stiffer regime based on tensile test results. However, due to increasing shape asymmetry, this last part tends to align with the flow, which will greatly reduce its contribution in fluid-elastic interactions. Therefore, at first assumption, a purely elastic law described solely by K_2 could be assumed. The effect of non-linearities will be discussed at the end of this chapter.

Due to the complex local morphology that evolves with elongation, finding a fluid loading formulation is challenging. Direct local measurement is not possible because introducing a sensor that is small enough to not affect the deformations is difficult. To overcome this experimental challenge, we conduct fluid force measurements on a simplified model system of parallel rigid blades that mimic the local geometry of stretched kirigami sheets. The measurements and associated derivations will be presented in a later section. For now, let us suppose that the fluid forces can be expressed as two components: one normal and one tangential to the deformed shape, as shown in Fig1.17b. $\mathbf{f}(S) = f_n(S)\mathbf{n} + f_t(S)\mathbf{t}$. Taking into account both the elastic behavior and the fluid force decomposition, Eq1.6 can now be expressed with the following system of equations:

$$\begin{cases} \varepsilon(S)\alpha'(S) + \dfrac{1}{K_2 L} f_n(S) = 0 \\ \varepsilon'(S) + \dfrac{1}{K_2 L} f_t(S) = 0 \end{cases} \tag{1.8}$$

1.4.2 Formulation for the fluid forces

To model the forces induced by the flow on the kirigami that causes its expansion, a semi-empirical approach is taken. Looking more closely at our specimens in Fig1.19a , we notice that the elongated part (red box) can be described as a network of blades with the same tilting angle along the deformation profile. To mimic the local geometry of stretched kirigami sheets, we set up a frame with parallel rigid aluminum tilting blades (see Fig1.19b). The whole system (frame and blades) is mounted on a six-component force sensor (FT-Nano-43 SI-9-0.125) which measures forces in the normal and tangential direction (to the array), we finally subtract forces on the support frame alone to obtain the load on tilted blades.

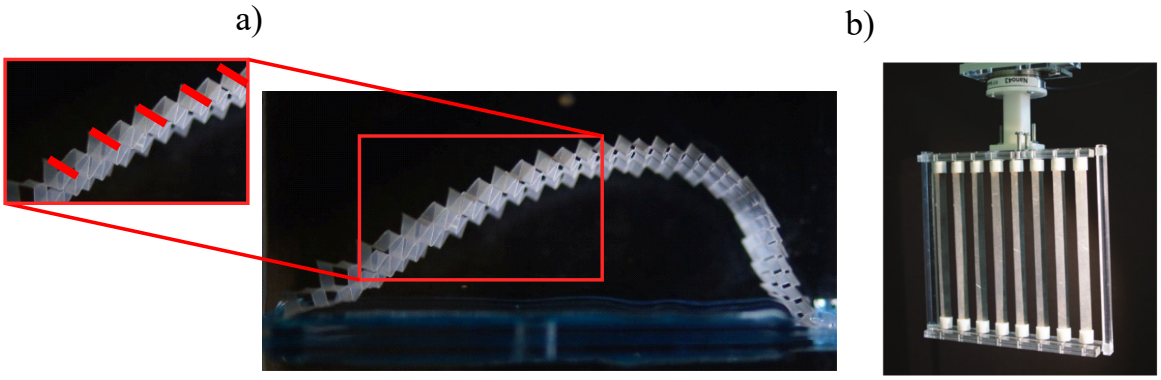

Figure 1.19: a) Zoomed view shows an alignment of blades (highlighted in red). b) A simplified system of parallel flat blades is used to experimentally characterize fluid loading and mimics the previous alignment of elementary cells in flow.

Frame and blade dimensions are detailed in Fig1.20b. We vary the orientation of the blades and their spacing to imitate the change of the kirigami macrotexture with stretching (with blades becoming increasingly tilted and spaced apart). The number of blades, n, can range from 6 to 12 by adjusting the spacing between them (maintaining a regular gap for all configurations) that effectively varies between $[1.1 - 2.2]$ cm. Each blade is attached to the frame via a 3D-printed cylinder that fits onto the blades; we reduce their impact on further measurements through their small size and round shape. All interface pieces are connected to the frame via pivots, as illustrated by the gray points in Fig1.20a. The blades can rotate relative to the frame by a common angle θ, and this tilting motion can be adjusted through two shafts placed on the top of the frame (represented by red points). The position of the blades is marked with a black line (Fig1.20a), and it is extracted through image analysis.

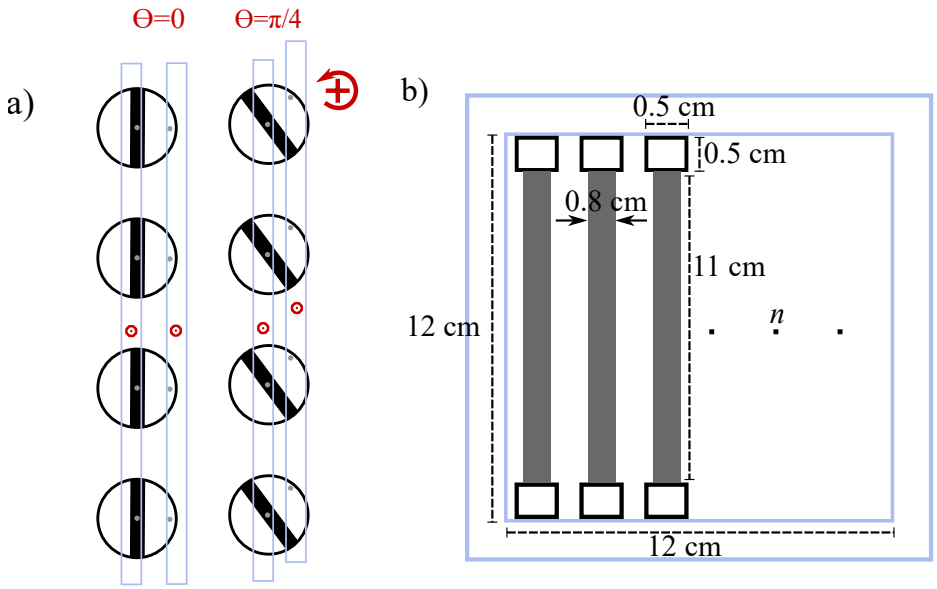

Figure 1.20: a) Top view of the blade array. Cylindrical 3D-printed pieces connect the blades to the support frame (with a pivot represented by the central grey dot) and to a movable part (grey dot on the edge of the cylinders) that allows the angle of the blades to be adjusted via external shafts (red dots). The 3D-printed pieces are marked with a black line to measure the blade angle a posteriori. b) Characteristic dimensions of the frame (in blue) and of the n blades (in grey).

Note that the entire setup (frame and blades) can be tilted by an angle α relative to the flow to mimic the local orientation of the kirigami sheet relative to the flow. This parameter will be explored later in the section. For now, let us place our system perpendicular to the

incoming flow and examine the impact of blade rotation and blade spacing on the measured fluid forces.

Normal and tangential fluid forces on the blades system

For each blade spacing (in practice, number of blades), we varied the blade angle θ in the range of $[0, \pi/2]$ at four different flow velocities: $U = [6.7, 10.1, 13.5, 16.8]$ cm/s. The force sensor recorded 1024 values per second for one minute at each angle, and the normal and tangential forces F_N and F_T on the array were calculated by averaging all recorded data. The results are plotted in Fig1.21a-b as a function of blade inclination angle θ. The flow speed corresponds to a marker type and the color represents the number of blades. The two force components exhibit a similar trend with respect to the tilting blade angle θ for all blade spacings and incoming flow velocities. In Fig1.21a, the normal fluid force F_N is highest when the blades are facing the flow ($\theta = 0$) and gradually decreases as they align with it ($\theta \to \pi/2$). The tangential forces, shown in Fig1.21b, are zero when the blades are perpendicular or aligned with the flow and highest for $\theta \sim \pi/4$. Note that no stall (a decline in the tangential lift component) is observed around the classical angle of $\theta \sim 15 - 20^\circ$ [65].

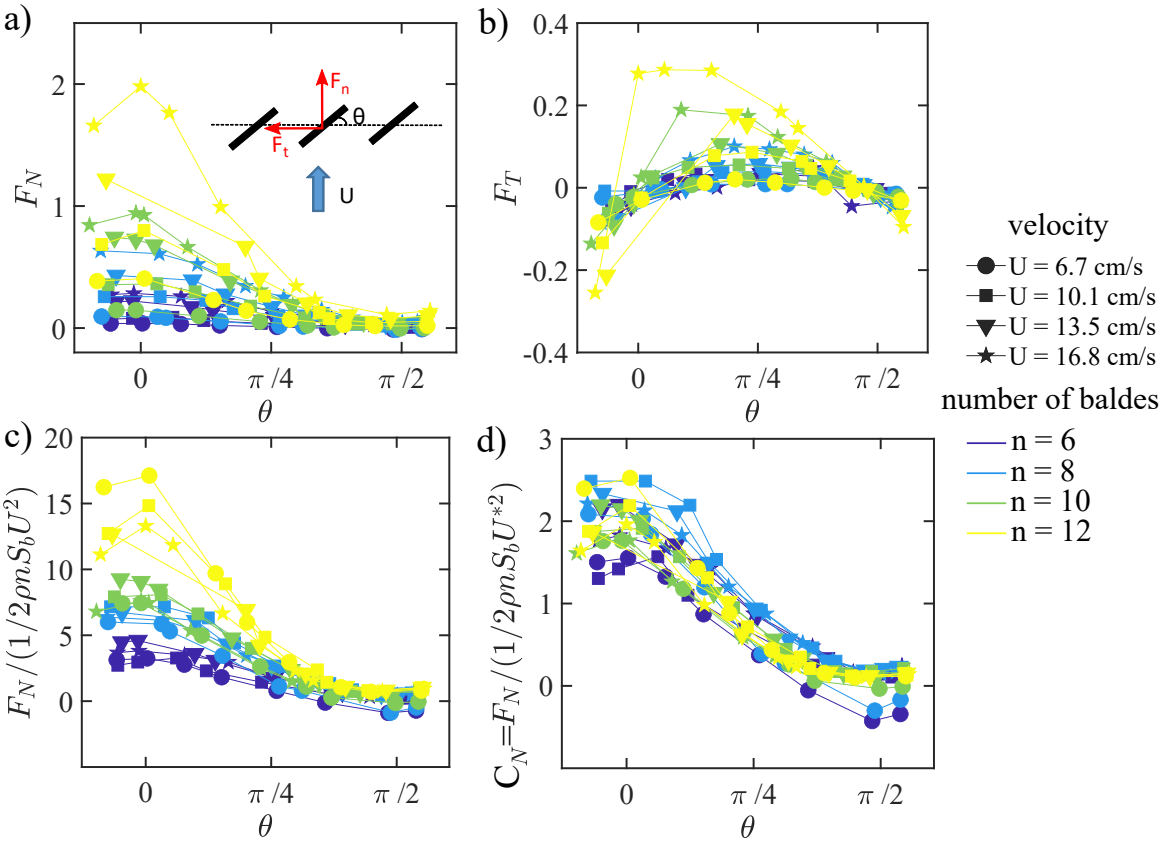

Figure 1.21: a) Normal and b) tangential fluid forces on the array of blades as a function of the rotation angle of the blades θ, for different flow speed U (denoted by the marker types) and a different numbers of blades n (denoted by the color: from blue for $n = 6$ to yellow for $n = 12$). b) Dimensionless normal force $F_N/(1/2\rho n S_b U^2)$, with A_b the area of a single blade, as a function of θ. c) Fluid force coefficient $C_N = F_N/(1/2\rho n S_b U^{*2}$, accounting for blockage effects through an effective velocity U^*.

In the following, we describe how fluid loading expressions are derived from measurements. We focus here on the normal fluid force on the array F_N, which is larger than its tangential counterpart F_T and thus more illustrative, but the same reasoning applies to F_T. As seen in Fig1.21a, fluid forces increase with flow speed and the number of blades (that is also the total exposed area). To reflect these trends, results are replotted in a dimensionless

form in Fig1.21c using the characteristic pressure force on the cumulated blade surface area $1/2\rho n S_b U^2$, where ρ is the water density and S_b is the rectangular area of a single blade. The collapse of the curves across U variations shows a consistent quadratic velocity dependence. However, significant differences appear when the number of blades varies, which affects the water tunnel blockage. To account for these blockage effects, we consider that the flow around the blades has a higher characteristic speed U^* than the flow ahead of the array U. This effective speed U^* is calculated through the conservation of mass flow rate through the open spaces:

$$U^* = U\frac{S}{S - nS_b} \tag{1.9}$$

with S the inner area of the frame. Replacing U by U^* in the nondimensionalization of F_N collapses all curves (see Fig1.21d). We can then define an effective fluid force coefficient (for the tangential force as well):

$$C_{N,T} = \frac{F_{N,T}}{1/2\rho n S_b U^{*2}} \tag{1.10}$$

Here we have therefore implicitly assumed an inertial flow regime. An estimate of the Reynolds number, Re, at around 10-2000, enables us to neglect viscous effects and focus solely on dynamic pressure forces.

Fluid force coefficients

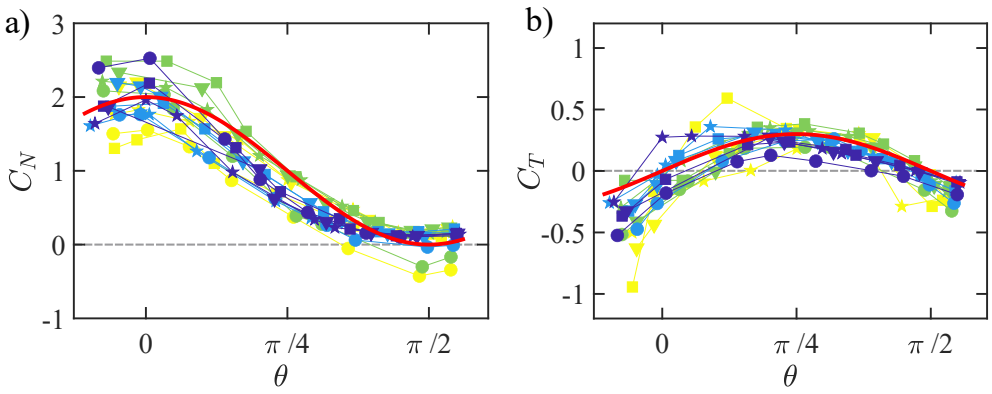

Figure 1.22: Fluid force coefficients C_N and C_T for the normal and tangential forces on the array, as a function of the blades' angle θ. The marker style and color line are the same as defined in Fig1.21. The red solid line corresponds to the formulation of Eq1.11

The evolution of the fluid force coefficient C_N and C_T the rotation angle of the blade is shown in Fig1.22, and we now seek to approximate it with an expression $C_{N,T}(\theta)$. The forces on angled plates or foils have been the subject of many studies [66, 67, 68, 69], however, most of them were restricted to low angles of inclination (below the stall angle). To our knowledge, the present blade arrangement has been little studied in the literature over such a range of angles. We follow a logic similar to Hoerner [66] and his cross-flow principle which states that fluid dynamic pressure forces on an inclined body correspond only to the velocity component perpendicular to its axis. For a single blade, this normal velocity component is $U^* \cos\theta$. We can then project the normal pressure force in both the normal and tangential directions to the blade array, giving respectively $1/2\rho C_{N0} S_b U^{*2} \cos^3\theta$ and $1/2\rho C_{T0} S_b U^{*2} \cos^2\theta \sin\theta$, with C_{N0} and C_{T0} numerical coefficients to be determined. The corresponding fluid force coefficient of Eq1.11 can then be formulated as:

$$C_N = C_{N0}\cos^3\theta \quad \text{and} \quad C_T = C_{T0}\cos^2\theta\sin\theta \tag{1.11}$$

Fits of the data in Fig1.22 (red lines) show reasonable agreement, and yield values $C_{N0} = 2$ and $C_{T0} = 0.8$, attesting that our description of fluid forces is enough accurate to be implemented into our theoretical modeling.

Effect of the centerline orientation

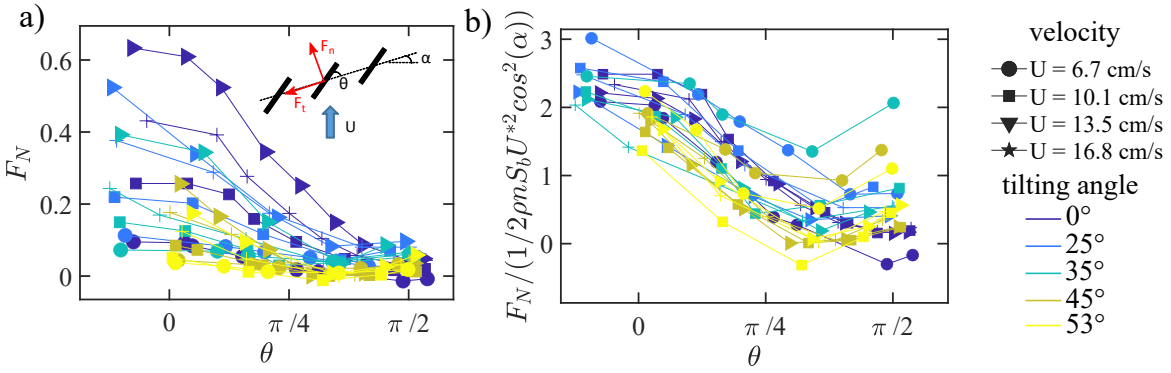

Figure 1.23: a) The normal force on the array F_N as a function of the blades' angle θ, for different angles for the array α (corresponding to colors, from dark blue 0^o to yellow $53°$) and for different flow speeds (distinguished by markers). b) Dimensionless normal force $F_N/(1/2\rho n S_b U^{*2}\cos^2\alpha)$ as a function of θ.

Our setup also allows us to change the angle of the frame itself α (the entire assembly rotates, including the sensor), to mimic the local orientation of the profile centerline in the flow. We measure forces at $\alpha = [0°, 25°, 35°, 45°, 53°]$, for a single configuration with $n = 8$ blades and four flow velocities (the same ones as previously). Fig1.23a shows the normal force component F_N as a function of the blades' angle θ. We see a similar θ-dependence in all cases, but the magnitude of the force differs: F_N is maximal when the array is perpendicular to the incoming flow and decreases as it aligns with it. This effect can be taken into account by considering only the velocity component normal to the array $U^*\cos\alpha$, as shown by the collapse of data requested in the dimensionless form $F_N/(1/2\rho n S_b U^{*2}\cos^2\alpha)$ in Fig1.23b. This approach is similar to the literature [60, 61], which accounts for the local angle of a flexible object relative to the incoming flow by assuming that it locally experiences a normal flow with speed $\mathbf{U}.\mathbf{n}$ (with $\mathbf{n}$ the normal unit vector).

Formulation for the fluid forces on the effective membrane

The final step is to extend those semi-empirical formulations for fluid forces to the case of our equivalent membrane. Unlike our model system of parallel blades, the blades' angle and the spacing between them do not change independently for kirigami sheets. As discussed earlier, it is related through:

$$\cos\theta = \frac{1}{1+\varepsilon} \quad \text{and} \quad \sin\theta = -\sqrt{1-\frac{1}{1+\epsilon}} \tag{1.12}$$

Together with previous results from the blades' array (see Eq1.11), it provides expressions for the effective fluid force coefficients $C_N(\varepsilon)$ and $C_T(\varepsilon)$ that are elongation dependent:

$$\begin{cases} C_N(\varepsilon) = C_{N0}\cos^3\theta = C_{N_0}\dfrac{1}{(1+\varepsilon)^3} \\ C_T(\varepsilon) = -C_{N0}\cos^2\theta\sin\theta = C_{T_0}\dfrac{\sqrt{(1+\varepsilon)^2-1}}{(1+\varepsilon)^3} \end{cases} \tag{1.13}$$

Note that Eq1.12 corresponds to a clockwise buckling orientation that matches experiments (that is $\theta \in [-\pi/2, 0]$). One can however change the direction of rotation of the blades through the $\oplus$ or $\ominus$ sign of the sin in Eq1.12, which changes the sign of tangential forces, as reported in the interlude $n^o 7$.

The fluid loading is normal and tangential to the membrane then writes:

$$\begin{cases} f_N(\varepsilon, \alpha) = \dfrac{1}{2}\rho H C_N(\varepsilon)(U^* \cos\alpha)^2 \\ f_T(\varepsilon, \alpha) = \dfrac{1}{2}\rho H C_T(\varepsilon)(U^* \cos\alpha)^2 \end{cases} \tag{1.14}$$

with H the membrane height. Note that f_N and f_T are defined per unit length of the reference unstretched configuration (parameterized by the curvilinear coordinate S). Unlike the inflation of pressurized balloon [19], the surface that is bearing fluid forces does not extend here (meaning that the kirigami constitutive sheet itself does not stretch).

In Eq1.14, $U^* \cos\alpha$ denotes the speed of the flow impinging perpendicular to the membrane. It reflects it local orientation in the channel α, and blockage effects through the effective velocity U^*. Similarly to the blades' array, the latter is related to the incoming speed U and the sheet opening upon extension through the conservation of mass flow rate. Namely, let us consider a small section of the sheet of length l and height H, which is smaller than the frame inner height H_f, leaving clearance spaces at the top and bottom (see Fig1.9c-d). Once the section is stretched with elongation ε, flow arriving in the extended area $l(\varepsilon+1)H_f$ with speed U passes through the openings in the sheet and clearance spaces with total area $l\varepsilon H + l(1+\varepsilon)(H_f H)$, with effective speed U^*. Conservation of mass flow rate then yields:

$$U^* = \gamma(\varepsilon)U, \quad \text{with } \gamma(\varepsilon) = \frac{1+\varepsilon}{\varepsilon + (1 - H/H_f)} \tag{1.15}$$

We take $H/H_f = 0.86$ based on experimental values. Note also that the additional term $(1 - H/H_f)$ associated with clearance spaces (with H_f the frame height), prevents fluid loading from diverging for small ε, reflecting the gradual kirigami deployment observed as flow speed increases from zero.

Eq1.14 and Eq1.15 give a formulation for $f_{N/T}$ that only depends on ε and α. This function is thus the same for all kirigami specimens, regardless of the cutting parameters. This is verified experimentally in the following section. Note also that we consider in Eq1.15 a uniform incoming velocity U, which does not account for potential retroaction of the sheet presence on the flow at a large scale.

1.4.3 Comparison of theoretical predictions with experiments

Injecting the fluid forces expressions of Eq1.14 and Eq1.15 into Eq1.8, and using the non dimensional spatial variable $\tilde{S} = S/L$, yields the equation for the membrane equilibrium shape:

$$\begin{cases} \varepsilon\alpha' + \dfrac{C_y}{2} C_N(\varepsilon)(\gamma(\varepsilon)\cos\alpha)^2 = 0 \\ \varepsilon' + \dfrac{C_y}{2} C_T(\varepsilon)(\gamma(\varepsilon)\cos\alpha)^2 = 0 \end{cases} \tag{1.16}$$

with $C_y = \frac{\rho H U^2}{K_2}$ the same Cauchy number as defined in the experimental section, and prime now denoting the derivative with respect to $\tilde{S}$. The boundary value problem given by Eq1.16 and Eq1.7, is solved using shooting methods, using the *bvp4c* function of Matlab. The initial

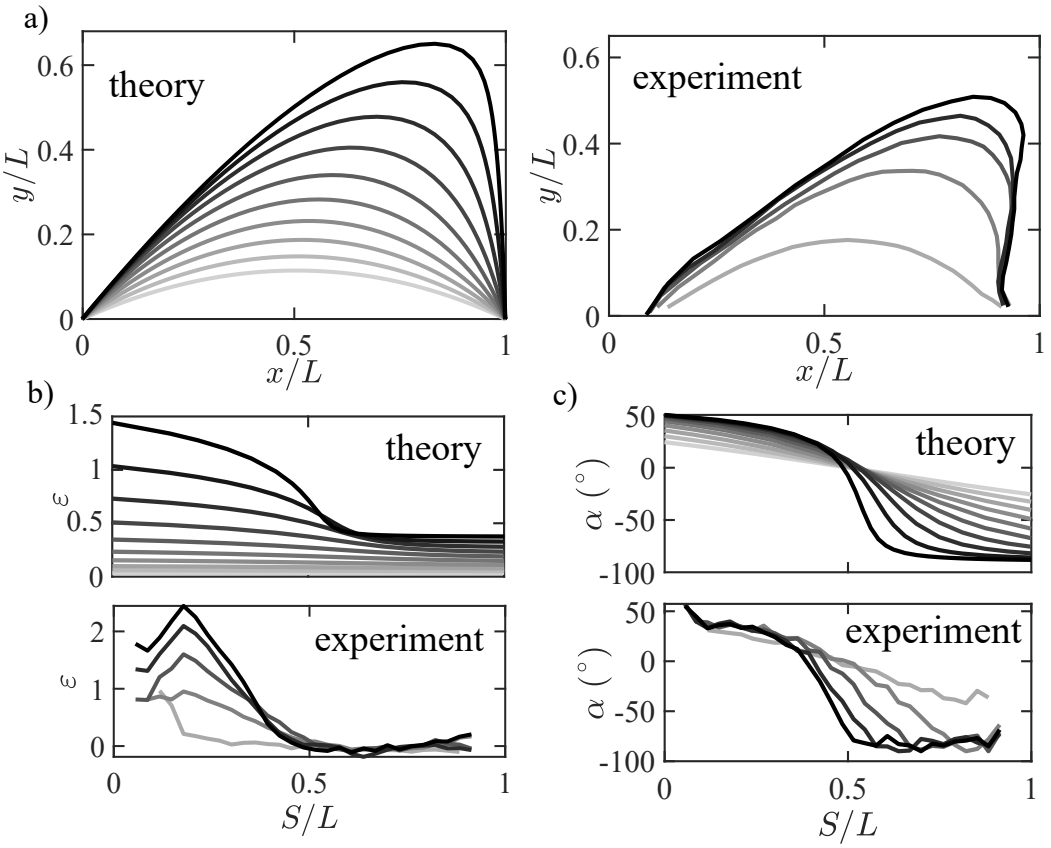

Figure 1.24: Comparison between theoretical predictions and experimental results (for the specimen with parameters $L_s = 3.16$ cm,$d_x = 1.9$ mm, and $d_y = 4.4$ mm). Theoretical predictions are computed for logarithmically increasing values of C_y in 10^3–10 (denoted by the gray scale). a) Shape profiles, b) Local elongation ε along the curvilinear coordinate S, c) Local inclination α.

seed is chosen to guarantee convergence at low Cauchy values. The shape is then calculated for increasing C_y values by using the previously obtained solution as the initial condition for the shooting method at each iteration. Note that the Cauchy number is the sole parameter, which captures both the impact of stiffness and velocity variations.

Fig1.24a shows the resulting shapes for Cauchy numbers in the same range as experiments. The model reproduces qualitatively the asymmetric expansion observed in experiments, with the gradual deviation of the lobe to one side. The model is also able to predict the local deformation field. In Fig1.24b, elongation ε follows the same pattern as the experiments, with half of the original sheet gradually elongating with C_y while the other half remains largely unstretched. A comparison of the local profile angle α also indicates good agreement, both in terms of the values and the trend, with the unstretched part becoming increasingly aligned with the flow for high C_y ($\alpha = -90^o$), see Fig1.24c.

Further analysis of the deformation amplitude, shown in Figure 1.25, shows that the model captures as well the experimental sublinear trend $y_{max}(C_y)$, although it overestimates the displacement. The agreement is however reasonable given the absence of any fitting parameter and the simplifying assumptions. Some of the discrepancies could stem from mechanical nonlinearities, which are discussed later in this section. This does not change the observed trends but tends to slightly reduce the elongation and amplitude of y_{max}.

This simplified model, therefore, corroborates experiments and captures the underlying fluid-elastic mechanisms governed by the dimensionless Cauchy number. It also reveals the critical role played by the kirigami substructure in modulating the magnitude and direction of local fluid forces. The evolution of pore size and shape affects the velocity of interstitial

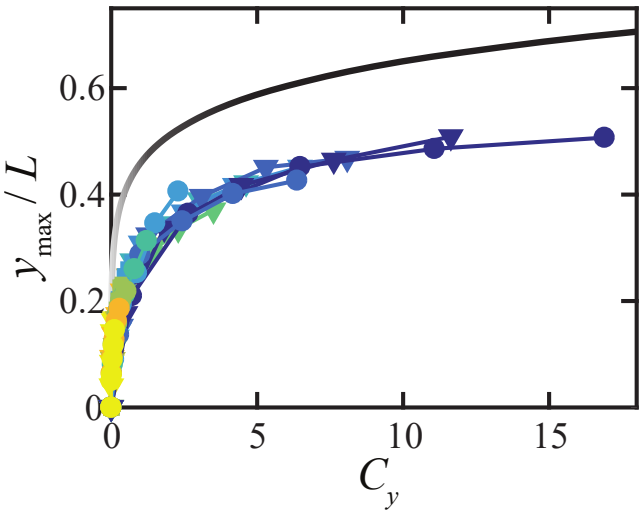

Figure 1.25: Theoretical evolution of the dimensionless deformation amplitude y_{max}/L with the Cauchy number C_y, compared to experimental data points (same legend as in Fig1.15).

flows (blockage effect) and therefore the fluid dynamic pressure, as well as the orientation of the surfaces subjected to these pressure forces.

Interlude n^o7 : Polarity - the first meeting

Polarity is defined as the direction of rotation of the elementary cells when they move out of the plane. As suggested in the Fig1.16, inverse the polarity of a uniform kirigami pattern (in practice flip the sheet side facing the flow) provide a symmetrical expansion pathway. To confirm this, we perform experimental measurement of a single pattern for the two polarity states identify by their respective sign ⊕ and ⊖. As expected the reached shapes expand symmetrically and the resulting lobe deviates in an opposite direction, with a similar amplitude of deformation (see attached graph).

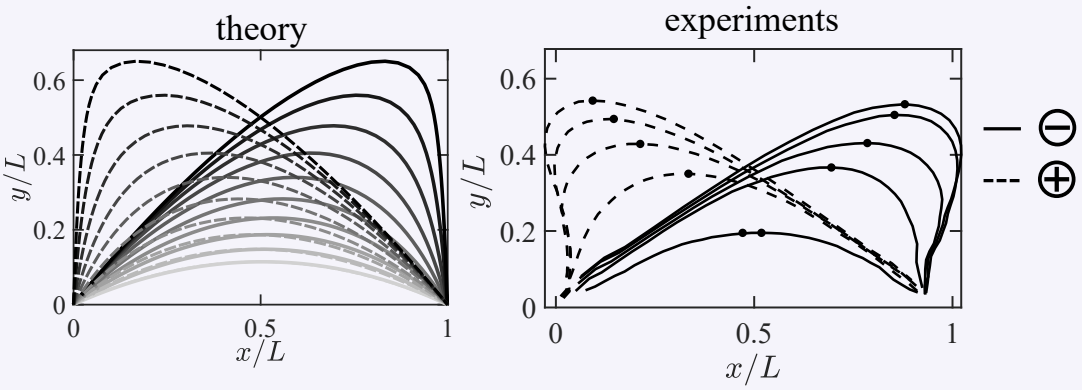

Reversing polarity theoretically involves changing the sign of the rotation angle θ (a variable that only depends on elongation), which results in a change of direction for the local tangential force f_t. The theory also predicts that the expansion will be symmetrical between the two polarities, which is supported by the above graph.

The theoretical model can be expanded to incorporate variations in the blade tilt orientation along the sheet (as described in Chapter 2), or non-uniform cutting patterns (resulting in non-uniform stiffness, as discussed in Chapter 3). It will also be valuable for inverse design (finding the cutting pattern that results in a specific shape), providing insights, and guiding optimization algorithms (as implemented in Chapter 4). We will now conclude this

section by discussing an intriguing aspect revealed by the model, namely that fluid forces are independent of the cutting pattern, and the impact of mechanical nonlinearities.

1.4.4 Fluid forces do not depend on the cutting parameters

We have demonstrated that the cutting pattern is crucial as it affects the sheet's elastic resistance to deformation and creates the blade-like mesostructure that produces asymmetrical shapes in flow. However, our previous analysis showed that the fluid loading on the sheet is only dependent on the elongation ε and the local orientation of the sheet in the flow α, and not on the cutting parameters. In fact, our theoretical description of the sheet as a continuous effective membrane does not include any information about the cutting geometry (L_s, d_x, and d_y), except for its impact on the stiffness K_2. In this section, we verify this point experimentally by studying the deformation of kirigami sheets in flow with different cutting patterns but the same effective stiffness.

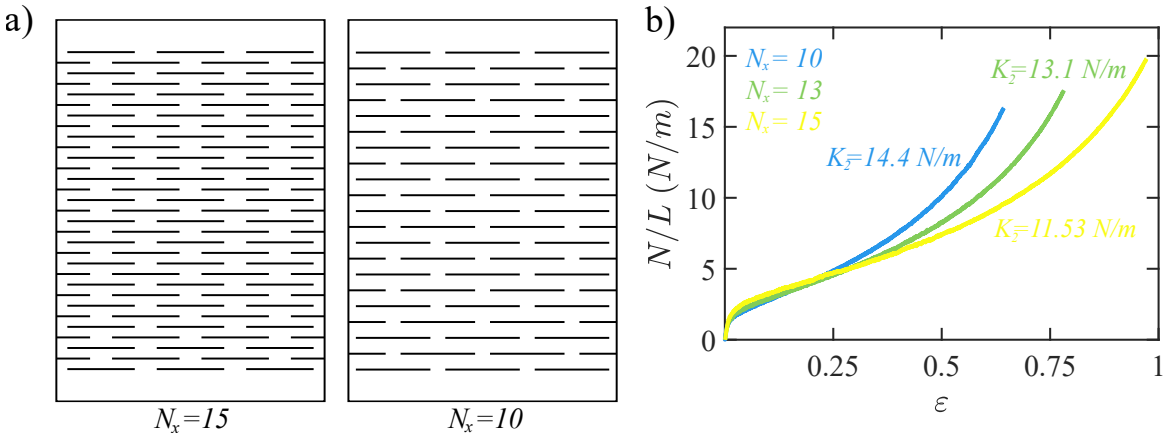

Figure 1.26: a) Example of two distinct cutting patterns with the same effective stiffness K_2. In the latter case, the wider spacing between rows of slits is balanced by longer slits. b) Force-elongation curves for three iso-stiffness kirigami sheets.

For two patterns A and B to have the same effective stiffness K_2 in the second regime of deformation, their cutting parameters must meet the following criteria (according to the stiffness law formulation of Eq1.2):

$$\frac{N_y^A}{2N_x^A}\frac{d_x^A}{(L_s^A - d_y^A)^3} = \frac{N_y^B}{2N_x^B}\frac{d_x^B}{(L_s^B - d_y^B)^3} \tag{1.17}$$

In practice, we choose to fix the parameters of one pattern and vary the spacing between rows of slits d_x of the other. This variation is then compensated in the transverse direction (slit length L_s and spacing d_y) to preserve the stiffness K_2. An example of two iso-stiffness patterns with different cutting parameters is shown in Fig1.26a. We manufactured three sets of kirigami sheets (with 3 to 4 specimens per set) with three different stiffnesses $K_2 = [1.2, 3.1, 11]$N/m. In Fig1.26b, we present the stress-strain curves obtained from tensile tests for three specimens with the same $K_2 = 11$ N/m. Despite some variations, behavior in the second regime is similar for all patterns, with similar values of K_2 (indicated on the graph). Deviations at higher strains are due to the emergence of the third regime of deformation, which is dependent on the cutting parameters [45, 58] and is not captured by Eq1.17.

Fig.1.27a shows the deformation profiles for increasing flow velocity, for the four kirigami sheets with $K_2 = 3.1$N/m, represented with different colors (for clarity, only five speeds are shown). The four specimens deform similarly in the flow. The evolution of the deformation amplitude is also shown in Fig1.27b, alongside two other sets of kirigami patterns

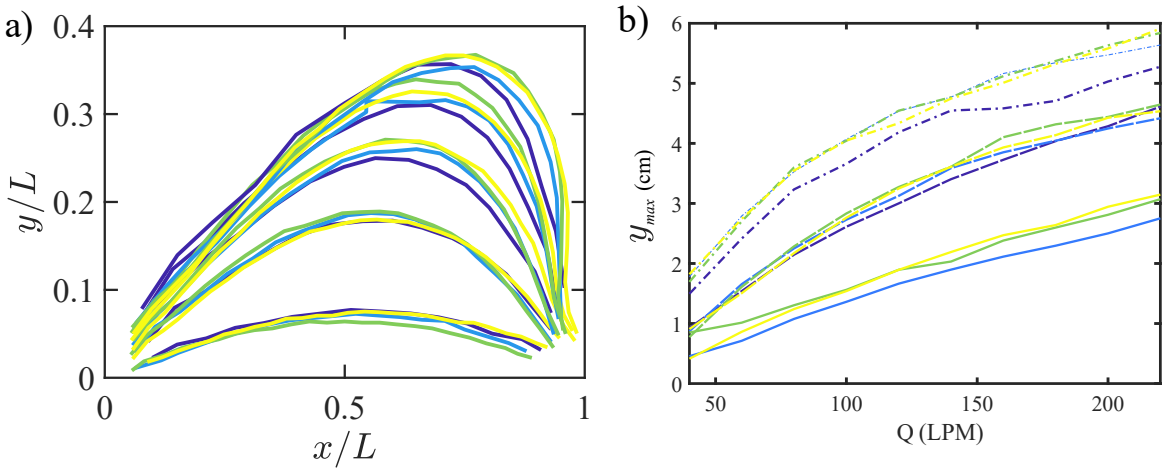

Figure 1.27: a) Shape profiles for increasing flow speeds for the four iso-stiffness patterns with the same $K_2 = 3.1$N/m, distinguished by different colors. b) Deformation amplitudes as a function of the incoming flow rate in liters per minute) for all specimens, with three sets of curves corresponding to the three tested stiffnesses (differentiated by line styles).

with different stiffnesses (denoted by the line style, with one curve corresponding to one specimen). Specimens with the same stiffness exhibit similar deformation amplitudes, even though some patterns have cutting cells that are up to twice as large as others. The cutting parameters thus primarily affect the effective stiffness, and not the evolution of fluid forces with elongation, which also supports the relevance of our continuous theoretical description.

1.4.5 Effect of mechanical nonlinearities

In our study, we modeled kirigami sheets as a membrane with linear elasticity in order to construct the simplest possible model that could replicate observed behaviors and capture underlying mechanisms. Mechanical nonlinearities can nonetheless be incorporated in the theoretical model to assess its effect on flow-induced deformations. To that end, in this sub-section, we are going to modify the membrane constitutive law to account for an initial stiffer behavior. As reported by Isobe et al. (2016) [43, 45], this first regime can be described by a linear force-extension relation, with associated stiffness K_1.

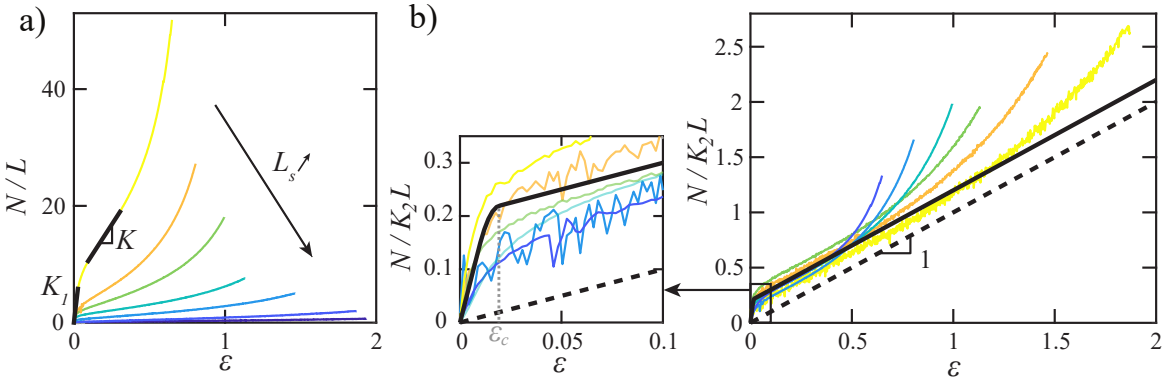

Figure 1.28: a) Tensile force per unit length N/L as a function of elongation ε, for specimens with varying slit length L_s. An initial linear regime with stiffness K_1 is followed by a second softer one with stiffness K_2. b) Theoretical non-linear constitutive law of Eq1.18 (solid line) superimposed to experimental force data replotted in dimensionless form $N/(K_2L)$. The dashed line corresponds to the elastic law $N = K_2L\varepsilon$ used previously.

This K_1 is dependent on the cutting parameters (as illustrated in Fig1.28a), but is related to K_2 by $K_1/K_2 \sim (d_x/t)^2$ with t the sheet thickness (see the previous section of mechanical

properties). The two regimes are indeed both associated with the bending of the elementary plates delineated by slits, but bending occurs in-plane for the first one and out-of-plane for the second. The cross-over from hard to soft regime occurs when the two competing energies of in-plane and out-of-plane deformations are equal, which happens for a critical elongation $\varepsilon_c \sim (t/d_x)^2$ (described in [43, 45]). Based on these scalings, force data can be recasted in dimensionless form $N/(LK_2)$ in Fig1.28b, showing a reasonable collapse in the two regimes discussed. This serves as a basis to define a constitutive law as a piece-wise linear function (solid black line in Fig1.28b), connected by a third order polynomial in the range $[\varepsilon_c - \Delta, \varepsilon_c + \Delta]$ (with $\Delta = 5.103$) to ensure differentiability:

$$\frac{N}{K_2 L} = \begin{cases} \lambda\varepsilon & \text{if } \varepsilon < \varepsilon_c - \Delta \\ \varepsilon + \varepsilon_c(\lambda - 1) & \text{if } \varepsilon > \varepsilon_c + \Delta \end{cases} \tag{1.18}$$

With $\lambda = K_1/K_2 = 15$and $\varepsilon_c = 1.4.10^2$, estimated experimentally from tensile tests and averaged overall kirigami specimens. Note that here, parameters λ and ε_c are taken as constants as a first approximation, disregarding their dependence on parameter d_x. Similar values are however obtained for the series of specimens with varying d_x.

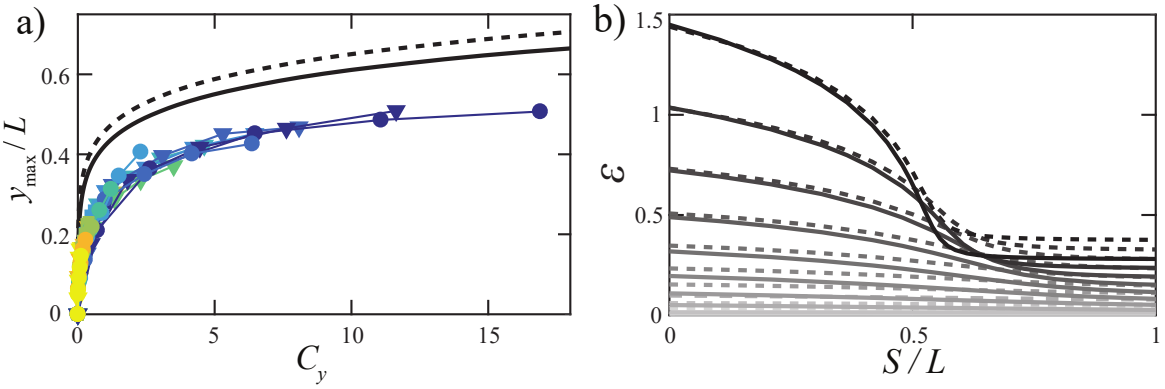

Figure 1.29: a)Theoretical and experimental evolutions of the dimensionless deformation amplitude y_{max}/L with C_y. b) Local elongation along the curvilinear coordinate S for logarithmically increasing values of C_y, for nonlinear (solid lines) and linear (dashed lines) mechanical properties

Theoretical deformations in flow are computed using the modified constitutive law of Eq1.18, for increasing values of the Cauchy number. Fig1.29a shows the evolution of the dimensionless amplitude y_{max}/L , which is compared to the results of the model with linear elasticity as well as experimental data. Accounting for mechanical non-linearities slightly reduces the amplitude of predicted deformations, but does not modify the observed trends. Further comparisons of local deformations fields for both models in Fig1.29d also show similar results, with slightly smaller elongations for the one with mechanical nonlinearities. Those smaller deformations can be interpreted in light of the positive offset in the force-extension curve of Fig1.28b. Higher tensile restoring forces are thus opposing fluid loading which decreases both the local elongation and global amplitudes.

A more realistic constitutive law leads to slightly better predictions compared to our previous linear elastic formulation. However, our linear approach offers a universal description without requiring any additional parameters, aside from C_y, to account for variations in the cutting pattern. Both models exhibit a similar trend that accurately captures experimental observations at all scales. As a result, we use the simpler elastic law in our subsequent analysis.

1.5 Conclusion

This chapter introduces the main tools needed to understand the interaction between a kirigami sheet and its surrounding fluid flow. We begin by explaining the singular mechanical behavior of a uniform cutting pattern consisting of parallel slits that turn flat materials into highly stretchable sheets with meso-textures emerging from the local cells bucking. We establish a direct correlation between cutting parameters, local structural deformation modes, and mechanical properties. We also reveal the existence of a nonlinear constitutive law determined by the local design. We finally provide an analytical expression for the effective stiffness, which describes the elasticity of the entire sheet, by modeling each elementary cell as a linear spring with a rigidity tune through the local design.

Our extensive experiment in a water channel revealed the mechanisms behind the expansion of a kirigami sheet in flows. More specifically, we pinpoint the role of the stiffness that modulates the amplitude of deformation, which then results in a balance between the structural elasticity and the external fluid loading, embodied by the Cauchy number. We also find a qualitative argument to describe the unusual asymmetric expansion of a uniform design: the local cell tilting leads to the emergence of a transverse fluid force that shifts the global shape aside.

The porous properties also influence the resulting shapes, the surrounding flow passes through our meta sheet and induces large deformation which impacts the local velocity field. This complex interplay is theoretically described through continuous modeling, which described our kirigami sheet as an elastic membrane that undergoes external fluid loads. The analytical expression of the latter is derived from a semi-empirical approach to analyzing a rigid system of blades network. After having dealt with the uniform cutting pattern, it is time to take the plunge and investigate a non-uniform one!

2

Global shapes tuning through polarity control

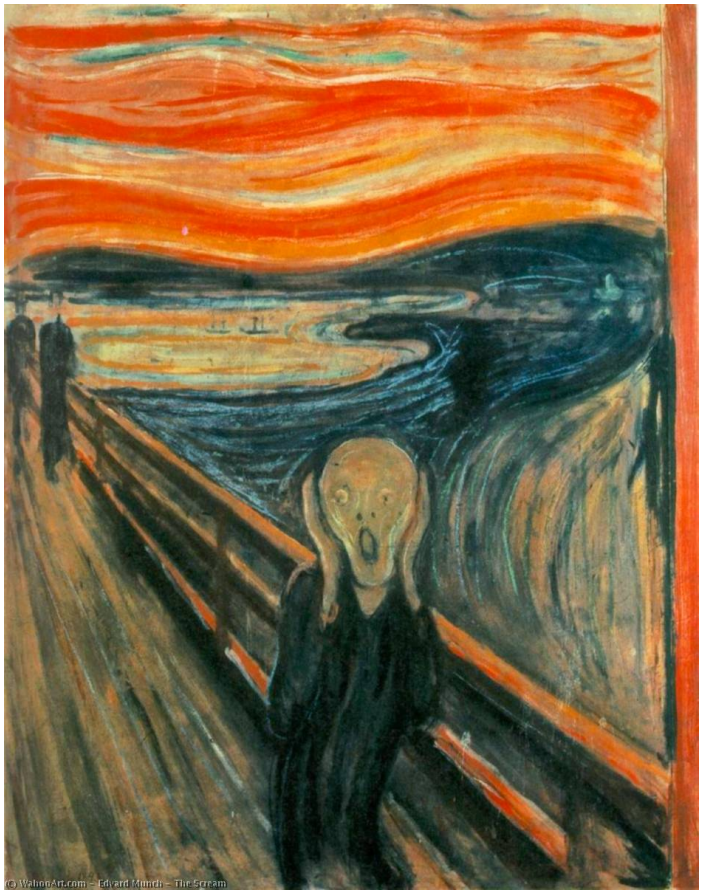

Edvard Munch : "Without fear and illness (**bipolarity**) I could never had accomplish all I have"

Our work has demonstrated that the 3D meso-texture formed during the out-of-plane buckling of kirigami cells determines the direction of fluid load. The direction of cell rotation, known as polarity, impacts local forces and creates asymmetrical shapes for unipolar patterns (Chapter 1). In this chapter, we will vary the local polarity spatially to study its effect on shape-shifting. We will begin by examining bi-zonal patterns with opposite rotations. By adjusting the size of each portion, we can move from an asymmetric to a symmetric shape, which has not been achieved with homogeneous patterns. Having established the role of polarity in fluid direction, we will extend our modeling to include this feature and test more complex multipolar configurations and show the limits of this new lever.

2.1 Fluid force orientations and polarity control

External loads commonly encountered in mechanics are typically uniaxial: tensile or compressive forces applied on materials to determine their behavior and nature, or the ubiquitous volumetric gravity load. In this line, kirigami sheets have been extensively studied through this type of load in order to characterize their mechanical properties and their link with the cutting pattern [43, 58, 45].

Here we are dealing with fluid loading, whose specific characteristics were discussed in the previous chapter as part of the development of the theoretical model, including the dependency of the orientation of the surface on which the force is applied. As we will see, we can modify our cutting technique to take advantage of this property. This will be further explained in the following introductory section.

2.1.1 Why is fluid loading so specific?

The forces exerted on deformable systems by the surrounding fluid are closely tied to pressure and velocity fields. One example of this is the static pressure force for an elastic balloon, as drawn in Fig2.1a. The pressure inside the balloon (P_i) is slightly higher than the external pressure (P_0), resulting in a force acting along the normal of the balloon surface (from inside to outside). This leads to the deformation of the membrane and an elastic tensile force in response, which ultimately results in the balloon's equilibrium state[70].

The "clapping book phenomenon" described by Buchak et al. (2010) [71] provides a more complex illustration. It involves a stack of partially clamped paper sheets placed in a wind tunnel (see Fig2.1b). The fluid flow lifts the pages, causing them to stack together, then gravity makes them fall, and the cycle repeats.

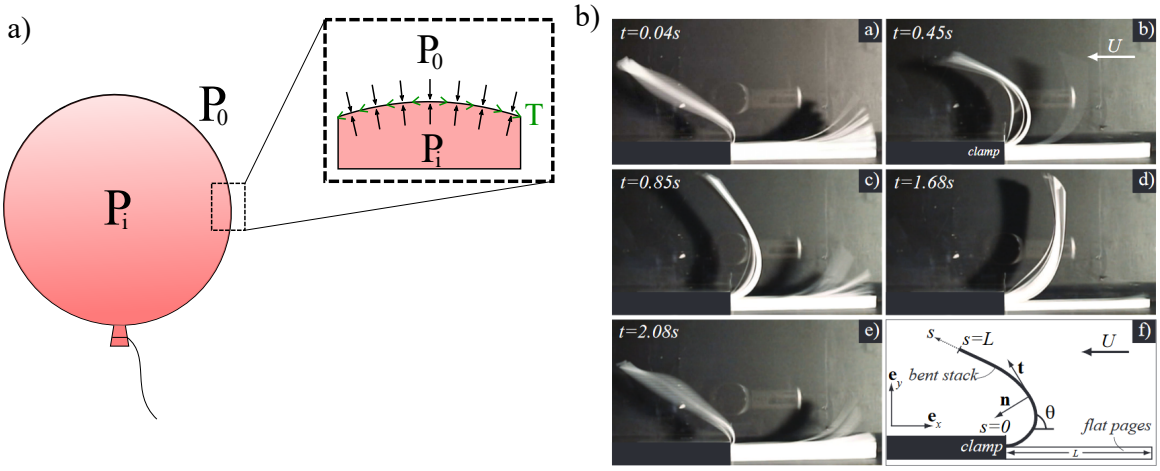

Figure 2.1: a) The fluid trapped inside the balloon imposes a loading purely normal (black arrows) on the elastic membrane inducing internal tensile stress (green arrows). b) Snapshots of the "clapping book phenomenon" at different time slots for a given fixed flow speed and its schematic view, extracted from [71].

The authors develop a theoretical model to explain the periodical clapping book phenomenon. They consider the fluid forces that depend on the local orientation of the sheet, represented by the angle θ (shown in Fig2.1b). They also incorporate a non-trivial dependence on the spatial variation of this angle, which takes into account the fluid acceleration that follows the sheet's shape (known as reactive forces). By balancing these fluid forces with the bending moment and gravity load, they can predict the periodic clapping process

As these examples illustrate, fluid forces act on the surface and depend on its local incline, making them particularly relevant for deformable systems that change shape in response to

external loads. This distinguishes fluid forces from other forces commonly encountered in mechanics, such as gravity, friction, and inertia [19]. We will now delve into the specificities that arise with kirigami sheets.

In our description of fluid loading, we considered the force distribution to apply to the normal of an equivalent membrane surface. However, the micro-texture created by rotating cells results in a second tangential component that runs along the membrane relative to the **polarity**. This is a key concept that refers to the direction in which the elementary cells rotate when they buckle out of the plane during expansion. In the following we will denote a counter-clockwise rotation as ⊕ and a clockwise rotation as ⊖.

In Chapter 1 we highlight that polarity causes symmetry breaking in flow-induced expansion. flipping the unipolar kirigami sheet (=inverting the polarity) leads to symmetrically inverted deformation lobe localization (see interlude n^o7). This first insight into the polarity effect paves the way for further investigation.

Up to now, we studied homogeneous specimens with a uniform polarity distribution throughout the pattern (unipolar kirigami sheet). In this chapter, we aim to manipulate the local polarity within the same pattern to gain control of local fluid efforts and provide new morphologies. Let's start by describing how to tune the cell tilt kinematics.

2.1.2 Buckling control: from Euler column to magic notches

In chapter 1, we discussed the nonlinear mechanical behaviors of kirigami structures and their connection to deformation states. Indeed beyond a critical tensile force, the uncut part of the sheet suddenly rotates out of the plane, and all elementary cells tilt in the same direction, referred to as polarity. This buckling transition is influenced by cutting parameters and well documented in the literature [43, 57, 56, 55, 44]. Our purposes are to bias this mechanical transition and gain control over the local polarity. One commonly used method for controlling the buckling process is adding defects, which we are going to illustrate with the following simplified example.

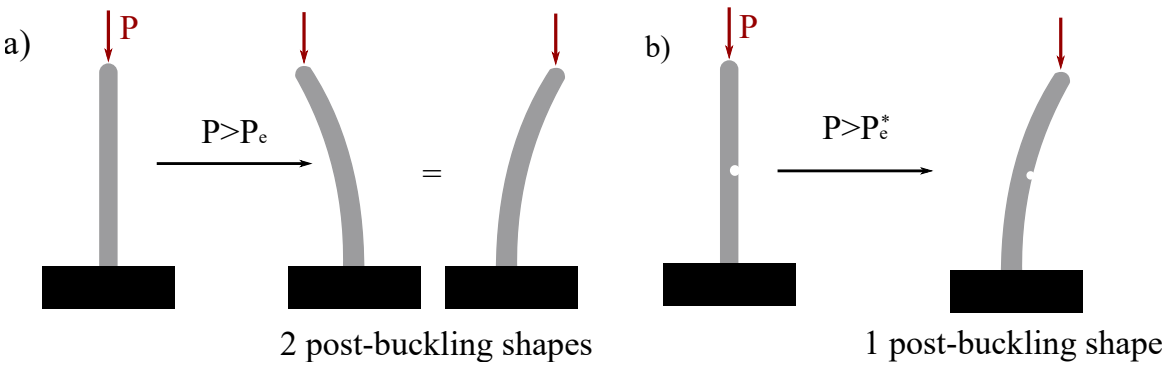

Figure 2.2: Euler's column (with free-clamped boundary condition) undergone a compressive force P gives: a) two post-buckling solutions. b) only one solution if a default is added

Let us consider a homogeneous and isotropic slender beam (known as an Euler column) as shown in Fig2.2. Beyond a certain load P_e the beam state changes; rather than being compressed, the beam is bending: this transition is a classical example of a buckling process. The critical force P_e depends on the beam material and boundary conditions. Despite being widely described and predictable [19, 20], the direction of beam bending is unknown. In a 2D system as in Fig2.2a, the buckled beam can bend in two directions (right or left), which are energetically equivalent.

To bias the buckling process, one common idea is to introduce defects in the system, as a cropped part in the beam in Fig2.2b. The latter creates a bias in compression forces

which favors the right solution, a new critical load P_e^*. Thus adding a preconditioned defect removes the final state degeneracy and allows better control of the resulting shapes of a buckling process, let us extend this idea to the kirigami pattern.

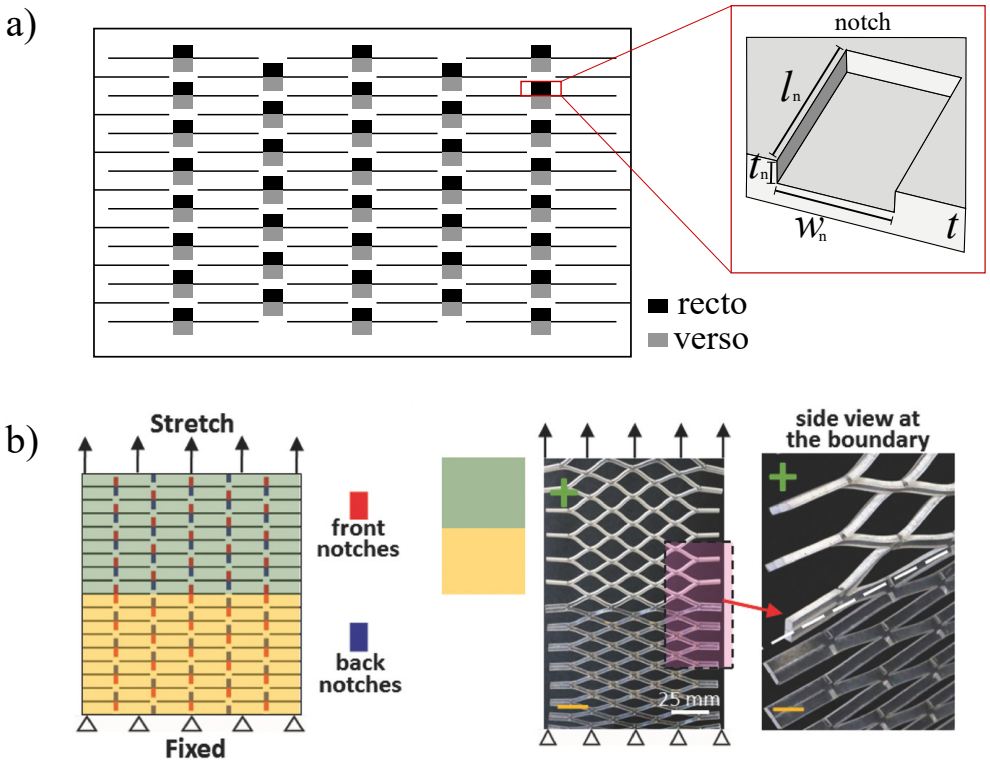

Figure 2.3: a) Cut (lines) and notch (rectangles) pattern of kirigami sheet, black rectangles for the front side notches and grey for the reverse side. A 3D schematic view of the notch sizes is in the red box. b) Bipolar kirigami specimen from [56], by inverse the position of notch pattern (recto- verso) they could invert the polarity at the middle of the pattern (green and yellow areas), the upper part turns counterclockwise, and the lower part clockwise.

For our kirigami sheets, the deflection of each cell, occurring between the in and out of plane deformation regimes, is similar to that of the Euler beam instance. Indeed at a first glance, nothing conditions post-buckling bending directions of the elementary cells, in other words, polarity is not directly controlled. However, as discussed in Chapter 1, the polarity is preserved throughout the sheet as all cells bend in the same direction. This can be attributed to our choice of cutting pattern, which is restricted to an asymmetric bending mode. This ensures uniformity in polarity, which is not predictable when the sheet is in its undeformed state. For more information, (more details in [55] and a quick overview on interlude $n^o 8$ gives some insights about the post-buckling shapes reached).

Thus for the uniform kirigami sheets, each polarity state $\oplus$ and $\ominus$ is enabled and leads to a symmetrical expansion of the deformation profile toward the left and right respectively.

In order to gain control of local polarity and access to new morphologies we need to influence the buckling process. In this way, Tang et al. (2017) had the ingenious idea of introducing a notch sub-pattern near each slit [56]. Notches are staggered on the front and back side (as shown in Fig2.3a), and their presence breaks the degeneracy related to the polarity by inducing a bias when the kirigami sheets experienced an external tensile force, such that the notches play a similar role as defects in Euler's column.

The authors go further and propose multi-polarity configurations, (ie where the notch pattern is non-uniform and changes along the kirigami sheet), for example, Fig2.3b presents a bipolar configuration, the lower half (colored in green) is designed to tilt for anti-clockwise

⊕. Repeating the same notch pattern as the bottom half but with switching the forward and back notches positions, the top half (colored in yellow) will then tilt clockwise ⊖.

The method developed by Tang then allows for bias of the buckling process and control of the rotation side of the elementary blades. Based on this technique we will probe the effect of a non-inform polarity across a given pattern. Let us begin with a bipolar configuration (two opposite signs) that we are going to describe in the next section.

Interlude $n^0 8$: Post-buckling shapes

We can predict the post-buckling shape of the elementary cells through the reduced beam model employed in interlude n^4. According to the picture below, each kirigami cell can be considered as a combination of two cantilevered beams undergoing flexion due to external load F (representing the global tensile force in a tensed kirigami sheet). The equation for deflection $y(x)$, with x as the curvilinear abscissa in the initial configuration, is derived from the Euler–Bernoulli beam theory.

$$EIy^{(4)} = 0 \quad \longrightarrow \quad y(x) = \frac{F}{6EI}x^2(3L - x)$$

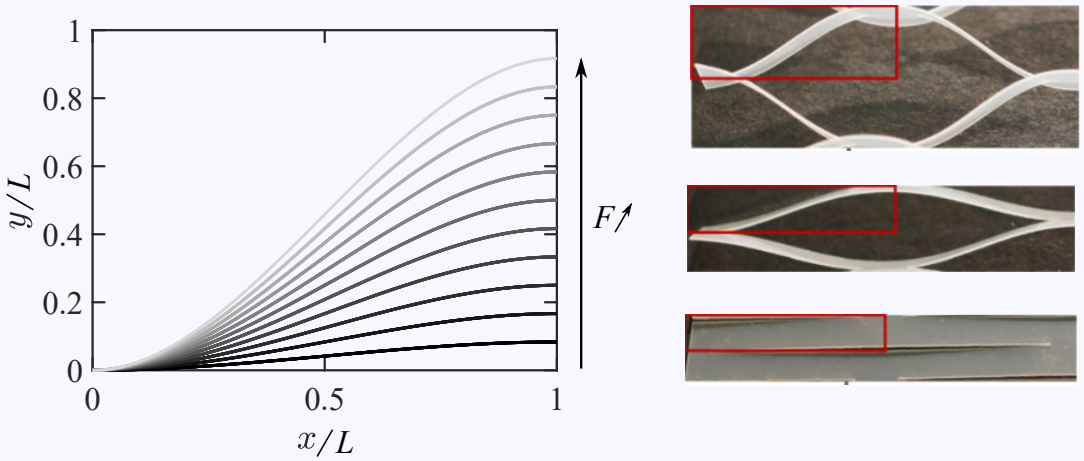

To gain an initial understanding, we set the bending modulus to $EI = 1$ and beam length $L = 0.5$ and plot the deflection for various values of F. These shapes resemble experimental observations and show good agreement, despite the assumption of low deflection.

2.2 A relevant specimen: bipolar case

The method developed by [56], allows multiple polarity inversion along the pattern. To be more familiar with the interplay between local polarity changes and deformation shapes in a flow, we mainly focused on a bipolar case, characterized by a single polarity inversion, that we are going to present in the following.

2.2.1 Parametric definitions

As defined in Fig2.4a, the polarity distribution along the cutting sheet is split into two parts (highlighted by the shaded area). The transition between each of them is localized by the parameter $a \in [0, 1]$, such as the length aL corresponding to the shaded part size, conventionally defined as the left portion of the pattern. The illustrative specimen in Fig2.4a represents the case $a = 0.5$ (i.e. a transition in the middle of the cutting pattern). Notice that the parameter a only localizes the transition, thus each part can have both polarities

(as a reminder: anti-clockwise: ⊕ and clockwise: ⊖), so we can have $\boxed{+-}$ or $\boxed{-+}$ for a given a.

Actually, the polarity is a property defined relative to the incoming flow direction U (see Fig2.4c) and can be inverted by flipping the pattern from a recto side to a verso one. In this way, each side corresponds to a polarity configuration (or state) distinguished by their signs $\boxed{+-}$ and $\boxed{-+}$ in the rest of the manuscript.

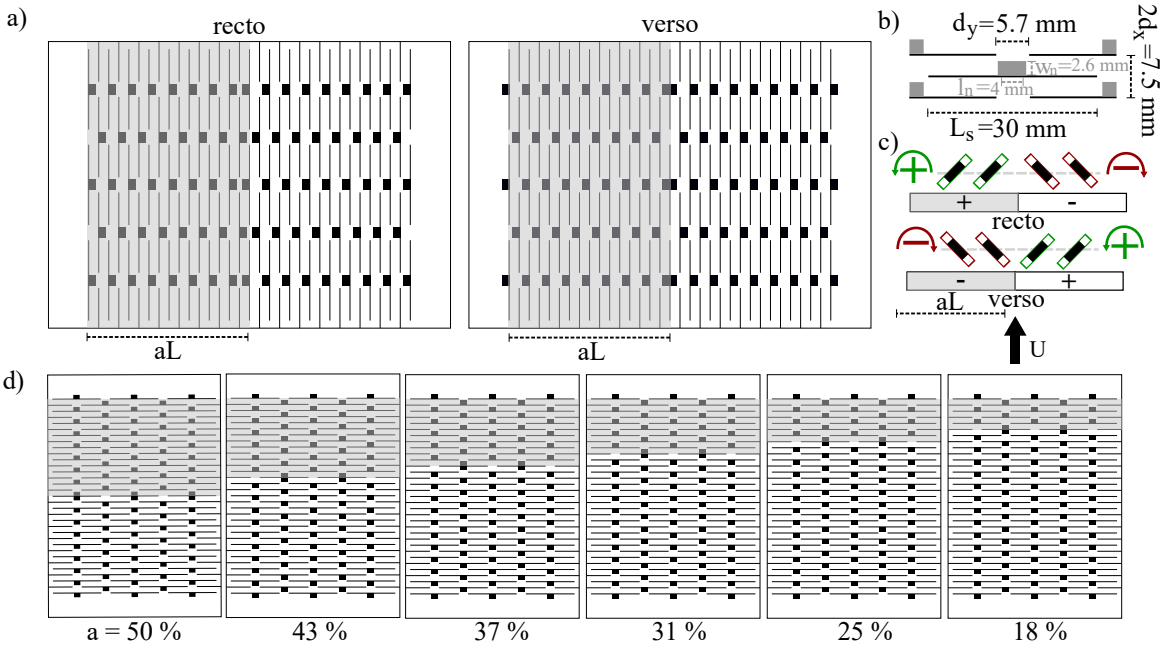

Figure 2.4: a) Both sides of a typical bipolar kirigami pattern, the notches network is staggered from one side to the other. The polarity inversion is localized at a distance $aL = 0.5L$ from the left end, each part of the kirigami sheet buckle along an opposite direction. b) Definition of cutting parameters for the parametric study on a : $(L_s, d_x, d_y) = (30, 3.75, 5.7)$ mm and notches definition $(l_n, w_n, t_n) = (0.4 \times L_s, 2.8 \times t, 0.6 \times t)$ with $t = 1.5$ mm. c) Schematic side views of the specimen a) each polarity configuration is defined according to the flow direction U, in practice to invert the polarity state we flipped the pattern which keeps a unchanged. d) All the patterns tested for our parametric study on a (verso view only)

Two parametric studies were carried out on these bipolar specimens; we first probe the effect of a, by varying this parameter from 0.18 to 0.5 through six different parameters all drawn in Fig2.4d. In this first experimental campaign, we impose a similar cutting pattern for all sheets detailed in Fig2.4b, which ensures to keep constant the effective stiffness as we will check in the next subsection.

By this means, we only vary the notches distribution and then shift the transition location. Notice also that we don't experimentally investigate values of a higher than 0.5, because we supposed that the case pattern a and $1 - a$ are equivalent, in the sense that they should deform symmetrically under flow (a further discussion will be proposed in the theoretical section of the chapter).

We also perform a second campaign in which we keep fixed the parameters $a = 0.5$ value and vary the effective stiffness by changing the length of the slit for three patterns $L_s = [2.75, 3, 3.25]$ with associated effective stiffnesses varying from $K_2 = [7.7, 3.9, 2.7]$. Through these two campaigns, we probe the effects of stiffness and polarity independently and then provide a first insight into nonuniform kirigami design.

2.2.2 Manufacturing process, notches between slits

To engrave notches near the cuts, we need to switch to a different material as the current thin mylar cannot sustain deep engraving without risking perforation. We opted for 1.5mm thick rubber sheets, which offer the same thickness and elasticity as the PDMS used by Tang et al. (2017).

However, laser cutting the new material is more challenging than Mylar films, so we use a two-step process. First, we create the slit tessellation, then we engrave the notches on each side of the previously cut sheet. To stay consistent with Tang's work, we selected characteristic notch sizes that are median to their values: $(l_n, w_n, t_n) = (0.4 \times L_s, 2.8 \times t, 0.6 \times t)$. These lengths remain constant for both campaigns previously mentioned, as they have little impact on the mechanical behavior in the out-of-plane regime, as noted in [56]. Let us check this point in the following.

2.2.3 Stiffnesses seem similar

To confirm that a value does not impact the mechanical property and determine the effective stiffness of the six specimens of the first campaign (same cutting parameters), we conduct uniaxial tensile tests on a Zwick machine equipped with a 100 N load cell.

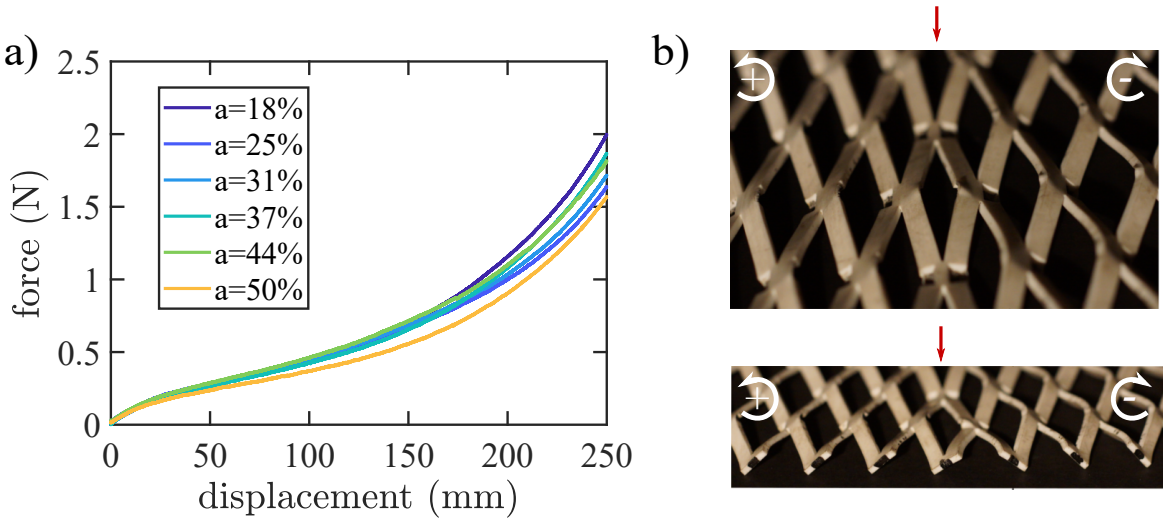

Figure 2.5: a) Tensile forces as a function of displacement for all kirigami bipolar specimens defined in Fig2.4, it exhibit the same trend so an equivalent effective stiffness $\overline{K_2} = 3.9N/m$ .b) Zoomed view of the polarity transition (red arrow) for the specimen $a = 0.5$ at the configuration $[+-]$.

Figure 2.5a shows the force-displacement curves for the bipolar pattern set, with each color representing a value of parameter a. The non-linear mechanical behavior mentioned in Chapter 1 is still evident, including the two linear regimes and the sharp increase in forces at high displacement. The variation in a has no effect on the behavior, as the curves remain similar regardless of the deformation regime and a value, suggesting that the mechanical behavior is solely determined by the cutting pattern. This leads to an estimated mean effective stiffness of $\overline{K_2} = 3.9N/m$. This implies that all specimens will have a comparable Cauchy number in subsequent sections (keep that in mind !).

One can also notice that the transition between deformation regimes is smoother with a rubber sheet compared to previous specimens made with mylar films. This is because the presence of notches reduces the critical force for out-of-plane cell buckling [56] and the gravity effect also tends to reduce the non-linearities and trigger the pore opening at low tensile load (see the interlude n^o9 for more details).

Before describing the result of the first experimental campaign, let us improve the image processing methods introduced in chapter 1.

Interlude n^o9: Impact of weight on tensile measurements

The rubber sheet is significantly heavier than the mylar one, due to the large difference in thickness (15 times thicker). As a result, the rubber kirigami tends to stretch under its own weight when in a vertical position, as shown in the attached picture. One may consider the impact of weight on displacement force measurements. To quantify this effect, we aim to estimate the typical displacement caused by gravity. We do this by balancing the elastic restoring forces with the weight of the kirigami along its length.

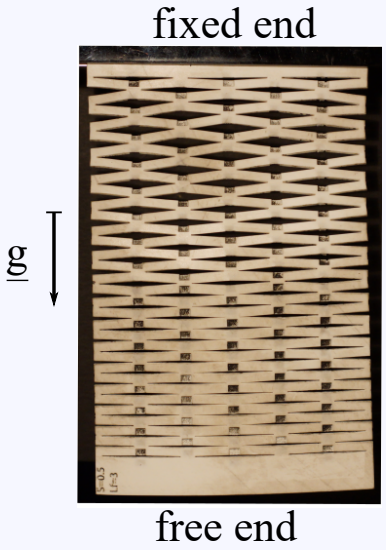

$$k\Delta L_g = \int_0^L \rho_r g t H x dx$$

by integrating :

$$\Delta L_g = \frac{\rho_r g t H L^2}{2k} = \frac{\rho_r g t H L}{2K}$$

A direct calculation shows that the change in length due to gravity (ΔL_g) is approximately 24 mm, which is around 10% of the maximum displacement reached during our tensile test. Thus, the effect of gravity on the stiffness measurement of the second regime K_2 can be disregarded. However, it's important to note that gravity alone is able to open the top part of the kirigami sheet. In this region, the weight loading is higher than the critical buckling force. This is why the transition from in-plane to out-of-plane deformation appears smoother for rubber kirigami sheets

2.2.4 Semi-automatic image processing methods

The previous chapter manually extracted deformation profiles by pinpointing the center of each elementary cell. This method allowed us to determine local variables such as elongation (ε) and profile inclination (α). However, this method is too much tedious and does not provide information on blade inclination. To overcome this and work faster, we developed a custom Matlab algorithm to automate the profile extraction which is processed in two steps as illustrated in Fig2.6a and described in detail below.

We "assist" cell detection by marking the cell centers with a black line (refer to Fig.2.5b). The line only marks the cells' centers, leaving a white gap between each blade. Such as during the thresholding step, our algorithm detects only the black line. Lastly, we use the Matlab function "regionprops" to fit all detected cells as equivalent elliptical shapes. These ellipses are defined by their "centroid" (which represents the center of the kirigami cell), and the inclination angle φ relative to the flow direction (as defined on Fig2.5c. The angle runs from -90 to 90 degrees, where $\varphi = 0^o$ represents a blade facing the flow, and $\pm 90^o$ corresponds to a parallel configuration. The sign follows the polarity definition, with $\varphi < 0$ indicating a $\ominus$ configuration.

Our semi-automatic method provides a rapid and precise extraction of deformation profiles and local variables. Its efficiency was checked by comparing it to our previous manual method and by verifying the angles with direct measurement on ImageJ for selected specimens, all present a very good agreement.

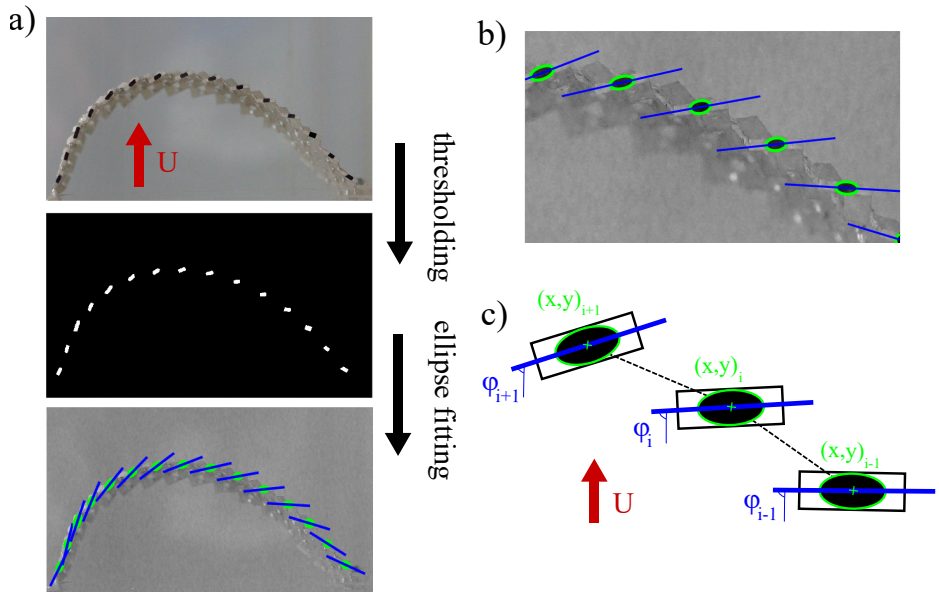

Figure 2.6: a) The image processing method is based on two major steps, 1) thresholding: from colorized pictures, we make a binary to extract the center of each blade (deformation profile extraction). 2) we fit each connected component with an ellipse (blades tilting angles extraction). b) Zooming view of extracted and fitted blades at the last step. c) Schematic view of variables extracted from our custom image processing program.

2.3 A-symmetry control in flows

In this section we will detail the different experimental studies on bi-polar specimens, we will evaluate the impact of the parameter a, the stiffness K_2, and the hiding role of polarity inversion, but first, let us start with the symptomatic and symmetric case $a = 0.5$.

2.3.1 Case a=0.5 symmetric profiles

According to the definitions introduced in section 2.2, the polarity inversion is located at the center for this specimen, such that each half portion rotates along an opposite direction, identified by their the $\oplus$ or $\ominus$ sign (depending on the direction relative to the flow). We will then distinguish the two polarity states, namely: $\boxed{+-}$ and $\boxed{-+}$. It's now time to put the specimen in the water channel.

Polarity control splits the response

Unlike the uniform patterns explored in Chapter 1, this bipolar kirigami achieves a symmetrical shape when in a flow as shown in the two pictures in Fig2.7a (one for each configuration), taken at $U = 21cm/s$. Both polarity states have their lobe localized in the middle of the water channel, but with different morphologies: the $\boxed{-+}$ case results in a parabolic-like shape, while the $\boxed{+-}$ exhibits a semicircular-like one.

This observation holds true at any flow rate and results in different expansion kinematics, as shown in the graph in Fig2.7b, with each configuration indicated by a different line style. Additionally, the amplitude reported in Fig.2.7c reveals that the parabolic shape of the $\boxed{-+}$ configuration has higher y_{max} values than the reverse polarity, especially for high flow speeds regimes.

Before discussing the development of local variables and the origin of these two splitting solutions, let us emphasize the new behavior that arises from the bipolar case. Unlike the well-known homogeneous case, where the $\oplus$ or $\ominus$ uniform polarity (unipolar specimen) provides two asymmetric deformation profiles, but which follows a symmetrical deviation of

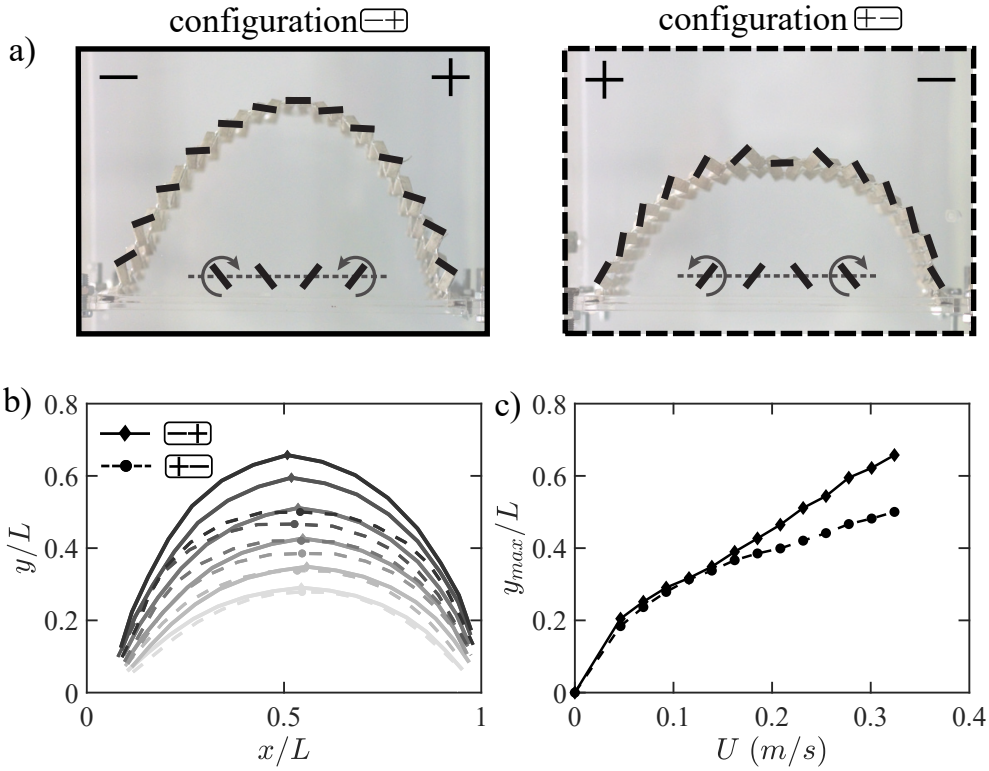

Figure 2.7: a) Symmetric deformation profiles of the bipolar kirigami sheets $a = 0.5$ at$U = 21cm/s$, for the $[-+]$ case the left half rotates clockwise while the right one rotates counterclockwise as indicated by the inset schematics, and inversely for the $[+-]$ case. b) Expansion kinematics of both polarity states when increasing the flow (denoted by the grayscale). c) Deformation amplitudes of graph b) spotted by their respective markers and line styles

the lobe to the right or left with a similar amplitude for both configurations (see chapter 1, and interlude n^o7). The bipolar pattern results in two non-symmetrical solutions according to the polarity state considered, each with a unique morphology and amplitude. Therefore, controlling the polarity of the kirigami sheet allows for two different solutions based on the flow direction. Next, we will examine the impact of this characteristic on local elongation and angular variables

Local variables as a function of polarity state

The local variables calculated from image analysis are shown in Fig 2.8. Let us begin with graph a) which displays the elongation at various flow velocities (denoted by the grey color gradient) as a function of the curvilinear abscissa S/L. As for the global shapes, each polarity state yields a different strain evolution. while the semicircular shape of $\boxed{+-}$ stretches mainly around the middle of the sheet, with a peak of strain around $S/L \sim 0.4 - 0.6$, the inverse configuration elongates the areas near the boundaries. These different trends are in line with the pictures reported in Fig2.7a, where the parabola solution is less deform at the center of the lobe and more at its edges than the semicircular one as suggested by the schematic view of the tilting blades (see inset of each photo). Thus, the differences in expansion kinematics and resulting global shapes can also be detected at the local level through the examination of the elongation for instance.

With our new image processing algorithm, we can now determine the φ angles that each cell forms relative to the incident flow (as defined on Fig 2.6c). These angles are shown on the graph in Fig2.8b and reveal a clear difference between the two polarity states. The $\boxed{-+}$ configuration shows values close to -90^o, meaning the cells are normal to the flow, while the $\boxed{+-}$ solution gradually moves towards 0^o as velocity increases, with blades almost aligned

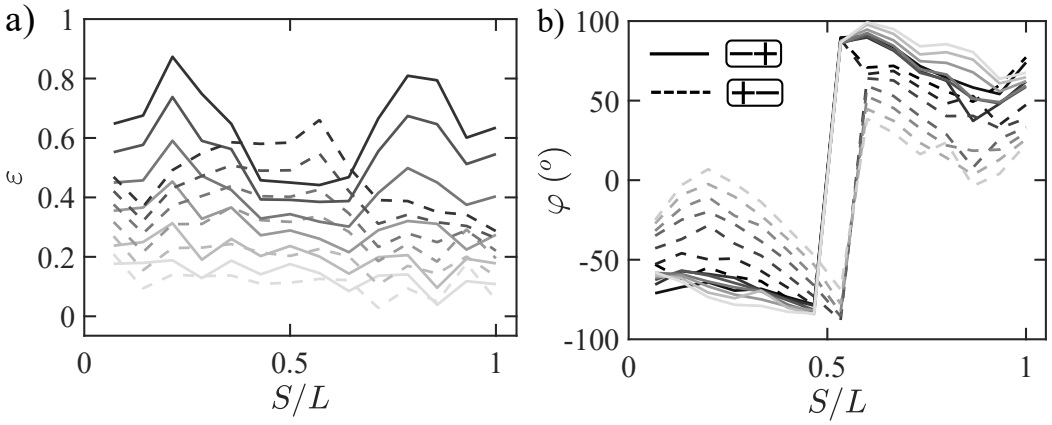

Figure 2.8: a) Local strains as a function of curvilinear abscissa for both polarity states (denoted by line styles) when increasing flow velocities (greyscale color). b) Local tilting blades angles φ relative to the flow direction.

with the flow direction for large flow rate. This trend can be also appreciated in the real images in Fig2.7a for both configurations.

All of these variables highlight the significant difference that emerges from bipolarity. This new lever thus induced the coexistence of two solutions for the same pattern depending on the side exposed to the flow (namely: configuration or polarity state). Having a better understanding of the typical response of a bipolar kirigami and the two configurations, we will now discuss the results of the first experimental campaign, which focuses on the impact of the parameter a.

2.3.2 Playing with a to adjust symmetry

The position of the transition, represented by the values of a, affects the size of each sub-portion of polarity. Here we study the impact of this parameter on shape-shifting caused by flows, by testing six values of a, whose patterns are shown in Fig2.4d.

To get a first idea, pictures of deformation profiles for different a at the same flow speed $U = 32$cm/s are reported in Fig2.9a-b, where each row corresponds to a polarity state and column a value. For each picture, the transition is highlighted by a red circle on the cell concerned.

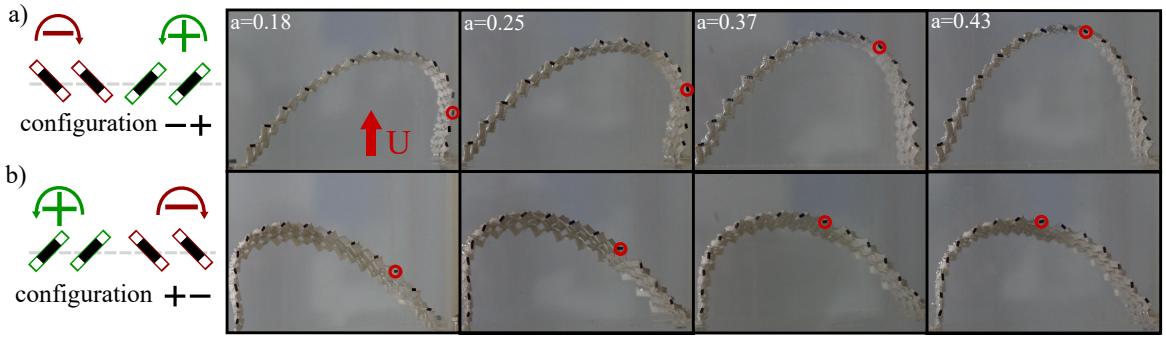

Figure 2.9: Typical shapes in flows for four specimens with varying a values from 18% to 43% at $U = 0.32$m/s, the transition is localized by a red circle around the concerned cell. Each row corresponds to a polarity state: a) [−+] and b) [+−]

After quickly reviewing the pictures from left to right (in increasing order of a), we see that for a fixed incident flow and polarity, the shapes vary. As a increases, the morphology becomes more symmetrical. A low a results in a nearly uniform pattern with most cells

rotating in the same direction, leading to an asymmetrical lobe as seen in chapter 1 (unipolar specimens). However, when the polarity inversion is close to the center and the symptomatic case of $a = 0.5$, the forms tend toward a symmetrical morphology. This holds for both polarity states (configuration), even if the shapes are slightly different.

Our observation is confirmed by Fig2.10a, which plots the deformation extracted from the pictures using a parula color gradient (from dark blue $a = 0.18$ to orange $a = 0.5$) to denote the a value. The deviation from an asymmetric to a symmetric shape can be easily distinguished at a fixed velocity and varied a. the polarity effect can be also noticed, with the $\boxed{-+}$ solution (solid lines) being more deformed than the $\boxed{+-}$ case (dashed lines). To highlight these two results, a new type of graph is presented in Fig2.10b, which we are going to detail.

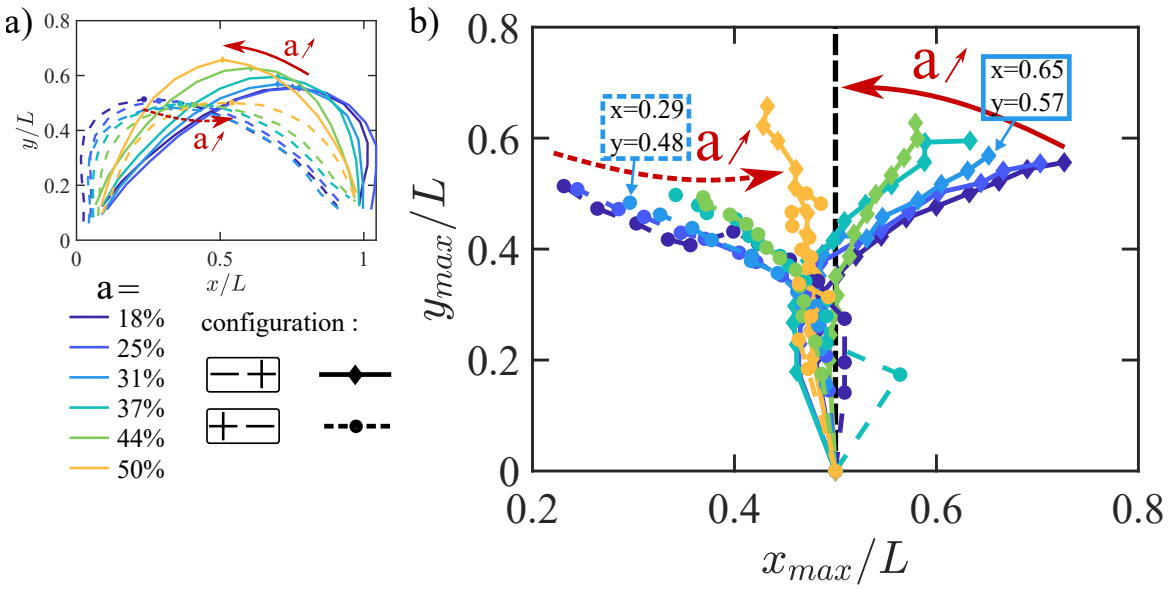

Figure 2.10: a) Deformations profiles for all a values (denoted by parula scale color) at their two polarity states (line styles) at fixed flow velocity $U = 0.32$ m/s (the same as in Fig2.9). b) Trajectories of the cells associated with the maximal deformation, each point corresponds to one velocity, each curve one pattern at their respective polarity state (line style). The deviation x_{max} are the abscissa attached to the amplitude y_{max}

Instead of just focusing on amplitude evolution (i.e y_{max}) as in the previous chapter, we propose here to include the corresponding x_{max} abscissa to better track the cell's trajectory with maximal deformation at each velocity (a point a speed). This plot (Fig2.10b) enables us to study the lobe trajectory and quantify its asymmetry. Thus, a symmetrical deformation lobe (orange curve for) associated with $a = 0.5$, will result in a trajectory close to the center of the vein ($x/L = 0.5$marked by a dotted red line), while an asymmetrical profile like that of the dark blue curve for $a = 0.18$ will show a curved trajectory shifted to the left for the $\boxed{+-}$ configuration or to the right for the opposite polarity state.

This graph exacerbates the impact of parameter a, which affects the symmetry of the shape underflow, as seen in the increasingly symmetrical order of the trajectories with increasing a. This graph also reveals the non-symmetry between the two polarity states, with the $\boxed{+-}$ configuration profiles having lower amplitude and greater lateral deviation than for $\boxed{-+}$. We will discuss this further when comparing with the theoretical model, which allows a more comprehensive examination across the entire range of a values (from 0 to 1).

2.3.3 Side campaign: stiffness and polarity

The second experimental campaign examines the variation and differences in shapes resulting from changes in effective stiffness (i.e. cutting pattern). Three patterns with a similar

number of cells ($N_x = 16$) and fixed value of $a = 0.5$, but different effective stiffness $K_2 = [7.7, 3.9, 2.7]$N/m, are tested in flows. We report their respective deformation profiles for both configurations in Fig2.11a-b, where each curve color corresponds to one pattern (i.e stiffness value).

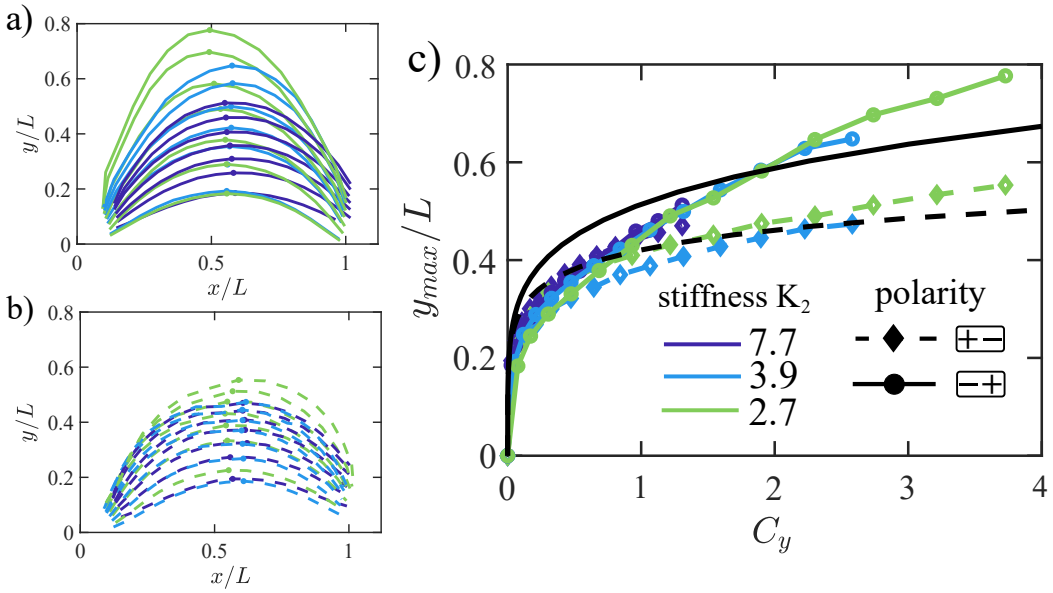

Figure 2.11: Deformation shapes of 3 bipolar kirigami sheets with $a = 0.5$ fixed and various slits length $L_s = [2.75, 3, 3.25]$ and their respective stiffness $K_2 = [7.7, 3.9, 2.7]$N/m for both configurations, a) $[-+]$ parabola-like shapes. b) $[+-]$ semi-circular-like one. c) Their respective amplitude y_{max} evolution against Cauchy number C_y, the black lines represent the theoretical prediction.

First note that the trends suggested by Fig2.11a-b, confirm the result of chapter 1: a higher stiffness results in lower expansion. This point is attested in both polarity states, which conserve their symptomatic shapes previously presented in the first insight of subsection 2.3.1: parabola like for $\boxed{-+}$ and semicircular for $\boxed{+-}$, all the more marked that the stiffness is low.

Our definition of the Cauchy number $C_y = \rho U^2 H/K_2$ and its associated hydro-elastic forces balance are used to cast the amplitude evolution in Fig2.11c, normalized by the sheet length L. The results reveal a collapse onto two different curves according to the polarity state. This master curve splitting is a reminiscence of the effect of nonuniform polarity and highlights that the Cauchy number fails to capture this effect: one pattern, one C_y but two shapes.

Our experiments demonstrate the effectiveness of using polarity to control flow-induced deformations in kirigami sheets. We present a simple yet significant bizonal scenario where the deformation and symmetry can be adjusted by altering the position of the polarity transition point a and its effective stiffness K_2. Our findings suggest that two different expansion kinematics and resulting shapes can be achieved by reversing the polarity state in a given bipolar specimen, a property style unobserved for the unipolar case.

2.4 What about theory ?

2.4.1 New ingredient and first results

We experimentally proved that programming the polarity gives access to a shape control lever. We seek here to introduce this property into the theoretical model established in Chapter 1.

Since polarity control has no effect on mechanical properties, we will only modify the fluid force expression. Let us recall that our fluid force model split the external load into two

components: normal (f_N) and tangential (f_T) relative to the surface of the equivalent membrane that represents the kirigami sheet. Hence, controlling the local polarity adjusts the direction of fluid forces, specifically the tangential component, which is dependent on the local cell rotation angle (θ) and its respective sign (polarity). We also assume that this new feature has no impact on the normal component. A more detailed examination of the role of each force component is proposed in the interlude n^o10.

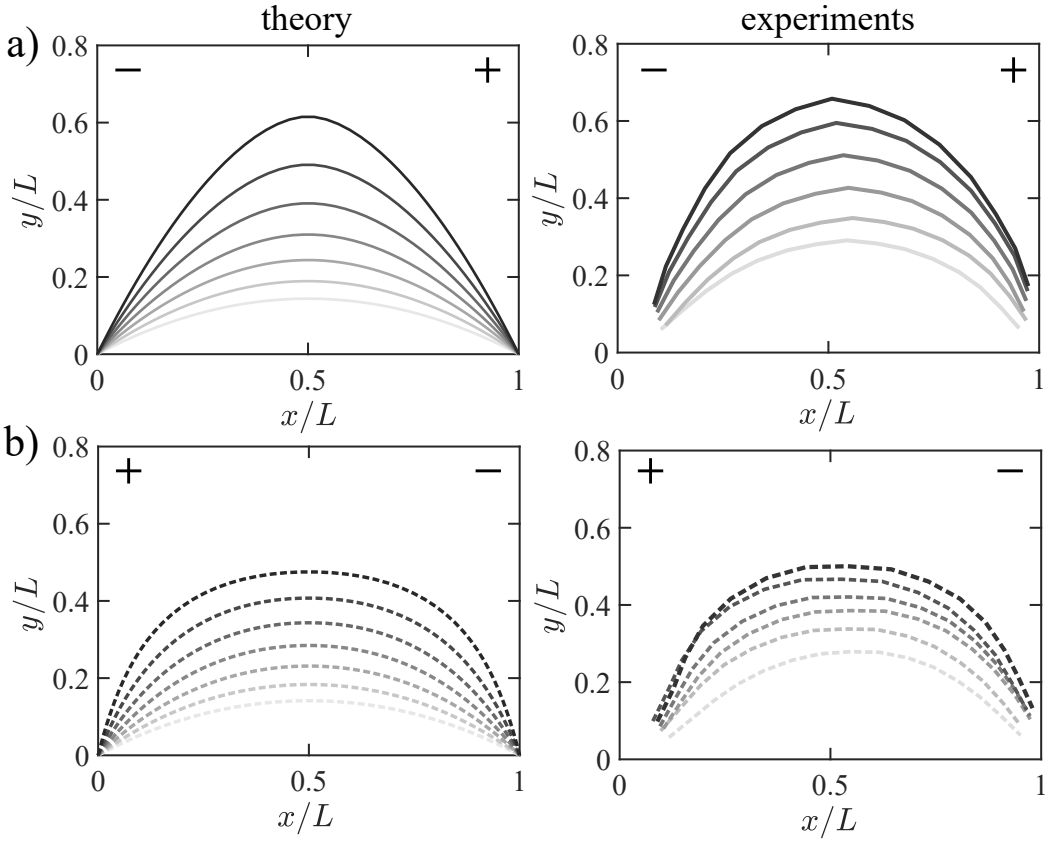

Figure 2.12: Direct comparison between theoretical prediction and experimental results on shapes for the same range of $C_y \in [0, 4.5]$ and both configurations for a bipolar kirigami pattern at $a = 0.5$: a) $[-+]$. b) $[+-]$

If we first only focus on the bipolar case with polarity inversion localized at a distance aL from its left edge (as described above), we introduce a new function $sgn(\tilde{S})$ to ensure the local sign changes (where $\tilde{S} = S/L$ curvilinear abscissa in its dimensionless form). The latter is defined as a step function with a $+1$ or -1 value depending of the polarity state encoded at each sub-part of the pattern, such as the tangential component per unit length for the $\boxed{-+}$ configuration is defined :

$$f_T = sgn(\tilde{S})\frac{1}{2}\rho C_T(\varepsilon)(U\gamma(\varepsilon)\cos(\alpha))^2 \quad \left| \begin{array}{l} sgn(\tilde{S}) = -1 \text{ if } 0 \leqslant \tilde{S} \leqslant a \\ sgn(\tilde{S}) = +1 \text{ if } a < \tilde{S} \leqslant 1 \end{array} \right. \tag{2.1}$$

Where $\gamma(\varepsilon)$ is a local factor for effective velocity $U\gamma(\varepsilon)$, and $C_T(\varepsilon)$ the coefficient that takes into account the blade tilting effect. We inject this expression into the equilibrium equations of the previous chapter which is now expressed as:

$$\begin{cases} \varepsilon\alpha' + \dfrac{C_y}{2}C_N(\varepsilon)(\gamma(\varepsilon)\cos\alpha)^2 = 0 \\ \varepsilon' + sgn(\tilde{S})\dfrac{C_y}{2}C_T(\varepsilon)(\gamma(\varepsilon)\cos\alpha)^2 = 0 \end{cases} \tag{2.2}$$

This system has been solved for a range of Cauchy numbers similar to the experimental values and will be directly compared in the following paragraphs. Let us begin with Fig2.12, which displays the predicted deformation profile for the case $a = 0.5$ in its two polarity states. The comparison with experiments reveals a remarkable agreement; our model successfully captures both the parabolic and semicircular morphologies (relative to the flow configurations) distinguished in our previous measurements.

Interlude n^o10: $f_t - f_t \sim f_n$? The impact of tangential component

Reversing the polarity sign of each portion for the bipolar kirigami sheet inverts the direction of tangential forces. This raises the question of whether this component still influences the deformation process for the specific $a = 0.5$. As each sub-part now pulls on the sheet in the opposite direction, it seems reasonable to assume that it cancels out the tangential loads, leaving only the normal component in the force balance. In other words, is setting $a = 0.5$ equivalent to having $f_t = 0$ across the entire profile?
To address the issue, we compare three theoretical solutions for $C_y \in [0, 4.5]$: first, the two states of polarity at $a = 0.5$, and the non-realistic case where only f_n is considered and $f_t = 0$. We observe that, although the deformation profiles remain similar, the amplitudes do not align with either of the two solutions and result in an intermediate evolution between the states. There are also some noticeable differences in shapes, indicating that tangential forces, regardless of their direction, can make the profile rounder or sharper depending on the polarity configuration.

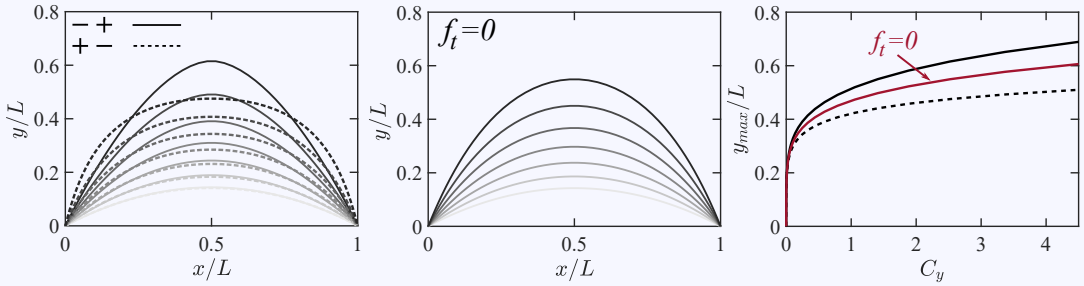

It's important to note that without tangential forces, our equilibrium equation system leads to a constant strain along the entire profile: $\varepsilon' = 0$. The value of this elongation is determined by the boundary conditions.

Fig2.11c also allows for a direct comparison of the amplitudes y_{max} and C_y for specimens with $a = 0.5$ and varying K_2 (second experimental campaign). The theoretical results (represented by black lines) accurately capture both the qualitative and quantitative aspects of the observations. The model particularly predicts that the $\boxed{+-}$ configuration experiences less expansion in flows compared to the $\boxed{-+}$ case.

The agreement is also confirmed at a local level on Fig.2.13 for both strain and profile inclination with a similar tendency as observed experimentally. Particularly for elongation, the polarity state $\boxed{+-}$ shows more deformation in the center ($S/L = 0.5$) while the $\boxed{-+}$ case has it along the edges, although the theoretical predictions appear slightly more pronounced than our observations.

Given the accuracy of our model for $a = 0.5$ pattern, we will now explore the impact of varying this parameter over a range that encompasses our experimental data.

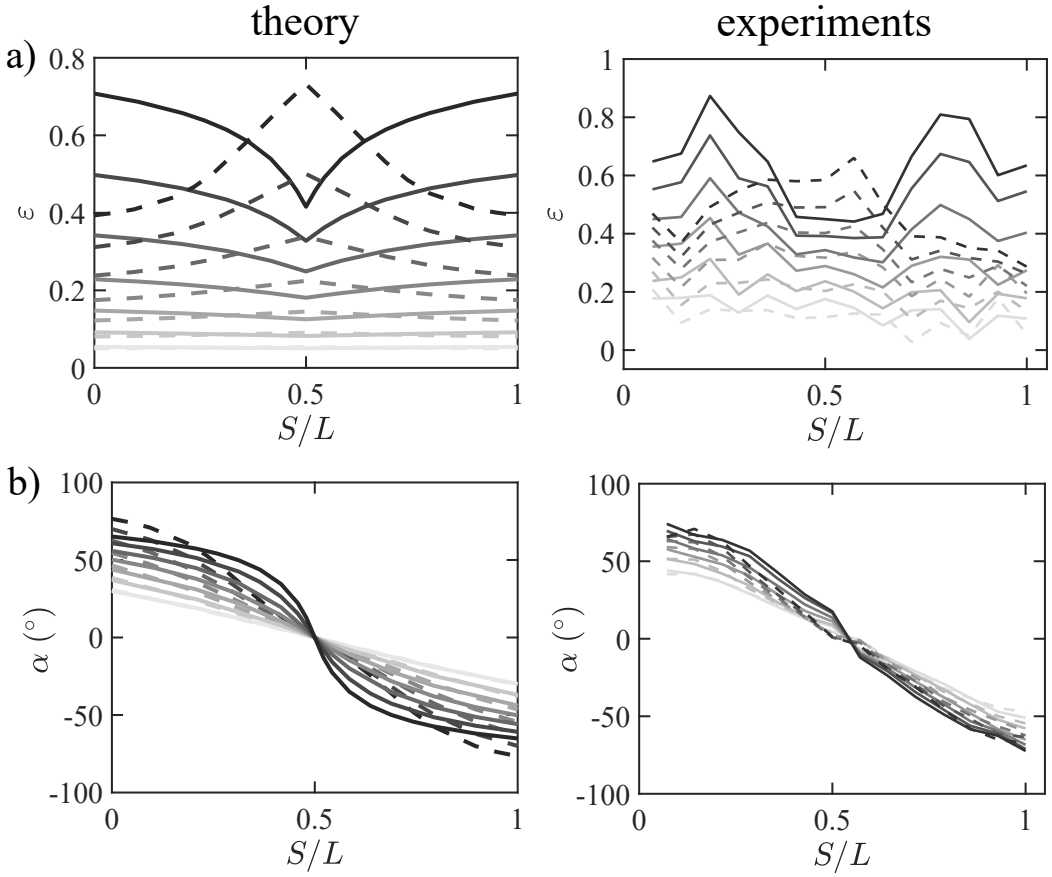

Figure 2.13: Trends comparison of local values (line style corresponds to a polarity configuration) for the specimen $a = 0.5$: a) elongation ε. b) Profile inclination α.

2.4.2 Let us push the theoretical prediction further

Let's compare the amplitude trajectory evolution (y_{max} vs x_{max}) for varying a. Fig2.14a combines experimental measurements from Fig2.10 for all six a values (denoted by the parula gradient color) and the theoretical predictions (colored lines). At a first glance, the theory appears to follow similar trends as the experiments with deviations to the right or left as a decreases. However, the model shows larger deviations than what was observed in the water channel. Despite this, our continuous approach still captures the progressive deviation trend as a changes. As reported by experimental data, the theoretical trajectories are not symmetrical according to the polarity state considered: for same a (i.e. color) dashed curves are not symmetrical to solid ones.

But let us expand our model. In the experiments, for symmetry reasons (assumed beforehand), we only considered values of a between 0.18 and 0.5. However, this constraint can be lifted by using the theoretical model, as evidenced by the different profiles shown in Fig2.14b and c. Where each colored curve corresponds to a different value of a, ranging from blue ($a = 0$) to yellow ($a = 1$) for a high Cauchy value ($C_y = 10$) to highlight the differences. We confirm our hypothesis: specimens a and $1 - a$ exhibit symmetrical expansions for a given polarity state (split into two graphs). Additionally, while the unipolar cases ($a = 0$ or 1) are identical for both configurations, the deviations and deformations for intermediate a values follow different pathways, with larger amplitudes for the $\boxed{-+}$ case and smaller ones for $\boxed{+-}$ as a approaches 50% as suggested by the red arrows.

Therefore, both theory and experiment demonstrate that for a bipolar specimen, influencing the value of a (polarity transition localization) offers a new tool for manipulating the shape-shifting symmetry. This results in a new behavior with the presence of two expansion

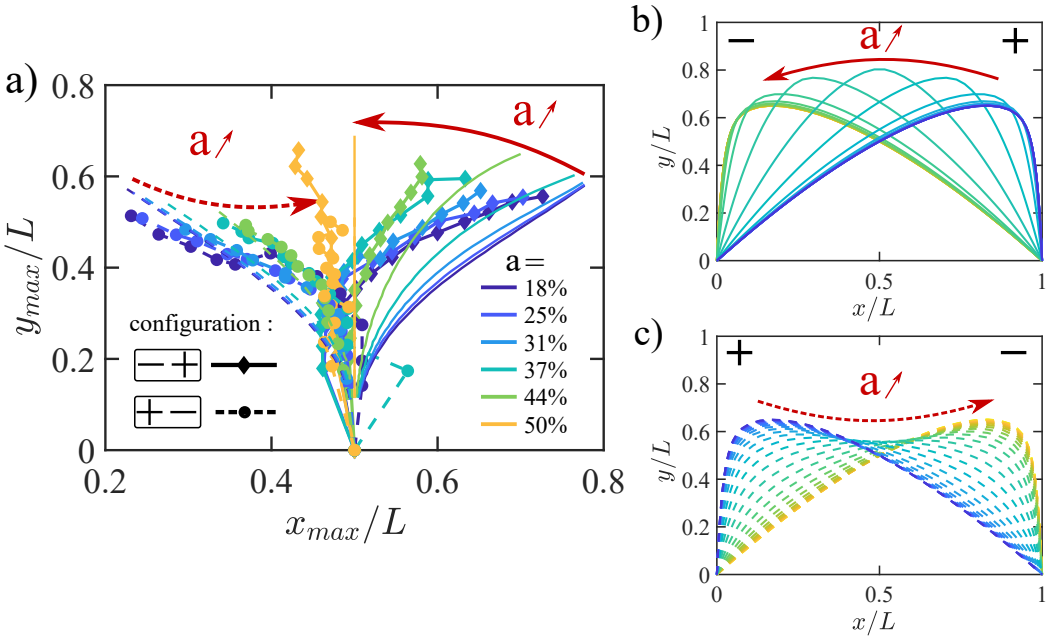

Figure 2.14: a) Amplitude trajectories for six specimens with a varying value of parameter a (parula grad color), the theoretical prediction is defined by the solid and dash line which follows the same color code. Deformation profiles derived from theory for a varying from 0 (blue curves) to 1 (yellow) at $C_y = 10$ for both polarity states : b)$[-+]$ and c) $[+-]$.

kinematics, depending on the polarity state, thus one pattern generates two non-symmetrical deformation shapes for a bipolar kirigami pattern. Based on this understanding, let us now examine multipolar configurations.

2.5 Multipolarity: ever more control ?

We have previously focused on simple bipolar patterns by modifying either the cutting or notch patterns. However, more complex cases with multiple inversions are supposed to provide richer results. As proposed in [56], the author presents specimens with complex shapes, as shown in Fig2.15 with a quadri- and tri-polar cases.

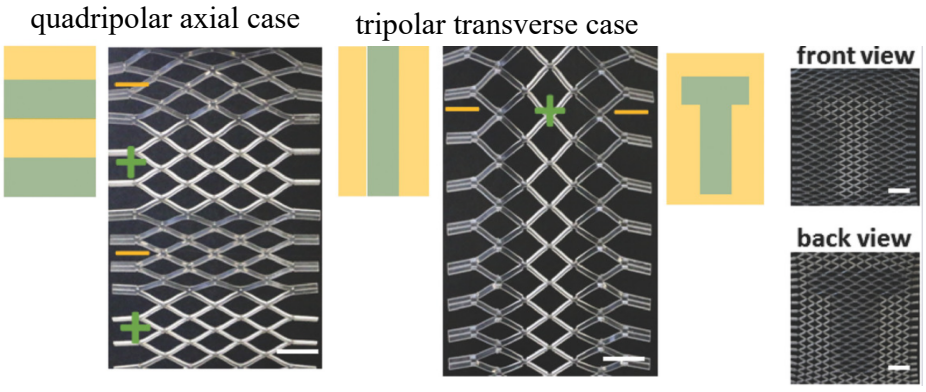

Figure 2.15: Multi-polar kirigami sheet with axial and transverse inversions. Tang et al. (2017 successfully showcased a "T" design within the pattern. All images sourced from [56].

We are exploring the effect of a greater number of polarity blocks on flow-induced deformations through experimental testing of quadri-polar specimens divided into four areas and three polarity inversions. For even more complex configurations, we will use theoretical modeling, which will be discussed later.

2.5.1 Experimental investigation: quadri-polar case

Even if the fabrication methods enable fine polarity control without size and complexity restrictions, the water channel and experimental setup sizes limit the number of cells and polarity inversions. Despite this constraint, we test a quadri-polar specimen following the same cutting parameters as previously defined in our first campaign (characterized by the effective stiffness $K_2 = 3.9\text{N/m}$).

As shown in Fig2.16a, the kirigami sheet is divided into four equal-sized blocks (three cells) with alternating polarity. Like in bipolar cases, the rotation side changes when the sheet is flipped (fluid low direction), leading to two different configurations, $\boxed{+-+-}$ and $\boxed{-+-+}$. An example of the latter in lows at $U = 0.21\text{m/s}$ is reported in the picture of Fig2.16b.

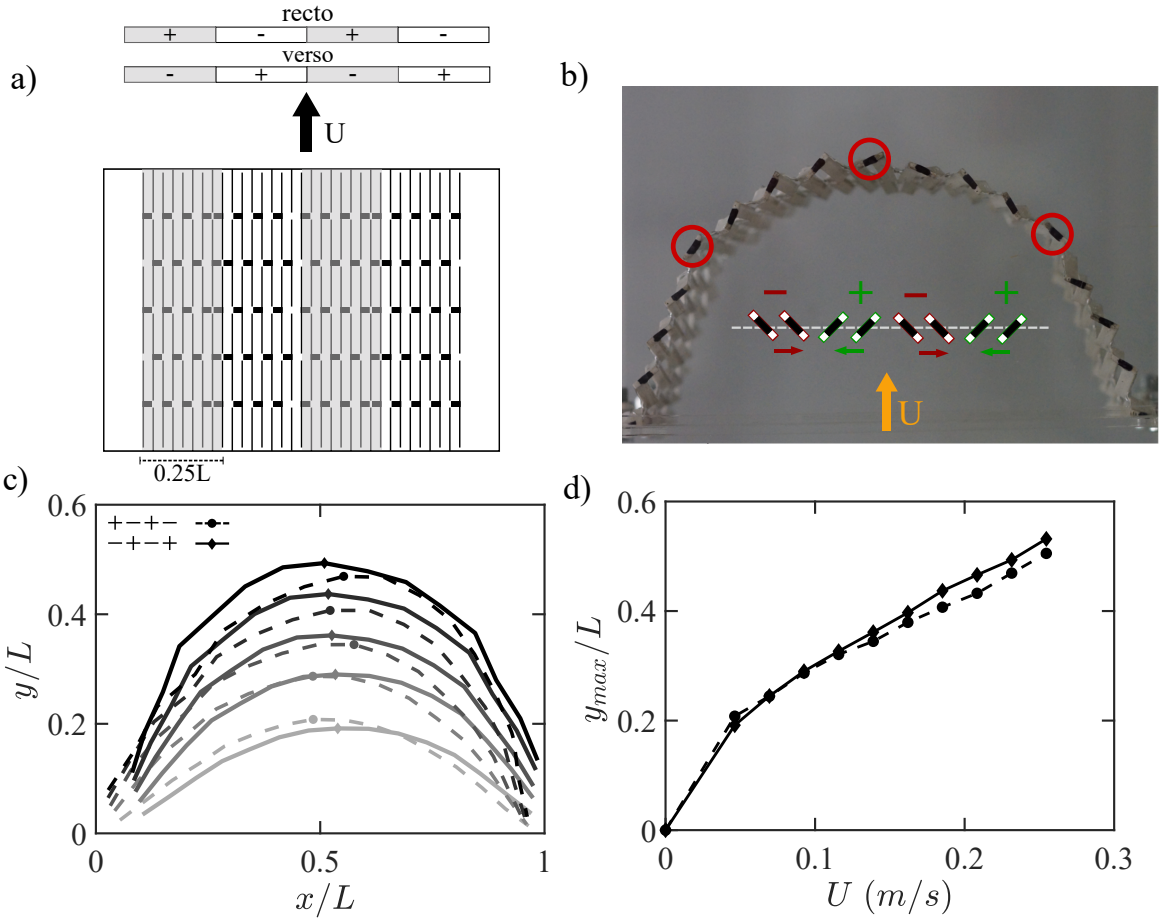

Figure 2.16: a) Quadri-polar Kirigami case viewed schematically (3 inversions, 4 blocks), each block represents 1/4 of the total size. b) $[-+-+]$ configuration in water flow, inversions shown by red circles. c) Deformation shapes extracted by using a custom Matlab program, (velocity denoted by greyscale color and polarity state shown by line styles). d) Amplitudes derived from c.

Fig2.16c and d present the deformation profiles and amplitudes of the quadripolar specimen in its two polarity states. It is observed that the deformation profiles are symmetrical, like the bipolar specimen at $a = 0.5$, for both configurations. However, here, amplitudes and shapes remain close throughout the kinematics (see Fig. 2.16d), which suggests that increasing the number of inversions reduces the impact of tangential forces on the macroscopic shape and converges toward a similar morphology. To confirm this hypothesis, further numerical analysis is required.

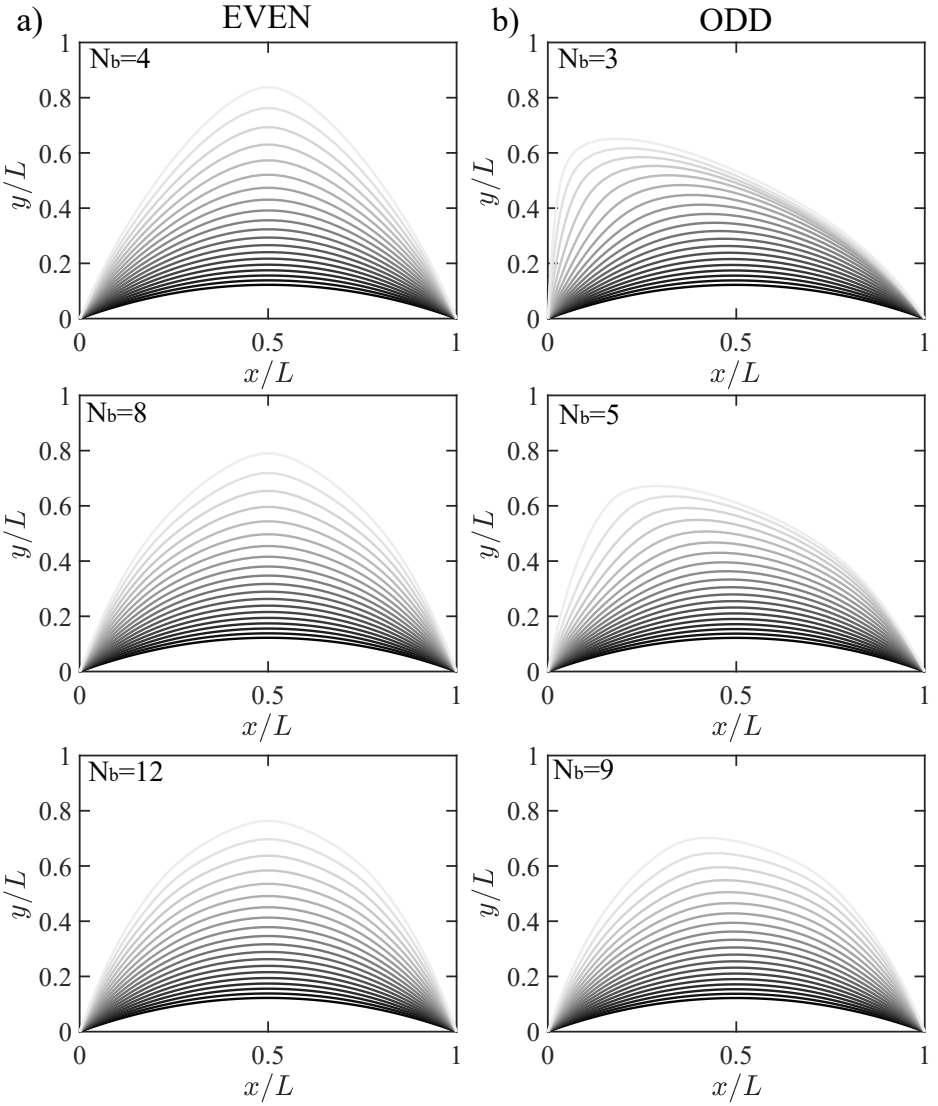

Figure 2.17: Theoretical deformation shapes obtain by varying C_y within the range $[0, 10]$ (denoted by an inverted greyscale) and changing the polarity block number $N_b = N_i + 1$. The results are split into two rows based on the parity of N_b: a) even and b) odd.

2.5.2 More and more inversions or less and less control ?

Increasing the polarity block number (i.e. polarity inversion), poses limitations in experiments (such as water vein and kirigami cell sizes, laser cutter precision,...). To overcome these constraints, we plan to study more complex cases using theoretical modeling. In practice, we modify the sign function $sgn(\tilde{S})$ to account for N_b blocks (or $N_i = N_b - 1$ inversions) in Eq2.2, which we assume to be equally spaced. Fig2.17a-b display six different multi-polar kirigami sheets with varying N_b, and increasing Cauchy numbers from 0 to 10. We categorize the profiles based on polarity block number parity (odd or even) into two rows.

The distinction between even and odd values of the number of polarity changes (indicated by N_b) is significant because it affects the response of the system in two ways. If N_b is even, as shown in Fig2.17a, the profile morphologies are similar to those of symmetrical bipolar cases ($a = 0.5$) with decreasing amplitude for higher numbers of inversions. On the other hand, if N_b is odd (see Fig2.17b), the deformation shapes turn from asymmetric to symmetric with lower lateral deviation as the block number increases (it should be noted that $N_b = 9$ is almost perfectly symmetrical and looks like $N_b = 12$), while the amplitude

marginally increases, in contrast to the even previous case.

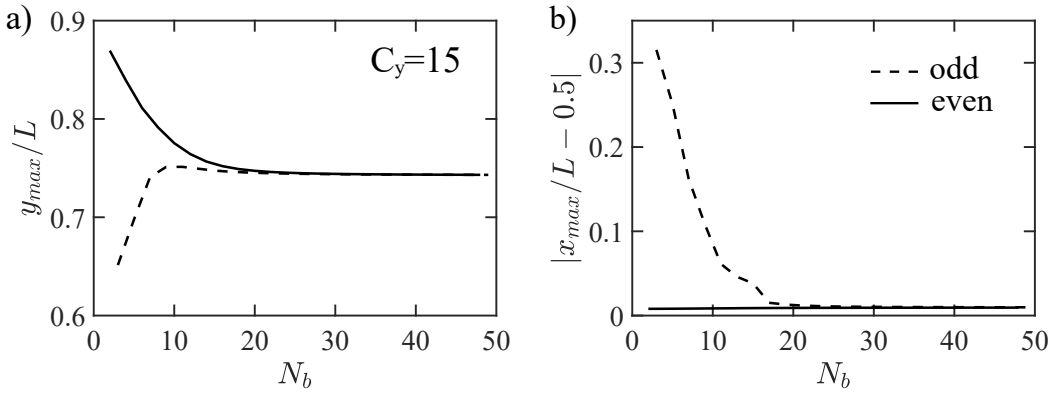

Figure 2.18: Evolution of deformed shapes maximum coordinates for a given $C_y = 15$ when N_b is increasing: a) amplitudes b) deviations, both odd and even block numbers (line style) are illustrated and converge to same values.

To analyze the deviation and amplitude variation of two parities, we present their evolution in the corresponding graphs of Fig2.18. Each line represents the y_{max} or x_{max} values attained for a constant $C_y = 15$ as the function of blocks number N_b. The previously noted trend in the shape-shifting graphs is evident, particularly the fact that as the number of inversions increases, both amplitudes and deviations converge to similar values, resulting in equivalent morphology. This implies a limitation in using polarity to control shape: the block sizes must be large enough to generate a substantial effect from tangential forces, otherwise the kirigami sheets will have similar shapes as noted in the interlude $n^o 10$.

2.6 Conclusion

In this second chapter, we examined a new set of kirigami patterns with a non-uniform polarity, through a simple but relevant example: bipolar specimens. These bipolar patterns are characterized by their structural stiffness K_2 and the parameter a, which defines the size of each portion. When the transition is localized in the center ($a = 0.5$), the resulting shapes under flow are symmetrical, unlike the uniform patterns from chapter 1.

We emphasized the significance of the polarity state relative to the flow for these patterns. Both configurations, $\boxed{-+}$ and $\boxed{+-}$, result in distinct responses. The first creates a parabolic-like shape with cells perpendicular to the flow, while the second exhibits smaller semicircular-like shapes with blades that tend to align with the incoming flow.

We conducted two experimental campaigns to study the morphological evolution of bipolar kirigami sheets with the same stiffness but varying a. Our results showed that altering parameter a affects the position and symmetry of the deformation lobe, while inversing polarity state provides non-symmetrical expansion kinetics (unlike the unipolar cases of chapter 1). In a second experimental campaign, we the effective stiffness while keeping the transition at the center ($a = 0.5$). Our results confirm that the stiffness effect described in Chapter 1 can be captured by the Cauchy number, however, here the two possible polarity states provide a distinct response in flow.

The theoretical model, previously expanded to include this new feature, is used to compare these two campaigns. Our continuous membrane description aims to determine the shapes and amplitudes using the same parameters, a and K_2, as those tested experimentally. The results show a remarkable agreement, confirming the reliability of the continuous description even for complex configurations with varying polarity. This theoretical modeling has enabled us to investigate the response of more complex configurations with multiple inversion

numbers. However, we find that multi-polar patterns converge to equivalent deformation profiles when the number of polarity blocks is "excessive" relative to the sheet size.

Hence, polarity control is a noteworthy solution for our shape control challenge under fluid loading. However, adjusting the orientation of local forces remains limited if they are only applied to a small part of the cutting pattern.

3

Reaching new shapes through spatial stiffness variation

Figure 3.1: "You're next, Hook(E) ! This time you've gone too far!" Peter Pan

The mechanical behavior of a kirigami sheet is mainly determined by the local design and characterized by its effective stiffness. In this chapter, we explore the impact of varying the cutting pattern by introducing heterogeneity and examining its effect on the shapes reached in a flow. We focus on nonuniform bizonal cases divided into two portions of different sizes and stiffness. Our experiments and a simplified model reveal new behaviors such as non-monotonical expansion kinematics or a surprising convergence toward a universal shape. The introduction of heterogeneities within the cutting pattern is then a new lever to reach new morphologies. Thus, our bizonal specimens pave the way for more complex stiffness distributions.

3.1 Non-uniform kirigami patterns

The pioneering works of Isobe et al (2016), followed by multiple research groups, have demonstrated the direct link between mechanical properties and the cutting parameters [43, 57, 58, 45, 72]. It promotes kirigami art as a method to tune the mechanical behavior by adjusting the local design. In chapter 1, we have introduced the effective stiffness of the whole kirigami sheet as a function of the local geometry, and its impact on expanding kinematics in flows. However, these studies and our work so far have dealt with uniform cutting patterns, it's time to go further and make it vary spatially.

Several studies have already investigated non-uniform cutting patterns and their effect on structural properties. Concerning our parallel-slit pattern, Taniyama et al. already probed the subject, their main motivation was to reduce the boundary effects that appear once a homogeneous kirigami sheet is stretched [73]. The latter concern the rows close to each clamped border, as illustrated in Fig3.2a, these two portions experience lower deformation than the middle part which induces an important Poisson's effect.

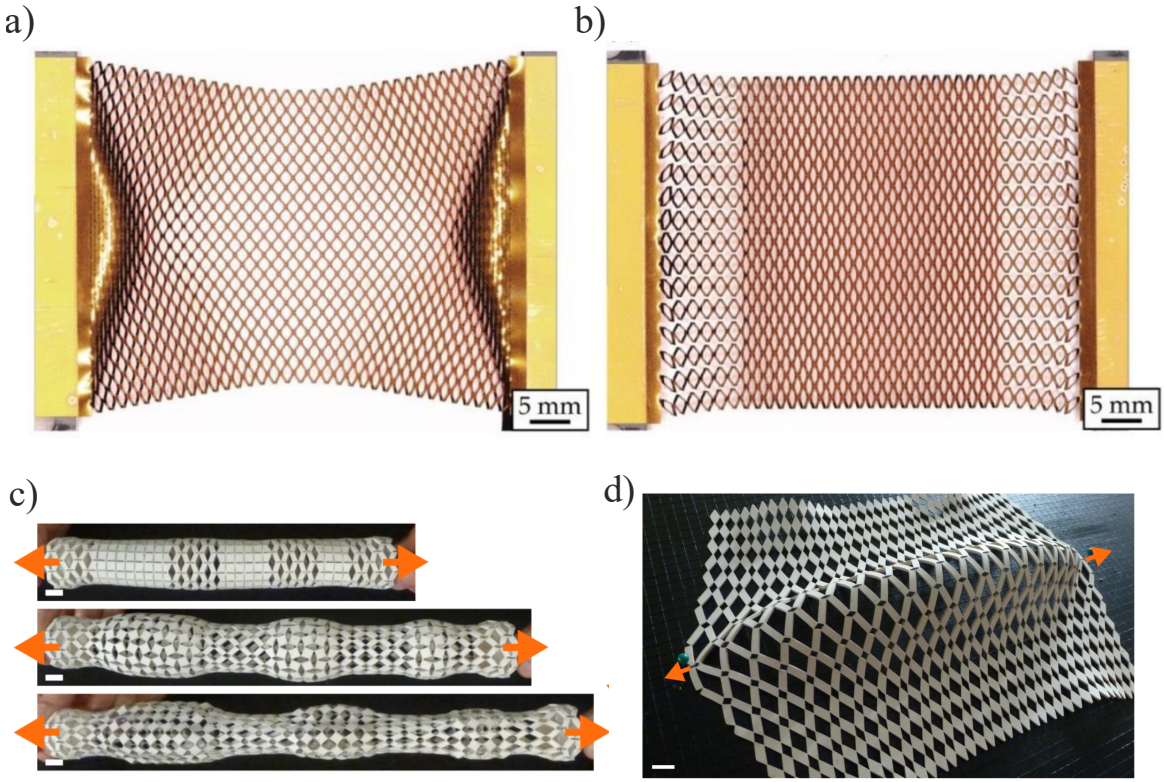

Figure 3.2: a) Classic homogeneous kirigami sheet, the clamped boundaries impede the buckling process and the slit opening at the edges. b) A heterogeneous cutting pattern limits those boundary effects and reduces the Poisson effect. c-d) A non-uniform kirigami cylinder or plate can respectively extend /contract radially and morph with a dome shape, according to the heterogeneities located within the cutting tessellation. Pictures (a-b) come from [73] and (c-d) to [47]

The authors proposed to reduce local stiffness near each edge to avoid non-uniform deformation. This is done by cutting cells in the axial direction, as seen in Fig3.2b. The resulting "softer" kirigami cells erase boundary effects, resulting in homogeneous deformation and a lower Poisson's ratio. Though it may seem counter-intuitive, a non-uniform pattern is necessary to achieve uniform deformation.

The heterogeneous patterns can be also used to control the out-of-plane deformation by geometric frustration [47]. These patterns cause local kinematic incompatibilities with neighboring cells, leading to programmable global shape changes, as seen in the kirigami pipe

with a variable section or the formation of a large bump on a flat sheet (see Fig3.2c-d).

As a third example, consider another family of patterns with a collection of squares that rotate relative to each other [25]. An et al.(2020) introduce a secondary subset of cuts on one half of a sheet, resulting in a non-uniform specimen (see Fig3.3a). Upon stretching, the kirigami sheet opens in two steps, with the top section expanding before the bottom one, as illustrated in Fig3.3b. This sequential opening is reflected as well in the mechanical response, where the stress-strain curve is a combination of the responses of the two individual patterns (Fig3.3c-d). This work shows that the mechanical behavior of a heterogeneous pattern can be inferred from the properties of each constitutive block (sub-portion). The mechanical response can thus be tuned by varying the arrangement of cuts along the sheet.

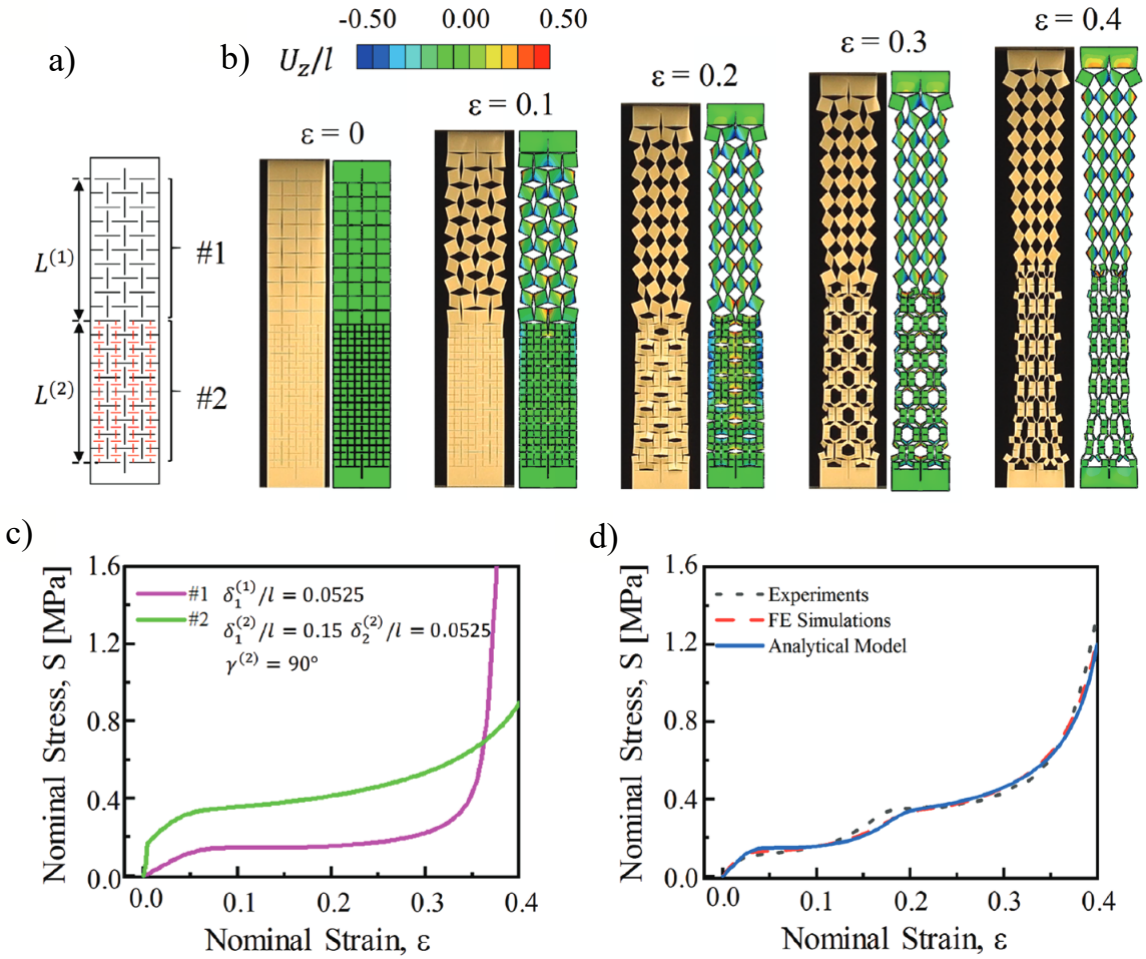

Figure 3.3: a) Hierarchical kirigami pattern, with two parts: the top portion has simple square cells, and the bottom one contains an additional subset of cuts. b) The pores open sequentially, with the top part first then followed by the bottom one. Stress-strain curves of : c) each portion separately, and d) the bi-zonal kirigami sheet [25].

These examples demonstrate the potential of the kirigami method. By using non-uniform patterns, new and more controllable mechanical and kinematic behaviors can be achieved, providing a new lever for shape control. This chapter examines the effect of adding heterogeneities on flow-induced deformation.

3.2 A two-part kirigami sheet

In our kirigami pattern with parallel slits, all three cutting parameters - (L_s, d_y, d_x) - can be varied spatially. Variation can occur along either the y-axis (by altering L_s and d_y) or

x-axis (by changing d_x). Our focus is on the latter option, as outlined in interlude n^o11. We will also deal with a simple heterogeneous configuration: a bizonal kirigami specimen, which combines two different patterns. Let us describe this pattern in the following section.

3.2.1 Bizonal kirigami pattern: user's guide

We define bizonal kirigami as the addition of two sub-patterns in series, such that each sub-part contains cells with different widths $d_{1,2}$. A typical example is reported in Fig3.4a with a color and number assigned to each part, red for the soft portion (1) and blue for the rigid one (2), the latter therefore leading to larger cell widths: $d_1 < d_2$. To ensure a representative parametric study, we keep constant both the total length of the kirigami $L = 12$cm and the nature of the soft part (d_1 common to all our patterns, keep that in mind).

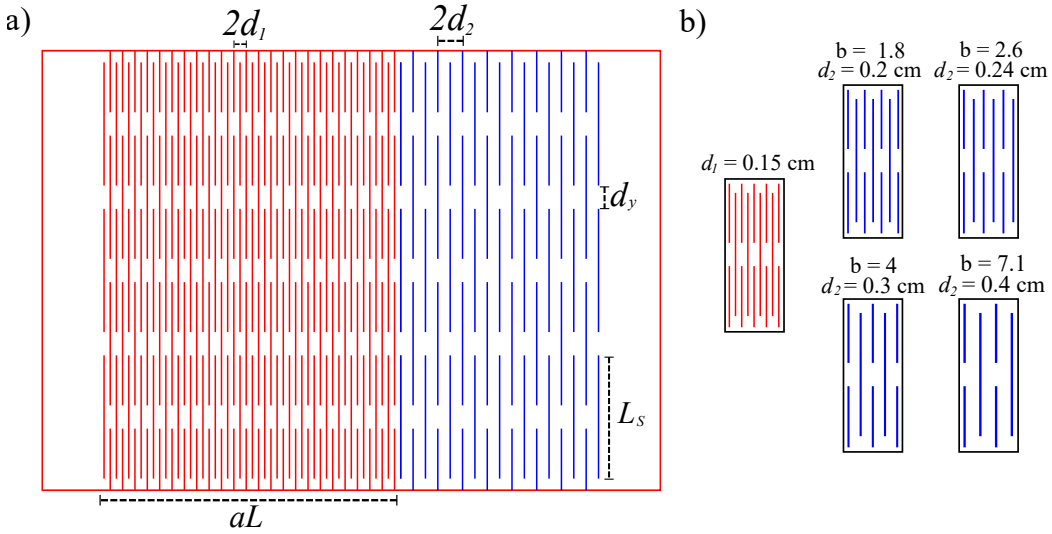

Figure 3.4: a) Example of a bi-zonal pattern, a characterizes the length of the soft (red) part, and b the relative stiffness. Each portion has a different cell width d_1 and d_2 (with $d_2 = \sqrt{b}d_1$), while L_s and d_y is kept the same. In this example, $(a, b) = (0.6, 4)$. b) The shared soft part is associated to four other patterns with their receptive b values.

Thus, the description of a bizonal pattern is reduced to only two parameters a and b associated respectively with the size of the portions and their relative stiffness. Note that the other cutting parameters (along y-axis): slits length $L_s = 3$cm and transverse spacings $d_y = 0.47$cm are fixed for all patterns.

The parameter $a \in [0, 1]$ is associated with the length aL which represents the size of the soft part, leaving then the rigid part covered in the residual length (i.e. $(1 - a)L$). Thus $a = 1$ corresponds to a homogeneous soft specimen illustrated of the Fig3.5b (specimen number

$$2N_1 d_1 = aL \qquad 2N_2 d_2 = (1 - a)L \tag{3.1}$$

The second parameter b compares the rigidity of each part. This ratio can be explicitly defined through the expression of effective stiffness defined in chapter 1, which leads to a simplified expression of b, which only depend on cell widths.

$$k_{1,2} = 32\frac{EN_y t^3 d_{1,2}}{2N_{1,2}(L_s - d_y)^3} \times 2d_{1,2}N_{1,2} \qquad b = \frac{k_2}{k_1} = \left(\frac{d_2}{d_1}\right)^2 > 1 \tag{3.2}$$

These two parameters completely define our bizonal specimens. As an example, we show two typical specimens on Fig3.5b. For number ②, the soft section covers 70% of the

total surface, and the rigid portion is 2.6 times more rigid, whereas specimen ③ has a main rigid portion, covering 60% and with a stiffness ratio about 7.1. All of the b values investigated are reported on Fig3.4b. The non-integer values of the b parameter result from our manufacturing method which we will not detail here but which ensures the respect of the geometrical constraints previously mentioned. In practice, we then adjust cell periodicities N_1 and N_2 and d_2 from $d_1 = 0.15$ to 0.4cm.

Interlude n^o11 : varying cutting parameters along y-axis

The previously discussed manufacturing method is limited to adjusting cutting parameters along the x-axis (tensile direction). In this interlude n^o11, we will explain why this choice is the optimal experimental option.
While cutting tessellation can also be tuned along the other direction by manipulating both slits length L_s and gaps d_y (as shown in the new bi-zonal design), there's a main issue. When tension is applied, non-uniform deformation occurs, leading to unequal stretching along one-half of the kirigami as seen in the pictures below. This results in non-uniform shapes along the y-axis, breaking the symmetry and significantly increasing complexity.

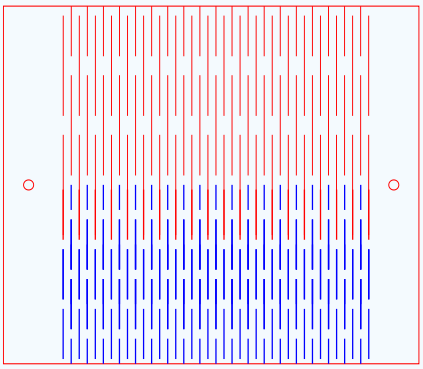

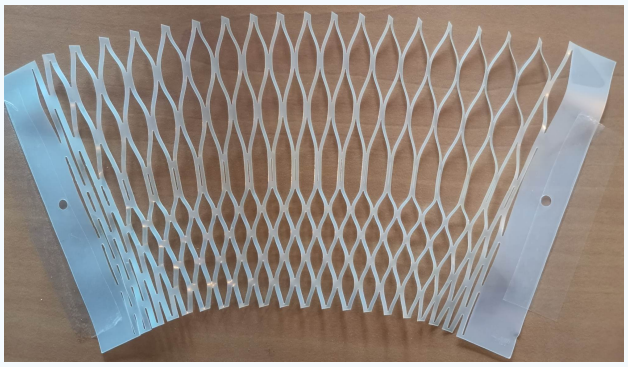

We also note that along the width direction the length of the slit constraint the phase space of (a, b) parameters, kirigami cells being longer than wide: $L_s + d_y > d_x$

Attention : here the index 1 or 2 on the stiffness k does not refer to the deformation regime in or out of the plane (as in chapter 1) but to the bizonal portion respectively soft and stiff.

To study the impact of two parameters on flow-induced deformations, we varied a from 0.2 to 0.8 for each of the four values of b, and added the uniform stiff $a = 0$ and soft $a = 1$ cases (i.e. 33 patterns in total) as illustrated by dots or squares in the phase diagram of Fig3.5a. Let us now explore in detail this vast parameter space!

This results in 33 patterns, shown as dots or squares in Fig.3.5a. We now delve deeper into this extensive parameter space.

3.2.2 Typical deformation in a flow

To give a first insight of a typical response of a heterogeneous kirigami sheet in flows, we choose to first present the results for $a = 0.5$ and $b = 4$ (at the medium range of our experimental parameter space) and compare its expansion kinematic to the reference soft case $a = 1$ (all data/curve relative to this specimen will be reported in black subsequently).

Once in the water flow we take pictures and extract data by following the same procedure as detailed in the two previous chapters (i.e. with a semi-automatic image process). For each specimen, both polarities have been probed. Notice that in this chapter all cells tilt along a samer direction, hence experiencing a uniform polarity, in the following, we will distinguish

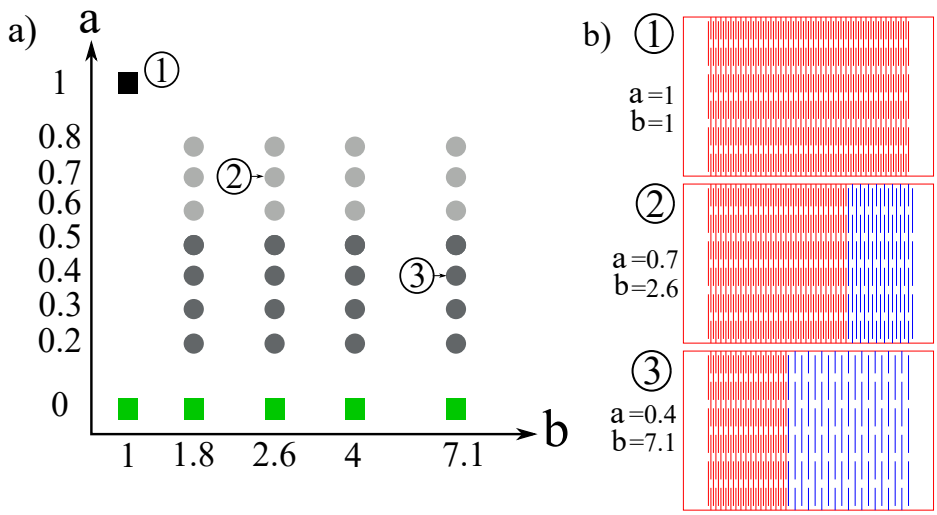

Figure 3.5: a) Phase diagram of parameters a and b, the squares correspond to homogeneous specimens and the rounds to non-uniform configuration. b) Three pattern , ① is the reference specimen $a = 1$, and cases ② and ③ of typical non-uniform bizonal patterns.

only two solutions identified by their sign: ⊕ or ⊖ which respectively correspond to counter-clockwise and clockwise rotation sides. Each polarity state is reminded on the Fig3.6a that shows the deformations of the two patterns (homogeneous -black box and bizonal - green box) at $U = 0.32$ m/s.

Recall first that as illustrated by the black curves profiles in Fig3.6b (associated to $a = 1$) a homogeneous specimen deforms into an asymmetric lobe progressively deflected as the flow speed increases. As detailed in chapter 1, this symmetry breaking comes from the local geometry of the rotating cells. At the local scale, such typical shapes correspond to a strong elongation of the half part opposite to the deviation side, while the other half remains unstretched as shown by the elongation variations of the black curves in Fig3.7b.

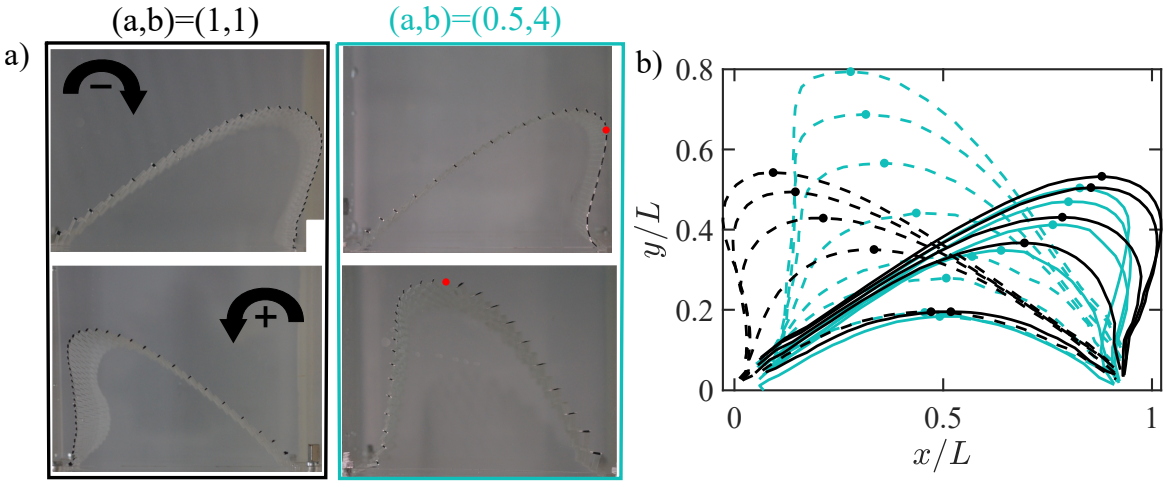

Figure 3.6: a) Raw pictures from experiments in a water channel for two specimens: uniform $(a, b) = (1, 1)$ and bi-zonal one $(a, b) = (0.5, 4)$ for both polarity at given inlet velocity $U = 0.32$cm/s, amplitudes are marked by a circle. b) Shapes shifting for an increasing flow speed for both specimens and polarities, transition cell is identified by a red square as in real pictures for the bi-zonal case. The line styles and color lines are described in Fig3.7

If the polarity of cell rotation is reversed, the shapes remain the same but with opposite symmetrical kinematics. More concretely, where the polarity state ⊖ corresponds to a lobe deviated to the right, the configuration ⊕ experiences a lateral symmetrical deviation

to the left (compare the solid and dash lines on Fig3.6b), with an equivalent amplitude (y_{max}). This symmetry is well marked in the trajectories evolution in Fig3.7a which tracks the position of the deformation amplitudes (x_{max}, y_{max}). Keep in mind that for uniform kirigami, the polarity states have equivalent shapes and elongations. Let us now compare it to a bizonal case.

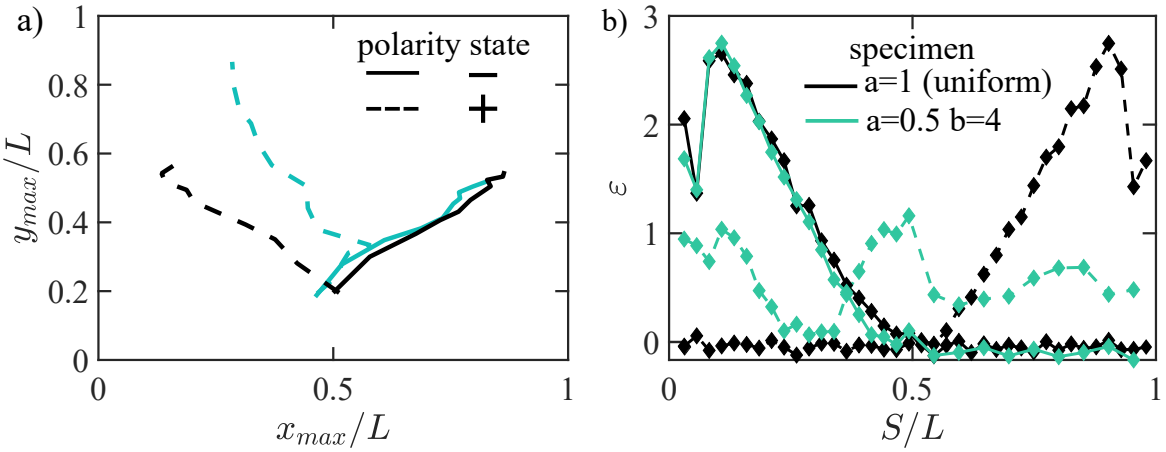

Figure 3.7: Respective trajectories (a) of amplitudes previously spotted by circle markers on Fig3.6. b) Local elongation ε as a function of curvilinear abscissa.

For the non-uniform specimen $(a, b) = (0.5, 4)$, things get more complicated. In one direction (polarity ⊖) the shapes, elongation and trajectories are remarkably similar to those obtained in the homogeneous case as if the presence of the four times stiffer half does not affect the deformation process.

While the opposite polarity ⊕ leads to another kinematics, profile expansions following quasi-symmetrical shapes (see green dash lines in Fig3.6b and associated picture in a). We report a more complex pathway in the trajectory graph in Fig3.7a, with a lobe that firstly deforms along the right, as for the ⊖ state, before shifting along the channel center (i.e. $x_{max} \sim 0.5$) and finally reached the right side. The deformation profiles are also marked by a larger amplitude than ⊖ solution or the uniform case (black dash line). At the local scale, the symmetrical and strongly expended morphologies result in an elongation of the whole pattern (see Fig3.7b), contrary to the uniform case with strain evolution which only concerns half part of the sheet.

In conclusion, the bizonal case highlights a new property: a single pattern corresponds to two different expansion kinematics according to the polarity state. While the solution ⊖ remains close to the reference soft specimen, the configuration ⊕ deforms in a new way with a changing trajectory and elongations distributed on the whole kirigami sheet. Let us discuss the two polarity states separately, as well as probe the role of the parameters a and b in the next section.

3.3 Influence of the relative size and stiffness

The preliminary results of the previous section indicate that the deformation of a bi-zonal specimen seems to follow non-trivial kinematics not yet explored. In particular, we distinguish two responses according to the two polarity states. Indeed cells tilting side plays a role in the stretched kirigami sheet portion which impact the resulting deformation shape. In this section, we will compare the behavior of our heterogeneous specimens with the soft reference ($a = 1$) and the purely rigid ones ($a = 0$ for all b).

At the same time, we aim to explore the parameters space (a, b), by fixing b and varying a. We'll begin with the solution ⊖ before flipping the kirigami sheet.

3.3.1 Polarity ⊖

In the previous section, we found that the bi-zonal specimen ($a = 0.5, b = 4$) displays similar expansion kinematics as the control ($a = 1$) for polarity ⊖ in terms of global morphology, amplitudes, deviation, and local elongations, with comparable values and trends.

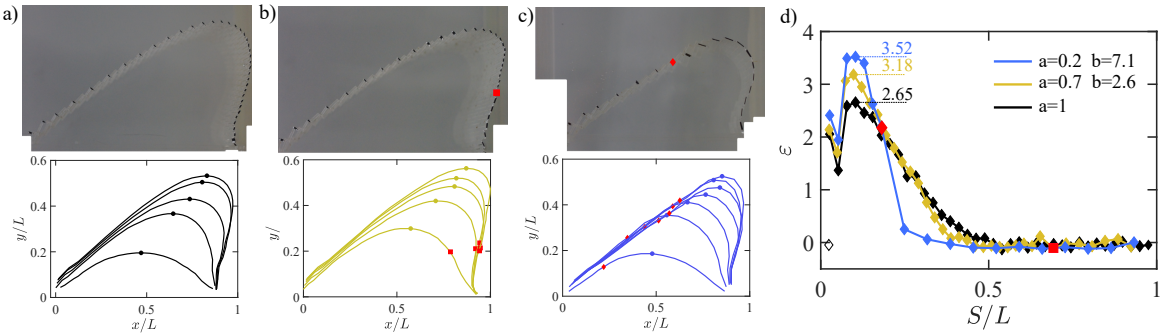

Figure 3.8: Pictures, deformations profiles and local strain for three specimens: a) homogeneous one, b) $a = 0.7$ and $b = 2.6$, c) $a = 0.2$ and $b = 7.1$. Elongation curves and experimental pictures are taken at the same velocity $U = 0.32m/s$.

Ch. 3

Before discussing the origin of these multiscale similarities, let us take a look at some other specimens. The pictures in Fig3.8a-b-c show the deformation for different values of a and b (taken at the antipode of the phase space). We notice that despite these gaps in parameters the morphologies reached at a similar flow speed ($U = 0.32m/s$) are qualitatively equivalent. Moreover, both profiles and local strain evolution (see Fig3.8d) confirm this insight and exhibit a similar trend whatever a and b.

This result can be generalized to the whole phase space. Indeed, if we look at the evolution of all trajectories on Fig3.9, where each graph corresponds to a value of b and each curve to those of a, we note the universality of the shape-shifting process. All profiles are deviated along the right side with fairly close amplitudes, despite the great disparities in stiffness ratio and size of the rigid part. All bizonal patterns deform like the control soft case (solid black line).

To understand this non-trivial and universal behavior, let us take a closer look at the bizonal case $(a, b) = (0.2, 7.1)$, whose parameters are the farthest from the reference case. If we track the transition between the stiff portion on this pattern, localized by the red diamond on Fig3.8c, this point tends to follow the trajectory of the deformation amplitudes (blue circles). We therefore suggest that the whole deformation is held up by the short soft part alone, while the stiff part remains almost unstretched.

Indeed, when we look at the three images as well as the corresponding spatial elongation variation (Fig3.8), we attest that in all cases, the stretching is mainly localized on the soft portion. Even if the latter represents a small percentage of the total sheet surface (only 20% in the previously mentioned case!).

More concretely, the counter-clockwise rotation of elementary kirigami cells (polarity ⊖) induces a symmetry break, which leads to the opening of the soft part. Thus fluid forces exerted on this portion push the profile towards the right where the rigid part is located, which is then in the unstretched zone, as shown by the evolution of the elongation for the three profiles surveyed. For the polarity ⊖, the stiff part has therefore little effect on the whole deformations which are fully driven by the soft one. Given that this portion is shared by all bizonal specimens, it leads to the universal expansion kinematics observed (see all trajectories in Fig3.9).

The effects of a and b are thus reduced here to disparities in amplitude, lower for specimens far from the reference case. But also on a local scale as suggested by maximal strain values

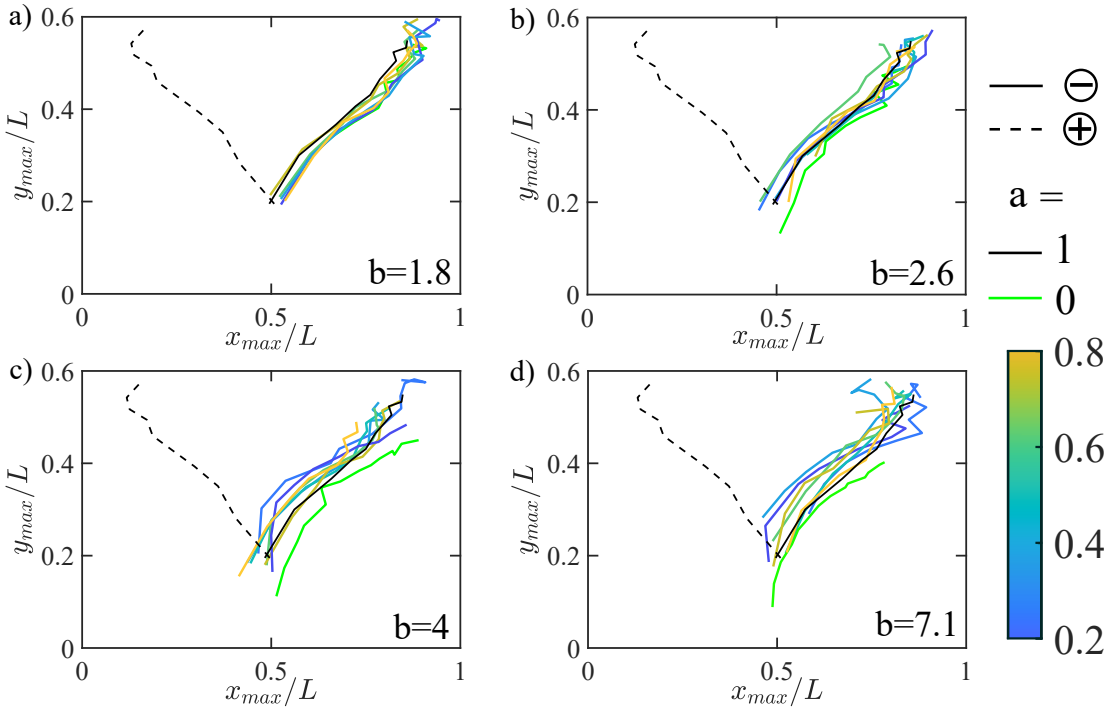

Figure 3.9: Trajectories linked to all profiles with a varying a values (parula color scale) and fixed b, such as a) $b = 1.8$, b) $b = 2.6$, c) $b = 4$ and d) $b = 7.1$

reported in Fig3.8d. Indeed, we note that the larger b and the smaller a, the more the soft part will stretch.

The weak impact of both parameters on the morphology for ⊖ is an unexpected result. Indeed very different cutting patterns actually return the same universal shape once in flows, testifying to a strong resilience of the soft part, which almost alone drives the opening kinematics. This result leaves a bitter taste as it suggests that adjusting stiffness may not be effective in generating new morphologies. Let's examine the kirigami sheet before making a hasty conclusion.

3.3.2 Polarity ⊕

The initial review in the prior section showed that configuration ⊕ produced new responses in flows. The high-amplitude, the quasi-symmetrical lobe was notably different from the homogeneous case (refer to the green dashed and solid lines in Fig3.6 and 3.7). Both stiff and soft parts were noted to be stretched, resulting in a "symmetrical" appearance. We will now closely examine the effect of parameters a and b on this polarity state.

Let us first emphasize that contrary to the previous configuration, the cells rotation side (here clockwise) should lead to the stretching of the stiff part. However, by definition, this portion is less deformable than its neighbor and therefore impacts the further opening kinematic in a flow. Thereafter, we split the parameter space at $a = 0.5$ value and distinguish two different behaviors in flows.

case 1 - soft parts outshine $a > 0.5$

Here we focus on a pattern with a predominant soft part only (light grey circles in the phase space, Fig3.5a). As an illustrative example, the Fig3.10 reports the evolution of three specimens at fixed $a = 0.7$ for all b values (row b-d-d) and the reference case (row a). For each deformation shapes we mark the transition position with a red diamond and the respective strain ε for only three velocities represented by different marker types. To highlight the cells width variation (b ratio), we also draw the pattern used.

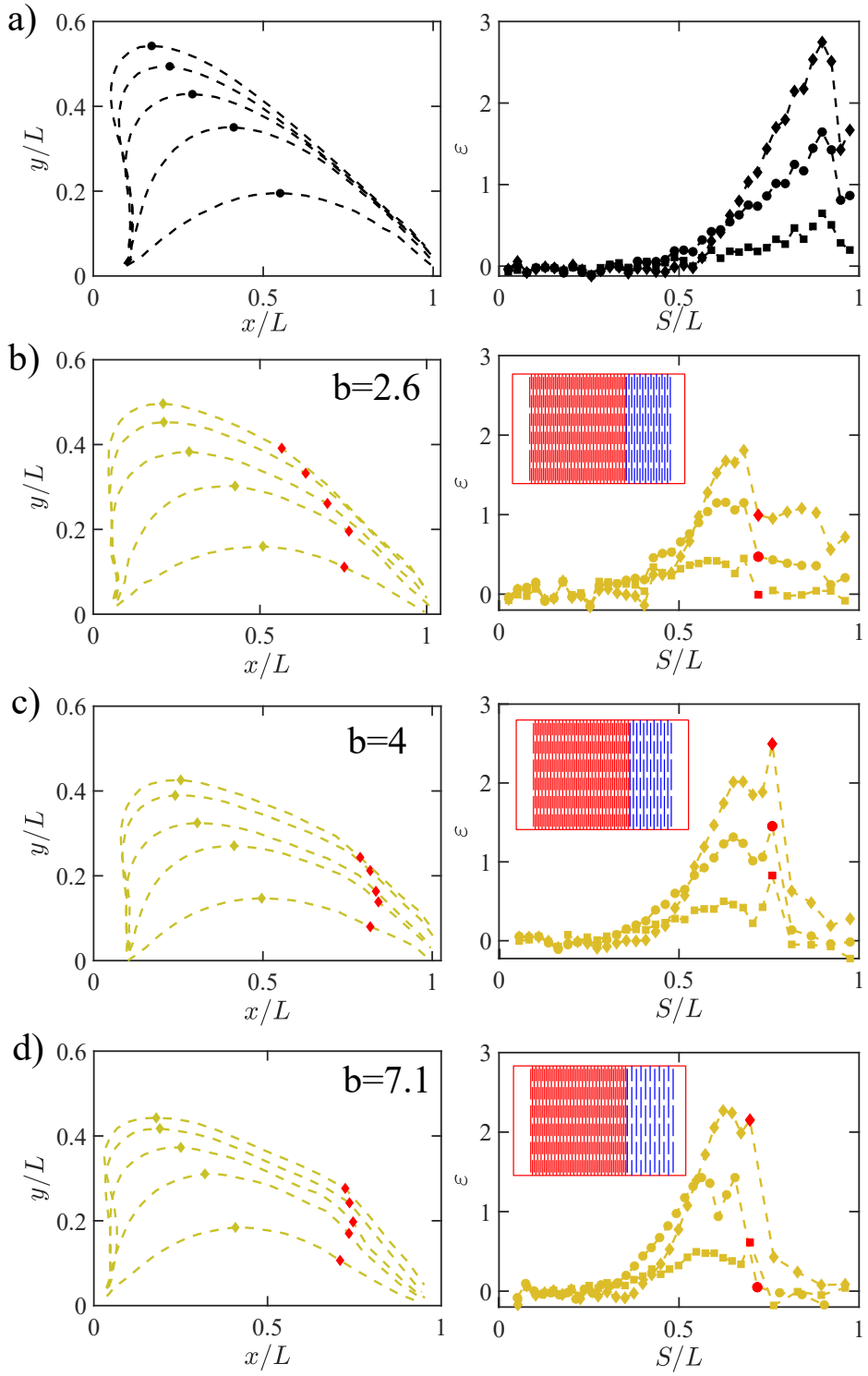

Figure 3.10: Shapes shifting and local strain evolution of the reference case a), $a = 1$ and three bizonal kirigami patterns with a fixed $a = 0.7$ (soft part in red on the pattern draw represent 70% of whole sheet area) and varying $b =$ b) 2.6 c) 4 and d) 7.1, for each bizonal specimen we report the respective cutting pattern.

As expected, the deformation lobes are all located to the left (see all shapes of Fig3.10). Indeed this polarity induces a clockwise rotation and the fluid forces push the profiles toward the soft part of the pattern. Note also that the shapes reached by the three bizonal specimens are close to the uniform case $a = 1$, as suggested by the evolution of their trajectories which converges onto the dash black line in Fig3.11a. This observation is generalized to all the

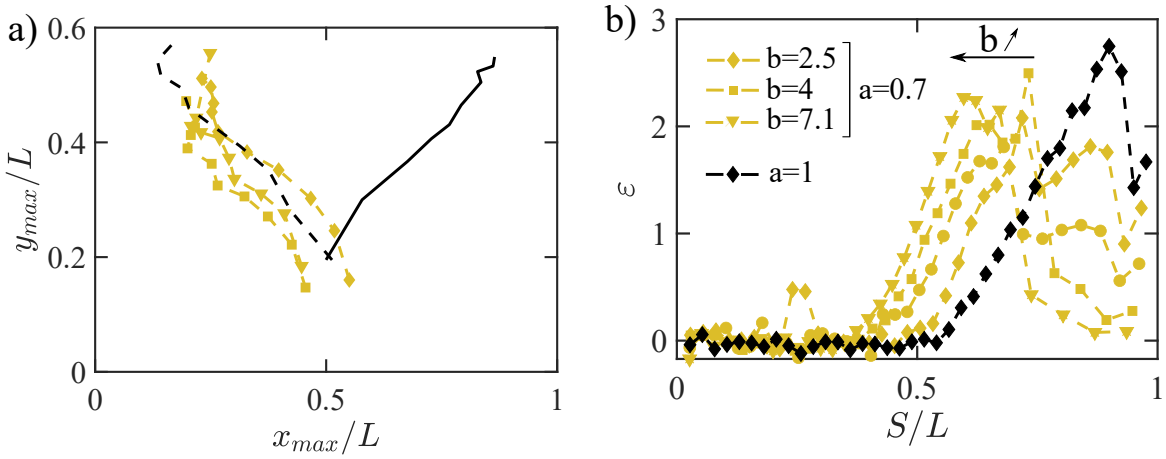

Figure 3.11: a) Trajectories of four patterns presented in Fig3.10, the marker type, corresponding to the different b values and black color to the reference state ($a = 1$). b) Direct comparison of elongation as a function of curvilinear abscissa, the increasing stiffness ratio shift the strain evolution to the left and concern more than half part of the sheet.

patterns with $a > 0.5$ as shown by the trajectories on Fig3.12 which all follow the kinematics of the reference case. Here again, the soft part seems to play a crucial role.

However, slight morphological differences are observed, with a slope break appearing near the stiffness transition (indicated by red diamonds on the deformation profiles in Fig.3.10). As previously noted, polarity $\oplus$ causes the rigid part to open, reducing local deformation and resulting in a steeper slope within the rigid region. This break results in a flatter morphology, more pronounced for larger b values as shown in Fig.3.10c-d.

Let us now study more closely the evolution of the local elongation $\varepsilon(S/L)$ associated with the deformation profiles previously discussed. We first note that the stretched part of the lobe still represents around 50% of the total sheet length, as for the homogeneous reference case (see Fig3.10a). However, this part is shared by the two portions of different stiffness: the 30% of rigid and about 20% of soft (as a reminder in the pattern of the Fig3.10b-c-d the soft part represents 70%). The transition between these two zones leads to a significant jump in elongation, particularly for high velocity and b values. velocity and b values.

This jump in strain induces a change of slope and a lower global amplitude as previously argued. We can also compare the elongation at the same flow rate and variable b plot in the same graph of Fig3.11b, and note that the greater the ratio the more the stretched soft part is extended on the pattern, with an area greater than 50% for $b = 4$ and 7.1 (the maximal strain shifts to the left as b increases). This additional participation of the soft part allows for reaching similar global shapes and trajectories.

Except for a few details (slope break, elongation on wider areas and flat profiles), the morphologies reached for the polarity state $\oplus$ and $a > 0.5$ tend towards the soft uniform solution. In light of the results established for the polarity$\ominus$, we point out that despite the presence of a small rigid stretched part the prevailing soft portion leads to similar monotonic expansion kinematics and ensure alone almost all the deformation. Let us now study the opposite case, in which the rigid portion predominates.

case 2 - stiff part is coming back $a \leqslant 0.5$

Up to now, we have dealt with configurations of polarity or parameter values that leave the soft part free to expand. In this section, we are going to focus on a range where the rigid portion drives the kinematics due to its predominance with $a \leqslant 0.5$ (indicated by a dark gray circle on Fig.3.5a , 16 specimens in total). These kirigami bizonal patterns are the

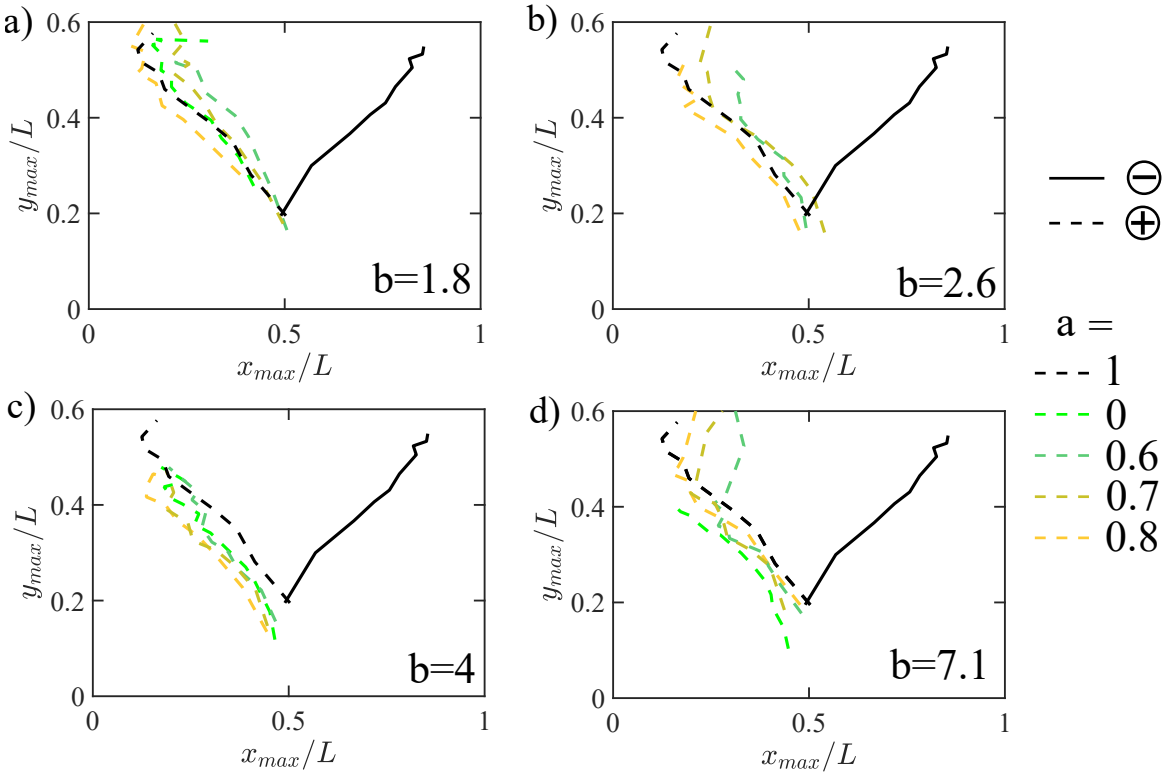

Figure 3.12: Trajectories for bizonal pattern with $a > 0.5$ values (parula color scale) and all stiffness ratio b, such as a) $b = 1.8$, b) $b = 2.6$, c) $b = 4$ and d) $b = 7.1$

most different from the reference case $a = 1$, and therefore are the most likely to generate new behaviors in flows.

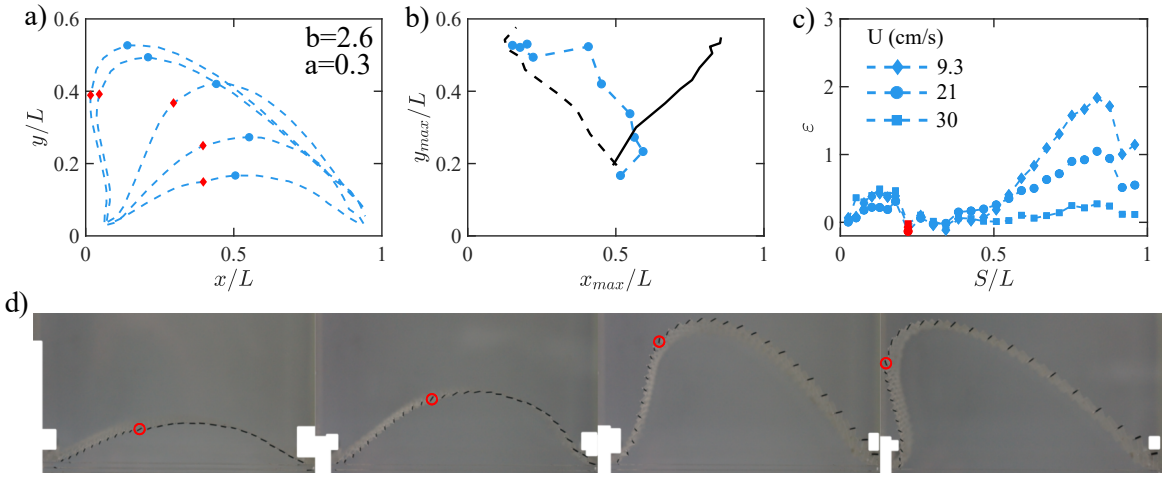

Figure 3.13: Profile expansions, trajectory evolution and local strain for three velocities, all for the specimen $(a, b) = (0.3, 2.6)$ and respectively reported in a-b and c). Finally, four pictures of its expansion are shown in d). The localization of the transition between the two portions is indicated by a red marker/circle.

To get a general idea, we plot the evolution of two specimens' trajectories and elongations, and profile evolutions in the middle of the parameter range ($b = 2.6$ and $b = 4$ for $a = 0.3$) in Fig.3.13 and Fig.3.14. Each figure also includes four pictures showing the state of deformation at different flow rates, increasing from left to right.

Let us start with the $b = 2.6$ pattern. We immediately notice that the lobe no longer deploys monotonically but experiences a changing asymmetry. Indeed, as suggested by the

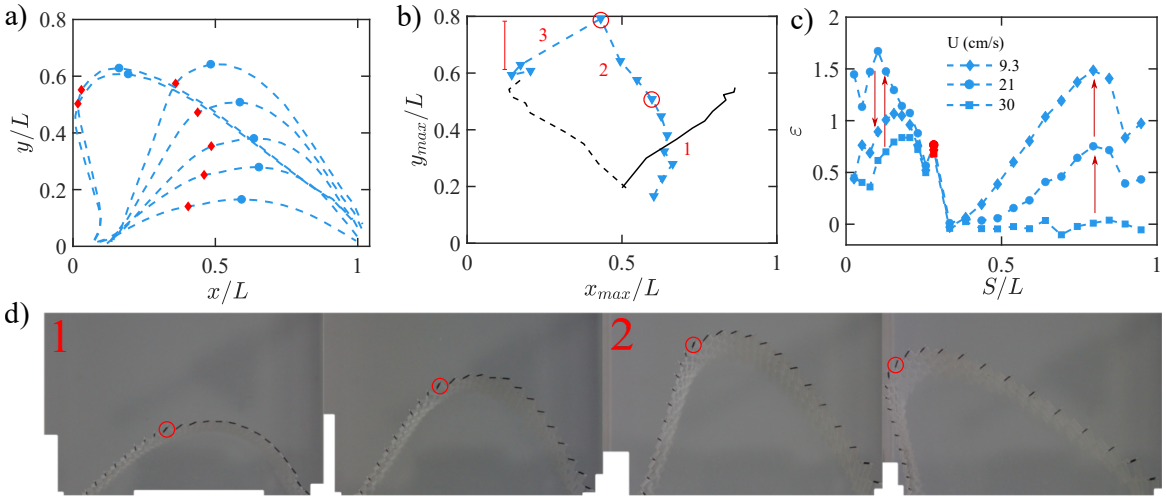

Figure 3.14: Profile expansions, trajectory evolution and local strain for three velocities, all for the specimen $(a, b) = (0.3, 4)$ and respectively reported in a-b and c). Four pictures of its expansion are shown in d, the lobe suddenly reaches the left side for high flow speed.

trajectory of the amplitude (see Fig3.13b) , the lobe first moves towards the right, which is the conventional direction of the solution ⊖, before recentering and finally moving towards the left, as expected for the polarity state.

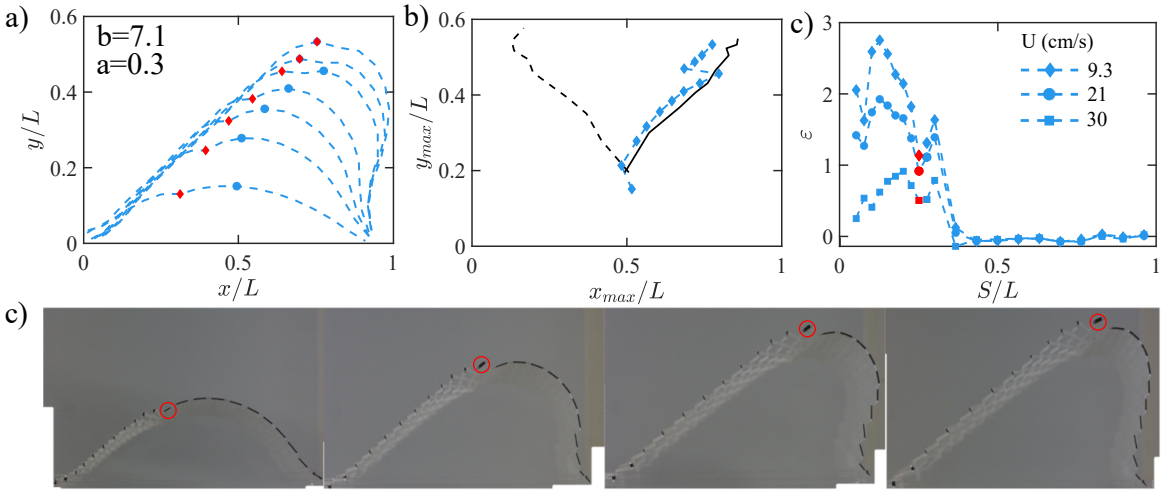

Figure 3.15: Profile expansions, trajectory evolution and local strain for three velocities, all for the specimen $(a, b) = (0.3, 7.1)$ and respectively reported in a-b and c). Four pictures of its expansion are shown in d and highlights that the stiff part remains close

This three-stage expanding process displays a new non-monotonic kinematic that we are going to detail by looking at the local scale. Indeed the essential difference between the previous case ($a > 0.5$) is that both sides of the lobe are stretched as shown in the elongation graphs of Fig3.13c and 3.14c. However, the gap in stiffness between the two parts leads to a two-step pores opening. As briefly discussed in the interlude n^o12, the soft portion buckles out of the plane first and is followed by a progressive opening of the rigid part. This phenomenon is all the more marked as the b ratio is high and a weak. Thus, at low flow rates, the short soft portion opens first and leads to an unconventional global lobe deviation towards the right. The opening of the rigid portion for higher speeds straightens the profile at the water channel center and at the end reaches the (conventional) left side, as the reference case. The rigid portion is thus more and more elongated while the soft portion tends to decrease its contribution as suggested by the red arrows on Fig3.14c.

On pictures and trajectories of the $b = 4$ pattern (see Fig3.14b and d), we observe a sudden decrease in amplitude and change in shape (from symmetrical to asymmetrical lobe) for high-velocity range. This state transition deserves a deeper investigation and constitutes one of the perspectives of my thesis work. We can just remark that this type of morphological modification appears as reminiscent of the phenomenon observed by Schouveiler et al. [74]: a continuous thin disk placed facing a flow, exhibits a rich variety of bending deformation, from cylindrical to multi-lobes shapes depending on the inlet flow velocity. The underlying mechanisms, therefore, involve notions of energetically favorable deformation states. In our case, it seems that stretching the single rigid portion is more favorable than extending both portions beyond a certain flow speed.

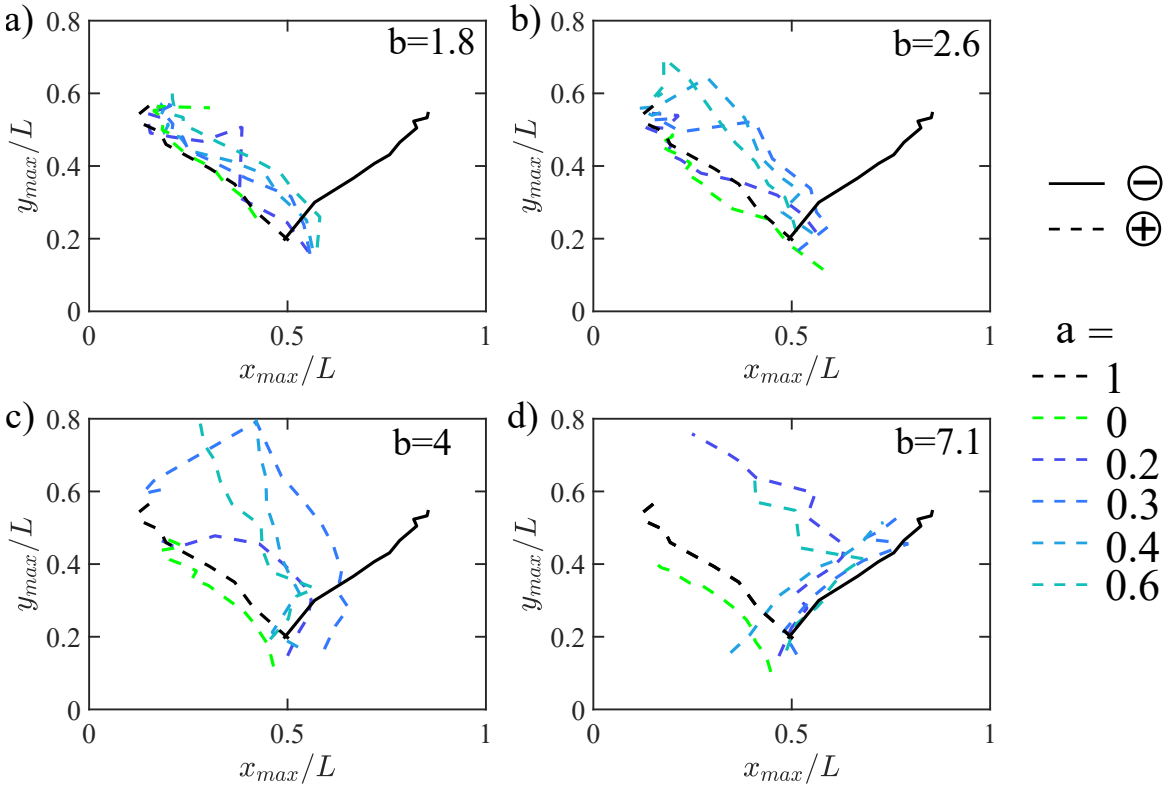

Figure 3.16: Trajectories for bizonal pattern with $a < 0.5$ values (parula color scale) and all stiffness ratio b, such as a) $b = 1.8$, b) $b = 2.6$, c) $b = 4$ and d) $b = 7.1$

To discuss the effects of the parameters a and b let us look at the set of trajectories for all $a \leqslant 0.5$ patterns on Fig3.16. For a given b, we note that the smaller the soft part the lower flow velocities needed to change lobe direction, i.e. for these graphs, it corresponds to lower values of y_{max} all identified by a red circle. While for a given a, the first deviation phase to the right will be more pronounced for large b with a transition to the left occurring for higher speeds. This last observation coincides with a later opening of the rigid part for patterns with a high stiffness ratio.

For the extreme parameters' values: $b = 7.1$ and $a \in [0.3, 0.4]$ we even note cases in which the rigid part remains closed and the lobe stays oriented along the right side as shown in the data sets of Fig3.15. The morphologies obtained as well as the trajectories tracking then correspond to the usual results obtain for the opposite polarity ⊖. However, the effective rotation side of the cells covering the stretched soft part respects counter-clockwise imposes by the state ⊕. Indeed, the combined effect of the strong elongation of the soft portion and the global profile inclination holds the lobe to the right. This particular regime is briefly discussed in the interlude n^o13 and mainly comes from mechanical nonlinearities.

Interlude n^o12 : Opening in two steps

The spatial evolution of the elongation in our bizonal cases shows that the cells of the soft portion buckle out of plane before the rigid portion, causing a delay in local pores opening and leading to non-monotonic deviation and asymmetric deployment. To demonstrate this two-step opening kinematics, a typical bizonal pattern $(a, b) = (0.5, 2.6)$ was subjected to an elongation test. A displacement Δ is then imposed and the average displacement of each of the two parts is reported in the graph below $\Delta_{1,2}$. The results show that the soft portion (red curve) stretches more and the rigid portion (blue) remains closed until reaching critical displacement Δ_c. At this point, the rigid portion buckles, opening the rest of the kirigami sheet. This implies that bizonal specimens have non-uniform local porosity, unlike the homogeneous cases discussed in chapter 1

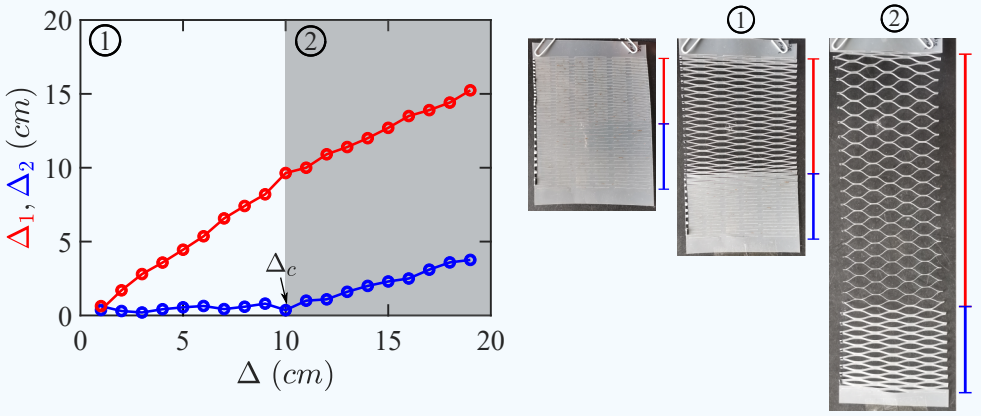

Further experiments on the values of Δ_c as a function of (a, b) parameters are under investigation and will allow identifying the non-linear mechanism leading to the new deformation laws in flows.

3.4 Theoretical analysis

After this extensive discussion on the experimental results of the bi-zonal kirigami sheets in a water flow, we complete our approach with a theoretical perspective.

We opt for a more simplistic approach than the continuous model used in the previous chapters. Indeed, at first sight, our experimental observations on bizonal specimens can be reduced to a competition between two elastic strands of different stiffness and a fluid loading oriented according to the polarity state. These external forces lead to the elongation of these two strands and deviate the simplified profile along the corresponding direction. This reduced-order model (only 2 degrees of freedom) allows us to isolate the essential physical ingredients.

3.4.1 Toy model: Two telescopic shafts

Let us then consider two extensible and inflexible shafts connected to each other at B and whose two remaining ends are placed in hinges A and C.

As illustrated in the schematic view of Fig3.17a, the junction Ⓑ is located by the coordinates (X, Y). The rest length of the strands (without loads) is provided respectively by L_1^0 and L_2^0 such as the total length writes $L^0 = L_1^0 + L_2^0$. A deformed configuration can therefore be described by the two rotation angle α_1 and α_2 and associated strains ε_1 and ε_2.

From the definition of our bizonal pattern, we introduce the parameter a such as $L_1^0 = aL_0$ and $b = k_2/k_1$ the ratio of the two rode's stiffness $k_{1,2}$, with $k_2 > k_1$. The stiffer part is always placed on the right side.

As illustrated in Fig3.17b Strands are subjected to an external set of load q, decomposed along the normal (q_{N1}, q_{N2}) (red arrows) and the tangential directions (q_{T1}, q_{T2}) (green arrows). These pressure forces induce an internal structural response: two tensile forces T_1 and T_2 assumed uniform along each elementary rode (blue arrows).

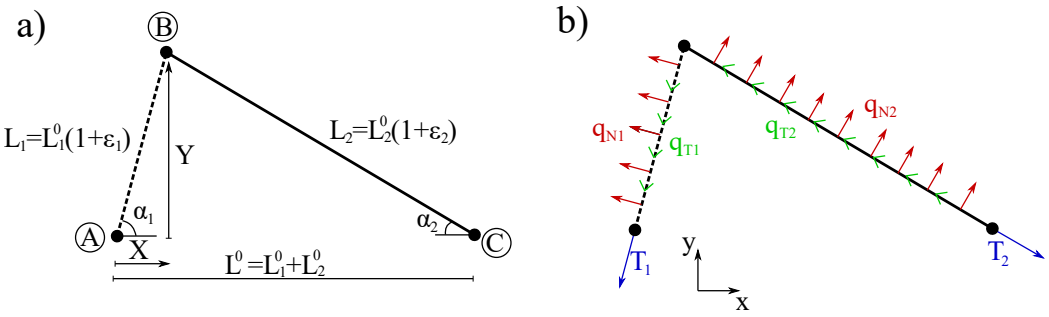

Figure 3.17: Schematic view of two rodes model link a the junction B localized at (X, Y) coordinates, geometrical details is provided on draw a) and forces balance on b).

Ch. 3

Before deriving the force balance, let us briefly detail the geometrical relations which reduce the geometrical description of the whole deformed configuration into only two degrees of freedom.

Geometrical relationships

By using elementary trigonometric relations, one can deduce two relations between the deformation parameters of rode 1 and 2 (see Fig3.17a) :

$$\left|\begin{array}{c} L_1^0(1+\varepsilon_1)\cos(\alpha_1) + L_2^0(1+\varepsilon_2)\cos(\alpha_2) = L^0 \\ L_1^0(1+\varepsilon_1)\sin(\alpha_1) = L_2^0(1+\varepsilon_2)\sin(\alpha_2) \end{array}\right. \tag{3.3}$$

The tilting angle α_2 and elongation ε_2 of the second bar can then be expressed in terms of the first one:

$$\left|\begin{array}{c} \alpha_2 = atan\left[\frac{L_1^0(1+\varepsilon_1)\sin(\alpha_1)}{L^0 - L_1^0(1+\varepsilon_1)\cos(\alpha_1)}\right] \\ \varepsilon_2 = \frac{L_1^0(1+\varepsilon_1)\sin(\alpha_1)}{L_2^0\sin(\alpha_2)} - 1 \end{array}\right. \tag{3.4}$$

As announced, the deformation profile is completely characterized by the strain and tilting motion of the first rode only (2 DOF) :

$$\left|\begin{array}{l} X = (1+\varepsilon_1)L_1^0\cos(\alpha_1) \\ Y = (1+\varepsilon_1)L_1^0\sin(\alpha_1) \end{array}\right. \tag{3.5}$$

Force balance - equilibrium state

We now aim to establish the equilibrium equations system, where each components are detailed on Fig3.17b. We first assume the force balance along the y-direction in the whole set of shafts:

$$-T_1\sin(\alpha_1) - T_2\sin(\alpha_2) + q_{N1}L_1\cos(\alpha_1) + q_{T1}L_1\sin(\alpha_1) + q_{N2}L_2\cos(\alpha_2) - q_{T2}L_2\sin(\alpha_2) = 0 \tag{3.6}$$

And along the x-axis :

$$-T_1\cos(\alpha_1)+T_2\cos(\alpha_2)-q_{N1}L_1\sin(\alpha_1)+q_{T1}L_1\cos(\alpha_1)+q_{N2}L_2\sin(\alpha_2)+q_{T2}L_2\cos(\alpha_2)=0 \tag{3.7}$$

The resolution of these two equations gives the position of junction (X, Y) as a function of the external forces q. The analytical expression of the tangential and normal loads are deduced from chapter 1 and depend on the deformation states.

$$\left|\begin{array}{c} q_N = \frac{1}{2}\rho C_N H U^2\cos^2(\alpha)\cos^3(\theta) \\ q_T = \mathrm{sign}\frac{1}{2}\rho C_T H U^2\cos^2(\alpha)\cos^2(\theta)\sin(\theta) \end{array}\right. \quad \text{with} \quad \cos(\theta)=\frac{1}{1+\varepsilon} \tag{3.8}$$

Where we take into account both rodes inclinations and cells tilting (cf chapter 1). Note that here the values of (α, ε) are constant along each strand, as well as the resulting external fluid force. It only remains to define the mechanical behavior of each bar.

Considering that each shaft is inflexible, we restrict the deformation mode to elongation only. As for the continuous modeling, we assume an elastic behavior with a linear evolution of the elongation $T_{1,2} = k_{1,2}\varepsilon$.

Thus, as for the continuous approach, we define the Cauchy number $C_y = \rho U^2 H/k_1$ to ensure a non-dimensional form of the equilibrium equation (rewritten expressions of Eq3.7 and 3.6 are not detailed here).

Our model's main constraint is that the transition between the two sections overlaps with amplitude (X, Y) (as the shape examined is a triangle). The impact of a cannot be solely studied as it affects the location of the maximum deformation and the expansion kinematics of the double bar network. Hence, we will set $a = 0.5$ (each rode has the same length).

3.4.2 Toy model: Results

Before testing our theoretical model for the bizonal case, let us begin with the typical solutions for a homogeneous configuration, i.e $b = 1$. The expansion kinematics of both polarity sates are reported in Fig3.18, the grey scale color corresponds to an increasing Cauchy number $C_y \in [0.01, 30]$

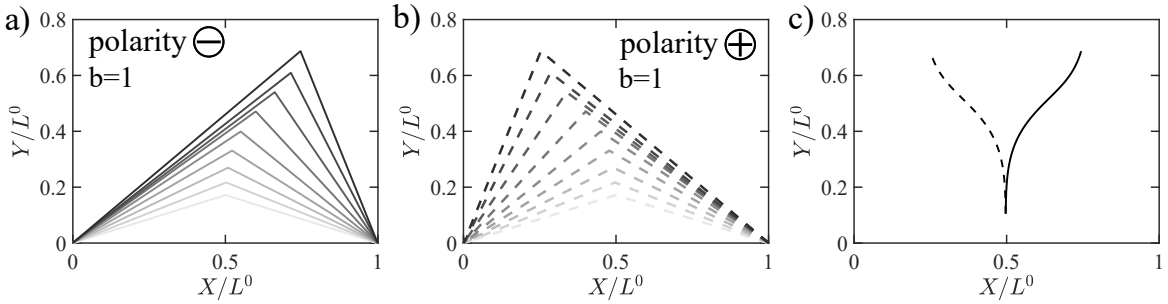

Figure 3.18: Expansion of a set of uniform elastic rodes, $b = 1$ according to their polarity states : a) ⊖ and b)⊕. Their respective trajectories are reported on c).

As for the continuous approach, this simplified model captures well the symmetry breaking, the higher the flow velocity (here C_y) the more the profile deviates laterally. The uniform configuration experiences a symmetrical expansion as suggested by the two trajectories corresponding to the polarity states in Fig3.18c.

Now let us get closer to the experiences, and introduce a difference in stiffness between the two bars through the ratio b, we performed the derivation for two values $b = 1.8$ and 4 in both polarities, (where the rigid part is along the right side), results are reported in Fig3.19.

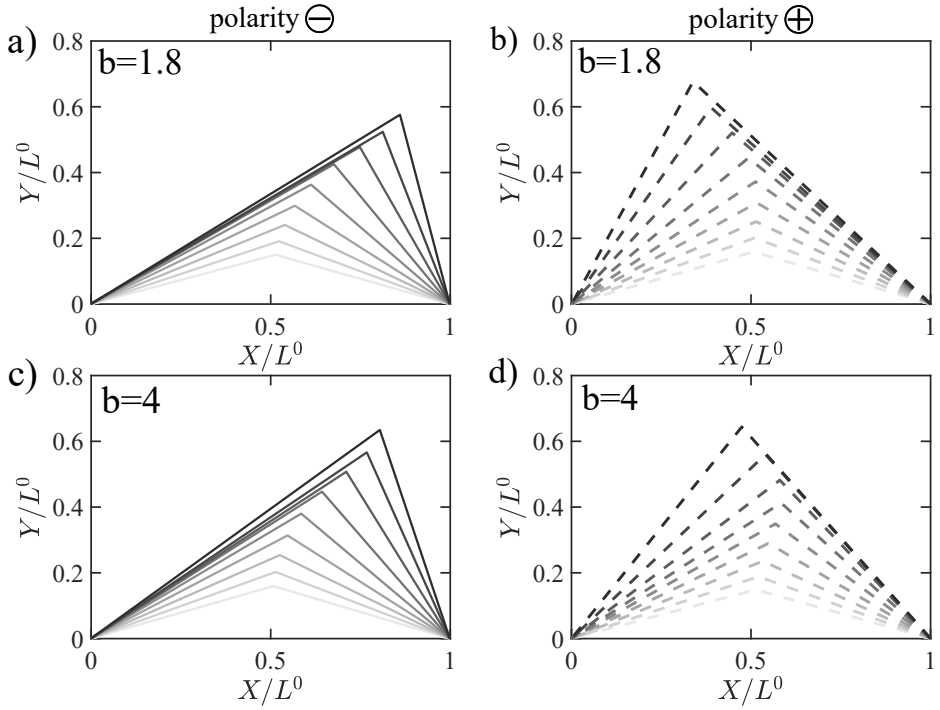

Figure 3.19: Deformation profiles for heterogeneous sets of shafts at their two polarity states: a) and b) for $b = 1.8$ c) and d) for $b = 4$

In contrast to homogeneous results, inverting the polarity state does not result in similar responses. Indeed, the ⊖ solution produces shapes close to those observed on the Fig3.18 for $b = 1$, with a clear deviation to the right, while the opposite configuration ⊕ presents a more complex pathway. The deviation of the junction is first to the right before reaching the center and finally moving right as expected for this polarity state. This typical non-monotonic expansion kinematics is reminiscent of the one previously identified in experiments with bizonal specimens with $a < 0.5$ and polarity ⊕.

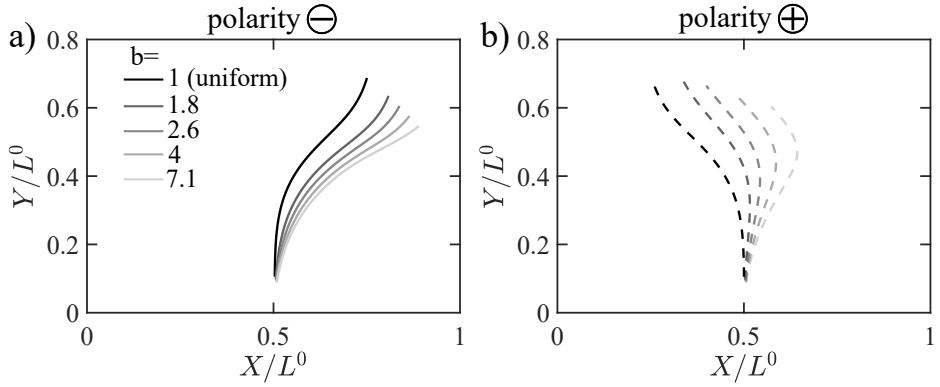

Figure 3.20: Trajectories evolution for varying b and polarity states

The comparison is furthered by varying parameter b within the experimental range, we report the trajectories evolution for both polarities in Fig3.20. Previous trends are confirmed: the trajectory of ⊖ follows monotonic kinematics with a stronger transverse deviation for high b values, while the polarity ⊕ exhibits a direction shifting from left to center-right, with a pathway more pronounced for larger b. The experimental trajectory trends are thus captured by using this simplified two-bar model. The difference in stiffness impacts the deflection of the deformation profile, which changes orientation depending on the fluid loading applied. The stiff shaft (right portion here), remains almost entirely undeformed at low

Cauchy values, while the soft portion lengthens, pushing the profile to the right. When C_y increases, the tension forces are sufficient to stretch the rigid rode which restores the profile towards the center before following the direction imposed by the polarity, i.e. to the left. Here again, b exacerbates the changing direction process.

Interlude n^o13: Critical velocity - opening (or not) the stiffer part

Before the profile moves from the center to the right (its conventional position), we have to distinguish the state where the stiff part cells are still closed and the one where they start to buckle. In this interlude n^o13, we will estimate the critical flow speed needed to induce the stretching of the rigid portion, and its dependence on bizonal parameters (a, b).
Let us assume that the opening process is allowed if the internal tension in the profile exceeds the critical tension $T_c = bT_0$ with $T_0 \sim 0.02$ N for the soft portion. Due to the stiffness gap, the soft part pulls on the rigid portion with a stress proportional to the fluid forces this specific portion which scale as $(\rho/2)U^2HaL$, where aHL represents the surface covered by the soft part. We balance the two forces to obtain an estimation of the fluid force needed :

$$U_c = \sqrt{\frac{2bT_0}{\rho HaL}}$$

The evolution of the critical opening velocity U_c is plotted on the graph below with an illustration of the transition between the two states previously discussed. The set of curves corresponds to four values of a that vary between 0.2 and 0.5. The red line represents the maximum velocity achieved by the water channel. Thus, it can be seen that based on this scaling, some specimens cannot be opened in our experimental setup.
Though this simple method ignores the gradual opening process of cells and the complex relationship between flow velocity and stiffness, it can still differentiate between specimens where the stiff part stays closed.

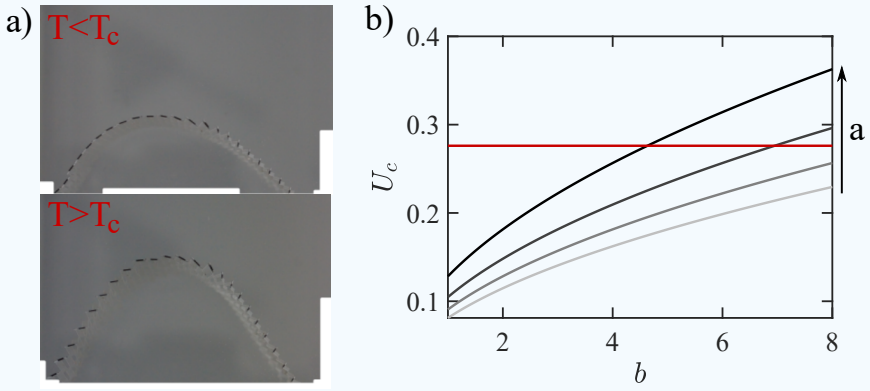

Nevertheless, we note that this simplified model does not take into account the observations mentioned at the end of the previous section with patterns whose rigid part remains closed (high b specimens). Indeed, this effect is linked to non-linear mechanical behaviors and cannot be captured by our current simplified model. We proposed a rough estimate for the critical flow velocity to open the stiff portion within the interlude n^o13

We demonstrated through a simplified model that reproducing the non-monotonic deformation kinematics seen in our experiments is possible. Under certain assumptions, the complex behavior of heterogeneous kirigami patterns can be described by two single elastic rodes.

3.5 Conclusion

As introduced in the first chapter the cutting pattern controls the effective mechanical response of the whole structure. Playing with this parameter along the sheet modifies both its cells opening kinematics under tensile stress and the shapes reached in a flow.

To examine the effect of stiffness variability within a kirigami sheet, we studied the response of a bizonal pattern. The sheet was divided into two regions: a soft section with close-set slits and a stiff section with wider spacing. To perform a comparative experimental campaign, we keep constant the pattern of the soft portion and changed both the length a and stiffness ratios b of the two parts. We then tracked the deformation of each specimen, according to their two polarity states $\oplus$ and $\ominus$, which leads to different behaviors.

Contrary to a uniform kirigami pattern for which both polarity states are symmetrically equivalent, the bizonal specimens propose a new deployment pathway. On the one hand, we first examined the configuration $\ominus$ that mainly involves the opening of the soft portion part which is common to all our specimens. Thus trajectories, shapes and elongations experience a similar trend and values whatever the parameters (a, b). The opening of the soft part drives the whole deployment process and leads to equivalent shapes as the reference case.

On the other hand, the polarity state $\oplus$ involves the opening of the rigid part. We have distinguished two types of responses according to the area covered by the soft portion (parameter a). If the latter dominates, the shapes obtained also tend towards morphologies similar to the homogeneous cases. While, if the rigid portion is predominant (i.e. $a \leqslant 0.5$), we note a non-monotonic expansion kinematics with a lobe deviation that passes from right to left as the rigid portion progressively stretched. We therefore suspect that the non-linearities in local pores opening imply this new shape-sifting process.

Finally, we have proposed a simplified theoretical model that captures the experimental trends previously described with a network of two extensible rodes of different linear stiffness which undergo external fluid forces. We show that this "toy model" is able to mimic the kinematics of the expansion of the bi-zonal kirigamis, with the subtleties related to the choice of polarity relative to the incoming flow direction.

We are now sufficiently equipped to attack the inversion of the problem which is at the heart of chapter 4.

4

Inverse problem : first steps

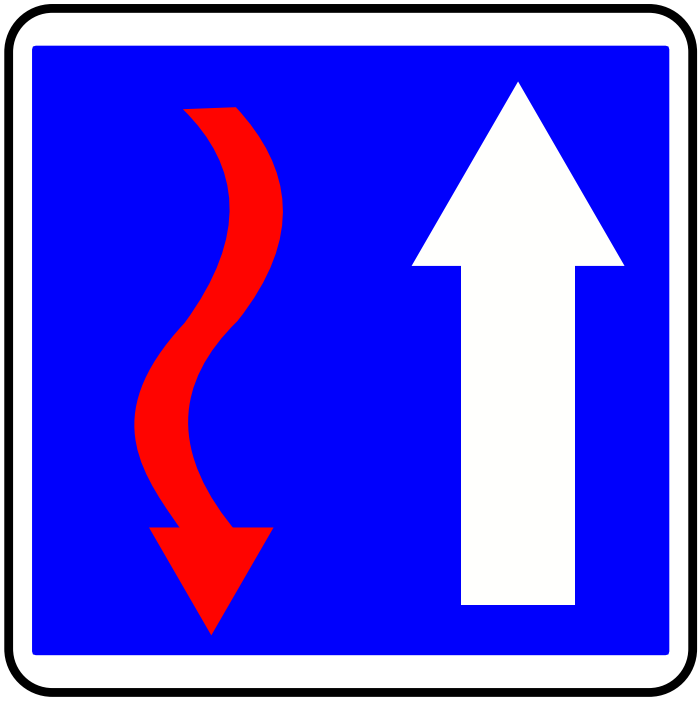

Figure 4.1: "L'acte d'étudier une question consiste à mobiliser des idées ; pas n'importe lesquelles, mais celles dont nous pouvons raisonnablement attendre la solution désirée." J. Hadamard

In previous chapters, we demonstrated that we can achieve various shapes by manipulating the cutting pattern and polarity. In this section, we will address the inverse problem: given a desired shape and a specified flow speed, we will seek to determine the appropriate cutting pattern that will allow us to attain it. In this chapter, we will present a first approach based on the theoretical model previously developed to find the spatial distribution of stiffness that approaches the desired shape. Due to the continuous nature of the model, the optimized continuous distributions will then be transposed into a pattern with a finite number of cuts, which is realized and tested experimentally in flow.

This chapter does not aim to provide a definite solution for shape morphing. The results presented are still preliminary and not entirely conclusive. Instead, the goal is to present the basic building blocks necessary for understanding and addressing this complex issue.

4.1 Inverse problem

4.1.1 Kirigami shape morphing problems

Controlling the shape of objects, known as shape-morphing, is a challenging problem in materials science and advanced engineering. It has potential applications in various fields such as aeronautics to optimize wing shapes and enhance flight performance [75, 76], soft robotics where it can be used to achieve new functionalities and pre-programmed movement of a robotic arm [77, 78], or even in the medical field for prosthetics or implants. The goal of shape-morphing is to produce deformable systems that tend towards a desired shape once subjected to a controlled external loading (pressure, gravity, tensile force, or fluid flow here).

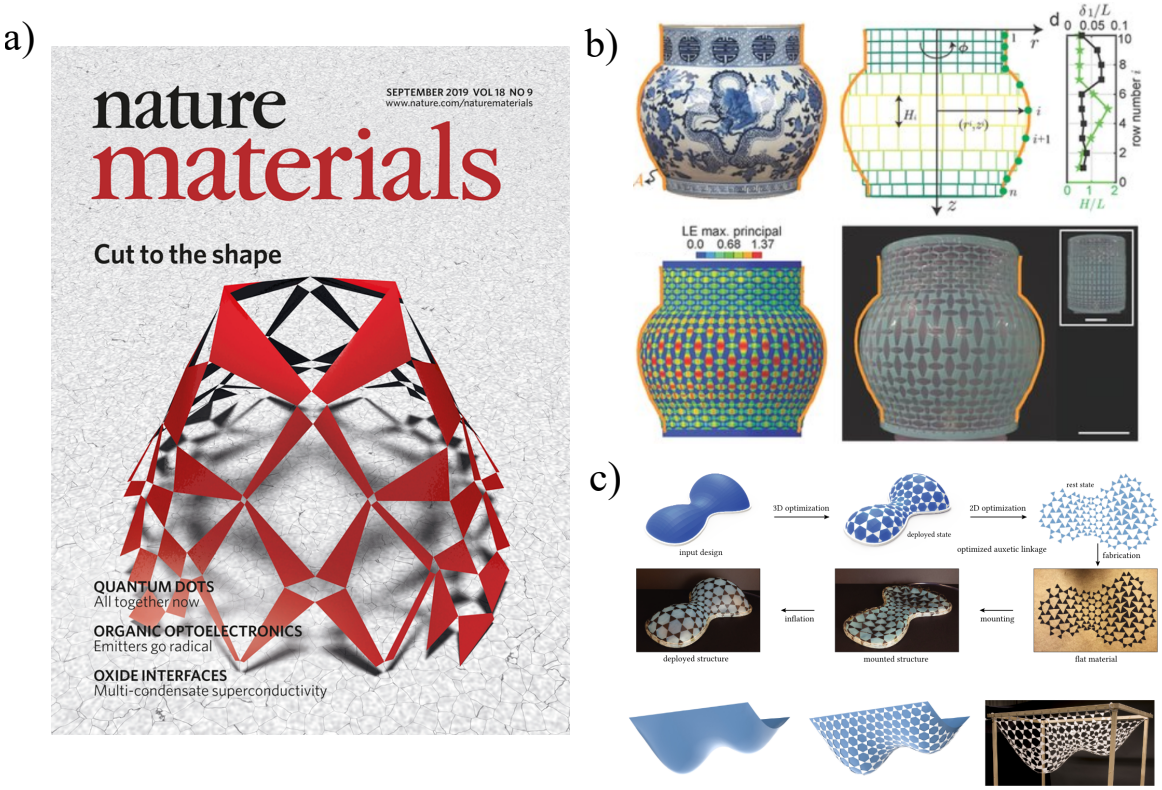

Figure 4.2: The adjustment of a cutting network on a thin sheet allows to reach desired shapes when subjected to a different types of external loads: a) tensile forces, [26], b) internal pressure forces on a kirigami embedded in an inflatable membrane, [49], or a gravitational loading applied to an auxetic pattern resulting in a surface with two minima [79].

The resolution of this problem depends on the characteristics of the deformable system such as its dimensions, mechanical and structural properties, and the external load applied. Kirigami's versatility makes it a valuable tool for shape programming, as demonstrated by its promising results in previous research studies. As shown in Fig4.2a, non-uniform kirigami patterns have been designed to reach complex three-dimensional shapes when subjected to external tension [26]. In [79], a cutting pattern with a network of rotating triangles is used to program multi-curved shapes under gravity, as illustrated in Fig4.2c. Finally, a Chinese vase can be obtained by embedding a non-uniform kirigami tessellation within a pressurized soft elastic cylinder (see Fig4.2b, [49]). In this chapter, we propose a new kind of external stimulus, which is a fluid flow. A specificity of this stimulus is the coupling between the deformation and the loading that is shape-dependent. Indeed the forces exerted by the surrounding flow change as the kirigami sheet deforms (unlike gravity), and with a non-uniform distribution over the whole sheet (unlike pneumatic) that depends on the local orientation with respect to the flow and elongation (that conditions 3D texture).

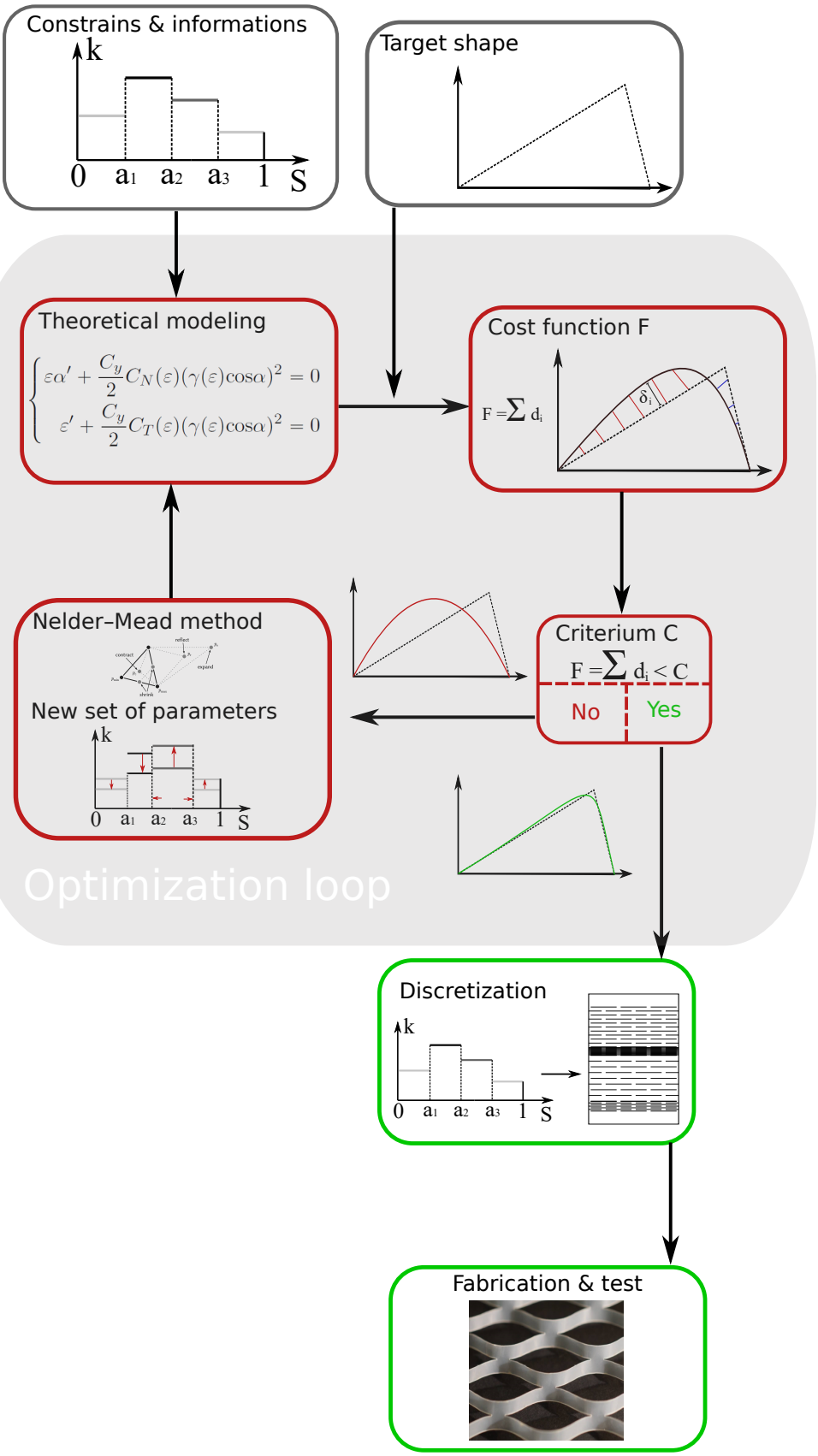

Figure 4.3: Resolution diagram for the inverse problem, each colored block corresponds to a part of the algorithm.

4.1.2 Overview of our inverse problem

Our objective is to determine the optimal non-uniform cutting pattern for achieving a specific target shape, given a water flow velocity. Before delving into the specific methods, we provide here an overview of the key points. The optimization algorithm is informed by the continuous theoretical model presented in Chapters 1 and 2. Our approach consists of three steps: initializing the optimization process with intuitive values, minimizing the difference between the target shape and the shapes generated by the model using an appropriate cost function and criterion, and finally transforming the continuous solution obtained into a discrete cutting pattern and evaluating it.

4.2 Steps of the inverse problem

4.2.1 Hypothesis and constraints of the optimization problem

To avoid the issue of "ill-posed" problems (or lack of information), as defined by Hadamard [80], we must first specify constraints or fix some parameters to ensure a unique solution.

Parameters for the kirigami sheet

As a starting point, we only manipulate the spatial distribution of cuts (and thus the effective stiffness distribution), without altering the polarity along the sheet (no notches). Additionally, to ensure a purely 2D deployment without geometrical frustration, we keep identical rows of slits and only vary their spacing d_x. The slit length L_s and spacing d_y along a row are thus kept fixed (as in Chapter 3). The varying parameter d_x is referred to as d for simplicity in the following.

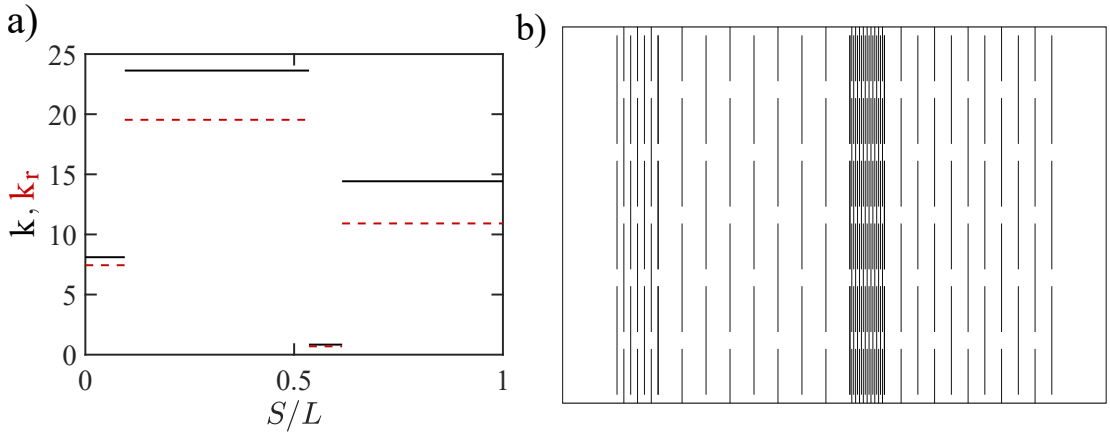

Figure 4.4: a) Distribution of stiffness per block of non-uniform kirigami pattern encoded to reach a triangular shape in flows, the optimal solution k from the model (black line) and their receptive discretized values. b) Cutting tessellation associated with the k distribution defined in a).

Instead of continuously varying d (which would be complicated due to the small length of our sheets), we vary it in blocks. The pattern is thus divided into N_b sub-blocks, which each contain N_i rows of cells characterized by a spacing d_i. The pattern is thus fully characterized by the distributions $\mathbf{d} = [d_i]$ and $\mathbf{N} = [N_i]$ with $i \in [1, N_b]$, which are the varying parameters of our optimization problem. The fixed length of the kirigami sheet $L = 12$ cm also imposes a relationship between parameters $\mathbf{d}$ and $\mathbf{N}$, :

$$L = 2 \sum_{i=1}^{N_b} N_i d_i \tag{4.1}$$

An example is presented in Fig4.4, showing a specimen with $N_b = 4$ blocks with $\mathbf{d} = [0.19, 0.66, 0.053, 0.42]$ cm and $\mathbf{N} = [3, 4, 9, 5]$.

Corresponding parameters for the theoretical effective membrane

In our model, the kirigami sheet is represented as a continuous elastic membrane, and the cutting parameters effectively alter its stiffness. The experimental parameters **d** and **N** are thus transformed into a set of stiffnesses and block sizes in the model. The size of each block is defined by vector **a**, such that the i-th block covers a portion $(a_i - a_{i-1})L$ of the entire kirigami tessellation. To avoid overlap, it must satisfy $a_i > a_{i-1}$, with $a_1 = 0$ and $a_{N_b+1} = 1$.

Each block has an effective stiffness per unit length k_i, relating the internal tension N_i to the elongation ε through $N_i = k_i\varepsilon$. Note that this stiffness per unit length is related to the stiffness K_i used in previous chapters by $k_i = K_i(a_i - a_{i-1})L$. This k_i is further defined with respect to a reference value k_0, as:

$$k_i = b_i k_0 \tag{4.2}$$

The reference k_0 is used to define the Cauchy number $C_y = \rho U^2 HL/k_0$, which is considered known here (with H the kirigami height, ρ the water density and U the flow velocity). The parameters of the theoretical model are thus $\mathbf{a} = [a_i]$ (with $i \in [1, N_b + 1]$) and $\mathbf{b} = [b_i]$ (with $i \in [1, N_b]$).

Finally, we impose an upper limit for the rigidity, that is $0 < b_i < b_{lim}$, to avoid portions that are too stiff and would not deform.

The system of equation for the local strain ε and profile inclination α for the i-th block then writes:

$$\left|\begin{array}{l} \varepsilon(\tilde{S})\alpha'(\tilde{S}) + \frac{C_y}{b_i} f_n(\varepsilon(\tilde{S}), \alpha(\tilde{S})) = 0 \\ \varepsilon(\tilde{S})' + sgn(\tilde{S})\frac{C_y}{b_i} f_t(\varepsilon(\tilde{S}), \alpha(\tilde{S})) = 0 \end{array}\right. \quad \text{with} \quad \tilde{S} \in [a_{i-1}, a_i] \quad \text{and} \quad C_y = \frac{\rho U^2 HL}{k_0} \tag{4.3}$$

Where $\tilde{S} = S/L$ is the non-dimensional curvilinear abscissa, and $f_{n,t}$ are the fluid forces per unit lengths as defined in Chapter 1.

4.2.2 Optimization: reaching the target shape

Our inverse problem is therefore to optimize the theoretical distribution of stiffness in a non-uniform pattern defined by blocks to create shapes approaching a specific target. One important question remains: what measure/indicator can we use to determine how close the model is to the target ?

Cost function and criterion

In shape morphing problems, we aim to minimize the distance between the curve predicted by theory and the target. But, what do we mean by distance? And how does this relate to a cost function? Let us first suppose that the desired form is described by a continuous function $\tilde{y} = \Gamma(\tilde{x})$ (where $\tilde{x} = x/L$ and $\tilde{y} = y/L$), while the theoretical curve corresponds to a finite number N_r of resolution points $(\tilde{x}, \tilde{y})_i$ with $i \in [1, N_r]$ (see Fig4.5a). The distance between these two curves is quantified by measuring the minimal distance δ_i between the target curve and each point of resolution, that is the minimum of $\sqrt{(\tilde{x} - x_i)^2 + (\Gamma(\tilde{x}) - y_i)^2}$. By summing the distances δ_i for all resolution points, we get a good indicator of the overall gap between the theory and the desired shape:

$$F = \sum_{i=1}^{N_r} \delta_i \tag{4.4}$$

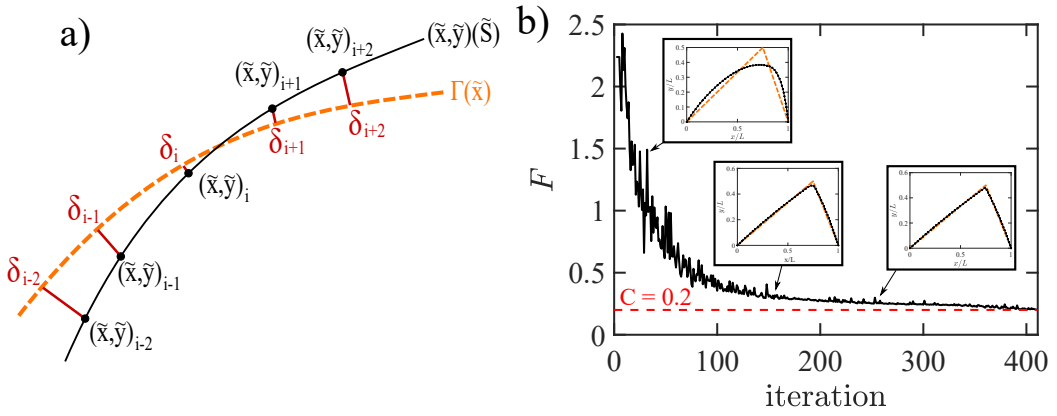

Figure 4.5: a) The minimal distances between the targeted curve $\tilde{y} = \Gamma(\tilde{x})$ and a set of theoretical points $(x, y)_i$ given by the model, are defined by the lengths δ_i (red lines). b) Evolution of the cost function F (sum of δ_i) as a function of the number of iterations, for a triangular target shape and four-block specimen ($N_b = 4$).

At each iteration of the optimization process, a theoretical profile is created and the value of the cost function F is determined. This value is then compared to a criterion C arbitrarily chosen (a scalar value). We then distinguish two cases: if the cost function is lower than the criterion ($F < C$), the loop will end, indicating that the theoretical shape is sufficiently close to the target shape. Otherwise, if ($F > C$), a new iteration will be done to further adjust the stiffness distribution. The Fig4.5b illustrates how the cost function evolves with the number of iterations for the triangular target form shown in the insets. For values of F close to the criterion (here, $C = 0.2$), the two shapes are almost overlaid.

The scalar C is defined as a tolerance distance (normalized by the length of the kirigami L), for which the theoretical profile is considered to be close enough to the target. If convergence is not guaranteed (too complex shapes) or if the initial parameters do not allow to reach the criterion, a stopping condition is implemented. To approach the target shape as closely as possible, it is necessary to choose low C. In practice, a value of $C < 0.5 - 0.7$ provides good enough results, as illustrated by Fig4.5b.

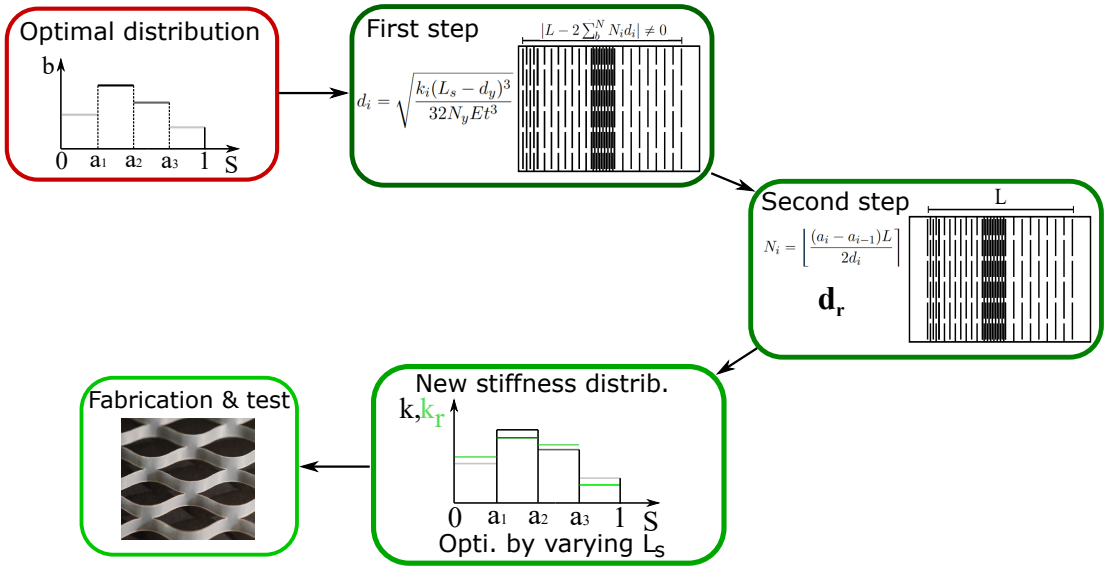

Figure 4.6: Schematic view of the discretization process, how can we transform the theoretical solution into a real pattern?

Optimization algorithm

At each iteration of the optimization process, a new set of parameters is generated using the *fminsearchcon* function in Matlab [81]. This function is based on the Nelder-Mead simplex method, which minimizes the cost function within a space of dimensions equal to the number of input parameters ($2N_b - 1$ here). This algorithm has already demonstrated effectiveness in programming the shape-morphing of a kirigami sheet embedded within an inflatable membrane. (see Fig4.2b) [49]. It notably allows to impose constraints on distributions, like restricting the values of **b** and maintaining the proper order in block sizes **a** to prevent overlap here.

Interlude n^o14: How to reduce errors on the stiffness distribution ?

A way to reduce the error on the stiffness $\mathbf{b_r}$ (in comparison to **b**) corresponding to the new distribution of spacings $\mathbf{d_r}$ is to modify the values of the other cutting parameters L_s, d_y and N_y (while keeping them uniform over the whole sheet). These three variables are related by the height constraint $H = N_y(L_s + d_y)$, and we actually only tune L_s and keep $N_y = 3$ and $H = 10.4$cm fixed (with $L_s > d_y$ see chapter 1 and [55])
In graph a) below, we vary L_s in the range of $[2.5, 4.5]$ mm and measure the cumulative difference (error) between the block stiffnesses $|\sum b_{r,i} - b_i|$ for a case where the target shape is triangular. We observe that the error varies non-monotonically with L_s, with several local minima. By selecting one of these minima, for example, by choosing $L_s = 2.76$ cm, we obtain a new stiffness distribution $\mathbf{b_r}$ with a low error value that is much closer to the solution predicted by the optimization loop as shown in the attached graph.

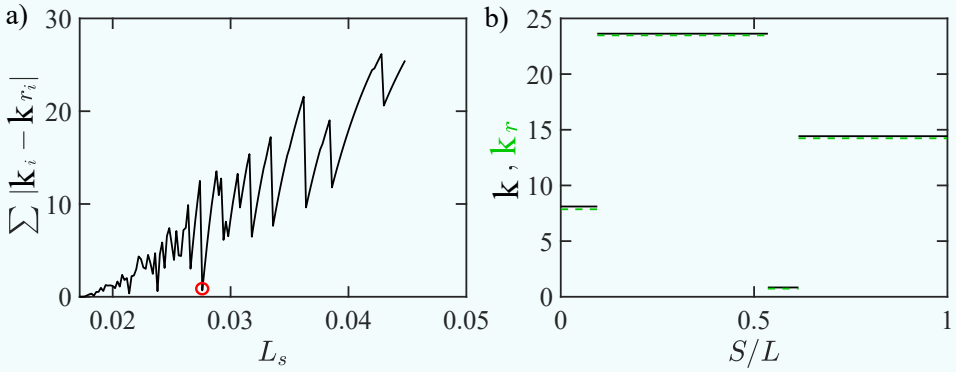

4.2.3 Discretization: from a theoretical prediction to a real cutting pattern

Upon reaching the optimization criterion, we obtain the optimal stiffness distribution characterized by the parameters **b** (stiffness values in each block) and **a** (block sizes). Let us detail in this sub-section how to transform these distributions into a real kirigami sheet with a finite number of cuts. Recall that we keep identical rows of slits (with the same L_s, d_y, and N_y) and only change the spacing between rows d_i and the number of cells' rows N_i in each block. We can relate (d_i, N_i) to (a_i, b_i) by using the relationship derived in Chapter 1 between the cutting parameters and the effective stiffness:

$$d_i = \sqrt{\frac{b_i k_0 (L_s - d_y)^3}{32 N_y E t^3}} \quad \text{and} \quad N_i = \left\lfloor \frac{(a_i - a_{i-1})L}{2d_i} \right\rfloor \tag{4.5}$$

With k_0 the reference stiffness previously defined (that is set by our choice of imposed C_y and U).

In Eq4.5, the number of rows of cells N_i must be an integer (as symbolized by the brackets [82]), which is most often not the case. To ensure this and maintain the total length (i.e. $L = 2\sum N_i d_i$), we slightly modify the distribution of spacings $\mathbf{d_r}$ (where "r" stands for "real"). This also results in a slightly different stiffness distribution $\mathbf{b_r}$ compared to the optimized solution $\mathbf{b}$. As an example, Fig4.4a compares the two distributions $\mathbf{k}$ (black line) and $\mathbf{k_r}$ (dash line), used to obtain a triangular shape To minimize the discrepancy between the prediction and reality, we adjust the cutting parameters along the y-axis (which are kept uniform throughout the pattern) and more information about this can be found in the interlude n^o14. The entire discretization process is illustrated in the schematic view of Fig4.6.

4.3 First tests, and ideas for improvement

4.3.1 Two tests for the inverse problem

A symmetrical shape with a uni-polar pattern?

In our first test, we want to reach a symmetrical trapezoidal shape in a flow with speed $U = 0.15$ m/s and a Cauchy number of $C_y = 1$. We (arbitrarily) impose a sheet made of four blocks ($N_b = 4$) and with a $\oplus$ polarity.

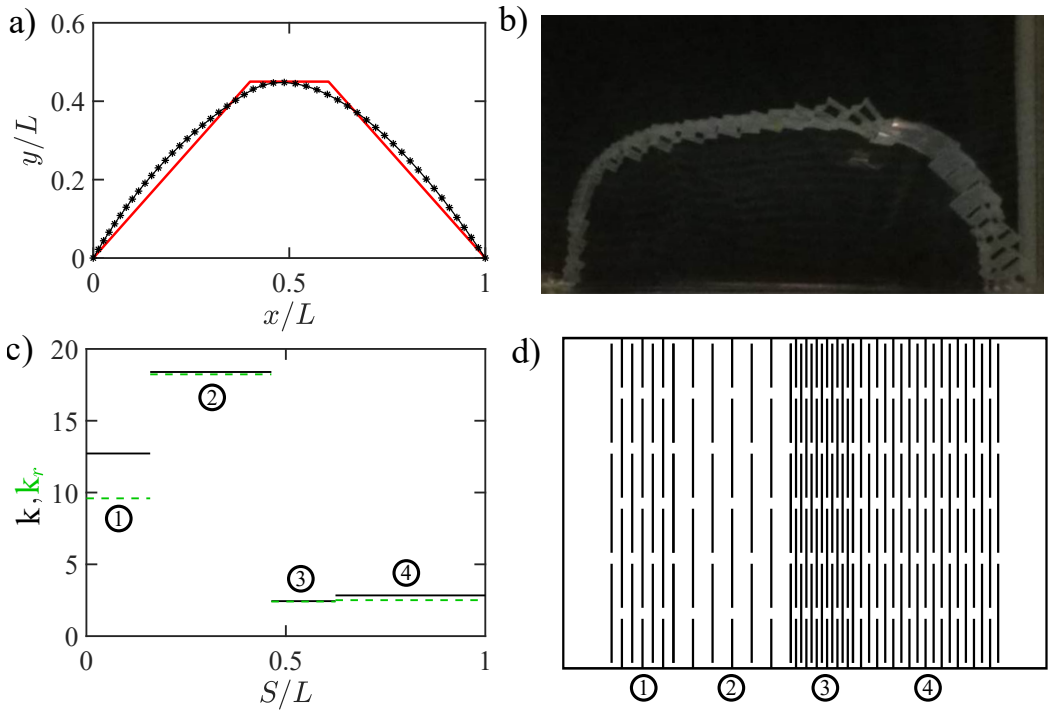

Figure 4.7: a) Symmetrical target curve (red) and optimized deformation profile (black) for a 4 blocks-kirigami sheet at $C_y = 1$. b) Shape obtained for the real kirigami in a flow with velocity $U = 0.15$ m/s. c) Optimized solutions $\mathbf{k}$ (black solid line) and real stiffness distribution $\mathbf{k_r}$ (green dotted line). d) Corresponding cutting pattern (with slits length $L_s = 3.12$ cm and $N_y = 3$).

Fig4.7a displays the target shape, which is symmetrical and consists of two slopes and a plateau at $y/L = 0.45$. Note that it is challenging to achieve a symmetrical shape for a unipolar specimen without adjusting the polarity (except in specific velocity regimes as observed in Chapter 3 for some bizonal cases). The optimization loop was run with stopping criterion C=0.7 and after N=382 iterations, the theoretical solution, shown in Fig4.7a with a black line, was obtained. This solution exhibits a symmetrical shape similar to the target,

but with a smoother geometry, as angular edges are difficult to reproduce using only four blocks.

Fig4.7c shows the associated solution for the stiffness distribution obtained through optimization $\mathbf{k} = \mathbf{b}k_0$ (in black). The distribution is finally discretized to produce the cutting pattern shown in Fig4.7d, where each block is identified by the same numbers in Fig4.7c. The corresponding real stiffness distribution $\mathbf{k_r}$ is shown with green dotted lines in Fig4.7c (these values were optimized using the method described in the interlude n^o14).

The kirigami sheet is fabricated through laser-cutting a 100 μm-thick Mylar sheet (as in Chapter 1 and 3) and placed in a water flow with a velocity of $U = 0.15$ m/s. As shown in Fig4.7b, the specimen deforms symmetrically, as desired. However, the amplitude and overall shape deviate from the target. Some parts of the kirigami have not been stretched, while the softest parts (2 and 3) carry the deformations alone. Possible explanations for this inconclusive result are proposed in the following section. Now, let us move on to the second test, where the target resembles... a slice of pie.

It's not a piece of cake!

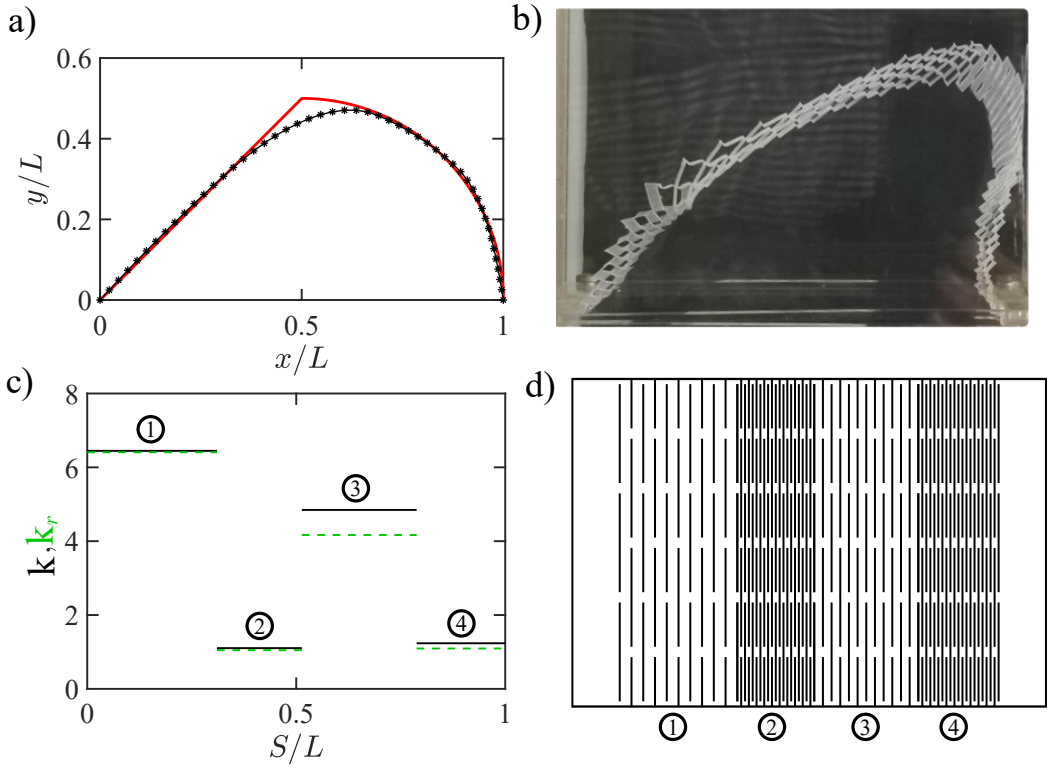

Figure 4.8: a) Target curve (red) and optimized deformation profile (black) for a 4 blocks-kirigami sheet at $C_y = 1$. b) Real shape obtained in a flow with $U = 0.15$ m/s. c) Optimized solutions $\mathbf{k}$ (black solid line) and real stiffness distribution $\mathbf{k_r}$ (green dotted line). d) Corresponding cutting pattern (with slits length $L_s = 2.98$ cm and $N_y = 3$).

The second example involves an asymmetrical target shape, with a circular arc on the right half and a constant slope on the left half (see red line in Fig4.8a), reached in a flow with $U = 0.15$ m/s for Cauchy number $C_y = 1.5$ and polarity ⊖. The theoretical optimized profile (with convergence criteria $C = 0.6$) closely resembles the desired shape (black and red lines in Fig4.8a). The Fig4.8c-d display the stiffness distributions and patterns to cut.

As for the previous case upon testing in a flow, the outcome was not matching with the shape except even if the deviation is aligned with the theoretical prediction (see Fig4.8b). A closer examination of the multi-zonal kirigami in the water flow reveals that sections 2

and 4 in Fig. 4.8d rotate in opposite directions, whereas the pattern should be unipolar. This will be addressed in the following section.

4.3.2 Ideas for improvements

Despite the inconclusive results of previous inverse problem tests, we will not abandon the effort. Let us examine the limitations of our method, particularly regarding the theoretical model and discretization process, and explore potential solutions to improve the algorithm's performance.

Discretization process

One potential source of error is the discretization process, which results in a cutting pattern with a stiffness distribution that does not perfectly match the solution generated by the optimization algorithm. This problem is particularly pronounced in our case due to the small size of the sheet and the limited number of cutting cells. To eliminate the need for a discretization algorithm, each row of cells could be modeled as an independent spring. This approach may be more computationally complex, but it provides a solution that already takes into account the final cutting pattern properties. This discrete modeling approach is commonly used to describe the mechanical behavior of kirigami sheets [46, 73], and holds promise for further exploration.

Accounting for mechanical nonlinearities in the model

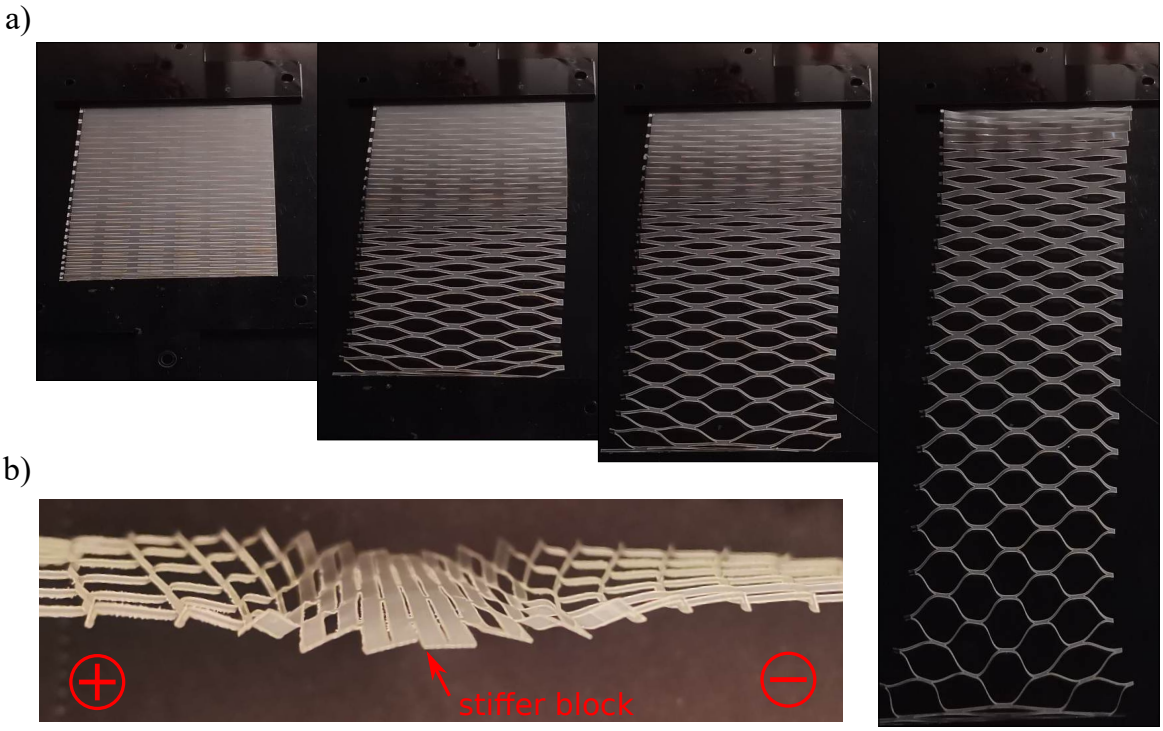

Figure 4.9: a) A Kirigami sheet with gradually increasing spacings d_x results in a coexistence of open and closed states. b) A rigid block sandwiched between two softer blocks can reverse the rotation direction of the cells.

We modeled kirigami sheets as membranes with linear elasticity, ignoring the initial stiff regime. These nonlinearities did not have a significant impact on the homogeneous kirigami specimens discussed in Chapter 1, as the unstretched part of the sheet is aligning with the flow. They also had a minor effect on the bipolar specimen made of rubber in Chapter 2, where the first stiff regime was less noticeable (see interlude n^o9. However, nonlinearities

may play a role in the non-homogeneous Mylar specimens analyzed here. As discussed in the general introduction and observed in the experiments here, this leads to the sequential opening of pores, with flexible portions opening while rigid ones remain fully closed (rather than gradually opening to a lesser extent). This phenomenon is illustrated in Figure4.9a with a "gradient kirigami" (without flow) where the spacing between cells gradually increases in the direction of tension, resulting in a clear transition from a closed to an opened state. The large differences in stiffness between blocks in our case might exacerbate these nonlinear effects. It would be interesting to further investigate this aspect through mechanical tests, by subjecting non-uniform specimens to tensile tests and measuring the cellular displacement field, and then incorporating the results into the model, for example using methods similar to those used in hierarchical kirigami studies [25].

Complex interaction between polarity and stiffness

Mechanical nonlinearities have another surprising effect on the direction of blade rotation. As shown in Fig4.9b, a rigid block that is not extended between two softer blocks can reverse the rotation direction of cells. This results in variations of the polarity along the sheet, which affect fluid loading in flow as for the "piece of cake"-like shape. Further investigation into the mechanical behavior of non-uniform patterns is necessary to notably determine the stiffness difference that causes this phenomenon.

Refining the model for fluid forces

In our model, the fluid forces are dependent on the angle θ of the blade-like cells relative to the centerline of the sheet, and the angle α of that centerline relative to the flow, which determines the velocity of the local normal flow (see Fig4.10a). Although this description accurately captures the experimental results in Chapters 1 and 2, it has limitations when there is a combination of large α and large θ (i.e. large elongations), which reverses the orientation of the blades relative to the flow (see Fig4.10b). In the configuration of Fig4.10b, our model would predict tangential fluid forces towards the right, while the orientation of the blades relative to the flow suggests fluid forces towards the left. A new formulation for fluid forces could be explored, taking into account the blade angle $\alpha + \theta$ relative to the inflow.

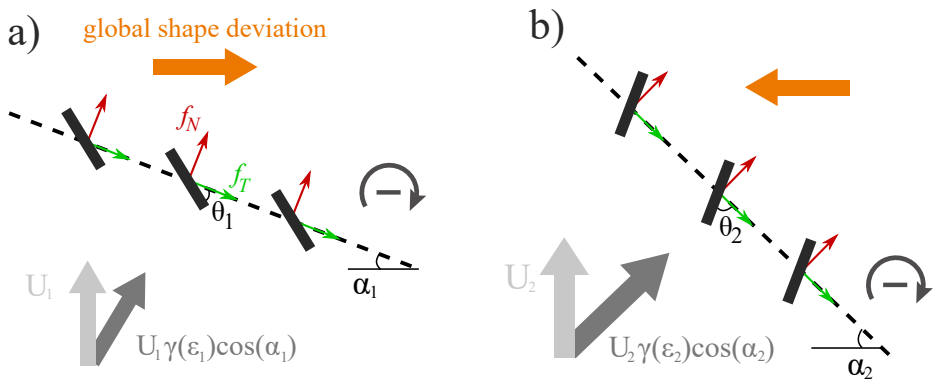

Figure 4.10: a) Fluid forces depend on the cell rotation angles θ and profile tilt α. b) For large values of θ and α, the orientation of the blades relative to the flow suggests tangential fluid forces towards the left, while our model would produce rightward forces.

4.4 Conclusion

The aim of this chapter is to integrate the findings from the previous three chapters on fluid-induced deformations of kirigami sheets, in order to address the inverse problem: to

determine the cutting pattern that results in a desired shape when subjected to a specific fluid flow.

As a starting point, we vary the cutting pattern in blocks, effectively modifying the distribution of effective stiffness. The optimization process is guided by the continuous membrane model described in earlier chapters. It approaches the target profile by adjusting the stiffness and size of each block. The optimal solution is then discretized to produce the cutting pattern, which is then fabricated and tested in a water flow. Our first two tests were not very conclusive, producing shapes that deviate somewhat from the target profile. However, they reveal interesting phenomena that would be worth exploring in future studies and could improve the inverse problem method presented in this chapter. In particular, we have identified the impact of mechanical non-linearity for non-uniform configurations, which affects both the opening kinematics of the pores and the polarity along the sheet. A more comprehensive study of fluid flow through the sheet would also help in refining our formulation for fluid forces, particularly in predicting high-deformation situations with significant variations in the blade's angle relative to the incoming flow.

PART II

DRAG REDUCTION OF CUT AND FOLDED STRUCTURES

5

Influence of slits on drag

Figure 5.1: "Fish," he said softly, aloud, "I'll stay with you until I am dead." E. Hemingway, The Old Man and the Sea

After studying the deformation of kirigami sheets in a flow, we now focus on how such shape changes alter the drag force on the system. The evolution of drag with flow speed is impacted by the macroscopic shape change, but also by the opening of pores and their evolving three-dimensional geometry. We show that this shape reconfiguration reduces the increase of drag with flow speed, compared to that of a rigid object. For a kirigami sheet with a uniform pattern, we further show that the drag scales with the sheet stiffness and its evolution with the Cauchy number are compared to our previous theoretical model. We then briefly address the effect of varying spatially the cutting pattern. We observed in chapters 2 and 3 that the same sheet may deform in different ways depending on the direction of the flow traversing it. Here we show that it leads to two different evolutions of drag with flow speed, a new feature compared to traditional porous surfaces.

5.1 Drag force on deformable porous structures

In the context of fluid-solid interaction, the only information on deformation is incomplete. In order to estimate the coupling between a structure of variable forms and a surrounding flow, it is particularly interesting to study the forces generated. By linking the morphology to a given fluid force, one can then predict both the kinematic evolution of the structure itself and the forces experienced.

For rigid systems, we are generally interested in the drag force, defined as the component of fluid load parallel to the incoming flow. The latter is at the heart of many studies on the resistance of systems subjected to a moving fluid in civil engineering to reduce the damage of a storm and in aeronautics, to reduce the fuel consumption of an airplane or increase flight performance. The flow regimes in these situations being characterized by a high Reynolds number, the effects of viscosity are usually neglected and the drag forces D are expressed through the dynamic pressure according to a quadratic evolution in velocity: $D \propto U^2$.

Nonetheless, things become more complex when the system in question is deformable, as discussed in the introduction, the modification of the shape induced by the flow changes the forces exerted on the deformed structure. This mechanism can lead to a reduction of drag, it allows plants and trees to withstand wind fluctuation. Also, whether for rigid or deformable systems, the knowledge of the drag law (force evolution as a function of the surrounding flow velocity) is an asset to predict system behavior in a fluid environment and then prevent vibrations or damage due to deformations.

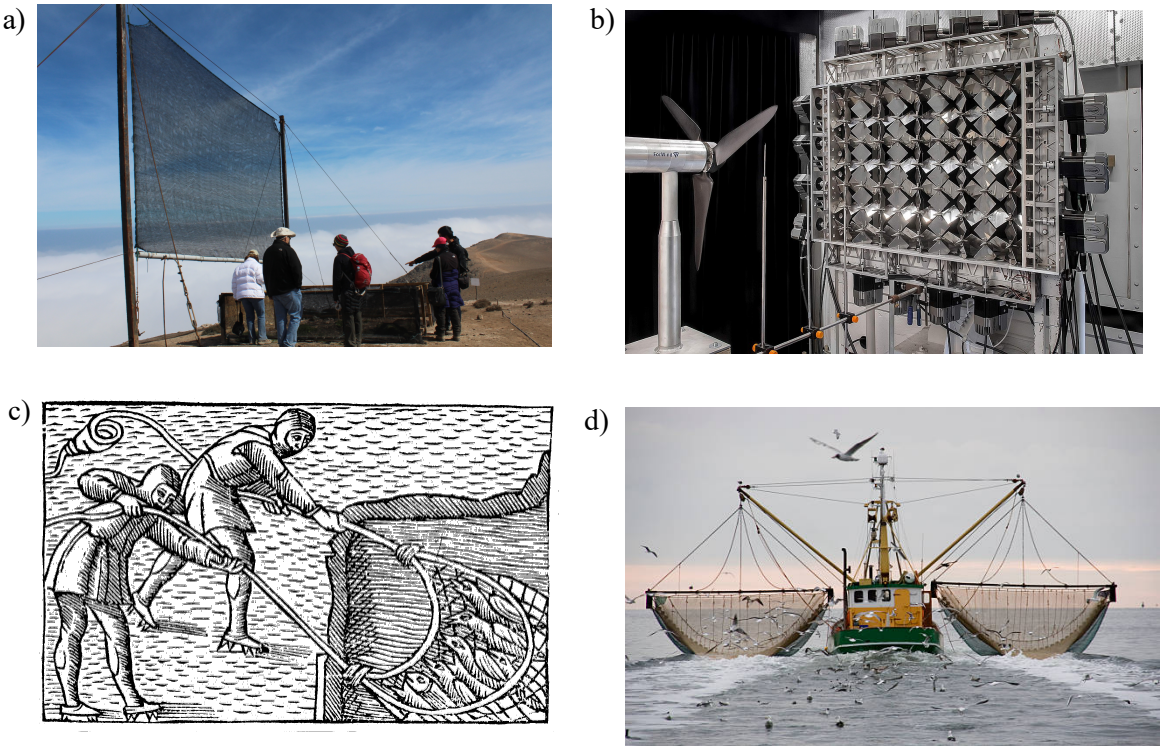

Figure 5.2: a) Fog collector in Alto Patache, Chili. b) Active grid to control the flow impacting a wind turbine (from [83]).c) Medieval Scandinavian ice fishing technique in 1555. d) Fishing boats using strong motors to raise their nets

In addition to being deformable, our kirigami sheets have the particularity of being porous. The modeling and measurement of drag forces on porous surfaces are at the heart of many current problems. For instance, fog nets (see Fig5.2a) are an ecological and innovative contraption that allows for the collection of drops suspended in the air, but depending on their geographical location the impact of the wind can be devastating, and break the whole

structure. It is then necessary to optimize the porosity to reduce the wind loading and keep a high collection efficiency at the same time [7, 84]. Even if constitutive fibers are soft, the pre-stress imposed to keep all fibers straight ensures global surface rigidity at constant porosity. Another example of a stiff porous system is the grid-like system to control air flow in a wind tunnel (see Fig5.2b); their porosity is adjustable to create the desired level of turbulence and pressure drop in a wind tunnel [85, 83]. Finally, porous surfaces and nets are also widely used for fishing, to the historical era and the fabrication method used, their braiding and sizing are adapted. Where an old seine net can be used by two peoples (Fig 5.2c), contemporary fishing dredge methods require a hydraulic engine with strong torque capacity mounted on a trawler to pull the net underwater (Fig5.2d). Thus in order to reduce the efforts required for their use, several theoretical modelings and reduced-scale experiments have been performed.

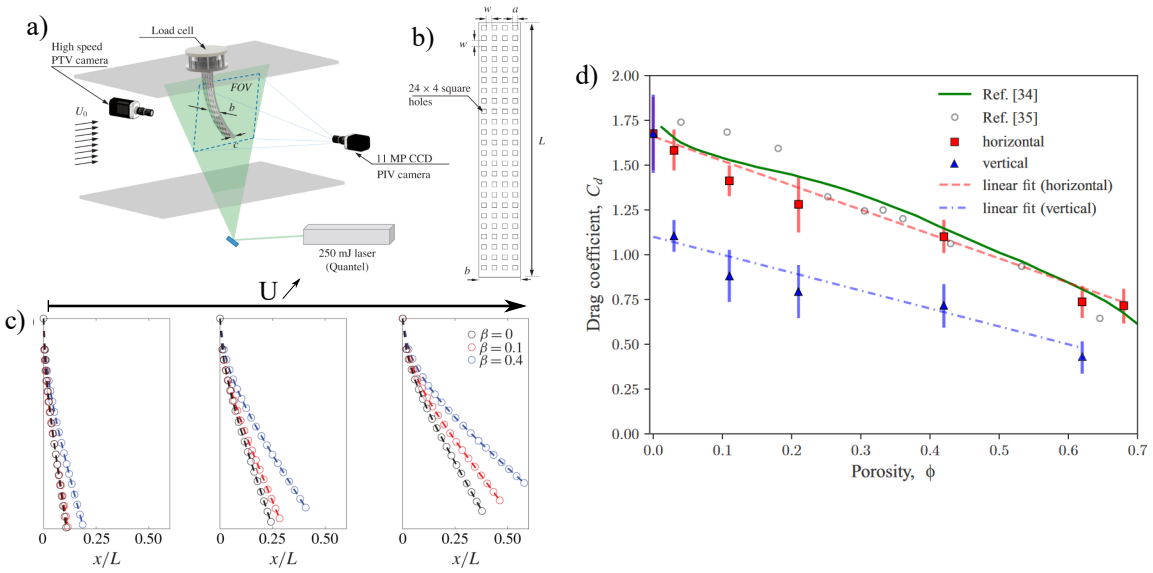

Figure 5.3: a) Experimental setup used in [61], that is able to extract both deformation profile, drag forces and velocity field of the flow that passes through a perforated strip. b) Typical distribution of the porosity in a ribbon. c) Equilibrium deformations shapes for an increasing velocity of three different porosity strips β. The three figures come from [61]. d) Drag coefficient as a function of porosity β, the blue and red dots are experimental data from [60] and their respective linear fitting $C_d = C_{dr}(1 - \lambda\beta)$

As will be discussed in this chapter, the experimental and theoretical study of systems like fishing nets is complex, so a continuous description with effective properties is often preferred. Fundamental studies have been conducted on flexible ribbons placed in front of an incident flow. A uniform circular or square pore array is affixed on this ribbon with one end clamped and the other free as exposed in Fig5.3a. The authors of both studies, measure the drag force experienced by the flexible porous ribbon as a function of the flow regimes and the imposed porosity (Fig5.3b). They also performed shape-shifting measurements by averaging the position, see Fig5.3c. Guttag et al. suggested the effect of porosity on fluid forces can be modeled by an empirical drag coefficient with a linear behavior: $C_d = C_{dr}(1 - \lambda\beta)$, where C_{dr} is the coefficient for a rigid strip and λ a fitting parameter (see Fig5.3d). Hence increasing porosity leads to reduced both drag and ribbon deflection [60].

While Jin et al. go further and complete the approach by analyzing the velocity field passing through the perforated ribbon by using the PIV method (see Fig5.3a), they also prove the presence of a second regime of drag evolution at high porosity and low velocity with a drag coefficient that first increases higher than for a rigid strip (positive Vogel coefficient) before decaying as previously discovered [61]. The authors suggested that the bending

induced by the flow on the perforated strip alters the local velocity which could explain this phenomenon. This complex evolution of drag in porous and flexible structures shows that both elastic response and porosity play important roles in deformations and forces experienced.

All previous examples and illustrative systems can be mainly deformed in flexion for the simple ribbon or through low stretching for the fishing net, let us now focus on our kirigami structure for which fluid passing through induces large expansion, with a complex evolution of the size and geometry of pores. We then address the following question: what is the drag law of an extensible and porous kirigami sheet in flows?

5.2 First experiments - drag law for uniform kirigami pattern

To understand the typical evolution of drag forces on a kirigami sheet, we first explore the response of patterns with a uniformly distributed cutting pattern (see chapter 1). First of all, let us detail the experimental protocol devised to measure these efforts.

5.2.1 Experimental set up

All experiments of the first thesis part have been conducted in a water channel, where the kirigami sheet is fixed inside a frame which is itself clamped at both ends in the test section (for more details see the sub-section n of chapter 1). This frame fastening system must be modified to allow measurement of the drag force on the pattern.

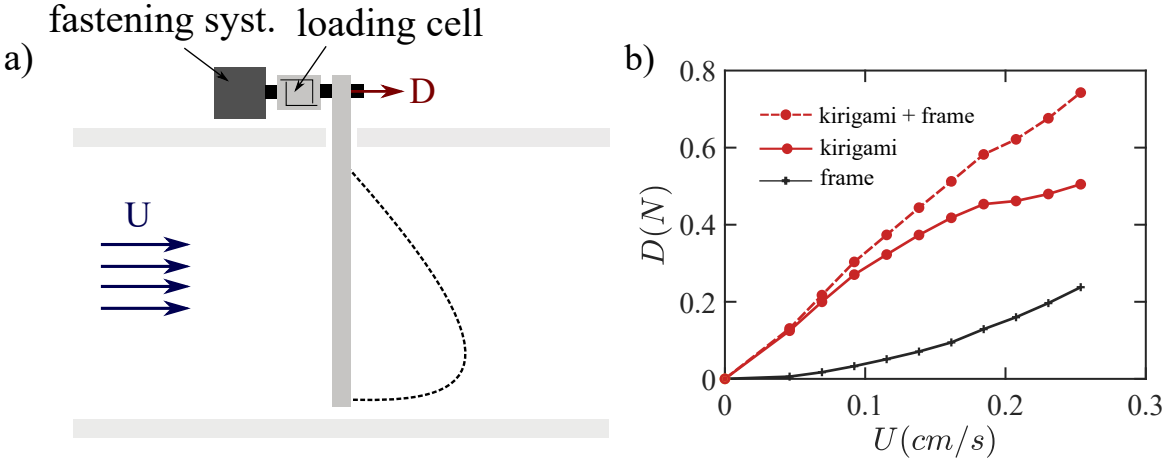

Figure 5.4: a) Schematic view of the experimental setup used to measure the drag force, a unidirectional load cell is linked to the kirigami's frame. b) Drag forces distribution as a function of flow velocity U, the kirigami sheet experiences the higher part of the load.

As shown in Fig5.4a-b the new experimental setup has only one fixing point, indeed the frame where the kirigami is attached is directly mounted on the force sensor outside the test section, while the other end is free. The load cell used (Futek-500g) allows unidirectional measurement; we connect the latter to the QuickDaq software via an acquisition card.

The boundary conditions (fixed-free end) of the frame can lead to a slight bending of the whole system in high flows. In order to reduce the impact of this parasitic deformation on our measurements, we work across a lower speed range than for deformation experiments. The sensor calibration is ensured by using a mass, wire and pulley system attached to the middle of the frame, which would roughly correspond to the point of application of the net drag force. The calibrated masses are gradually added in order to find the linear relationship that links the sensor output voltage and the force experienced.

To validate our force measurement system, we have previously evaluated the drag coefficient on a smooth sphere also placed in the middle of the test section, with a similar lever arm to our {kirigami + frame} assembly. Indeed the drag force experienced on a smooth sphere is well known, with a classical bluff body law in U^2 and a drag coefficient C_d almost constant in our Reynolds number range, our setup provides $C_d \sim 0.43$ which is consistent with existing literature.

The force measurement is performed at a fixed frequency (1024Hz), with a continuous acquisition for 30 seconds, the real drag force D (only the kirigami sheet) is deduced from the average value of D_t total drag force on the whole system {frame+kirigami} minus the drag experienced on the frame alone D_f such as $D = D_t - D_f$. To illustrate the typical intensity of each drag component, all are reported in Fig5.4b. This graph exemplifies the quadratic evolution of drag force on the frame. Note that it plays a minor role in the total drag sum which is dominated by kirigami the component, especially for the low velocities range (low deformation).

A 3D printed piece ensures the junction between the sensor and the frame and allows easy removal of the frame once the experiment is done without moving the sensor. The sensor is itself mounted on an external Norcan assembly, kept fixed during the whole experimental campaign.

This experimental setup has been used in all the measurement campaigns presented in this chapter, let us begin with the study of the drag of homogeneous cutting patterns.

5.2.2 Experimental results

Shape shifting of kirigami sheets induced by surrounding fluid flow has been extensively discussed in the four previous chapters. We have highlighted that the complex coupling between the local fluid forces and the tensile forces controlled by the cutting parameters can explain the versatile shapes reached by our kirigami sheets immersed in a water channel. In this section, we will enrich the set of these results by measuring the global drag on these meta-structures. Let us focus on the case of homogeneous patterns characterized by their effective stiffness K_2 as described in chapter 1.

The Fig5.5 shows the drag evolution results of five specimens whose distance between slits rows d_x varies between 1.5 and 4 mm, while the cutting parameters along the transverse direction are kept fixed: $(L_s, d_y, N_y) = (30, 5.7, 3)$ mm. This induces modifications on the effective stiffness K_2, which evolve between 0.35 and 3.3 N respectively (note that these specimens are those used in chapter 3).

For each pattern, both polarities (i.e elementary cells rotation side) $\oplus$ and $\ominus$ have been tested, according to line the style used. As a reminder, the polarity induces the formation of symmetrical lobes (same amplitudes) along the left or right direction depending on the rotation side of the cells. We change it by simply flipping the assembly {frame + kirigami}.

All the raw results are present on the graph in Fig5.5 that we will discuss in the following paragraphs.

A first glance

First of all, one cannot help but notice that kirigami sheets exhibit drag laws that do not follow a classical U^2 evolution for a rigid object but experience slower increases in drag with velocity (see Fig5.5a). Indeed the deformation occurring when the flow passes through the structure leads to a quasi-linear dependence in U. This trend is actually common for flexible systems, one can mention the example of a thin sheet that bends when facing the flow, where the drag evolves as:$D \propto U^{1.33}$ or a cut disk which rolls up on itself $D \propto U^{0.67}$ (from

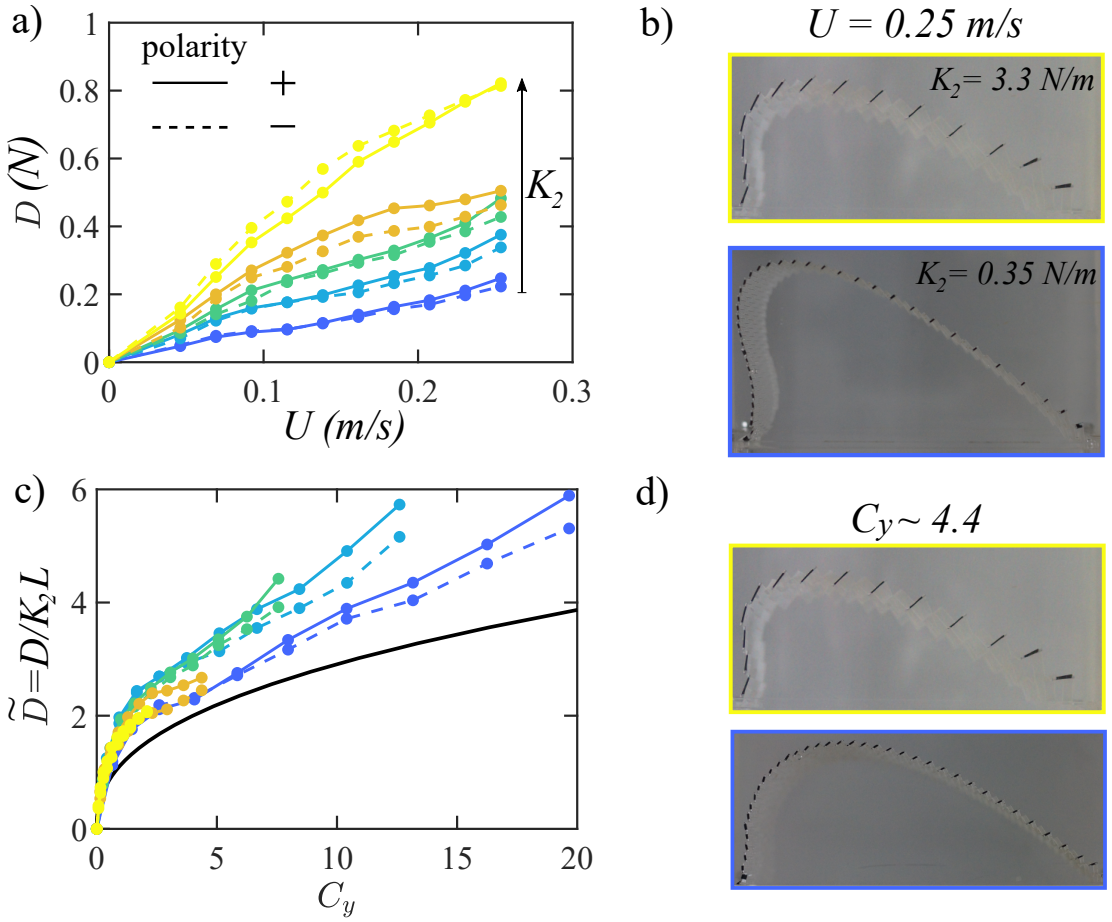

Figure 5.5: a) Drag force D on five kirigami sheets as a function of fluid velocity U, stiffness evolution K_2 varies according to the parula color, in practice, our parameter is the gap d_x between slits rows. b) Asymmetrical deformation shapes associated to drag curves (a), for the stiffest specimen (yellow curve) with $K_2 = 3.3$N/m and the softest one (blue curve) $K_2 = 0.35$N/m for a given velocity $U = 0.25$ cm/s. c) Dimensionless drag forces against Cauchy number make all data collapse onto a single master curve. d) Deformation profiles for the two different specimens of (b) at a similar $C_y \sim 4.4$, we observed that the same global shapes experienced the same drag force in flows.

[16, 15]). Before discussing qualitatively the origin of this reduction and this symptomatic trend, let us focus on other non-trivial results.

The polarity inversion does not impact the amplitudes of the drag forces generated, the dashed and solid curves being very close for a given pattern (thus at given stiffness K_2) in Fig5.5a. In part 1 of the thesis, we reported that the polarity inversion did not modify the morphology for a uniform pattern and led to a similar evolution of amplitude and elongation. In the same way, the global drag forces are identical for a pattern whatever the flow direction (polarity).

One also notes that the forces are stronger the stiffer the kirigami sheets are, to understand this curve order we can take a look at the shapes. The pictures of Fig 5.5b are taken at the same velocity which illustrates that stiffer kirigami deforms less and therefore experiences larger drag forces. The coupling between drag and deformation level is reminiscent of the analyses conducted in part 1.

Stiffness: a key for re-scale

All our previous observations suggest a strong link between the expansion state and drag force. That conveys the result of the competition between the external fluid force linked to

the flow velocity and the internal elastic force linked to the stiffness of the profile. It seems clear (for the assiduous reader that you are!) that Cauchy's number is not far away.

This number drives the deformation in flows, as suggested by the pictures in Fig5.5d where two different stiffness patterns (the same as those reported in Fig5.5b) reach the same deformation shape for a given Cauchy number (estimated around 4.4). Nevertheless, this value of C_y will not be reached at the same velocities, where the rigid profile (yellow) is subjected to a flow at $U = 0.25$ m/s, the softer one (bluer) is taken at a lower velocity of 0.09 m/s.

Interlude n^o15: Same stiffness involves similar drag forces ?

We previously demonstrated in chapter 1 that similar deformations occur in various cutting tessellations with the same effective stiffness see graph below). This indicates that the details of the local geometry have no significant impact on the expansion pathway. Here we want to check if it is also the case with drag force.

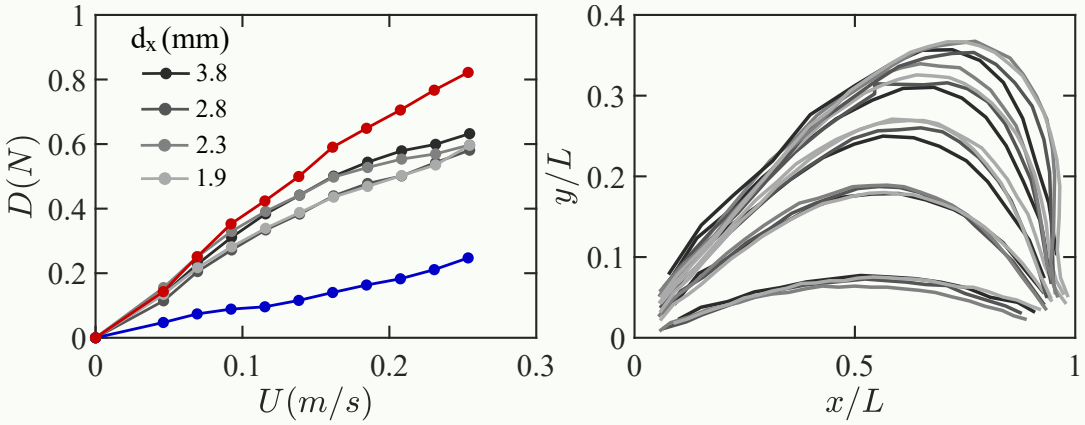

The graph above shows the evolution of drag force for four iso-stiffness patterns with stiffness of $K_2 \sim 3.1$ N/m (taken from chapter 1 studies). The color gradient represents the spacing between slits, as indicated in the legend. To show the variation in drag forces for the iso-stiffness patterns, two additional curves from Fig.5.5 (in red and blue) are added to provide a typical difference in drag.
We observe that the measurements obtained stay well grouped regardless of the d_x values, as long as K_2 is kept constant, and no order seems to be established between them. We can therefore conclude that, like the shapes and amplitudes of these four specimens, the associated drag laws are substantially similar. This once again emphasizes the significance of K_2 in describing the overall mechanical behavior.

This difference in speeds will induce a gap in loads, to reduce it we normalize the drag by the order of magnitude of the tensile force K_2L. In this way specimens of higher stiffness that exhibit low deformations and high drag value will be divided by a larger coefficient. By recasting the raw data previously presented we obtain the graph of Fig5.5c, in which all curves gather onto a single master curve. This universal behavior attests that both rescalings are able to capture the stiffness effect and velocity differences. Another proof of the link between stiffness and drag forces is given in the interlude $^o15$, where we investigate the global load evolution for iso-stiffness pattern. Nevertheless, the Cauchy number can not explain the origin and the drag trends experienced...

As briefly discussed in the general introduction as well as extensively covered in several studies dealing with the reconfiguration process [3, 16, 7]. The drag reduction of a flexible device comes mainly from the two effects of the frontal surface decaying (relative to the in-

cident flow) and the streamlining of the structure itself, both resulting from the deformation induced by the surrounding flow. These two effects are often coupled but can be isolated as we will see in the last chapter for origami structures. However, in our current experiments, a third component linked to the porous nature of the kirigami has to be taken into account. Indeed the expansion opens the pores which modify the local flow speed. This variation of effective velocity modulates the local forces and thus impacts the global drag force. Due to the strong interplay between the three mechanisms, it is difficult to quantify their contribution independently. We then propose to extend our theoretical model which is able to consider these three mechanisms, to compare the force predictions with the experimental results.

5.3 Theoretical prediction for the drag

5.3.1 It's a long (scientific) way to kirigami

Theoretical characterization of fluid forces acting on a porous structure has been widely studied for various applications: from the optimization of fishing net meshes to minimizing fluid stress on fog nets. The challenge is to understand how the porosity and deformation of such systems can influence the fluid loading on the one hand and the surrounding flow on the other hand. With more and more accurate theoretical predictions significant improvements have been made in the manufacture of fishing nets increasing their resistance, capacity and efficiency, let us briefly introduce two classical ways to describe such fluid-structure interplay problem.

The first modeling approach is based on a discrete description, in Morrison's model [86, 87] all periodic elements constituting the screen (knots and strands for a net, cells for a kirigami) are considered as independent and evolving within a flow not disturbed by their neighbors. To estimate the global drag force, the idea is to sum the contribution of each elementary component. This approach has been used as a basis for many studies and has already shown its effectiveness. Nonetheless, its accuracy decreases for the configuration with low porosity, because it is no longer allowed to ignore the backflow induced by neighbors elements (a recent more complex theoretical derivation probes a way to take into account this effect, see [63])

To overcome such limitations, a series of more recent models proposed a different approach [64, 63, 62], which is based on a continuous description of a porous surface, that is reduced to an equivalent flexible and porous membrane. While porous properties can be then taken into account by ensuring a correction on the effective velocity passing through the nets. This model is similar to our theoretical approach, already used in the previous chapter. So let us begin by extending our previous prediction to capture drag force evolution.

5.3.2 Get back and continuous

Using the force model outlined in Chapter 1, we can adopt a similar approach as those used in [64, 61, 62], where the porous surface is described as a continuous membrane. First, let us recall that our fluid force modeling is based on a semi-empirical law where we divide the external load into two components: f_N, normal to the screen, and f_T, along the tangential direction (as shown in Fig5.6a).

From this vectorial splitting, the total drag force experienced by our equivalent membrane is obtained by integrating along the kirigami length the projection of each component as follows:

$$D = \int_0^L \left[f_N(\varepsilon, \alpha)\cos(\alpha) + f_T(\varepsilon, \alpha)\sin(\alpha) \right] (1+\varepsilon) dS \tag{5.1}$$

Where $f_N(\varepsilon,\alpha)$ and $f_T(\varepsilon,\alpha)$ (defined by units of length) represent explicit functions of local elongation $\varepsilon(S)$ and profile inclination $\alpha(S)$. Their formulations also take into account the there effects as previously mentioned and highlighted by three different colors :

$$\left|\begin{array}{l} f_N(\varepsilon,\alpha) = \frac{\rho U^2 H}{2}\gamma(\varepsilon)^2 C_N(\varepsilon)\cos^2(\alpha) \\ f_T(\varepsilon,\alpha) = \frac{\rho U^2 H}{2}\gamma(\varepsilon)^2 C_T(\varepsilon)\cos^2(\alpha) \end{array}\right. \quad \& \quad \left|\begin{array}{c} C_N(\varepsilon) = C_{N_0}\cos^3(\theta) \\ C_T(\varepsilon) = C_{T_0}\cos^2(\theta)\sin(\theta) \end{array}\right. \tag{5.2}$$

We then distinguish the blockage effect implied by porous properties and which involves velocity correction, the blade tilting rotation as a function of local elongation $\theta(\varepsilon)$ and the fluid flow orientation where we consider only the component of the velocity field normal to the membrane.

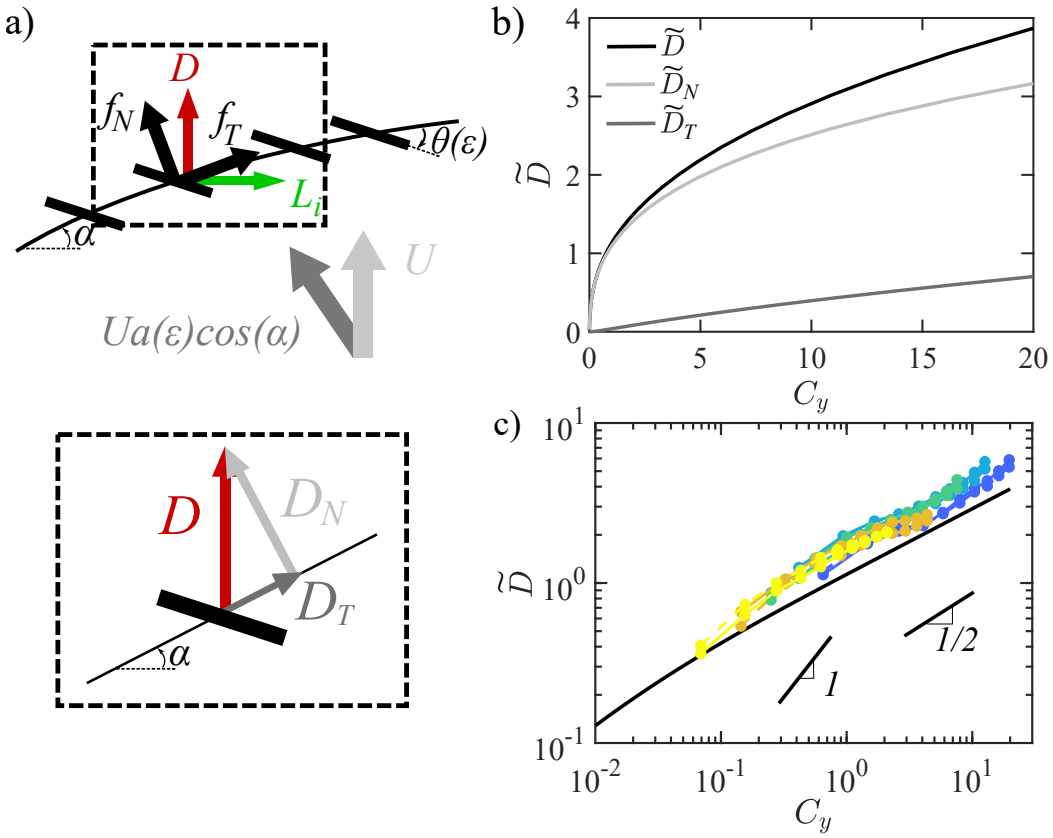

Figure 5.6: a) Local fluid loading depends on the orientation α of the membrane relative to the flow, and the internal mesostructures of tilted surface elements via angle θ. Our theoretical modeling described kirigami sheets as an equivalent elastic membrane that experiences normal f_N and tangential f_T distributed loading, from which we derive global drag D and lift L_i forces. b) Theoretical predictions of dimensionless drag force $\tilde{D} = D/K_2L$ as a function of Cauchy number C_y. c) Comparisons with experimental measurements on the uniform kirigami design from Fig5.5c, the log-log scale highlights the deviation from bluff body law (slope 1) to linear behavior of drag forces identified with the slope 1/2 .

By incorporating each individual force component (as defined in Equation 5.3.2) into the overall drag equation (Equation 5.1), and normalizing the result by the internal tension K_2L, we can express the total drag force in dimensionless form, similar to how it was done for the experiments :

$$\tilde{D} = \frac{D}{K_2 L} = \frac{C_y}{2} \int_0^1 \gamma(\varepsilon)^2 [C_N(\varepsilon)\cos^3(\alpha) + C_T(\varepsilon)\cos^2(\alpha)\sin(\alpha)]\,(1+\varepsilon) d\tilde{S} \qquad (5.3)$$

Where we have defined two dimensionless variables: the Cauchy number: $C_y = \rho U^2 H / K_2$ and curvilinear abscissa $\tilde{S} = S/L$. An illustrative schematic view of each component for drag force definition is shown in Fig 5.6a. Note that the definition of the lift component can also be derived from our continuous description and is discussed further in the interlude $n^o 16 - 17$.

Interlude $n^o 16$: what about lift force ?

This chapter focuses primarily on drag force, but it's important to note that fluid forces come in pairs, including lift. In our experiments, we only measure drag using a load sensor, but we can estimate the magnitude of lift using our theoretical model. As for drag forces, we derived a dimensionless form for lift $\tilde{L_i} = L_i / K_2 L$:

$$\tilde{L_i} = \frac{C_y}{2} \int_0^1 [-C_N(\varepsilon)\cos^2(\alpha)\sin(\alpha) + C_T(\varepsilon)\cos^3(\alpha))]\, dS$$

The figure below shows how the lift changes as a function of the Cauchy number. Both polarities are shown and correspond to the same lift values, but with opposite signs according to local blades rotation and lobe deviation side. In comparison with Fig5.6b, lift forces are of the same order of magnitude as the drag component. Additional experiments using a six-component sensor could be done to confirm this observation.

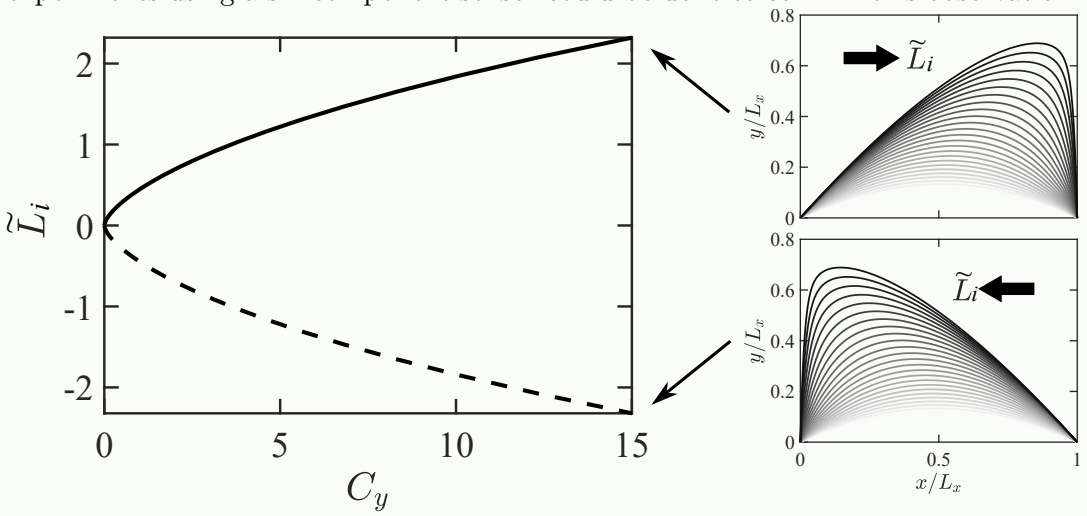

The graph on Fig5.6b features the dimensionless drag evolution $\tilde{D}$ as a function of C_y with the details of each component D_N and D_T (as defined in Eq5.3) according to the color of the curve. This splitting shows the main contribution to the drag is the force component normal to the membrane ie D_N. Polarity inversion provides similar results in force and is not reported here (while differences in sign exist for lift as indicated within the interlude $n^o 16$).

We finally propose two direct comparisons with experimental results and theoretical predictions for the same range of C_y. On the Fig5.6c both are reported in a log-log scale, in order to better estimate the non-quadratic evolution with velocity (slope one for Cauchy number). Indeed here the drag force tends to follow a linear evolution highlighted with 1/2 slope ($C_y^{1/2} \sim U$), this tendency is confirmed by our modeling which provides an accurate qualitative load description. We also directly compare the drag force value in Fig5.5c, which indicates an acceptable quantitative agreement in view of the strong hypotheses imposed in

the theory. Indeed, if we refer to our results in chapter 1, our theoretical modeling overestimated the deformations. Larger elongations, therefore, lead to a weaker blocking effect with a lower local velocity and thus lower global forces.

Despite this deviation (specially marked for large Cauchy number), our theoretical description of the three underlying mechanisms is able to capture the non-trivial evolution of fluid forces on expanding kirigami sheets in flows. As for part 1, we now turn to more complex configurations and probe the effect of adding heterogeneity on the evolution of the global force.

5.4 Drag force on non-uniform kirigami specimen

After having measured and modeled the fluid forces of uniform slits tessellation, it is time to move on to the more complex cases of non-uniform configurations and their impact on the evolution of drag.

Indeed, in chapter 2, we mentioned that playing with the local rotation side of the cells induces different shapes for the same flow velocity. We suspect that this gap could therefore imply two distinct force evolution.

5.4.1 Bipolar case: the role of cells tilting

Let us start by looking at the drag of bipolar kirigami, as a reminder these specimens present a non-uniform polarity, the elementary cells once out of the plane, tilt in an opposite direction, with a transition located at distance aL with $a \in [0, 1]$ (see chapter 2). In practice, we added notches near each slit in order to control the direction of the post-buckling rotation of the cells. We performed two experimental campaigns, one varying the stiffness (through different slits lengths) where three specimens with a polarity inversion placed at $a = 0.5$ (the half of the sheet) were tested and a second campaign in which we changed the position of the transition while keeping the same stiffness (same cutting pattern). Let us now look at the drag force evolution for these two campaigns.

Drag for varying stiffness ($a = 0.5$)

In chapter 2 we established that if the transition was placed at the center $a = 0.5$, the shape obtained once in the flow was symmetrical, with an amplitude depending on the global stiffness and polarity considered (i.e. $\boxed{+-}$ or $\boxed{-+}$). As a reminder, the $\boxed{-+}$ configuration experienced a parabola shape with a higher amplitude than the $\boxed{+-}$ case characterized by its hemispherical morphology (see Fig 5.7b). Thus the same pattern leads to two shapes, what about their drag evolution?

To answer this question, we measure the drag loads of three different cutting patterns, with associated effective stiffness: $K_2 = [2.7, 3.9, 7.7]$ N/m (curve colors) and the transition localized in the middle of the pattern ($a = 0.5$). Measurements were carried out on both polarity configurations (line styles) and the results as a function of the input velocity are exposed in Fig5.7a. As for the uniform cases, we first note that a stiffer pattern experiences a higher drag. Nonetheless, a significant difference must be noticed: for the same pattern, the two polarities do not evolve along the same tendency.

This difference is especially marked for high velocities, with the parabolic shape of the $\boxed{-+}$ polarity (solid lines) which experienced stronger drag than the $\boxed{+-}$ configuration (dash lines). This increasing gap comes from the fact that each polarity exhibits a different drag trend, the case $\boxed{-+}$ assuming an almost linear evolution, while $\boxed{+-}$ tending towards a plateau at high speed. The difference in force between the two configurations of the same cutting pattern is a notable finding: a bipolar specimen presents two different laws depending

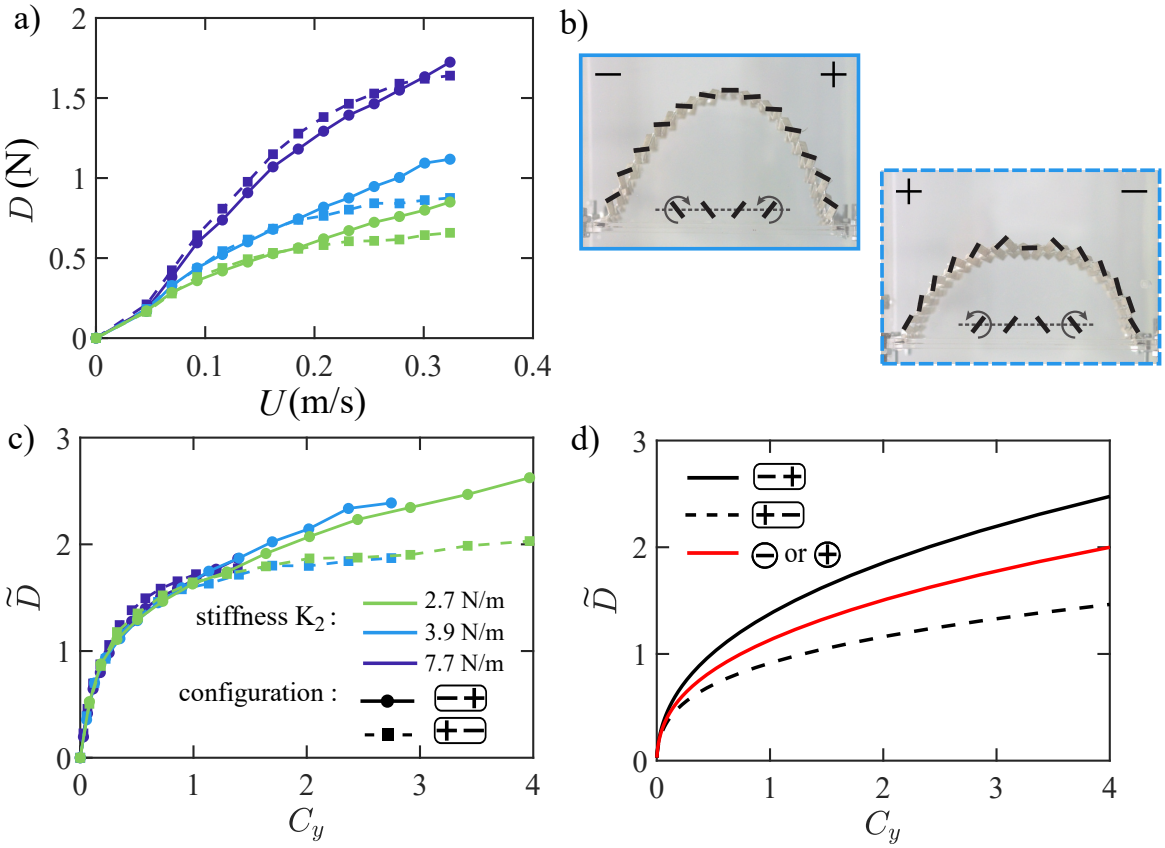

Figure 5.7: a) Drag force evolution as a function of inlet flow velocity for three bipolar specimens of different stiffness (curve colors) and different polarity configurations (line styles). b) Pictures of the two polarity states, for the medium stiff kirigami sheet (blue curves) at the same flow speed $U = 0.21$ m/s. c) Dimensionless drag against Cauchy number C_y, the collapse provides two sets of curves, one for each configuration. d) Theoretical results for drag force in the same range of Cauchy number, with the uni-polar case in red.

on the direction of flow (i.e. polarity). In contrast, a traditional fishing net made of fibers and knots does not exhibit this property, as flow directions are equivalent in both cases (in terms of drag and shape).

Introducing the same dimensionless variables as for the uniform patterns, we recast the data on Fig5.7c. Here, contrary to the previous case, two sets of curves clearly emerge. The collapse in stiffness is still valid, but the master curve obtained is split into two parts according to the polarity state (line styles), which is a reminiscence of the amplitude evolution reported in chapter 2. Thus, differences in expansion of the same pattern induced by a non-uniform polarity bring a new behavior; the drag laws can differ for the same pattern depending on the polarity relative to the flow.

These results are corroborated by theoretical predictions as shown in Fig5.7d. Each configuration gives a different drag evolution whose order and trends are in agreement with the experiments. We then compare these predictions to the global drag force of a uni-polar cutting pattern (whose shape under flow tends toward an asymmetric lobe) which experiences a load in between the two symmetrical bipolar configurations. This theoretical observation suggests the effect of varying the transition position (value of parameter a), which will be investigated in the following section. But before moving on to this effect, let us try to explain why no collapse occurs.

Frontal area

The origin of these two master curves splitting is therefore related to the different expanding pathways between the two configurations. More than global morphological differences (parabolic/hemispherical-like shapes), there are local dissimilarities when we look at the cell scale. As seen in Fig5.7b, the cells in the $\boxed{-+}$ case are almost perpendicular to the flow, while those in the $\boxed{+-}$ case are partially parallel. One can intuitively guess that the first configuration will experience stronger fluid loads, as the drag contribution is greatest when an object is facing the flow.

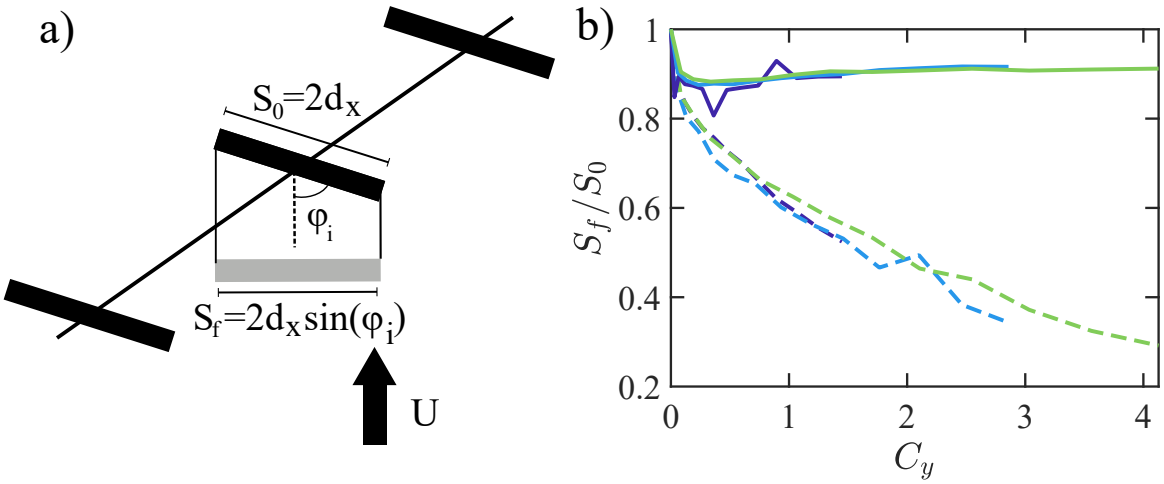

Figure 5.8: a) φ_i angle defines the orientation of the i-th blade relative to the flow and allows the definition of the frontal surface highlighted with a grey rectangle. b) Frontal area evolution of the three bipolar kirigami sheets of Fig5.7 against Cauchy number

An interesting indicator of such consideration may be given by the frontal area of the whole kirigami S_f. This surface is the one relative to the incoming flow and is obtained by summing up the contribution of each tilted cell. In practice we project the length of each cell relative to the flow direction, through the angle φ as indicated by the gray rectangle on Fig5.8a, such as the total frontal area is defined :

$$\frac{S_f}{S_0} = \sum_{i=1}^{N} \sin(\varphi_i) \tag{5.4}$$

Where the index i corresponds to the i-th elementary blade-like cells. The evolution of the projected surface, for the three previous bipolar patterns, normalized by the surface in the absence of deformation S_0 as a function of the velocity C_y is plotted in Fig 5.8b.

At first glance, the frontal areas of different stiffness patterns also collapse onto singles trends according to their polarity state. In fact, the parabolic $\boxed{-+}$ case stays almost constant with values of S_f close to S_0, ($S/S_0 \sim 0.9$) whereas the $\boxed{+-}$ configuration exhibits a decay by almost 70 % at high flow speed for the softest specimen. Indeed the lower the stiffness the higher the deformations hence the lower surface relative to the flow.

Comparing the differences in frontal areas to those in drag forces (Fig5.7c) between two polarity states shows that surface reduction alone does not explain the distinct trends in load. Other factors must be considered to understand why such large differences in areas lead to small gaps in fluid forces. However, we note that the trends are well respected with the highest surface area for the polarity that experiences the stronger forces (i.e. $\boxed{-+}$ case).

Interlude n^o17: Symmetric shapes induce lift force ?

The bipolar specimen at $a = 0.5$ expend in a lobe that points to the center of the channel; the two portions of the kirigami sheet are therefore similarly stretched. So one can wonder: what is the result of the transverse lift forces of such a morphology? Using the theoretical formulation of the lift presented in interlude ^{o}17, we deduce the evolution of $\tilde{L}_i = L/K_2L$ for the symmetrical bipolar case ($a = 0.5$) reported in the graph below (in which we add the lift of uni-polar cases)

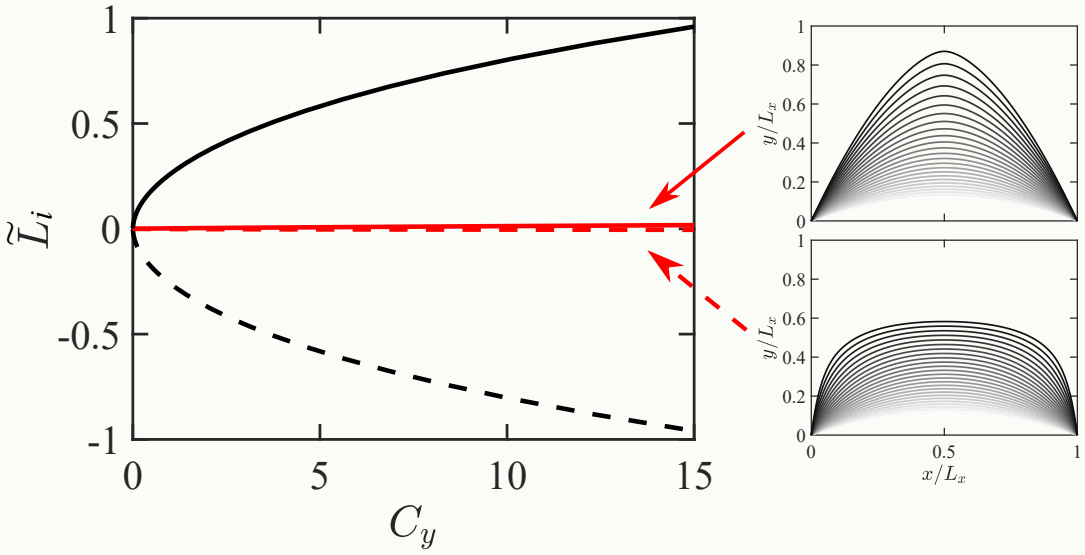

As expected the symmetrical shape experiences no global lift forces which implies a strong interplay between shapes and fluid forces. By tuning morphology we can adjust force as well and even cancel lift load.

Drag for varying a (fixed stiffness)

This first campaign on the three bipolar specimens of different stiffness has highlighted that the polarity state plays a role in the drag law by splitting the trend according to the flow orientation. In chapter 2 experiments also showed that varying ($a \in [0, 1]$) changed the overall shape, particularly the localization of the lobe, from a symmetrical form at $a = 0.5$ to an asymmetrical one when a is close to 0 or 1 (unipolar case). We finally pointed out that the two configurations $\boxed{-+}$ and $\boxed{+-}$ were not equivalent in their deformation shapes for a given a (compare Fig5.9b and d), so we can expect a difference drag force as well.

Ch. 5

In order to investigate the mixing effect of a and polarity selection, we measure the drag on six specimens with the same effective stiffness $K_2 \sim 3.9$ N/m and a evolving between 0.18 and 0.5 (see chapter 2 for more details). As for the previous measurements, both configurations have been tested, and the set of results are reported in Fig5.9a, as a function of the Cauchy number.

The data is separated into two groups of curves based on the configuration distinction outlined earlier: the $\boxed{-+}$ case (represented by circle markers) shows almost linear drag growth, while the $\boxed{+-}$ configuration (represented by square markers) results in forces plateauing for high C_y. No noticeable order appears in the a value for each curve group. Let's examine what theory predicts.

Fig5.9c presents theoretical drag force results for a values identical to those tested experimentally. It confirms the idea that different configurations produce different drag laws. A solid red line highlights the unipolar case ($a = 0$ or 1) and separates the two sets of

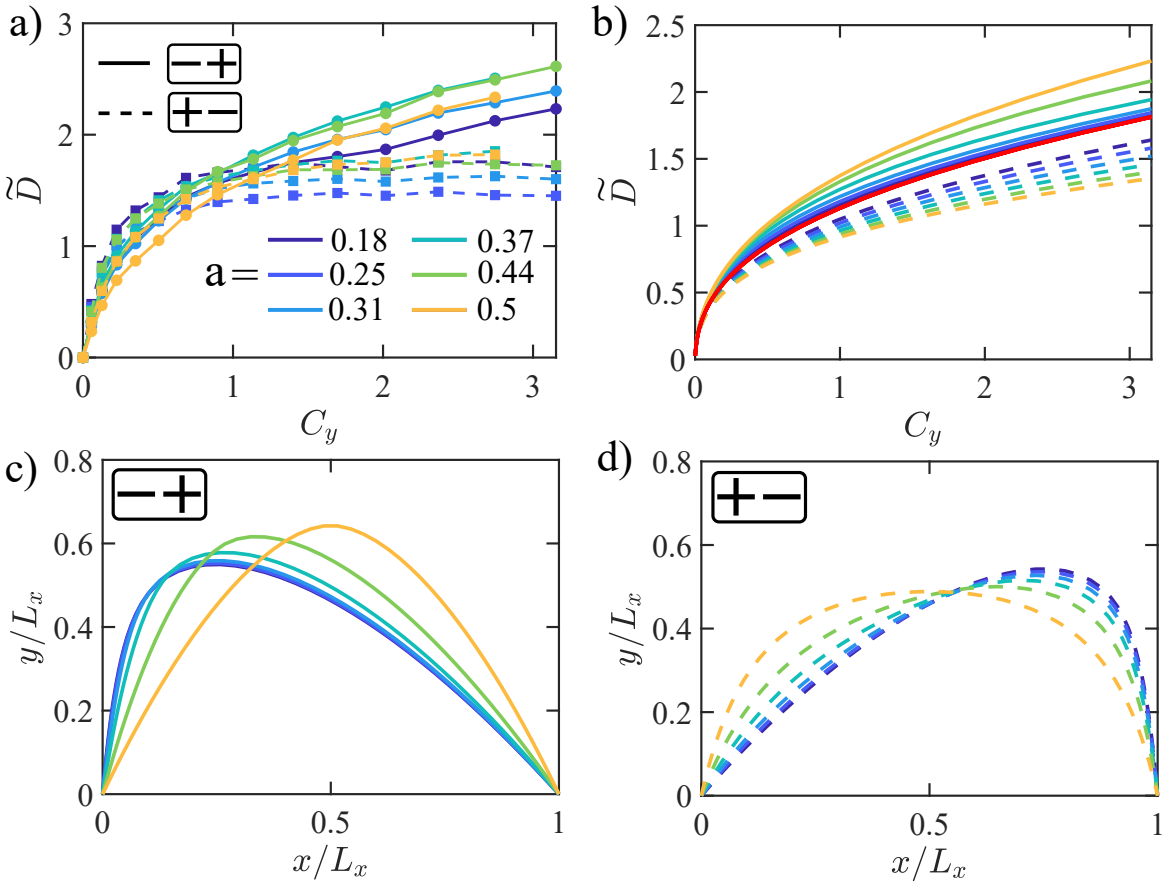

Figure 5.9: a) Dimensionless drag force as a function of Cauchy number for varying a (polarity transition localization), line style is associated to polarity state and color to a value. b) Theoretical predictions for drag force experienced by kirigami sheets whit the same a value as experiments and compare to the uniform solution (red curve). c) and d) Typical profiles for the six different specimens at $C_y \sim 3$, both configurations are reported (from theory).

curves. Changing the a value affects the force intensity and moves the curves within their sets, but all curves follow an order according to a. Values close to 0 (e.g. $a = 0.18$) have drag forces that approach the unipolar solution, while symmetrical forms (e.g. $a = 0.5$) majorize/minorize the drag of each set. The dispersion in our measurements (Fig5.9a), may be due to slight differences in stiffness between the specimens (see the section on elasticity in chapter 2).

The measurement of drag on bipolar non-uniform cases opens the way to a wider variety of behaviors. Indeed, the absence of collapse when normalizing by stiffness and Cauchy indicates that this parameter does not capture all the underlying mechanisms. This observation is a consequence of variations in shapes presented in chapter 2: a bipolar kirigami sheet has two dissimilar deformation profiles depending on the polarity relative to the flow, in the same way, two different drag evolutions are noticed. By playing on the local inclination of the cells it is then possible to reduce or increase the drag of a kirigami according to the configuration, in addition to making its profile symmetrical.

After having investigated the fluid loading of non-uniform polarity, let us move on to the case of the specimens of heterogeneous stiffness.

5.4.2 Bizonal case: two stiffnesses lead to two drag evolutions

Chapter 3 presents the effect of the deformation of adding a stiffer portion within the pattern. We have shown that playing on the size of this portion $(1 - a)L$, its stiffness with

respect to the soft part (parameter b) and the polarity relative to the flow influence the kinematics of expansion of the bi-zonal kirigami sheets. Indeed each polarity state imposes the opening of the respective soft for ⊕ and stiff part for ⊖, which induce notable changes in the morphology according to the chosen polarity (direction of rotation of the elementary cells). The opening kinematic requires greater efforts for the rigid portion, the shapes then differ for a given flow speed. As in the bipolar cases, a bi-zonal kirigami then exhibits two associated shapes for the same pattern. Thus, after having shown that the addition of a simple rigid portion opens a range of new morphologies and behaviors, let us investigate its impact on the drag force law.

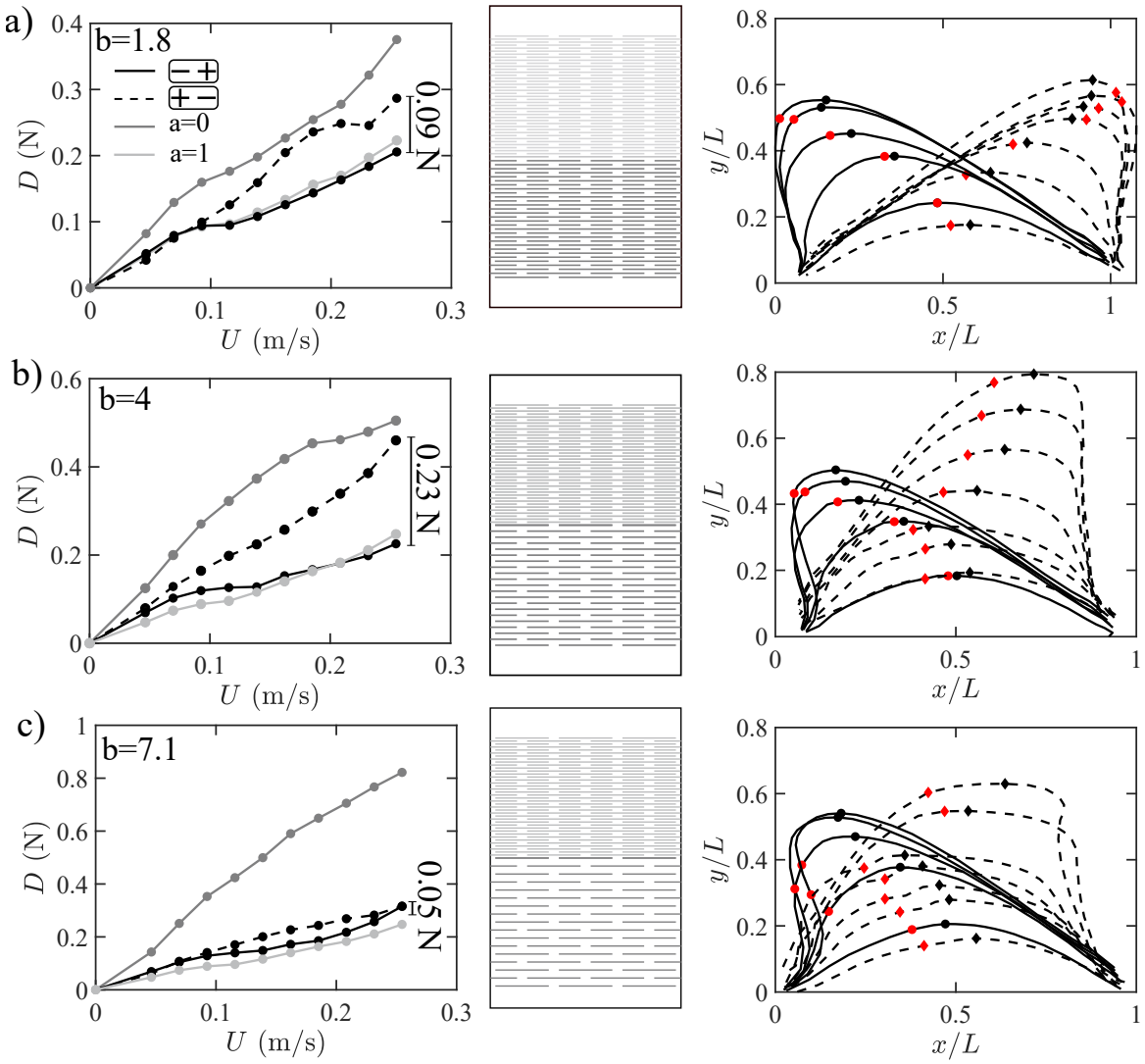

Figure 5.10: Drag forces evolution against fluid velocity for both polarity states (line styles) of the following specimen (all with $a = 0.5$): a) $b = 1.8$ b) $b = 4$ c) $b = 7.1$. For comparison, the dark grey curve corresponds to $a = 0$ case (full stiff pattern) and the light one to $a = 1$ (full soft). For each graph, the cutting pattern is recalled with the rigid part on the bottom half, characterized by wider cells. Their respective expansion pathways are also reported, with red markers to localize the transition.

In order to present the main features of the bi-zonal kirigami tessellations, only three specimens will be discussed in this section. To examine the effect of stiffness ratio (b), a was fixed at 0.5 so each portion covers half of the sheet. Fig5.10 shows the graphs of drag force vs. flow speed for each b, with their respective cutting patterns and expanding pathways in flow. The forces and shapes for the bizonal patterns are plotted as black curves with differ-

ent line styles for the polarity states. For comparison, the case of $a = 1$ (soft specimen) is represented in light grey and $a = 0$ (stiff specimen) in dark.

Our observation shows that in all bi-zonal cases, the drag force falls between the values for soft and stiff specimens. For all patterns, the polarity $\ominus$, which induces the opening of the soft part, experiences drag forces close to the fully soft one (light grey curve). This portion of the sheet actually drives both deformation kinematics with similarity on shapes (an important result of chapter 3) and global fluid loads, whatever the stiffness of the second half!

Flipping the pattern (inverting polarity) shows that the $\oplus$ configuration has a different drag response and heavily depends on the b value. With a low ratio, $b = 1.8$ (seen in Fig5.10a), both configurations have a similar drag with a maximum difference of about 0.09N at high flow velocities. The deformation profiles (dashed lines) show symmetrical pathways with those of the $\ominus$ state. Hence the ratio value is not enough important to induce a large difference, let us increase this value.

Fig5.10b presents the $b = 4$ case, which demonstrates significant differences in drag and shape changes between the two polarities. The profiles are symmetrical and correspond to high fluid loads. The last graph shows that the highest tested ratio ($b = 7.1$) results in similar drag evolution (see Fig5.10c), with a close expansion in flow. In this case, the stiff part remains close for both polarities, and only the soft part expands, explaining the similarities in shape and load.

Our experiments have shown that similar shapes result in similar drag forces when using our reasoning on shape-drag links. The response in loads is tightly connected to the flow expansion and must be evaluated individually based on the values of a and b. So keep just in mind that such interplay allows an original lever to tune flow response both in shapes and now in drag forces.

5.5 Conclusion

A deformable system placed in a fluid modifies and adapts its shape according to flow speed and effective structural elasticity. This shape-shifting process is accompanied by an evolution of the fluid forces which depend on the deformation kinematics. In this chapter, we have completed the morphological studies developed in part 1 of the manuscript by measuring and modeling the evolution of the drag force of our homogeneous, bi-polar and bi-zonal kirigami sheets.

We first established a close link between mechanical stiffness, deformation and drag. Thus a uniform and stiff specimen will be less deformed than a soft one for a given speed and will experience higher global drag forces. This behavior is a reminder of the competition between the external fluid forces which tend to expand the structure and the internal elastic restoring forces. As for the amplitude of expansion in flow, the introduction of the Cauchy number and the normalization by the stiffness allows the collapse of the drag law, thus showing the universal character of this competition, which then drives both results in shapes and forces.

However, things become more complicated when heterogeneity is introduced into the cutting tessellation. The bipolar case shows that the variation of stiffness for the symmetrical shape induces two different laws in force evolution, the notion of polarity relative to the fluid becoming relevant. Thus, a type of morphology gives a trend in drag and so on. This link between shapes and forces is exacerbated when we look at the response of the bi-zonal cases where the difference in force can reach a factor of 2 for the same specimen depending on the side exposed to the fluid. Thus our kirigami sheets pave the way to the development of smart sails or nets that could adapt both their forms and forces depending on flow intensity and direction.

6

Origami folding sets an upper limit on drag

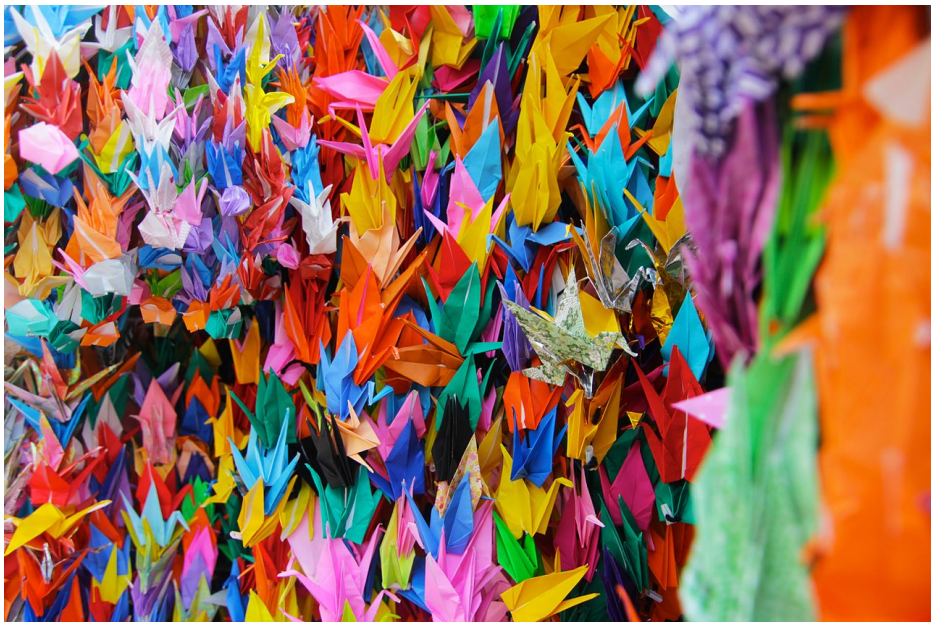

Figure 6.1: "One thousand origami cranes", is a Japanese legend, which tales if a person folds 1000 origami cranes, gods will grant one wish...

In this last chapter, we present a new type of meta-structures based on origami methods. The presence of folds in a structure localizes the deformations and induces large changes in shape once placed in flows. These morphological variations lead to new drag laws depending on the crease pattern. We will see how and why the presence of creases allows an important reconfiguration process of the structure and involves a surprising saturation in drag, with a non-dependence on surrounding flow velocity. These experiments are finally compared to a theoretical model based on real geometry and the underlying physical phenomena are explained using a simplified model.

6.1 Introduction

As illustrated in the general introduction and at the beginning of the previous chapter, the shape-shifting of a flexible system subjected to a flow modifies the forces exerted on it. This mechanism is known as the reconfiguration process, in the sense that the deformable structure changes its configuration according to the velocity and direction of the incoming flow. This phenomenon also deeply impacts the fluid forces exerted on the structure and induces the reduction of drag. The origins of this process come from a combined effect of reduction of the frontal surface, and streamlining induced by the deformation [16, 7].

6.1.1 Origami in science - a quick reminder

The studies cited in the general introduction, concern mainly deformations by bending. The latter is isometric and imposes shape and drag law limitations. Our idea is therefore to access the new deformation mode and gain control of the reconfiguration process. The previous chapter provided a first insight into the force response of an architectured structure in flows. We highlighted that the drag reduction process was modulated by the effective stiffness of the kirigami pattern and that a non-uniform sheet led to different fluid force evolution depending on the flow direction. It is high time to put the kirigami aside, after five chapters on the art of cut paper, let us deal with the art of folding: origami.

A fancy way to overcome this shape limitation and induce larger deformation and more generally to program shape morphing is to localize the deformation along a pattern on flat material, which is the hallmark of origami technique.

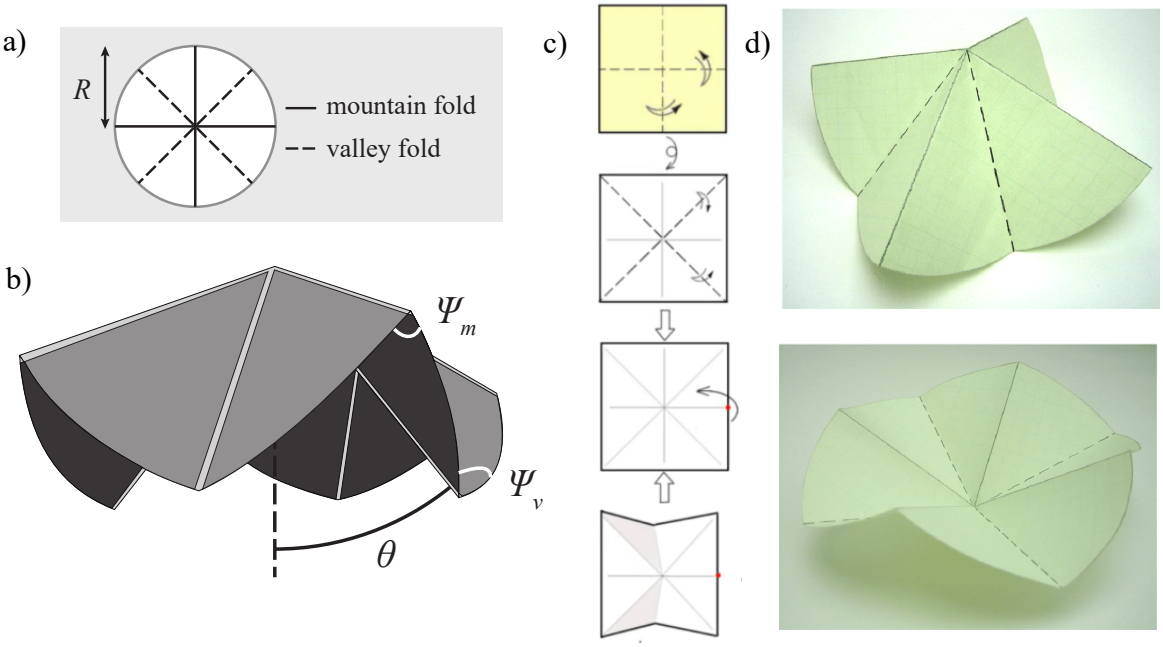

Figure 6.2: a) Waterbomb crease pattern with $N = 8$ folds on a disk with radius R. b) Folded state characterized by the opening angle θ between a valley fold and the central axis passing through the vertex. The angles of mountain and valley folds, Ψ_m and Ψ_v, respectively, are derived from the chosen parameter θ for this single degree-of-freedom mechanism. c) Folding instruction to obtain the origami water-bomb cell from a flat sheet. d) Waterbomb unit in its two stable states, from [88].

The elementary principle of this Japanese art is to affix a creases tessellation on a sheet. Each fold is defined along a direction called a valley or mountain according to the angle sign. More concretely adding such folds on a plane condition the 3D configuration reaches once folded can allow large and quick changes in shape from the initial flat end to expand the state to a fully compact one.

As previously illustrated in the main introduction, folded structures are already widely used in the engineering field. The presence of folds in a structure allows it to exhibit new and programmable mechanical and geometrical properties [89, 90].

However, to our knowledge, the mechanical response to a flowing fluid has been little explored, to the exception of two recent studies on the tumbling of an origami unit and a crumpled sheet in a viscous shear flow [91, 92]. So let us pave that way!

6.1.2 Umbrella-origami

Origami folding offers nearly limitless possibilities for pattern creation, each with its own unique characteristics that must comply with mathematical principles to maintain face rigidity [24]. Our aim is to find a simple pattern for flow experiments and theoretical modeling, while still allowing enough shape transformations to compare with traditional continuous cases. We chose the well-known waterbomb base, a basic origami unit that serves as a building block for more intricate designs, previously used for self-deploying medical stents [93, 94].

The waterbomb base is an origami cell characterized by its umbrella shape and its bi-stable property (see Fig 6.2b and d). Before going any further, I recommend the reader to use his/her manual skills and fold the sheet of paper attached to the manuscript following the steps indicated in Fig 6.2c. The crease pattern, shown in Fig6.2a, consists of a disk of radius R patterned with an even number N of creases, radiating from a central vertex and separated by equal sector angles. It folds into an alternation of mountain and valley folds, which form $N/2$ lobes.

This origami unit is also known for its large shape changes with well-characterized kinematics that has the particularity of having a single degree of freedom. Note that it is the case only if all origami faces are rigid (see next section) and if the folding is symmetric, meaning that all lobes close in the same way. Each crease is characterized by its angle Ψ_m or Ψ_v, for mountain or valley type respectively. Based on previous kinematics studies [88, 95, 96], we choose to describe the whole folded state using the opening angle θ as the single degree of freedom, which is the angle between a valley fold and the central axis passing through the vertex as shown in Fig6.2b. As θ goes from 0^o to 90^o, the units morph from a flat disk to a very compact configuration. This large shape change is likely to have a significant impact on the fluid forces acting on the structure.

Note that a simple manipulation of the unit (do it !) exhibits the existence of the two equilibrium configurations. This property is not at the heart of our studies but will be the subject of the last section of the chapter as a future opening.

Before placing this cell in an airflow, we are going to discuss the mechanical properties of our folded structure.

6.2 Mechanics behind folds

6.2.1 Creases everywhere, even in the trash

The presence of folds in a flat structure is the signature of origami art but folds commonly form in thin sheets that undergo large deformations. Fig6.3 shows the example of a crumpled sheet: when compacting an initial flat piece of paper into a ball, a set of creases appears. Several studies [97, 98, 59] interpret the physical origin of such folds and their statistics through arguments based on the balance between bending and compression energy, forming singularities along lines: the folds (See Fig 6.3b).

From this view, an unfolded crumpled paper sheet becomes a kind of origami with a random crease pattern. The formation of folds in a thin sheet thus proceeds from localization of

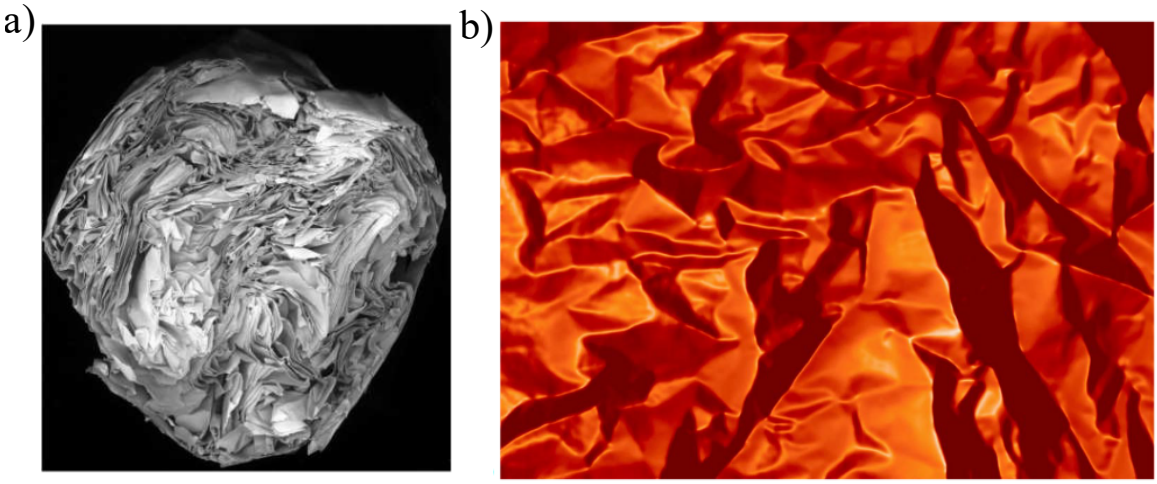

Figure 6.3: a) Cross section of a paper dumpling, the compression of the sheet leads to the presence of folds, whose distribution follows a random pattern as shown in b). From [99, 100]

the deformations, to gain control of the latter and to study experimentally their mechanical behavior let us investigate a simplified case of inflexible facets.

6.2.2 Rigid face hypothesis

As presented in the introductory part, one interest of origami is the ability to control the deformation kinematics through simple geometrical arguments. However, this programmable property is better achieved if the deformation is localized along the folds, while facets remain rigid. The flat facets than simply rotate around the flexible creases.

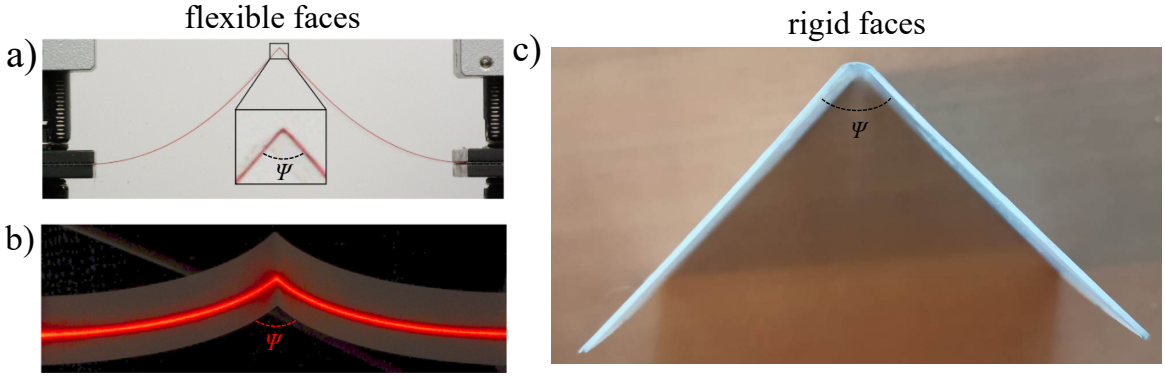

Figure 6.4: a) Example of a fold with flexible facets (from [101]). b) laser line on flexible facets, the fold is localized through the sharp angle (from [96]). c) Flexible and thin Mylar sheet makes the link between two rigid and thick panels, this fold was made using the manufacturing process described below.

This "rigid facet approximation" [89, 96] greatly simplifies the kinematic and mechanical description. Each of the folds is then fully characterized by a single opening angle Ψ, and its mechanical response can be modeled as two rigid panels (facets) connected by an elastic hinge (crease). Note that this approximation can be related to a length comparison, when the size of the facets is smaller than the characteristic "origami length" as detailed in the interlude n^o18.

Figure 6.4 shows two typical modes of deformation. Figs 6.4a and b are made from a single sheet of thin Mylar, deformation under traction opens the folds and causes bending of the faces. The deformation affects the entire system {fold + faces}. While in Fig 6.4c, faces are

made with a thicker Mylar sheet which ensures their height bending rigidity and deformation will only occur at the crease. Let us now describe our manufacturing method.

Interlude n^o18: Origami length and deformation modes

In their article [96], the authors study the mechanical behavior of a single crease made of a homogeneous Mylar sheet. They define a characteristic length (called origami length) L^* which compares the fold stiffness κ and the bending stiffness of the facets B :

$$L^* = \frac{B}{\kappa W}$$

One can therefore distinguish two regimes: if the facet length is larger than the origami one $L > L^*$ then the flexibility of the facets drives the deformation, conversely, if $L < L^*$ the facets can be considered as undeformable, and the fold is like a torsional spring connecting two rigid panels.
In this study, we want to fall in the second case, by increasing the facet thickness ($350\mu m$, while the creases are around $65\mu m$ on average, see manufacturing section). We thus obtain a large bending rigidity $B \sim 0.0278N.m^2$ for faces in comparison with the fold stiffness $\kappa \sim 0.03N$. In our case, the origami length is thus around $L^* \sim 0.93m$. Given the size of our systems (around $0.07m$ for the larger specimens), the "rigid facet approximation" is thus ensured for our experiments.

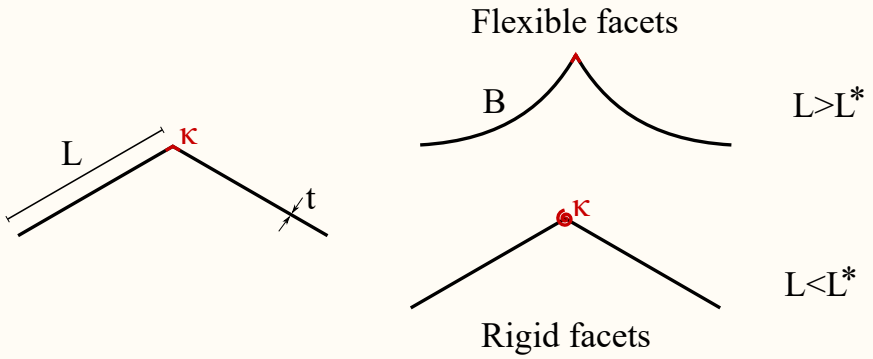

6.2.3 Manufacturing process: overlaying Mylar sheets

The objective of our manufacturing method is to produce origami specimens with rigid facets and deformation localized at the folds. To that end, we overlay two sheets of PET Mylar of different thicknesses (see Fig 6.5a). This thermoplastic material has already been used in several studies to build folded structures [102, 103, 104], and it is the same material that we used to fabricate our kirigami sheets. We first laser-cut a thick $350\mu m$ sheet that is previously covered with double-sided tape. This first layer will constitute the facets, and it is then affixed to the thinner sheet that will form the folds. To ensure precise positioning of the facets, the latter are connected to each other through an outer ring, which is removed post-assembly. Facets are separated by a 2.5 mm spacing, which delineates the flexural hinge that will act as a fold through bending (see Fig6.5b for the typical thickness of the different layers).

The flat specimen is then folded manually into an alternation of mountain and valley folds. An important step remains: how to prescribe the rest configuration? That is the state in the absence of mechanical loading. Inspired by previous work [104], we use the thermoplastic property of Mylar to set it through annealing. In the latter study, they shaped folds with a specific angle by heating PET thermoplastic sheets in a mold and then cooling it down. This protocol was shown to produce folds with a reversible mechanical response, returning to the same assigned reference configuration once the loading is removed. In line with this

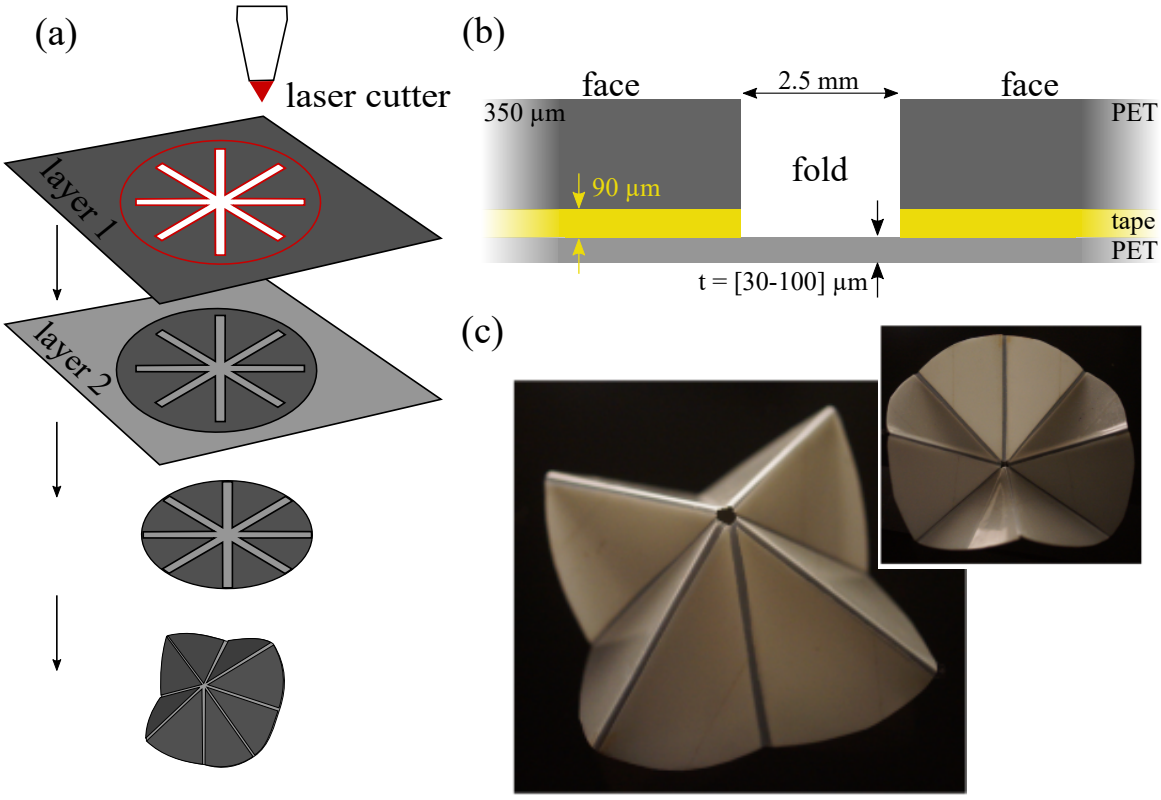

Figure 6.5: a) Cells are fabricated through the layering of a thick and thin Mylar sheet (attached with double-sided tape), forming stiff facets and flexible creases. The flat structure is then hand-folded to the desired extent and placed in an oven to set its rest configuration through annealing. b) Fold layering details. c) Example of an origami specimen, in its two stable rest configurations.

technique, our origami units are fastened in the desired rest configuration, placed in an oven at a temperature of $75°C$ for one hour, and then left to cool down at room temperature for an hour. This temperature is chosen around the glass transition temperature of PET (around $70-80°C$), but below the maximum operating temperature of the double-sided tape ($80°C$) to prevent facets from unsticking. We thus impose the rest configuration, which is characterized by the initial opening angle θ_0 (see Fig 6.5c) with an accuracy of $\pm 2^o$.

The layering method enables rigid facets and concentrates deformation on folds. We therefore adjust fold rigidity by varying Mylar sheet thickness for creases, in our study four thicknesses have been investigated: $30, 48, 75$ and 100 μm, which we are going to mechanically characterize below.

6.2.4 Crease stiffness measurements

In this section, we characterize the mechanical properties by probing the response of a single fold, manufactured using the protocol described above.

As discussed earlier, in the "rigid facet approximation", folds can be regarded as a torsional hinge that connects two unbending panels [96]. This hinge is characterized by a torsional stiffness κ that relates the applied torque T to the resulting angular deflection relative to the rest position $\Psi - \Psi_0$. We have: $T = \kappa W(\Psi - \Psi_0)$, with $W = 4cm$ (here) the crease width.

We measure the evolution of the crease opening angle as we apply an increasing pulling force to the center of one square facet, while the other is attached to a vertical support (see Fig6.6a). In practice, the force is applied by adding weights of controlled mass M in a bag attached to a string at the center of the free face. The torque T is evaluated from the fold

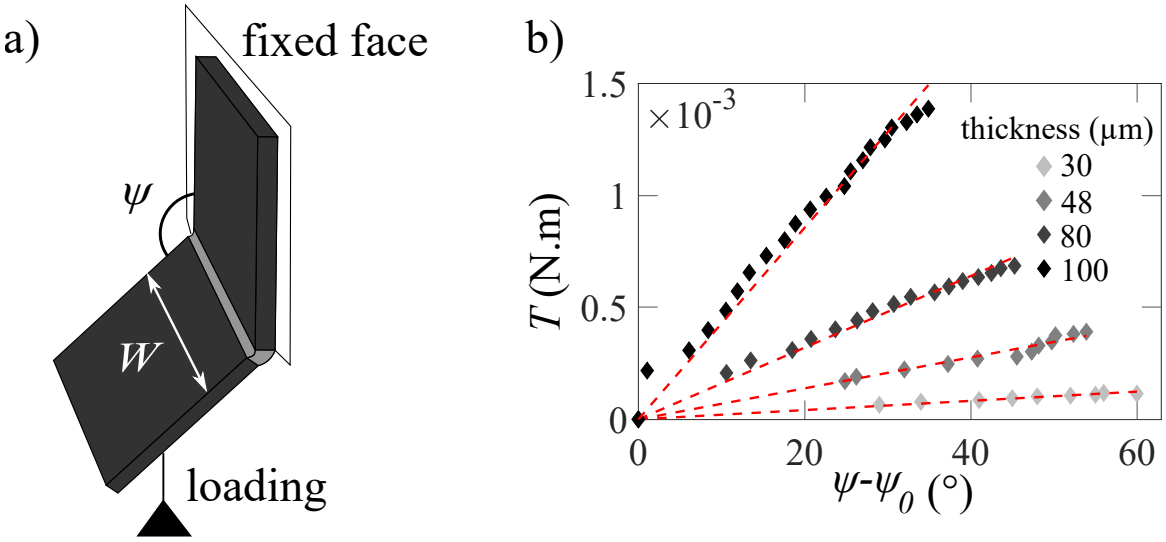

Figure 6.6: a) Experimental set-up to measure the crease stiffness. b) Applied torque T as a function of the angular deflection relative to the rest angle $\Psi - \Psi_0$ for folds made with flexible sheets of variable thickness and $\Psi_0 = 100^o$.

opening angle and the lever arm between the rotation axis and the point of application of the force $T = Mg(W/2)\sin\Psi$. The mass of the hanging facet is taken into account in the expression of the total mass M.

Results are shown in Fig6.6b for samples made of flexible sheets with different thicknesses t and similar rest angle $\Psi_0 \sim 100^o$. Folds exhibit a linear relationship between the torque T and the angle deflection $\Psi - \Psi_0$, over a range of 60^o. Similar to those attained in wind flow experiments for our waterbomb origami unit. Linear fits yield the following values for the crease stiffness (red dash lines):

thickness t (μm)	30	48	80	100
stiffness κ ($.10^{-3}$N)	3.0	9.9	21.3	61.3

The relationship between the thickness of the Mylar sheets used for the folds and the torsional stiffness is further illustrated in Fig 6.7b. From this plot, one obtains a power law $\kappa \propto t^{2.3}$ that is consistent with the scaling laws reported in the literature. Indeed, two different fold stiffness laws have been observed depending on the crease manufacturing method: a sharp crease angle induced by plastic deformation in a single thin Mylar sheet (see Fig6.4a and b) leads to a quadratic dependence $\kappa \propto t^2$, [96, 105]. While a fold formed by a flat flexible plate as described in Hanna et al. [88, 95] gives $\kappa \propto t^3$. Our power law gives an intermediate value between those expected by the scalings, which indicates that the mechanical response of our folds lies in between that of a highly localized crease and of a flexural pivot. A deeper discussion is proposed in the interlude n^o19.

To evaluate the impact of the initial opening Ψ_0 on the fold stiffness, we performed measurements on four folds with the same sheet thickness ($t = 80\mu m$) and different Ψ_0 values. The collapse of the load-deflection curves in Fig 6.7a shows that κ depends primarily on the constitutive flexible sheet and its thickness, and little on the rest angle. To further assess the variability of mechanical properties, we performed measurements on twelve independent folds with identical parameters ($t = 80\mu m$, $\Psi_0 = 90^o$). It shows good repeatability (consistently with Fig 6.7a), with a standard deviation of $0.3.10^{-3}$ N.

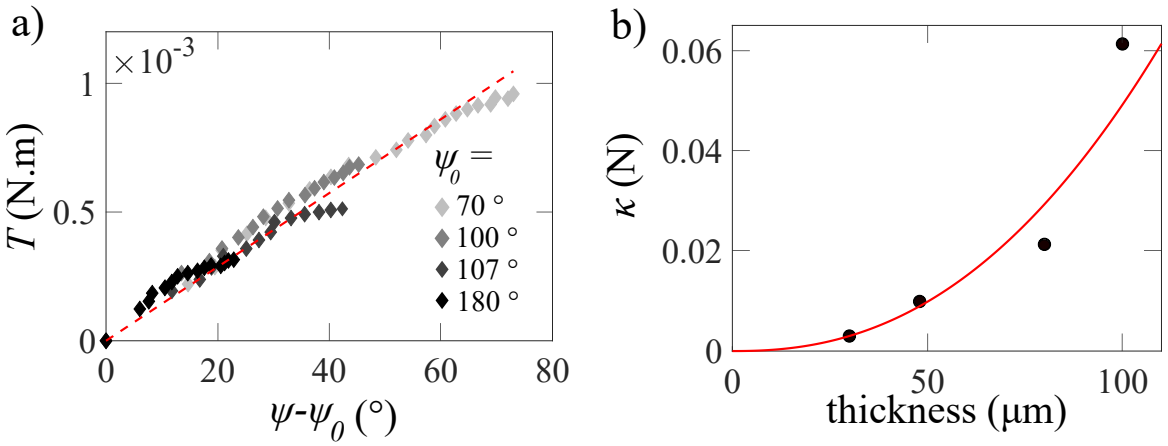

Figure 6.7: a) Torque as a function of the angular deflection for folds with different rest angles Ψ_0 and the same sheet thickness $t = 80$ μm. b) Crease stiffness κ as a function of the sheet thickness t, fitted by a power law (red line) yielding $\kappa \propto t^{2.3}$.

Interlude n^o19: Relationships between the fold stiffness and the sheet thickness

The relationship between the crease stiffness and the thickness of its constitutive sheet depends on the fabrication process of the fold. There are two types of folds: marked folds (sharp angle) made through crushing or molding [96, 105]. The elastic energy of a crease E_{el} is then associated to bending within a region of length W and width t with curvature $1/t$ (see schematics a), and scales as $E_{el} \propto BtW/t^2$ with B the sheet bending rigidity that varies as t^3. It thus yields a t^2 dependency for the crease elastic energy, and hence for its stiffness (since $E_{el} = 1/2\kappa W(\Psi - \Psi_0)^2$).
While the second type of fold is a flexural joint made of a flat plate without a crease that connects two rigid facets (see photo b adapted from [88, 95]). The elastic energy of deformation will come from the plate bending, then $E_{el.} \propto t^3$ and so does the crease stiffness.

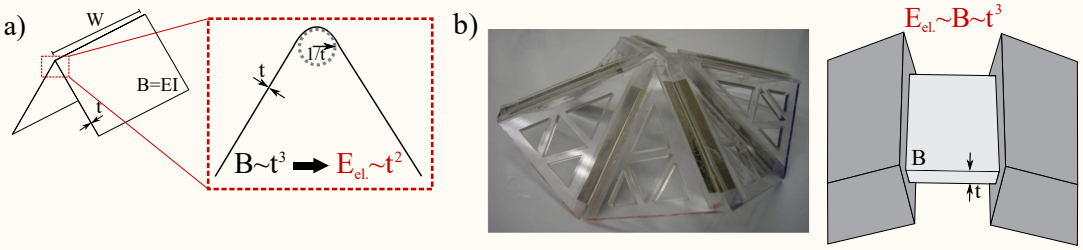

6.3 Origami in the wind

We manufactured and tested thirteen waterbomb specimens. We systematically varied the radius $R = 4-7$ cm, fold stiffness $\kappa = 3-60\times10^{-3}$N (by changing the Mylar sheet thickness as described above), the angle of the rest configuration $\theta_0 = 14-57^o$ and the number of folds $N = 6-12$. Each parameter has been varied independently while fixing the other ones. All those series share one specimen serving as a reference, with intermediate parameter values: $R = 5$cm, $\kappa = 9.9 \times 10^{-3}$N, $\theta = 32^o$ and $N = 8$.

6.3.1 Exprimental set-up

We characterize the response of the origami units in a flow following the protocol described in the following. Structures are subjected to a controlled uniform air flow generated by an

open jet wind tunnel with a square test section of $40 \times 40cm^2$, and a flow velocity that is varied gradually within $U = 1 - 19$ m/s and calibrated with a Pitot tube. The origami cell is attached at its vertex to an upstream elbow and held at the center of the channel with its convex side facing the incoming flow (Fig.6.8a). We take particular care to ensure that the fastening system does not prevent the folding of our origami unit. The mount is connected to a six-component force balance that measures the drag of the specimen F_d. The drag on the support alone is measured and subtracted from the data (as for kirigami and frame drag forces in chapter 5).

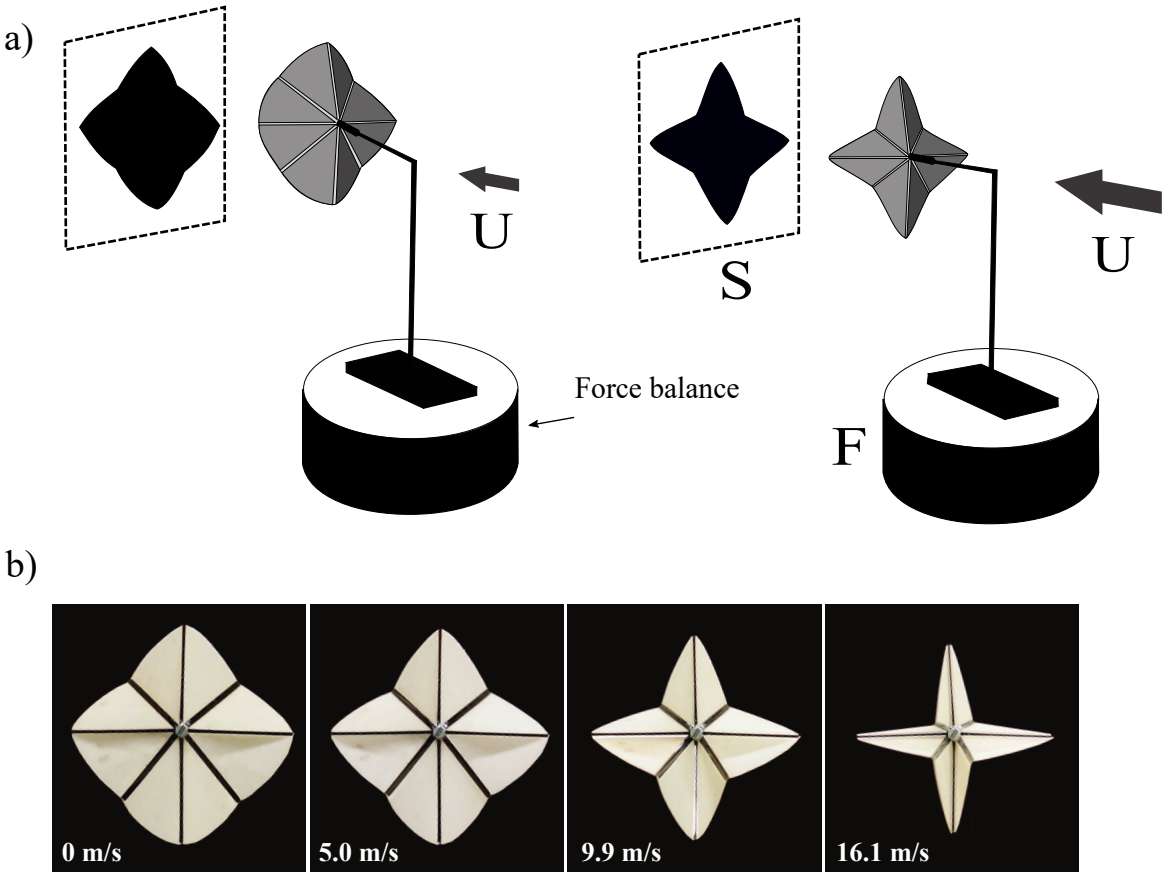

Figure 6.8: a) An experimental system with the origami cell held in an incoming uniform air flow with speed U. The drag force F_d is measured by a force balance, while simultaneously extracting the frontal area S to quantify shape changes. b) Typical reconfiguration experiment in a flow of increasing speed, for a specimen with $N = 8$, $R = 5$ cm, fold stiffness $\kappa = 9.9.10^{-3}$ N, and rest angle $\theta_0 = 32^o$.

The shape changes induced by the flow are quantified using the cell frontal area S, which is the one projected in the plane perpendicular to the flow. It is imaged by a camera placed downflow of the set-up and extracted through Matlab custom image analysis. As shown in Fig6.8b, the cell deforms symmetrically and the folding kinematics is thus consistent with the 1-DOF mechanism discussed earlier and details in the following section. The full shape of the cell can then be inferred from the S area metrics, which will be used to characterize its degree of closure. The geometrical relationship between S and θ will be explicitly derived in the theoretical section later.

6.3.2 Behavior of a typical origami cell

Fig6.8b presents a typical experiment for an eight-creased specimen. In the absence of flow ($U = 0$ m/s), the cell is in its reference configuration. Flow loading then induces a nearly symmetrical closing of the four lobes, which is all the more pronounced as the velocity U

is increased. The corresponding frontal area is reported as a function of the incoming flow in Fig 6.9a. Fluid loading induces a significant shape reconfiguration, with a decrease of the frontal area with U, around 60-70% compared to the unloaded reference state S_0. Note however that the fastening system does not allow for a complete cell closure.

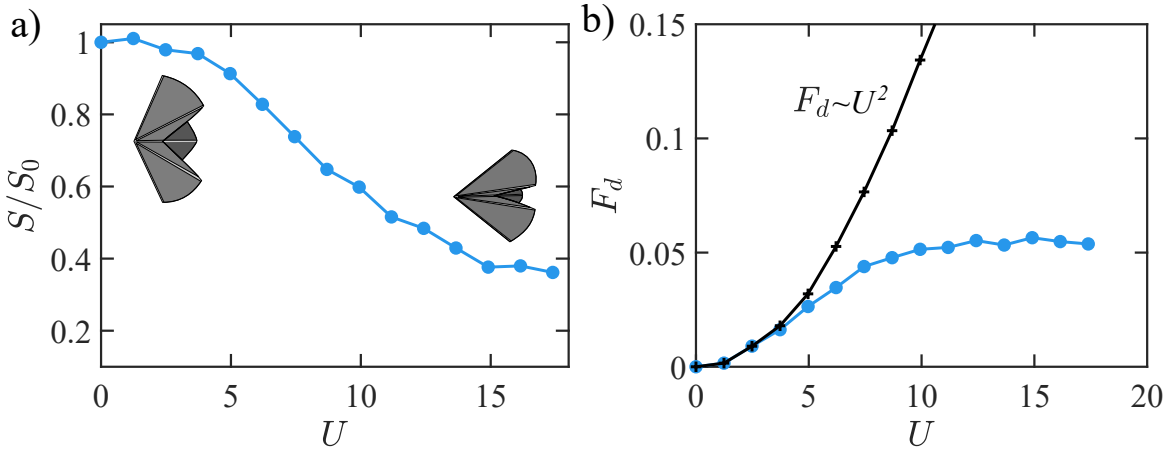

Figure 6.9: Evolution as a function of the free-stream velocity U of a) the cell frontal area S relative to the area at rest S_0 , and b) the drag force F_d. The cell parameters are: $N = 8$, rest angle $\theta_0 = 32^o$, radius $R = 5$cm, and fold stiffness $\kappa = 9.9.10^{-3}$ N. The drag on the equivalent rigid origami cell (i.e. with the same geometry) is reported by a black line for comparison.

This large shape variation and the reduction of the frontal surface significantly impact the drag on the structure. As illustrated in Fig 6.9b, it allows the cell to drastically reduce the load it has to sustain, compared to the drag it experiences when frozen in its reference state (black curve).

While the rigid unit exhibits a classical U^2 quadratic bluff body behavior, F_d increases more slowly for its flexible counterpart and reaches an upper limit at higher flow velocities, where it ceases to depend on U. Drag reduction is commonly observed for flexible structures deforming in flows, but such cancellation of the velocity dependence for F_d has rarely been reported. We can quote the exception of the flexible ribbon weighted at its end by [106], which also features such drag evolution at high flow speed.

Large shape reconfiguration thus has a significant impact on drag which plateaus at high flow speed, despite increasing U. Let us now change the fold stiffness and cell size in the following sub-section.

6.4 Stiffness and size: hello Cauchy my old friend

One can guess that changing size and elastic properties should impact both the deformation and drag force on origami units. To investigate these two parameters, we performed experiments with four different cell radii (solid lines) and fold stiffness (dash lines). All the results are reported in Fig 6.10, where markers differentiate specimens with varying crease stiffness κ (and the same radius), while the color gradient denotes the radius R (for the same κ). Here, the number of folds is kept constant at $N = 8$, as well as the rest opening angle $\theta_0 = 32^o$.

Let us first have a look at size effects. At low velocities, we observe that larger waterbomb units experience stronger drag, which is expected given their greater area exposed to flow. However, the four various-sized cells reach the same constant F_d at higher flow velocities, thus resulting in speed- and size-independent drag.

Regarding the fold stiffness, κ affects the degree of structure closing in the flow, with less area shrinkage for the most rigid specimens (see Fig6.10b). As a result, the latter exhibit

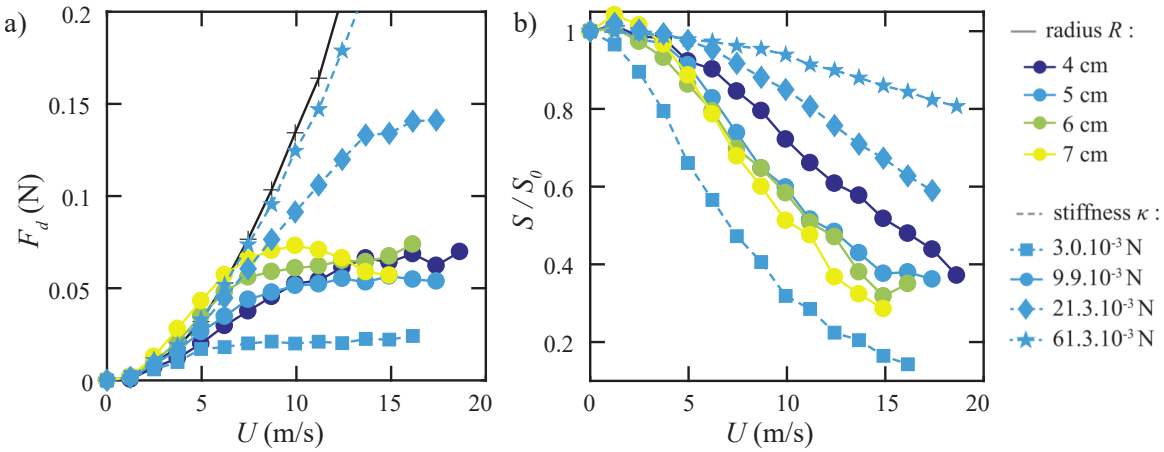

Figure 6.10: Evolution as a function of the free-stream velocity U of a) the drag force F_d. Cells share the same $N = 8$, and rest angle $\theta_0 = 32^o$. The same rigid specimen than Fig 6.9 is reported for comparison, and b) the cell frontal area S relative to its area at rest S_0.

a higher drag. Fig6.10a shows that drag eventually flattens for all cells but for a value and past a critical speed that both depend on κ. Indeed the plateau behavior is reached at $U = 15$m/s for a stiff cell ($\kappa = 21.3 \times 10^{-3} N$), while the softest one starts experiencing a constant drag force around $U = 5$m/s. The interlude n^o20 discusses the flow regimes occurring in our experiments, we especially prove that despite the large deformations the inertial regime can be always considered.

Those trends reflect the competition between the fluid loading and the elastic restoring force that underlies the structural reconfiguration. In line with previous chapters, we therefore define (again) an associated Cauchy number :

$$C_y = \frac{\rho U^2 R^2}{\kappa} \tag{6.1}$$

Unlike the one used to describe the expansion of kirigami sheets in a flow, here we used the fold stiffness κ to take into account for structural rigidity. It compares the magnitude of the work of pressure forces that scales as $\rho U^2 R^3$ and the elastic energy κR. One can then recast all the previous data in dimensionless form by introducing $\overline{F_d} = F_d/\kappa$ on Fig6.11.

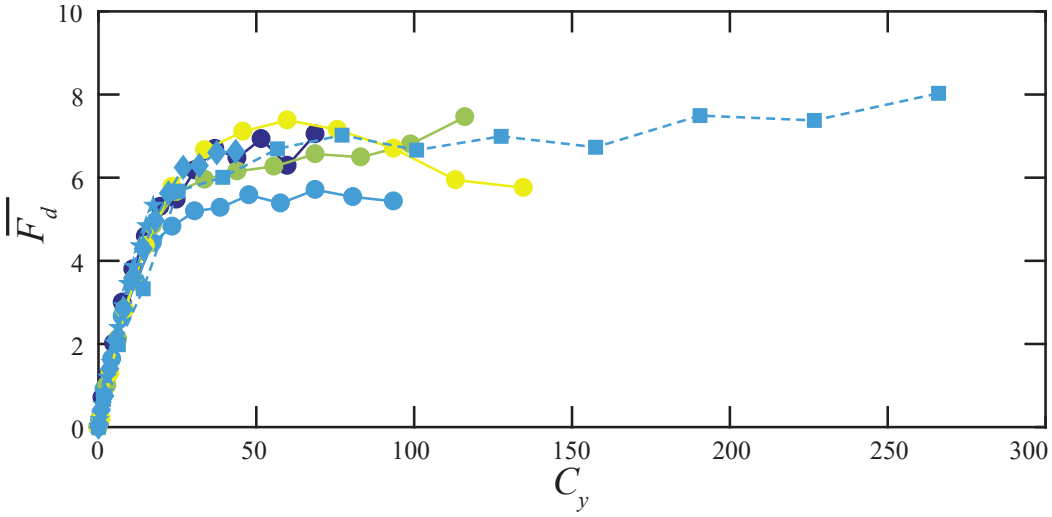

Figure 6.11: Dimensionless drag $\overline{F_d} = F_d/\kappa$ as a function of the Cauchy number C_y. Legends are the same as in Fig6.10.

The data for all specimens collapse onto a single curve. This master curve highlights the general and shared tendency: large morphological changes lead to a saturation of the drag at higher C_y, with the plateau height related to the elastic resistance to deformation κ.

The behavior of the cells is thus governed by this Cauchy number, which captures the competition between rigidity and fluid loads. This dimensionless number notably reflects the effect of origami size and stiffness on shape reconfiguration in the flow. Before presenting experimental results for more specific parameters (rest angle θ_0 and fold numbers N), we will deeply detail our theoretical approach in the following section.

Interlude n^o20: Let us talk about Reynolds number(s)

The dimensionless number widely used to characterize the flow regime is the Reynolds number R_e, which compare inertial and viscous fluid forces. For our origami, we can first define a $R_e = UR/\nu$ based on the cell radius $R \sim 3 - 7$cm, and which roughly varies in from $R_e = 10^3 - 10^5$. Alternatively, we can define a Reynolds number that accounts for the change in frontal area S of the cell as it folds in the flow: $R_e^* = U\sqrt{S}/\nu$, based on the characteristic length $\sqrt{S}$. Values of R_e^* are shown in the figure attached for the specimens with varying radius R and crease stiffness κ that are featured in Fig6.10. We observe an initial increase of R_e^* with flow speed, which is then offset by the decrease of S with U. For all specimens, values are within the same range as for the original Reynolds number Re, and consistent with a flow regime dominated by inertial forces.

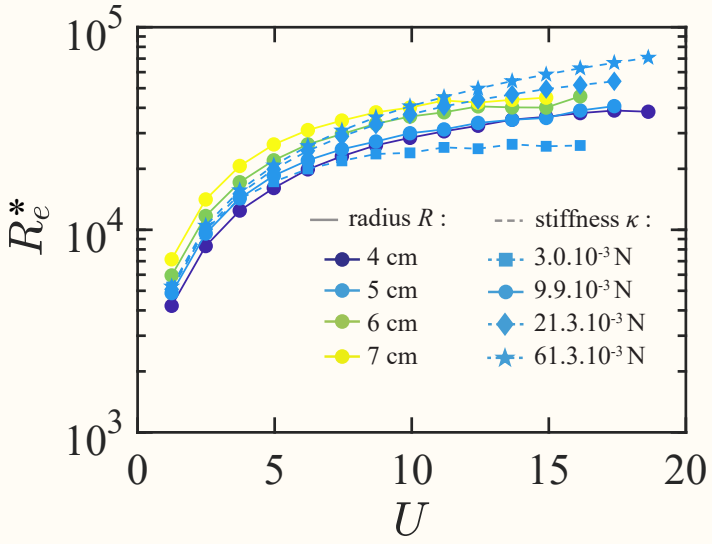

6.4.1 Blockage effect in wind-flow experiments

Regarding drag force measurements on kirigami structures (refer to Chapter 5), one can wondering about the influence of the origami structure on the fluid flow. As previously mentioned, the presence of a blockage effect generally leads to increased fluid velocity, thereby altering the aerodynamic characteristics of the object within the flow. Several studies [107, 108] have explored this effect on drag coefficient measurements, considering various blockage factors denoted as $\beta = S/S_v$. Here, β represents the ratio between the frontal area of the object under investigation, denoted as S, and the cross-sectional area of the wind tunnel, known as S_v. Collectively, these studies suggest that the impact of the blockage effect becomes noticeable when β exceeds 3% in the case of closed wind tunnels and bluff bodies (such as plates or other similar geometries [107, 109]).

In our set-up, we can estimate this factor by considering the maximum value of $S = S_0 \sim 0.5\pi R^2$, which corresponds to the area of the kirigami structure in its unfolded state without any load. This estimation yields a blockage factor of $\beta \sim 2.4\%$ for a channel section with dimensions $S_v = 40cm \times 40cm$. Given that our wind tunnel is open (low border impact), we can safely neglect the blockage effect in our future analysis. Therefore, the primary

contribution to drag reduction in our case arises from the reduction in frontal surface area and the associated streamlining effects.

6.5 Theoretical modeling

In order to rationalize our experimental results, and get more insight into the interplay between flow and our folding cell, we derive a simplified theoretical model in the following. We start with a 2D toy model of a single fold in a flow to introduce our theoretical approach and then move on to a 3D geometry more faithful to the waterbomb cell.

The models are based on an energetic approach. The static equilibrium of the cell (or fold) in a flow with a given speed is obtained by minimizing the energy $E_{el} - W$. It takes into account the elastic potential energy E_{el} associated with crease folding, and W the work of fluid forces acting on the facets. From this equilibrium configuration, we can determine the drag force exerted by the surrounding fluid on our structure.

6.5.1 Two panels and one hinge in a steady flow

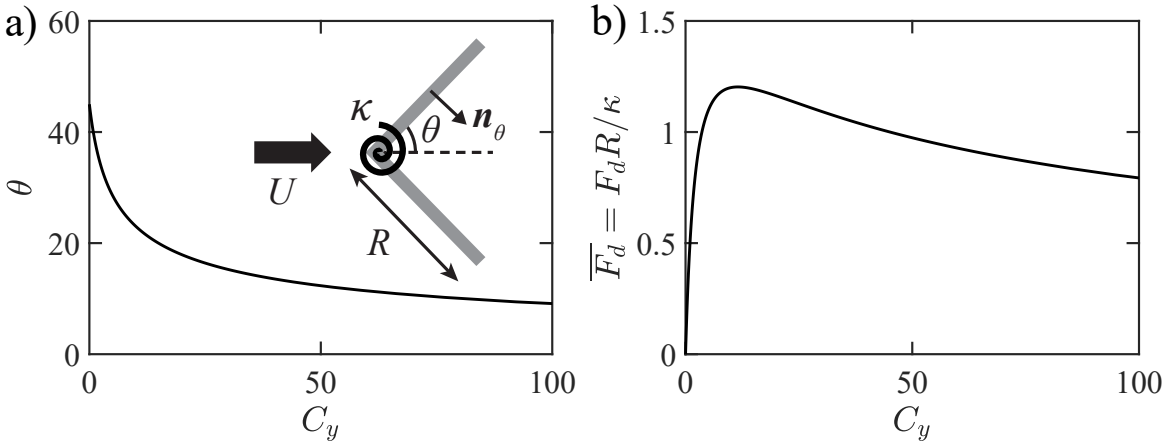

Figure 6.12: a) Opening angle θ evolution as a function Cauchy number C_y. (inset : 2D toy model system : one crease of length R is modeled as an elastic hinge with stiffness κ and described by its opening angle θ). b) Dimensionless drag force $\overline{F_{dp}} = F_{dp}R/\kappa$ on a 2D fold rest angle $\theta_0 = 45^o$

Let us first consider a 2D fold made of two rigid facets of length R as illustrated in Fig 6.12a, and invariant along the third dimension. As previously discussed, the crease is modeled by an elastic hinge characterized by a torsional stiffness κ. This single-fold faces an incoming uniform flow with velocity U. The closing induced by the fluid flow is assumed to be symmetrical and characterized by the opening angle θ, which varies between the rest angle θ_0 and the closed configuration $\theta = 0$. The elastic potential energy per unit of length writes $E_{el} = 1/2\kappa(2\theta - 2\theta_0)^2$. This term is then balanced by the work of pressure forces acting on the facets. Remark that in our flow regime, characterized by a Reynolds number within a range $10^3 - 10^5$ (see interlude n^o20) the dynamic pressure forces are preponderant and the frictional component can be first neglected. Inspired by models previously developed in the literature [16, 15, 17, 60, 61], this load scales with the momentum carried by the flow in the direction perpendicular to the facet: $\rho(\mathbf{U}.\mathbf{n}_\theta)^2 = \rho U^2 \sin^2(\theta)$, with $\mathbf{n}_\theta$ the normal unit vector. The work of pressure forces is then obtained by integrating along the trajectory $xd\theta$ of each facet, where x is a radial coordinate evolving along the face, the total energy of the system per unit length can be expressed as :

$$(E_{el} - W)_{2D} = \frac{1}{2}\kappa(2\theta - 2\theta_0)^2 + 2\int_{\theta_0}^{\theta}\int_0^R \rho(\mathbf{U}.\mathbf{n}_{\theta'})^2 x dx d\theta' \tag{6.2}$$

Energy minimization, that is the zero of $d\left(E_{el}-W\right)_{2D}/d\theta$, gives the equilibrium angle θ for a given Cauchy number C_y, which then satisfies :

$$(\theta-\theta_0)+\frac{C_y}{4}\sin^2\theta=0 \quad \text{with} \quad C_y=\frac{\rho U^2R^2}{\kappa} \tag{6.3}$$

The equation is solved numerically for increasing Cauchy number, and the results are plotted in Fig6.12a. As expected, increasing the Cauchy number leads to the closure of the fold. From these equilibrium positions, we can deduce the drag force by integrating and projecting the pressure field along the direction of the incoming flow. The dimensionless form $\overline{F_{dp,2D}}=F_{dp,2D}R/\kappa$ is the 2D analog of the one introduced previously for our experimental data in Fig6.11. It writes:

$$\overline{F_{dp,2D}}=2\frac{1}{\kappa R}\int_0^R(\mathbf{U}.\mathbf{n}_\theta)^2.\sin(\theta)dx=2C_y\sin^3(\theta) \tag{6.4}$$

The evolution of the force with C_y is reported in Fig6.12b. Although the geometry is highly simplified, our toy model reproduces the main features observed experimentally: the flow-induced folding limits the increase of drag with the Cauchy number. This effect is large enough to saturate $\overline{F_{dp,2D}}$, and finally leads to a drag decrease at higher C_y as the cell further closes. This theoretical decaying phase is however not observed experimentally,

Before moving to a more realistic 3D model, we further use this simpler 2D model to discuss different modeling for fluid dynamics. We compare our constant-pressure formulation to a more realistic pressure field and take into account skin friction that can be relevant for a high degree of closing when facets tend to align with flow.

6.5.2 A more realistic pressure field

The geometry of the 2D model is similar to a wedge, which has been widely studied in the literature on fluid dynamics. We use the Falkner-Skan approach here that models the two-dimensional laminar boundary layer forming on such wedge-shaped bodies [110, 111], as illustrated in Fig6.14a. We distinguish two regions: a near-wall boundary layer affected by viscosity (in gray on Fig6.14a), and the outer flow where viscous effects are neglected and that satisfies Euler equations. While the boundary layer is described by Prandlt equations [112, 65], which provide an expression for the pressure and shear stress along the walls.

The main assumption of the Falkner-Skan analysis is that the pressure across the boundary layer varies a little along the y axis normal to the wedge surface. Thus the outer flow actually imposes its pressure field. Euler's equations provide a self-similar solution for the velocity at the boundary layer edge and in the outer region: $u_e(x)=U(x/R)^m$, where x is the coordinate measured along the wedge wall, and $m=\theta/(\pi-\theta)$ is the self-similarity coefficient that depends on the wedge angle θ. This model of the external flow assumes that the velocity at the downstream edge of the facet is equal to the far-field velocity: $u_e(R)=U$. It means that the pressure in the wake is equal to the far-field pressure. The differential pressure P across a facet is then given by Bernoulli's equation $P(x)+1/2\rho u_e^2(x)=1/2\rho U^2$, which yields:

$$P(x)=\frac{\rho U^2}{2}\left[1-\left(\frac{x}{R}\right)^{2m}\right] \tag{6.5}$$

As previously, we evaluate the work W done by the pressure forces, which competes with the potential energy of the elastic hinge. The total energy per unit length is then expressed as:

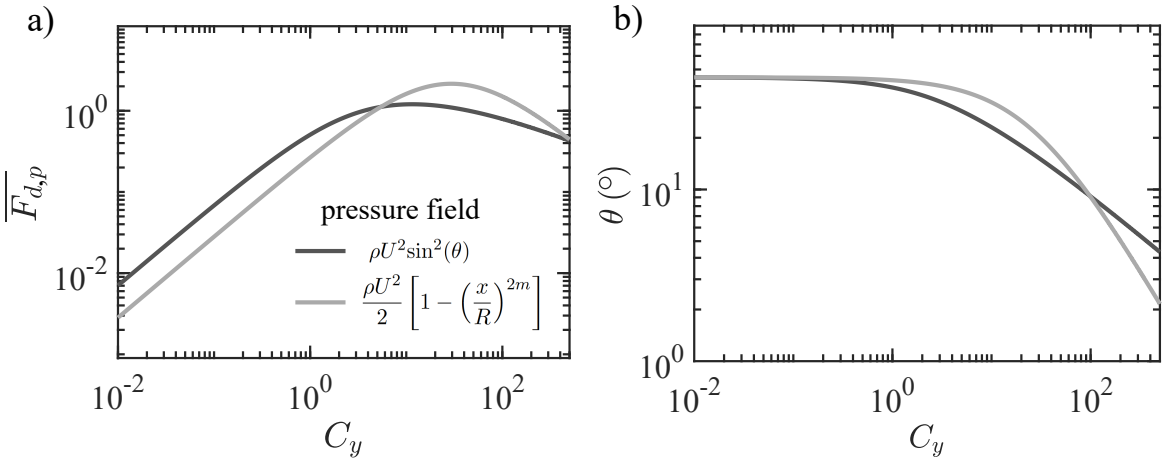

Figure 6.13: a) Dimensionless pressure drag $\overline{F}_{dp,2D} = F_{dp,2D}R/\kappa$, and b) opening angle θ, as a function of the Cauchy number C_y, for a fold with rest angle $\theta_0 = 45^o$. The black line corresponds to the predictions with the pressure formulation based on momentum conservation arguments, and the grey one to the pressure distribution from Falkner-Skan model.

$$E_{el}-W = \frac{1}{2}\kappa(2\theta-2\theta_0)^2+2\int_{\theta_0}^{\theta}\left(\int_0^R P(x)xdx\right)d\theta = \frac{1}{2}\kappa(2\theta-2\theta_0)^2+\frac{\rho U^2R^2}{2}\int_{\theta_0}^{\theta}\left(1-\frac{1}{m+1}\right)d\theta \tag{6.6}$$

The equilibrium angle then corresponds to the minimum of $E_{el}-W$, and can be analytically expressed as :

$$4\kappa(\theta-\theta_0)+\frac{\rho U^2R^2}{2}\left(1-\frac{1}{m+1}\right)=0 \quad \longrightarrow \quad \theta = \frac{\theta_0}{1+C_y/8\pi} \tag{6.7}$$

The evolution of θ as a function of Cauchy number is then reported in Fig6.13b, and compared to the results obtained for the simpler uniform pressure field $\rho U^2 \sin^2\theta$. In the same way, drag force can be computed as the component of pressure forces in the direction of the flow $F_{dp,2D} = 2\int_0^R P(x)dx\sin\theta$, which can be expressed in a dimensionless form:

$$\overline{F_{dp,2D}} = 2C_y\frac{m}{2m+1}\sin\theta \tag{6.8}$$

It is also compared to the previous pressure drag (Eq6.4) in Fig6.13a. The two models predict values of drag that are consistent (with a factor of two), and show a similar trend: the drag reaches an upper limit at a comparable Cauchy number (with a factor of 3 between both models) before decreasing. This evolution of drag is correlated with similar evolution of the fold opening angle in Fig6.13b, with some disparities for high Cauchy values. The uniform pressure model thus provides a reasonable approximation of the more rigorous flow model derived from the Falkner-Skan analysis. It also has the advantage of being easier to implement for 3D geometries and will therefore be used later when modeling the waterbomb geometry. Before addressing this theoretical extension, let us have a look at the effect of skin friction.

6.5.3 Skin drag

To evaluate the effect of skin friction, we then incorporate the shear stress on the wall from the Falkner-Skan boundary layer solution. The flow in the boundary layer is derived from Prandlt equations, with a no-slip condition at the wall and a boundary condition at the layer

edge that is given by the outer region solution (discussed earlier). Falkner and Skan (1931) showed that auto-similarity solutions can be obtained when the velocity and boundary layer thickness are power law functions of x, as is the case here [110]. The stream function can then be expressed in terms of a function $f(\eta)$ with the similarity variable $\eta = y\sqrt{\frac{(m+1)U}{2\nu R^m x^{1-m}}}$, where y is the coordinate perpendicular to the wall (see Fig6.14a) and ν the kinematic viscosity of the air. It satisfies the Falkner-Skan equation:

$$f''' + ff'' + \frac{2m}{m+1}(1 - f'^2) = 0, \text{ with } m = \frac{\theta}{\pi - \theta} \tag{6.9}$$

where primes denote differentiation with respect to η. The boundary conditions previously discussed are : $f(0) = f'(0) = 0$, $f'(\infty) = 1$. Eq6.9 is solved numerically with a classic shooting method. One can then derive the velocity, and the shear stress along the wall [111]:

$$\tau(x) = \rho\nu \left(\frac{\partial u}{\partial y}\right)_{y=0} = \rho\sqrt{\nu U^3 \frac{(m+1)}{2} \frac{x^{3m-1}}{R^{3m}}} f''(0) \tag{6.10}$$

where m and $f''(0)$ are function of the opening angle of the wedge 2θ, $f''(0)$ is given by solving Eq6.9.

This shear stress induces tangential friction forces on the facets. Note that the latter does not impact the equilibrium shape, as it is tangential and thus induces no torque on the crease. It however adds a new contribution to the total drag, which is the skin drag $F_{ds,2D} = 2\int_0^R \tau(x)dx \cos\theta$ corresponding to the component of friction forces in the direction of the flow [113]. In a dimensionless form, it writes:

$$\overline{F_{ds,2D}} = F_{ds,2D}R/\kappa = \frac{2\sqrt{2(m+1)}}{3m+1} \frac{C_y}{\sqrt{Re}} f''(0)cos(\theta) \tag{6.11}$$

With $Re = UR/\nu$ the Reynolds number. Note that in previous inviscid flow models, drag depends on the flow velocity and fluid parameters (like the density ρ) only through the Cauchy number $C_y = \rho U^2 R^2/\kappa$. Accounting for viscous boundary layers however introduces the Reynolds number as a new dimensionless parameter. The drag-vs-C_y curve will thus no longer be universal, as it is Reynolds-dependent. To evaluate $\overline{F}_{ds,2D}$ as a function of C_y, the velocity appearing in the Re of Eq6.11 is thus determined from C_y as $U = \sqrt{\kappa C_y/\rho R^2}$, taking a value $\kappa = 30 \times 10^{-3}$N chosen in the mid-range of experimental values.

The total dimensionless drag now takes into account the contribution of the pressure drag and the skin drag: $\overline{F_{d,2D}} = \overline{F_{dp,2D}} + \overline{F_{ds,2D}}$. It is shown in Fig 6.14b (solid red line), and is to be compared to the pressure drag alone (solid grey line) and the skin friction along (dashed grey line). Skin friction has a negligible contribution, about an order of magnitude smaller than form drag, except at large deflections as facets nearly align with the flow. It then causes a re-increase of the total drag for the high Cauchy number. Accounting for skin friction is thus not expected to significantly alter the conclusions of our theoretical analysis, except at large deflections. Note that the drag plateau that is observed in the experiment (rather than a decay) could notably be attributed to such skin friction effects, although we would need to reach higher C_y in experiments to confirm it.

This discussion on a more accurate description of flow shows that such considerations can be put aside at first, and our previous simplified approach based on a uniform pressure field is enough to capture the phenomenon of reconfiguration and drag reduction of a folded structure. It is now time to transpose this model to the real geometry of a waterbomb cell.

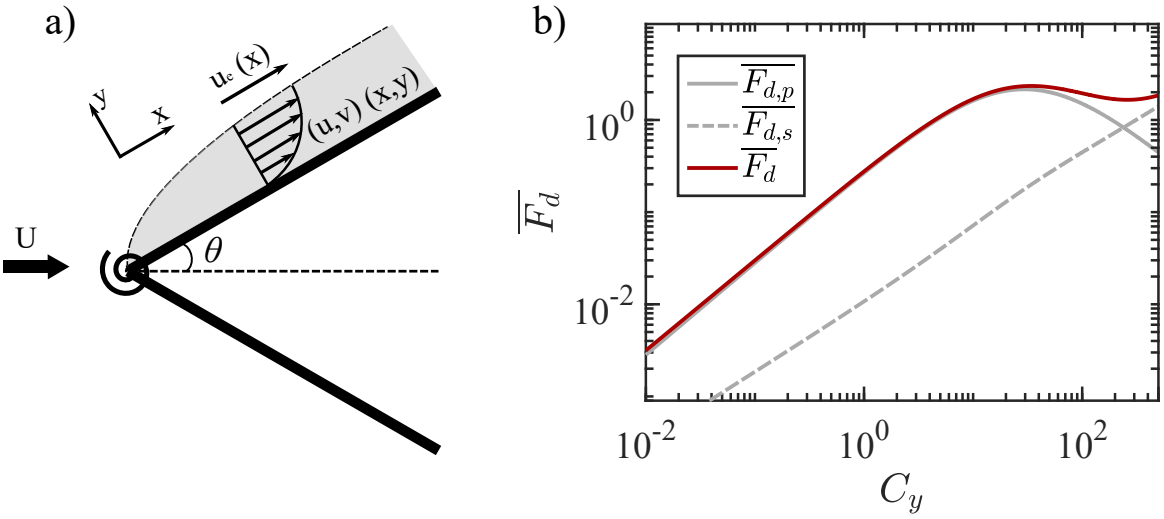

Figure 6.14: a) Schematics of the Falkner-Skan boundary layer on the wedge-shaped fold. b) Dimensionless friction drag $\overline{F_{ds,2D}} = F_{ds,2D}R/\kappa$, pressure drag $\overline{F_{dp,2D}} = F_{dp,2D}R/\kappa$, and total drag $\overline{F_{d,2D}} = \overline{F_{ds,2D}} + \overline{F_{dp,2D}}$, as a function of the Cauchy number, computed with parameters: $\theta_0 = 45^o$, $\kappa = 30 \times 10^{-3}$N, $\rho = 1.225$ kg.m^{-3} and $\nu = 1.471 \times 10^{-5}$ m^2.s^{-1}.

6.5.4 Model for origami 3D cell

We now extend the modeling to the three-dimensional geometry of waterbomb cell, using the same energy approach. Before deriving the total energy of the cell, let us have a closer look at the geometry of the waterbomb unit and its folding kinematics. We indeed need to know the opening angle of each fold to compute the elastic potential energy, and the trajectory and orientation of the facets to calculate the work of pressure forces.

Origami geometry and folding kinematics

The origami unit is modeled as rigid facets connected by torsional hinges. All motion is thus localized at the hinge simplifying the kinematics analysis. As observed in experiments, we assume that the cell deforms symmetrically, meaning that all mountain or valley folds are deflected by the same amount. The folded state can be entirely determined from a single variable, chosen as angle θ (see Fig6.15a-b).

A kinematic analysis of waterbomb bases is presented in the papers from Hanna et al. (2014, 2015), modeling the units by using spherical trigonometry tools [88, 95]. Brunck et al. (2016) proposed an alternative analysis that expresses the deformation in terms of vectors associated with the crease network [38]. We use the latter formalism, which is more convenient here and yields compact expressions. In the following, we succinctly recall the main results adapted with our notations.

The geometry of the waterbomb base is described by unit vectors $\mathbf{w}$ that lie along each crease. For a symmetrical deformation, components of these vectors in the Cartesian coordinates system shown in Fig6.15b write as:

$$\begin{aligned} \mathbf{w_{2p}} &= (\sin\phi\cos 2p\alpha, \sin\phi\sin 2p\alpha, \cos\phi) \\ \mathbf{w_{2p+1}} &= (\sin\theta\cos(2p+1)\alpha, \sin\theta\sin(2p+1)\alpha, \cos\theta) \end{aligned} \tag{6.12}$$

With $\mathbf{w_{2p}}$ and $\mathbf{w_{2p+1}}$ the unit vectors corresponding respectively to mountain and valley folds, where $p = 0, ..., (N/2-1)$ and $\mathbf{w_0} = \mathbf{w_N}$, and $\alpha = 2\pi/N$ the sector angle of a facet, which links to successive folds. Here, ϕ denotes the angle between a mountain fold and

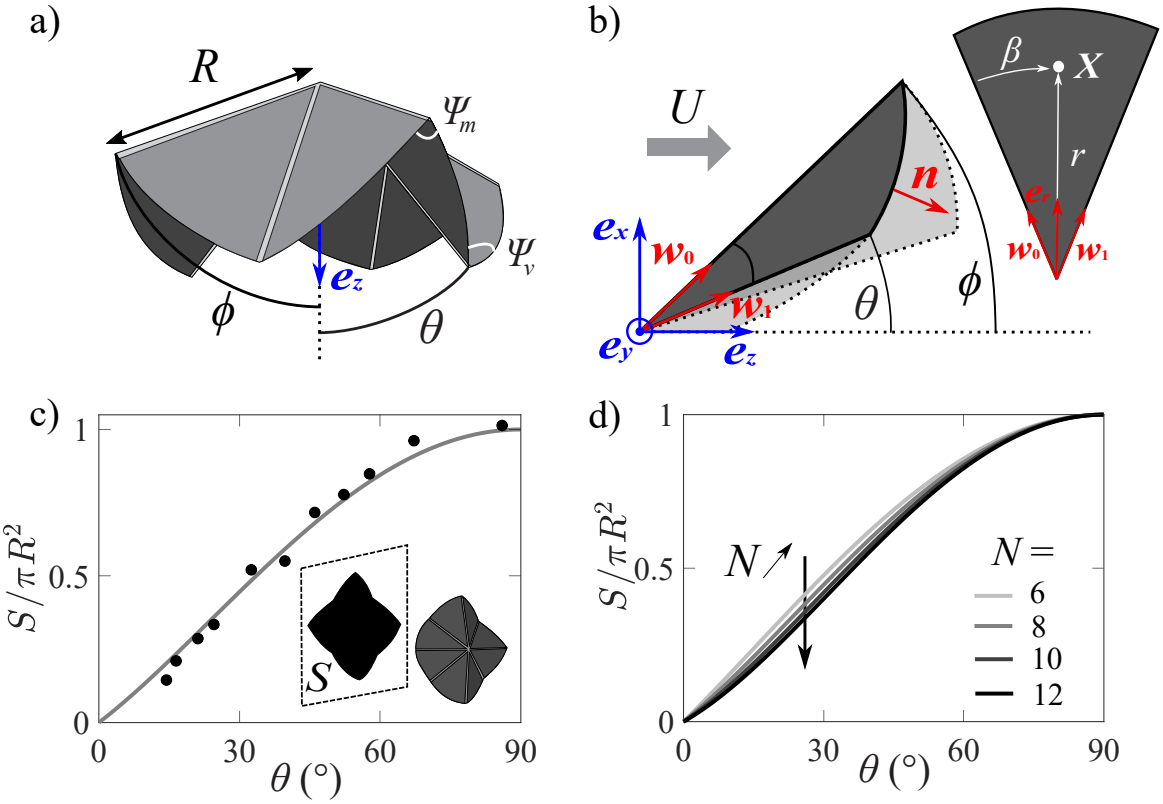

Figure 6.15: a) Folded state of the waterbomb base, characterized by the opening angle θ between a valley fold and the central axis passing through the vertex. All other angles are functions of this input parameter. b) Unit vectors lying along each crease, shown for one of the facets and all defined by Eq6.12. The inset shows the parameterization used to compute the work of fluid forces on a facet and further pressure drag derivation. c) Experimental measurements of the dimensionless frontal area $S/\pi R^2$ as a function of θ for a cell with $N = 8$ folds and a radius $R = 5cm$ (data black points), compared to the theoretical prediction (solid line) provide by Eq6.16. d) Evolution of S as a function of θ for cells with different number of folds N.

the central axis (see Fig6.15a-b) and is a function of θ as expressed below. Note that the direction of the Cartesian unit vector $\boldsymbol{e_z}$ is chosen here based on the direction of flow speed and is opposite of the one used in [89], thus affecting the angle definition.

Rigid facet approximation imposes a geometrical constraint: the conservation of the dot product between two successive unit vectors $\mathbf{w_{2p}}.\mathbf{w_{2p+1}} = \cos\alpha$. This equality yields a relationship between ϕ and θ:

$$\cos\theta\cos\phi - \cos\alpha(1 - \sin\theta\sin\phi) = 0 \tag{6.13}$$

It rewrites as :

$$\phi(\theta) = \begin{cases} \arccos\left(\dfrac{\cos\alpha\cos\theta}{1+\sin\theta\sin\alpha}\right), & \text{for} \quad 0 \leqslant \theta \leqslant \pi/2 \\ \arccos\left(\dfrac{\cos\alpha\cos\theta}{1-\sin\theta\sin\alpha}\right), & \text{for} \quad \pi/2 < \theta \leqslant \pi - \alpha \end{cases} \tag{6.14}$$

Each expression corresponds to a different regime of motion on each side of the flat configuration: the opening part from $\pi/2 < \theta \leqslant \pi - \alpha$ and the closing one when $0 \leqslant \theta \leqslant \pi/2$. Except in the last section, all our studies will be in the closing regime. We can then define the unit vector perpendicular to the facet $\mathbf{n}$, which reflects the orientation of the facet in the flow and will be used to compute the work of fluid forces:

$$\mathbf{n} = \frac{\mathbf{w_0} \times \mathbf{w_1}}{\|\mathbf{w_0} \times \mathbf{w_1}\|} = \frac{1}{\sin\alpha}(-\cos\phi\sin\theta\sin\alpha, \cos\phi\sin\cos\alpha - \sin\phi\cos\theta, \sin\theta\sin\phi\sin\alpha) \tag{6.15}$$

From this normal vector, we can also derive the frontal area S of the cell (i.e. projected in the xy plane) that has been serving as a metric for its degree of folding in experiments:

$$S = N\left(\frac{\pi R^2}{N}\mathbf{n}.\mathbf{e_z}\right) = \pi R^2 \sin\theta\sin\phi \tag{6.16}$$

To validate this geometrical formulation, experiments have been performed on a classic waterbomb cell ($N = 8$). In practice, we placed the origami unit on a low-friction plane and pushed down the vertex to open symmetrically the origami at a given θ angle. By taking pictures from above, the frontal area is obtained and compared to the geometrical prediction in Fig6.15c. The good agreement between experiments and theory supports the rigid face approximation and the one degree of freedom kinematics. We can also have a look at the effect of the number of folds N. This parameter modifies the sector angle α in the expression of ϕ, Eq6.14, and impacts the folding pathway. Nonetheless, it induces little differences in the evolution of frontal area S with θ, as shown in Fig6.15d.

Interlude n^o21: Whole energy landscape and bi-stability

The evolution of the potential energy reported on the Fig6.16 corresponds to only one part of the kinematics for $\theta \in [0, \pi/2]$, and around a single equilibrium point identified as θ_0.
The waterbomb cell is however also well famous for its bistable property [88, 95, 38]. The latter is graphically "visible" if we extend the domain of definition of the opening angle to $\theta \in [0; \pi - \alpha]$. We therefore notice the existence of a second stable configuration marked by θ_0^* within the range $[\pi/2; \pi - \alpha]$. Three values of θ_0 are reported and their respective second equilibrium angle in order to probe the effect of these parameters on the (whole!) energy landscape. One can clearly note that shifting θ_0 changes both the value θ_0^* and global curve shapes, as well as the energy barrier of the unstable state localized at $\pi/2$ (flat configuration). The link between θ_0 and θ_0^* will be briefly discussed in the interlude n^o24.

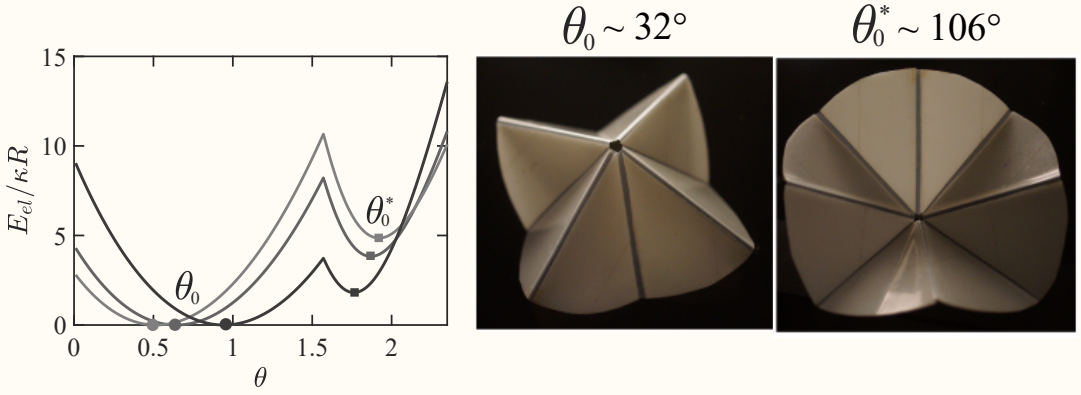

Potential energy landscape

Based on our mechanical modeling of a single fold as a torsional spring, here we extend this approach to a real waterbomb unit. Each valley and mountain fold of length R is modeled as an elastic hinge of rigidity κ. The elastic potential energy of a unit E_{el} is then the sum of the contributions of the $N/2$ mountain and $N/2$ valley creases:

$$E_{el} = \frac{NR\kappa}{4}[(\Psi_m - \Psi_m^0)^2 + (\Psi_v - \Psi_v^0)^2] \tag{6.17}$$

Where the angular deviation of each mountain and valley fold with respective angles Ψ_m and Ψ_v (see Fig6.15a) is considered with respect to their position at rest (denoted by 0).

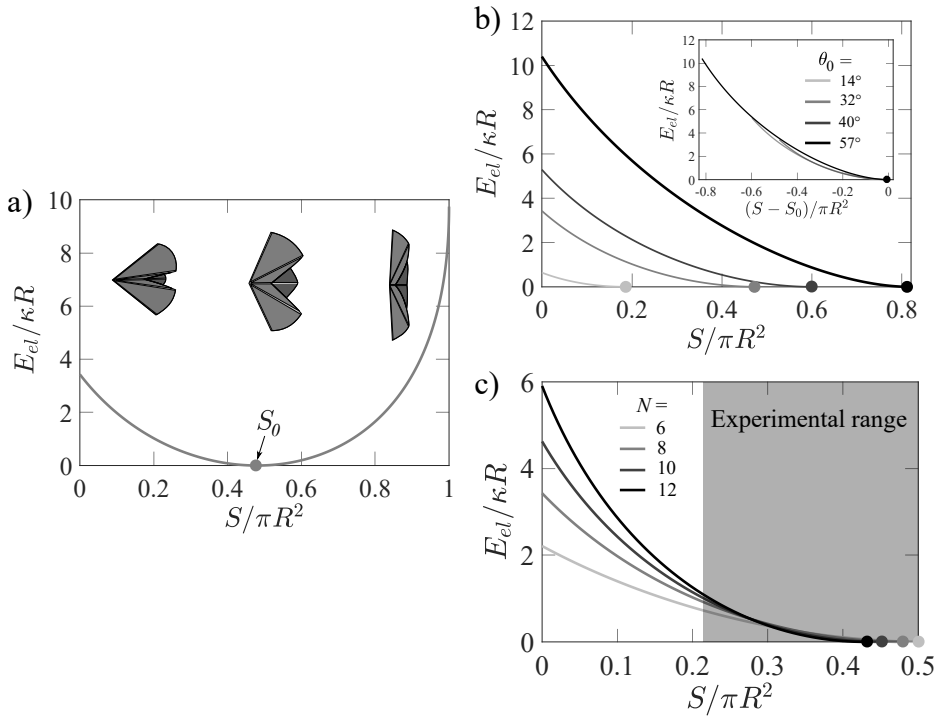

Figure 6.16: a) Dimensionless potential energy $E_{el}/\kappa R$ as a function of the dimensionless frontal area $S/\pi R^2$, for a cell with $N = 8$ folds and rest angle $\theta_0 = 32°$ (rest frontal area S_0). Potential energy landscape for cells with b) different rest angles θ_0 and $N = 8$ folds, and c) different N and $\theta_0 = 32°$. In the inset of (b), results are re-casted as a function of the deviation of S to its rest value S_0. The cell parameters are the same as the ones tested experimentally. For each curve, only the closing kinematic part is plotted.

A geometrical analysis based on vector projections yields the expressions of these angles as a function of the opening angle θ [89]:

$$\Psi_v = 2\phi \quad \text{and} \quad \Psi_m = 2\theta \tag{6.18}$$

Thus, as for folding kinematics, the elastic potential energy of a waterbomb cell is a function of the single degree of freedom θ. Note that values of Ψ_v^0 and Ψ_m^0 are determined from the prescribed rest angle θ_0, from Eq6.18.

Fig6.16a shows a typical evolution of the potential energy as a function of the frontal area S (instead of θ), for consistency with experimental measurements. However, another plot is proposed in the interlude n^o21 as a function of the opening angle θ, for the whole angular range. For this first curve the rest state is chosen at $\theta_0 = 32°$ (that is $S_0/\pi R^2 = 0.48$, with S_0 the frontal area at rest) localized by a circle marker of the Fig6.16a. Our experiment focuses on the closing motion under fluid loading and thus only the left side of the rest position is studied, as illustrated by the schematic above the curve.

Fig6.16b reports the effect of changing the configuration at rest θ_0 (or S_0) on the potential energy. The four rest angles chosen are the same as the ones used in the experimental campaign. When replotting the results as a function of $S - S_0$ (inset graph), one can compare the energy landscape around each equilibrium state. All curves present a similar

evolution of E_{el}. Slight differences are attributed to the non-linear evolution of the crease angles with the input parameter θ along the folding kinematics.

Finally, Fig6.16c shows the last parameter, the number of folds N, and its impact on the mechanical response. As for our experimental cells, all curves have the same θ_0, associated with slightly different surfaces S_0 (see disparities in Fig6.15d). The grey zone represents the deformation range investigated experimentally; in this domain, all cells have comparable evolution of the energy despite different fold numbers. Indeed, although more folds involve more springs, those springs require less torsion to attain a given global shape (that is a given S). Divergences however arise for a higher degree of closure of the cells, but outside of the experimental range.

As for the previous 2D models, it is now time to describe the other part of the energy balance: the work of fluid forces.

Work of fluid forces

As discussed earlier, only the pressure form drag will be considered for this 3D model, as the skin friction forces are not expected to significantly change the analysis except for the largest deflections. We also take a uniform pressure field over each facet, as for the first version of the 2D toy model. Let us compute the work produced by the fluid force on each origami facet.

Due to the symmetry of the unit, the work done by the pressure forces on each facet will be the same. As the origami deforms from the rest state θ_0 to a given equilibrium position θ', the total work will write:

$$W = N \int_{\theta_0}^{\theta'} \int_{S_f} P dS_f \mathbf{n}.d\mathbf{X} \tag{6.19}$$

The pressure $P = \rho(U\mathbf{e_z}.\mathbf{n})^2$ is obtained through momentum conservation arguments as before, with $\mathbf{n}$ the normal unit vector expressed in Eq6.15. It sums the work of pressure forces exerted on each surface element of the facet (whose area is $S_f = \pi R^2/N$), as it is displaced by $d\mathbf{X}$ along its trajectory. Note that $\mathbf{n}$ and $\mathbf{X}$ are functions of the folded state θ. The expression of $\mathbf{dX}$ is derived below.

The path of each surface element can be derived from the previous kinematics analysis. We consider the facet of Fig6.15b associated to the two successive crease vectors:

$$\begin{aligned} \mathbf{w_0} &= (\sin\phi, 0, \cos\phi) \\ \mathbf{w_1} &= (\sin\theta\cos\alpha, \sin\theta\sin\alpha, \cos\theta) \end{aligned} \tag{6.20}$$

From the parameterization of the facet reported in Fig6.15: the position vector $\mathbf{X}$ is identified by its distance $r \in [0, R]$ from the vertex and polar angle $\beta \in [0, \alpha]$. It writes as $\mathbf{X} = r\mathbf{e_r}$, with $\mathbf{e_r}$ the radial unit vector that lies in the $(\mathbf{w_0}, \mathbf{w_1})$ plane and can thus be expressed as a linear combination of those two fold vectors:

$$\mathbf{e_r} = \frac{\mathbf{w_0} + C\mathbf{w_1}}{\|\mathbf{w_0} + C\mathbf{w_1}\|} = \frac{\mathbf{w_0} + C\mathbf{w_1}}{1 + 2C\cos\alpha + C^2} \tag{6.21}$$

With the parameter C that verifies $\mathbf{e_r}.\mathbf{w_0} = \cos\beta$. It is a function of the facet geometry α and the angle β, and its expression can be derived from Eq6.20-6.21:

$$C = \cos\alpha\left(\frac{1}{2\cos\beta} - 1\right) + \sqrt{\cos^2\alpha\left(\frac{1}{2\cos\beta} - 1\right)^2 + \frac{1}{\cos\beta} - 1} \tag{6.22}$$

As the waterbomb unit folds by $d\theta$, the points of the facet move as $d\mathbf{X} = \frac{d\mathbf{X}}{d\theta}d\theta = r\frac{d\mathbf{e_r}}{d\theta}d\theta$. It then writes as:

$$d\boldsymbol{X} = \begin{pmatrix} \frac{d\phi}{d\theta}\cos\phi + C\cos\theta\cos\alpha \\ C\cos\theta\sin\alpha \\ -\frac{d\phi}{d\theta}\sin\phi - C\sin\theta \end{pmatrix} \frac{r d\theta}{1+2C\cos\alpha+C^2} \tag{6.23}$$

The expression of the work done by fluid forces on the entire origami unit in Eq6.19 can thus be explicitly rewritten as :

$$W = -\frac{NR^3\rho U^2}{3}\int_{\theta_0}^{\theta'} \sin^2\theta\sin^2\phi\left[A\frac{d\phi}{d\theta}\sin\theta + B\sin\phi\right]d\theta \tag{6.24}$$

with $\phi(\theta)$ given by Eq6.14, and A and B integrals that depend only on the number of folds (through α):

$$A = \int_0^\alpha \frac{C}{1+2Ccos\alpha+C^2}d\beta \text{ and } B = \int_0^\alpha \frac{1}{1+2Ccos\alpha+C^2}d\beta, \text{ with } C(\beta,\alpha) \text{ given by Eq6.22.} \tag{6.25}$$

The sign of this work is a consequence of the definition of our frame; unfolding kinematics will lead to a positive sign and closing kinematics (as is the case here) to a negative sign. Using the expressions of the two energetic sources, namely the elastic potential energy (Eq6.17) and the work of external fluid force (Eq6.24), we are presently able to establish the equilibrium equation.

Mechanical equilibrium and dimensionless drag

The static equilibrium configuration in a flow is obtained through the minimization of the total energy $E_{el.} - W$, as performed previously. The equilibrium angle θ is thus given by the zero of $d(E_{el.} - W)/d\theta$. We obtain the equation satisfied by θ:

$$\left(\Psi_m - \Psi_m^0\right)\frac{d\Psi_m}{d\theta} + \left(\Psi_v - \Psi_v^0\right)\frac{d\Psi_v}{d\theta} + \frac{2}{3}C_y\sin^2\theta\sin^2\phi\left[A\sin\theta\frac{d\phi}{d\theta} + B\sin\phi\right] = 0 \tag{6.26}$$

with the Cauchy number defined as in the experimental section $C_y = \rho U^2R^2/\kappa$. This equation is solved numerically using the nonlinear system solver *fsolve* of Matlab. From the obtained equilibrium angle θ, we then calculate the frontal area of the cell S using Eq6.16 and the dimensionless drag force $\overline{F_d} = F_d/\kappa$, to compare it with experimental results. The drag force is given by projection along wind flow direction $F_d = N\left[PS_f\boldsymbol{n}\right].\boldsymbol{e_z}$, which yields:

$$\overline{F_d} = \pi C_y\sin^3\theta\sin^3\phi \tag{6.27}$$

In the next section, we are going to present further experimental results on parameters specific to waterbomb crease pattern (number of folds and rest angle) before comparing those theoretical predictions to our experimental measurements.

Ch. 6

6.5.5 Theoretical overview on experimental parametric study

From the equilibrium angle obtained through energy minimization of Eq6.26, we infer both the evolution of the drag force and the frontal area for different Cauchy numbers. Those theoretical predictions are plotted in the dimensionless form in Fig6.17 (solid lines), and

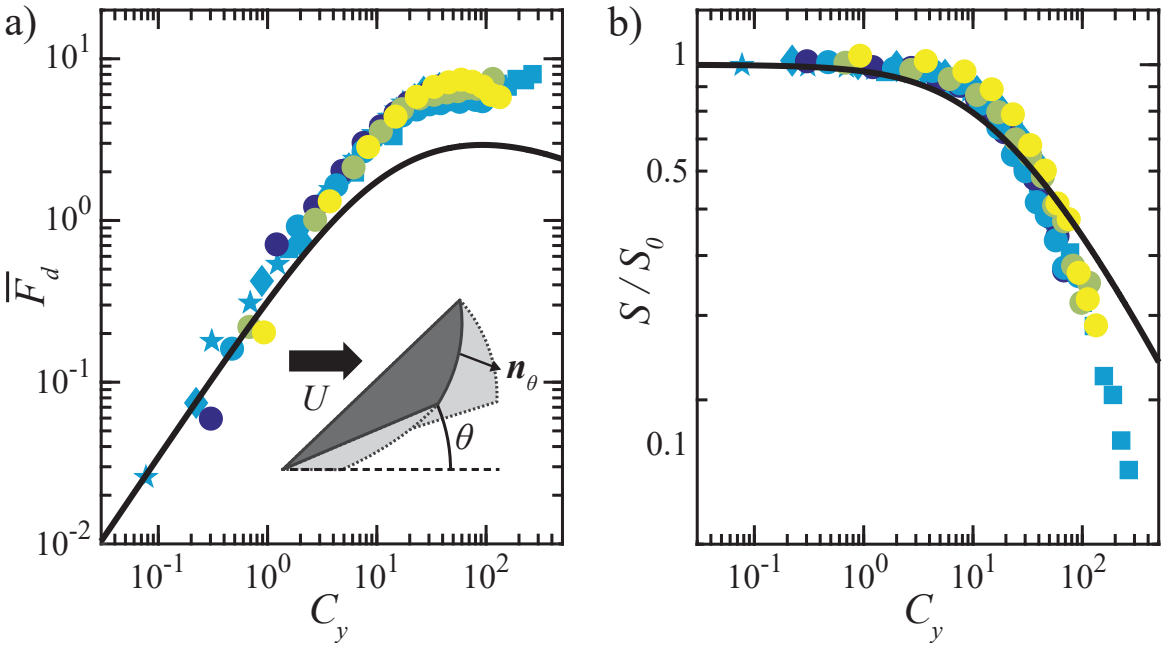

Figure 6.17: Theoretical prediction of a) the dimensionless drag force $\overline{F_d} = F_d R/\kappa$, and b) the relative frontal surface S/S_0 as a function of C_y (solid black lines), for the 3D origami geometry shown in the inset (only one facet and its neighbors are represented). Theoretical results are compared to experimental data, reported with the same markers and color code as in Fig6.11.

compared with experimental data of the series with varying stiffness and size (markers and parula colors already defined in Fig6.11).

Theoretical predictions show reasonable qualitative and quantitative agreement with experimental data, especially without any fitting parameters and given the simplifying assumptions on the fluid force formulation. Indeed, even if the model underestimates the drag force (Fig6.17a) and overestimates the frontal area (Fig6.17b) at larger C_y values, it captures the global trend. For low Cauchy numbers, the origami cell barely deforms and $S/S_0 \sim 1$; the drag force thus follows a quasi bluff body law: $\overline{F_d} \sim C_y$. Past a critical Cauchy number $C_y \sim 10 - 20$, the plateau in drag appears, which correlates with the strong decay of the surface area jointly observed by experiments and models.

In accordance with the two-dimensional fold model of Fig6.12, theoretical predictions suggest that this plateau-like behavior is more of a transition preceding a decrease of $\overline{F_d}$ with C_y. However, this range of larger Cauchy number is not attainable with our experimental setup. As suggested by our further analysis on two-dimensional, a contribution of friction drag is also expected in this large-C_y regime, which will tend to prevent the force decay.

This fruitful comparison encourages us to further investigate the effect of parameters more specific to our crease pattern

6.6 Number of folds and rest configuration

We have established that size and stiffness affect the balance between fluid loading and elastic restoring force, results confirm by our realistic theoretical modeling. Our origami fabrication allows us to change less straightforward parameters: namely, the rest configuration sets by θ_0, and the number of creases N.

First, we consider four origami units with rest angles ranging from $\theta_0 = 14 - 57^o$, shown in Fig 6.18a (the stiffness $\kappa = 9.9 \times 10^{-3}$ N, radius $R = 5$ cm and $N = 8$ are kept constant). The drag force is reported in the dimensionless form as a function of the Cauchy number.

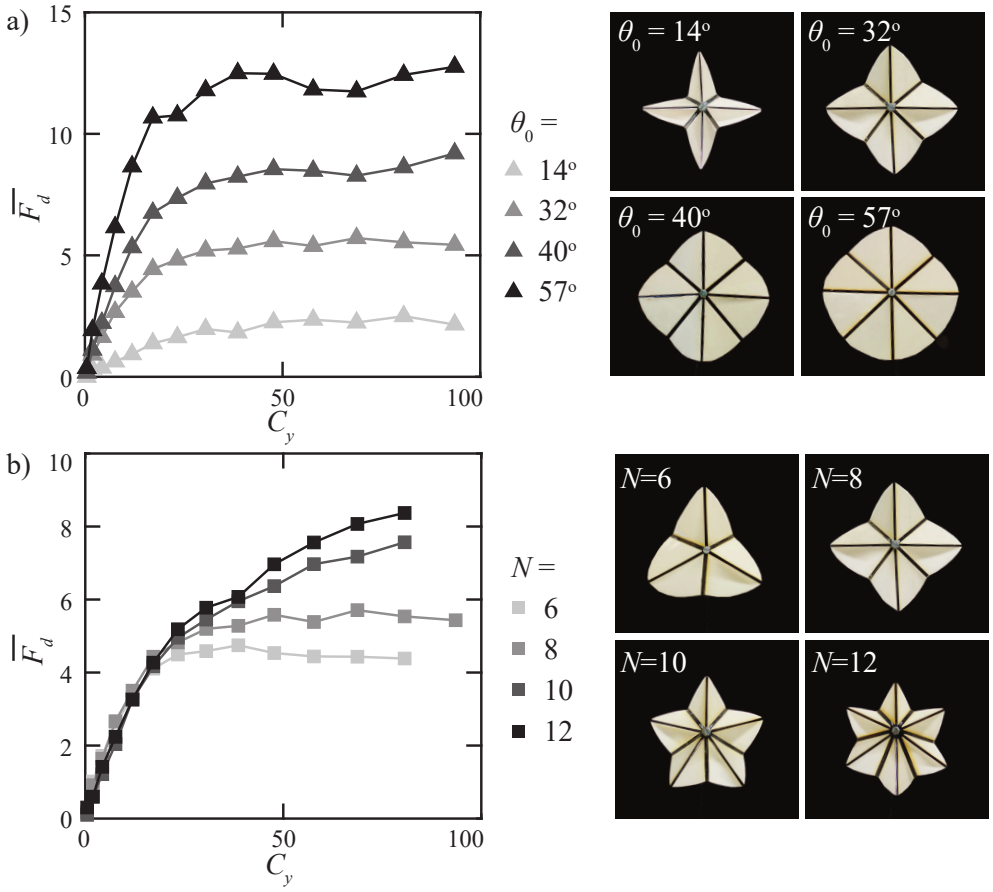

Figure 6.18: Dimensionless drag force $\overline{F_d} = F_d/\kappa$ as function of the Cauchy number C_y for cells with a) different rest angles θ_0 and $N = 8$ folds, and b) different number of folds N and $\theta_0 = 32^o$. Frontal (taken down-flow) images illustrate the geometry of the specimens of each parametric series in their rest state. All specimens in (a-b) have the same radius $R = 5$ cm and crease stiffness $\kappa = 9.9 \times 10^{-3}$ N.

While changing θ_0 does not affect the folding pathway along which the unit deforms, it shifts the starting point. This is reflected through different initial slopes of the $\overline{F_d}$-vs-C_y curve for each specimen: a cell that is initially more open experiences a larger drag force than a compact one, owing to its greater frontal area and less streamlined shape. All specimens eventually enter a plateau-like phase at higher velocities (higher C_y), but its height increases with the initial degree of opening of the cell. For example, the specimen with $\theta_0 = 57^o$ has a force plateau six times higher than the one with $\theta_0 = 14^o$. In this way, θ_0 variable is another lever to adjust drag force law (as for fold stiffnesses).

Then, we test four values of the number of creases $N = 6, 8, 10$ and 12 (parity constraint [38]), with fixed κ and R and $\theta_0 = 32^o$ defined for all cells as the angle between a valley fold and the central axis. The units are shown in their rest position in Fig6.18b, which correspond to barely different frontal area S_0 (see geometrical basis description above). The crease pattern (number of folds) conditions the morphing kinematics, as well as the elastic properties through the number and arrangement of torsional springs. The N value is thus excepted to impact the shape reconfiguration and the subsequent drag reduction process. Nonetheless, the drag force evolution reported in Fig6.18b shows that all cells experience similar drag as the flow velocity (or C_y) is gradually increased from zero, with deviations only arising at higher C_y, a quick discussion on how to capture the N impact on drag is proposed in the interlude n^o22.

The 3D model enables examination of a generalized waterbomb design, where the number

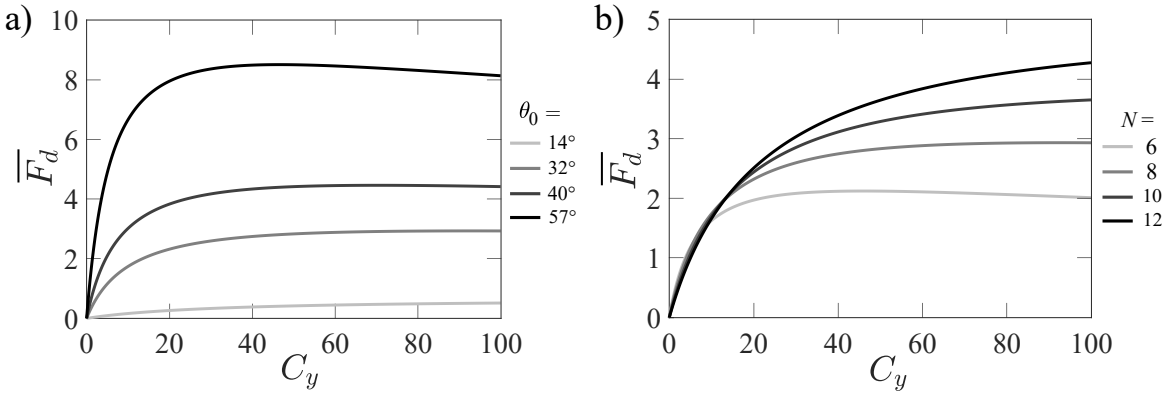

Figure 6.19: Non-dimensional drag force $\overline{F_d}$ as a function of the Cauchy number C_y a) for different rest angles θ_0 and $N = 8$, and b) for different numbers of folds N and $\theta_0 = 32°$ predicted by our 3D theoretical analysis. Values of N and θ_0 correspond to those of the specimens tested experimentally.

of folds N and the rest configuration θ_0 can be changed by adjusting the elastic potential terms in Eq.6.26 and 6.17. Let us present the theoretical prediction for these less trivial parameters.

The Fig6.19 presents the trends of the model, which should be compared to our data in Fig6.18. As in experiments, theoretical predictions in Fig6.19a show that cells starting from a more open rest state (higher θ_0) experience a larger drag force, before reaching an upper plateau whose height increases with θ_0. Meanwhile, Fig 6.19b presents the drag for origami cells with different N, which experiences a similar force at low Cauchy number with a deviation when C_y increases. Those trends can be interpreted using our analysis of the origami elastic energy landscape in Fig6.16c. Close to their rest configuration, all specimens with different numbers of folds have a similar elastic potential energy. Deviations occur at higher deformations, following the N order, which is consistent with the trend observed in the drag.

Interlude n^o22: (N)o collapse ?

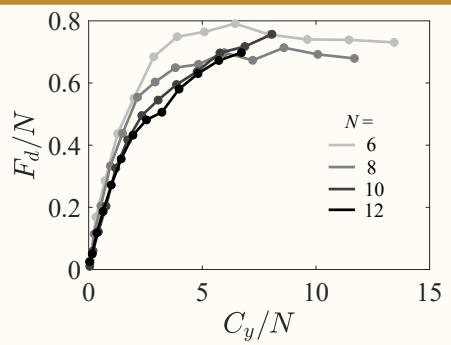

The experimental curves for different resting positions θ_0 and fold numbers N (Figures 6.18 and 6.19) do not collapse, suggesting the Cauchy number does not account for these two parameters. To address this, we propose a simple scaling for the N parameter based on the potential energy of deformation in the theoretical model, represented by torsional springs arranged in series. We deduce that the effective stiffness of the unit K scales as $K \sim N\kappa$. Normalizing the drag force and the Cauchy number by N leads to a collapse of the drag laws towards a single curve, suggesting the waterbomb cell can be modeled as a series of linear springs.

Having established that our theoretical model is consistent with experimental trends, we now compare those answers to the literature on continuously flexible systems, to highlight the role of folds in flow-induced reconfiguration and its impact on drag reduction.

6.7 Reconfiguration process of an origami cell

All the tested specimens involve a drag reduction process in comparisons of an equivalent rigid geometry that differs according to the imposed parameters (stiffness κ, size R, position θ_0, geometry N). Thus, in order to give an overview of all the results, we introduce a new quantity: the reconfiguration number $\mathcal{R}$.

6.7.1 A universal character ?

Introducing the reconfiguration number $\mathcal{R}$ is a common practice in the literature on drag reduction through deformation [15, 16]. Here, $\mathcal{R} = F_d/F_{d,r}$ compares the drag force on a deforming origami cell F_d to that on a rigid unit with the same geometry $F_{d,r}$. This rigid reference corresponds to the cell frozen in its rest configuration, and thus differs for each specimen. The corresponding drag $F_{d,r}$ is evaluated by fitting a rigid body U^2 law on drag measurements at low speed where the deformation is still negligible.

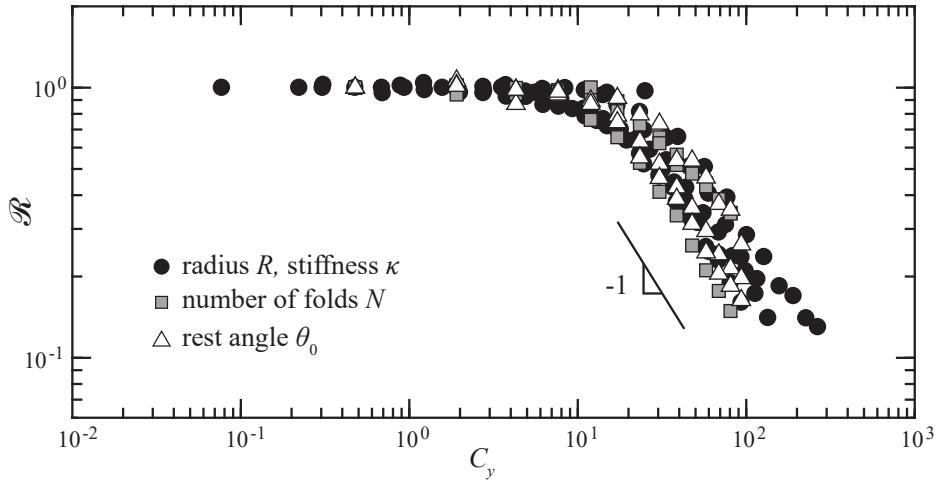

Figure 6.20: Reconfiguration number $\mathcal{R} = F_d/F_{d,r}$ comparing the drag force on a deforming cell F_d to that of a rigid one with the same geometry $F_{d,r}$, plotted as a function of C_y. Symbols correspond to different parametric series of cells.

The evolution of $\mathcal{R}$ as a function of the Cauchy number is reported in Fig 6.20, with one marker type for each series as detailed in the legend. The remarkable collapse onto a single universal curve reflects similar effects of deformability for all waterbomb origami geometries. The curve also shows a clear transition of the drag scaling with flow speed (or with C_y). At low C_y, when the fluid loading is small compared to the origami cell rigidity, the drag follows a bluff body law, hence $\mathcal{R} \sim 1$. When C_y increases, fluid forces become dominant and result in significant deformation. The reconfiguration number then decays. In log-log scale this decay follows a constant slope near -1, which is consistent with a plateau-like drag force evolution : $\mathcal{R} \sim C_y^{-1} \sim F_{d_r}^{-1} \propto U^{-2}$, which leads to $F_d \propto U^0$.

More discussions on this number and a comparison with the literature will be performed at the end of this section, let us first investigate the origins of this drag reduction process.

6.7.2 Streamlining and surface reduction

To investigate the universal character of the drag reduction process, we further look into its origins, namely: the shrinkage of the frontal area exposed to the flow, and the evolution of the drag coefficient characterizing the effect of shape streamlining.

In order to probe the streamlining effect, we first compute the instantaneous drag coefficient of our folded shapes defined as $C_d = F_d/(1/2\rho U^2 \pi R^2)$ where we take the flat state πR^2 as

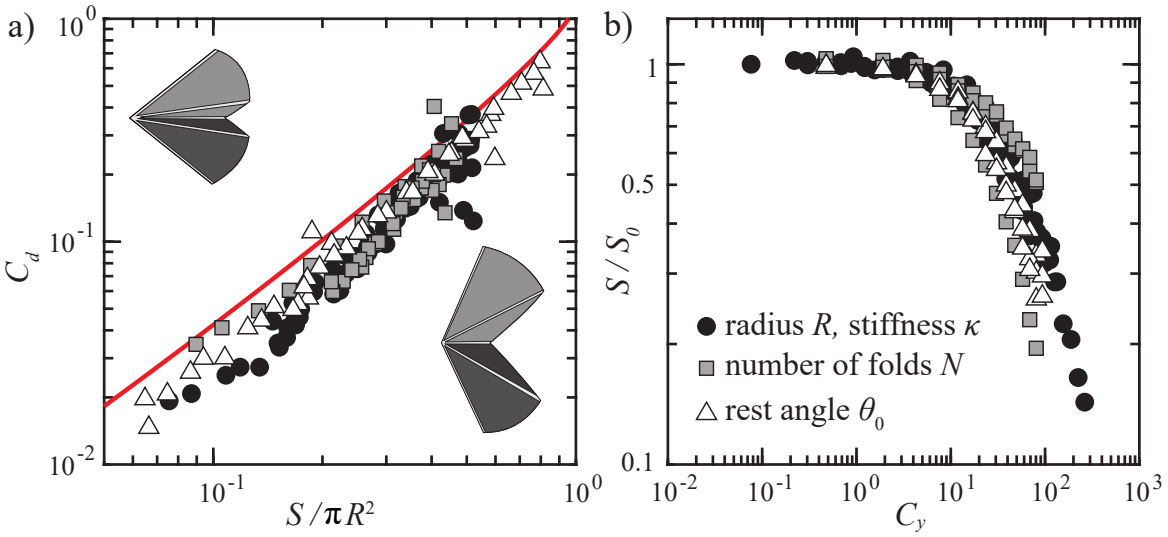

Figure 6.21: a) Instantaneous drag coefficient $C_d = F_d/(1/2\rho U^2 \pi R^2)$ as a function of the frontal area S (normalized with the flat disk area πR^2), characterizing the cell aerodynamics as it folds. Data are compared to that of a hollow cone with varying opening angles (red line), adapted from a linear fit of Hoerner's data in [114]. b) Dimensionless frontal area relative to the one at rest S/S_0 as a function of the Cauchy number C_y.

the reference area. The values of C_d are reported in Fig6.21a as a function of frontal area $S/\pi R^2$ normalized by the flat area, which reflects its degree of closure. Data collapse onto a single curve. It is expected for cells with the same $N = 8$ crease pattern, corresponding to data points of the $\kappa-$ and $R-$series (circle markers), and of the θ_0-series (triangles). Those specimens indeed fold along the same kinematic pathway, meaning that they go through the same continuous sequence of shapes that determines instantaneous fluid forces. The collapse of data for cells with varying N (squares) is however less expected, as their crease patterns produce different geometries and folding pathways. Nonetheless, origami cells with the same degree of closure (i.e. same $S/\pi R^2$) but a different number of lobes, appear to have similar drag coefficients. As a baseline for comparison, we also report the experimental data of Hoerner, [114] for a nearby but simpler geometry of hollow cone with varying opening angle (red line in Fig.6.21a). Despite their more complex shapes, origami values are consistent with that of a cone, although slightly smaller overall.

In Fig6.21b, we report the shrinkage of the frontal area exposed to the flow S/S_0 for all our origami specimens. Here again, data gather onto a master curve. A given flow thus induces similar area reduction regardless of the number of folds or the initial state. This non-dependence on θ_0 is surprising: deployed units (large θ_0) are subjected to stronger fluid loading, and we would therefore expect greater relative closure than for small-θ_0 ones. The minor influence of the number of folds is also non-intuitive as it determines the shape of the cell and its mechanical properties, which both play a role in its reconfiguration in a flow. Regarding the latter shape aspect, Fig6.21a tends to show that geometrical differences related to the number of lobes affect little the aerodynamics of the cell. As for the mechanical properties, we discuss in the section on theoretical models the similarities between the elastic potential energy landscape associated with each folding pattern (see 6.16), which would offer a possible explanation for the collapse of Fig6.21b.

The two figures thus show that origami cells feature a similar evolution of the frontal area with the Cauchy number, and of the drag coefficient relative to this area. Taken together, those shared empirical trends lead to the universal curve for $\mathcal{R}(C_y)$ (see interlude $n^o 23$ as well). We therefore understand that the drastic area decay past a critical Cauchy number, combined with the streamlining effect, works together to counteract the increase of dynamic

pressure forces with flow speed. It leads to the observed velocity-independent drag that we are going to compare with the typical response of flexible continuous systems.

Interlude n^o23: Collapses for C_d and S/S_0 provide $\mathcal{R}$

The master curve obtained when plotting the reconfiguration number as a function of the Cauchy number in Fig6.20 can be "mathematically derived" from the collapse of the data in Fig6.21a and Fig6.21b. Fig6.21b shows that $S/S_0 = f(C_y)$, meaning that the surface ratio (for all specimens) is a function of C_y. Additionally, the linear trend in the log-log plot of Fig6.21a suggests that C_d is a power law function of the frontal area: $C_d = \left(S/\pi R^2\right)^{\lambda}$. By definition, the instantaneous drag coefficient is related to the drag force by $F_d = 1/2 C_d \rho U^2 \pi R^2$, the reconfiguration number rewrites as $\mathcal{R} = F_d/F_{d,r} = C_d/C_d(S_0)$. Using the previous relationships, we get:

$$\mathcal{R} = \left(\frac{S}{S_0}\right)^{\lambda} = f(C_y)^{\lambda} \tag{6.28}$$

Note that this derivation predicts $\lambda = 3$ (by combining Eq 6.16 and 6.27) and and the experimental fitting gives $\lambda \approx 2.3$.

6.7.3 Super-Reconfiguration

The waterbomb unit significantly differs from the continuous flexible structures of the literature. In particular, due to the nature of mechanical deformation that is focused on creases. The latter act as torsional hinges and control the deformation's kinematics, enabling significant shape changes.his leads to a significant change in fluid forces, resulting in a drag component that is no longer dependent on the incoming flow velocity for large deformations.

Despite this, our findings align with previous studies on fluid-elastic behavior in continuous flexible materials. The shape reconfiguration is still determined by the equilibrium of fluid forces and structural stiffness, as reflected by the Cauchy number[13, 15, 16]. However, the source of elastic restoring forces in our case comes from folds rather than bending, thus requiring a revised definition of the Cauchy number.

The evolution of $\mathcal{R}(C_y)$ for our folding structure (Fig6.20) exhibits the same trend as a flexible plate or disk, shown in Fig6.22c. A critical C_y triggers a shift in the dependence of drag on flow speed, as fluid pressure surpasses elastic resistance to deformation. The drag then departs from a solid object behavior $\mathcal{R} \sim 1$, and decreases with a constant logarithmic slope. The associated power law differs depending on the geometry of the object, as shown in Fig6.22a. A rectangular plate that bends downstream in a flow reduces its drag as $\mathcal{R} \propto C_y^{-0.65}$, while it follows $\mathcal{R} \propto C_y^{-0.55}$ for a disk cut along a single radius that rolls up into a cone (Fig6.22b). Here, the drag reduction is even more pronounced with a reconfiguration number that follows the power law $\mathcal{R} \propto C_y^{-1}$, reflecting the plateauing of drag with flow speed. This is attributed to the folds' ability to allow very large deformations: facets can almost align with the flow, and the frontal area exposed to the flow collapses. Thus, with a simple origami cell, we reach a state of "super-reconfiguration".

6.8 Further investigations

In this section we will briefly present some preliminary results, exploring avenues for future research on waterbomb units in a flow. First, we will go back to a property of our origami cell that we have not exploited yet: its bistability, and see its impact on both the deployment kinematics and the drag evolution. Then we will probe the impact of stiffness heterogeneity within the cell on the reconfiguration phenomenon.

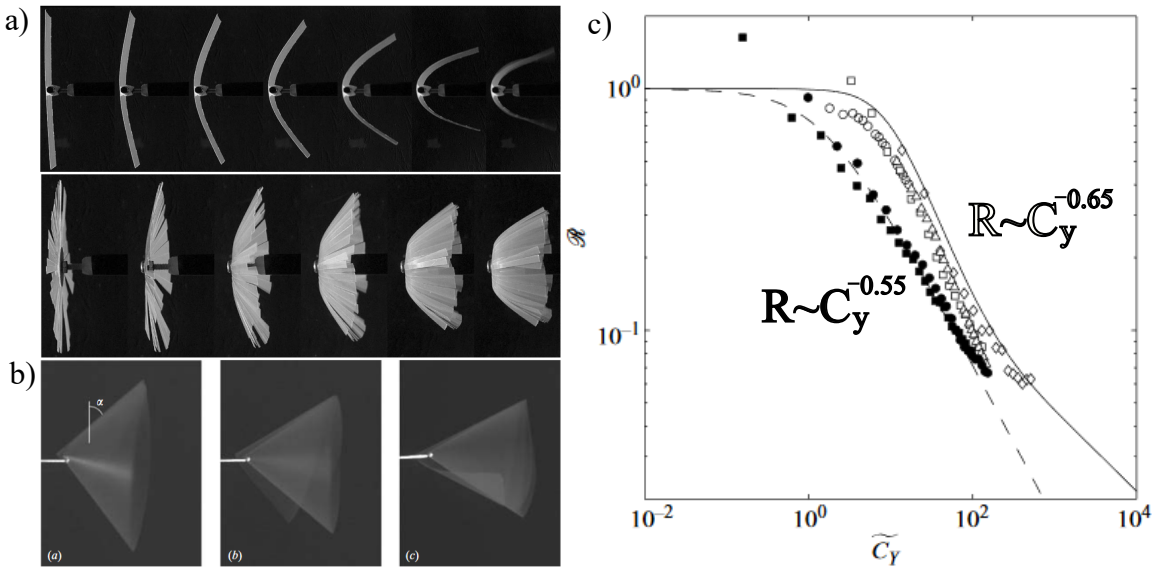

Figure 6.22: Flow-induced deformations of several continuous flexible devices: a) thin plat and disk cut along many radii b) or single radius, the latter rolling up into a cone shape. c) Reconfiguration number $\mathcal{R}$ against Cauchy number$\tilde{C}_y$ (adapted form to take into account for blockage effect) for the two flexible cut disks, which experience different drag reduction processes. All pictures and graph come from [16, 15]

6.8.1 Bistability

One of the most sought-after properties of mechanical studies on foldable structures inspired by origami technology is multi-stability. Whether it is a complete multi-vertex partition or a simple cell, the presence of several stable configurations allows one to predict the shape of an object and program its resting state. This is particularly valuable for systems such as Miura-ori folding maps in Fig6.23, where one clearly distinguishes the two stable states: the compact configuration and the unfolded one; to ensure their stabilities the manufacturer plays on the angle α that define the elementary pattern (inset in Fig6.23a)[89]. Another insight is given by the origami tube which uses a zig-zag crease pattern to program a curvature once unfolded. Here again compact and deployed states are both stable (see Fig6.23b). The multi-stable property also allows for significant shape changes with weak external loading variations, making it valuable for fluid-structure interaction.

As mentioned before, the waterbomb cell has two stable rest configurations, with respective angles θ_0 and θ_0^*, and it can snap from one to the other by passing through the unstable state $\theta = 90^o$ (see Fig6.23c and interlude n^o21). Nevertheless, we have not exploited this bistability yet, as we have focused so far on the closing of origami units in a flow starting from the rest angle θ_0. To exploit it, we just have to turn the origami around, with its concave side facing the incoming flow. As we increase the flow speed, the cell then opens towards its flat state, as shown by the evolution of the frontal area S in Fig6.24a. It induces a strong increase of the drag force, which is then larger than the load on a rigid origami with the same geometry, shown in black in Fig6.24b. As it reaches its planar state, the origami snaps to its second equilibrium configuration θ_0^*, with a convex side now facing the flow. This sudden shape change $\Delta S \approx 0.33\%$ induces a drop of the drag force $\Delta F \approx 0.14N$ (63% of the maximal value) in Fig6.24b. Note that the flat configuration is unstable so that the slightest perturbations coming from the flow or other sources can overturn the origami before reaching a totally flat state (that is $S/S_0 = 1$ in Fig6.24a). Therefore the critical velocity U_c is expressed experimentally as an interval as illustrated by the red shaded area in Fig6.24a.

After the snap transition, the deformation kinematics is the same as described in the pre-

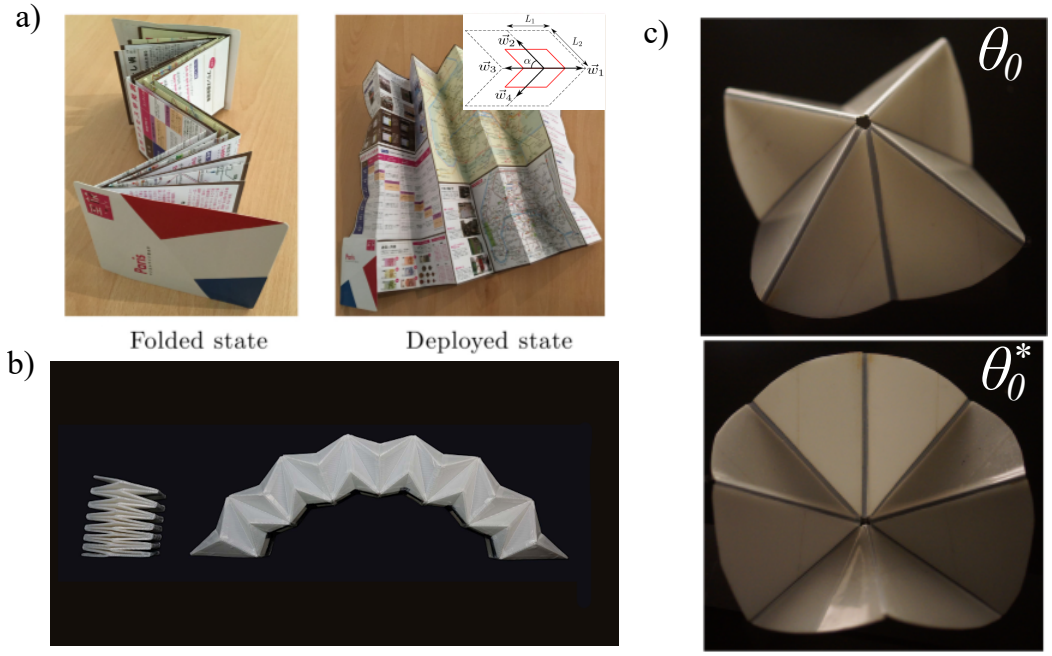

Figure 6.23: a) Folded map in this two equilibrium states, based on the miura ori crease tessellation (from Miura-ori Lab and [89]).b) Origami arch in its two stable states, compact and deployed [115].c) Classic waterbomb unit in its two stable rest configurations, characterized by θ_0 and θ_0^* respectively.

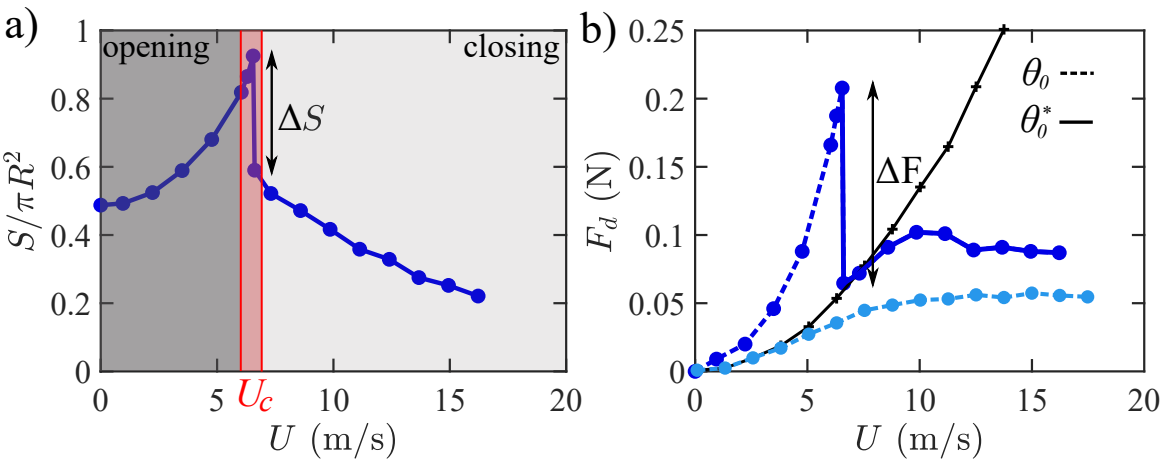

Figure 6.24: a) Evolution the frontal area $S/\pi R^2$ relative to the area of the flat configuration, as a function of the free-stream velocity U. The transition between the opening and closing regime occurs in velocity interval around the critical velocity $U_c = [6, 7.3]$ m/s (red area). b) Evolution of the drag force with U, with a drop ΔF (in dark blue). It is compared to a rigid origami (in black line) and with the flipped configuration with the same cell parameters: $N = 8$, $\theta_0 \sim 30^o$, $\kappa = 9.9 \times 10^{-3}$ N and $R = 5$cm. All experimental data come from R. Nain's experiments

vious sections, with a decrease in the surface area and a plateauing of the drag force. For comparison, the force curve associated with the closing process is reported in the dash light blue line on Fig6.24b. One can note that if the two origami units have the same initial and mechanical parameters, the plateau does not converge to a similar force value. This difference is explained by the fact that the equilibrium state is no longer the same for the two curves. Indeed, in the case of a pure closure pathway, the cell has θ_0 as the reference state, whereas the second one equilibrates at θ_0^* after snaping. The differences and the links between θ_0 and θ_0^* are briefly presented in the interlude n^o24, but let us simply remember that this second equilibrium state corresponds to a larger surface and therefore to a more

consequent force setting. As proven by our experimental series on θ_0, more open angles generate larger drag forces.

Experimental studies (which will not be detailed here) have been carried out by Rishabh Nain on the effect of the origami parameters (stiffness, geometry,...) on such behavior and on the value of the critical speed U_c. This work shows that it is also possible to tune both the transition speed and the force jump by changing the fold stiffness, the initial configuration, the radius and the number of folds. These results are also captured by a theoretical model similar to ours, extended to encompass the entire deployment kinematics. In his PhD, Rishabh Nain also proposes a possible application of the waterbomb cell to create of a passive valve: it uses bistability to modify the pressure drop within a duct, an illustrative overview of its work is proposed in the main conclusion.

Note that we studied a single origami geometry here, but it opens the way to the investigation of other patterns with multiple vertices, or non-uniform fold arrangements, which will have various kinematics of deployment. One can also think of a heterogeneous distribution of fold stiffness, as we will probe in the next subsection.

Interlude n^o24: Two stable states : θ_0^* as a function of θ_0

The gap between the two drag force curves and the origami pictures (Fig6.23c) indicates that the two states of stability correspond to different opening angles. The geometrical analysis of the waterbomb cell in the theoretical section showed that θ_0 is the angle that minimizes the elastic energy with a zero value ($E_{el} = 0$). To determine the second equilibrium state θ_0^*, we need to find the second root of $dE_{el.}/d\theta_0$ in the second domain of definition ($[\pi/2, \pi - \alpha]$).

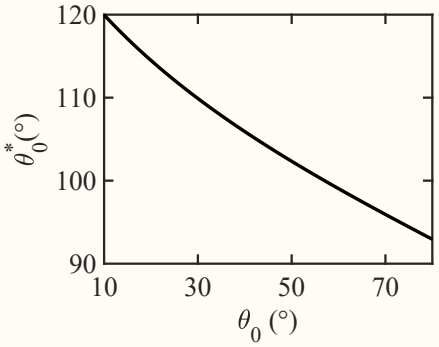

$$2(\theta_0^* - \theta_0) + (\phi_0^* - \phi_0)\frac{d\phi}{d\theta}|_{\theta=\theta_0^*} = 0$$

¨Our direct numerical resolution shows the evolution of $\theta_0^*(\theta_0)$ on the graph. We observe that the two states are not symmetrical with respect to π and then lead to different plateaus of drag.

6.8.2 Folds with different stiffness

So far we have studied the response of symmetrical crease patterns, with folds that have the same stiffness. But many folded structures in nature, such as insect wings or tree leaves [116, 117], have complex networks of folds/veins with varying stiffness distribution. In order to probe the effect of adding heterogeneity in our study, we have modified the stiffness of a single crease in a waterbomb cell and studied its reconfiguration (closure kinematics only).

The cell tested (shown in Fig6.25a) has seven folds of stiffness $\kappa_1 = 9.9 \times 10^{-3}$ N and one almost five times stiffer $\kappa_2 = 5.3 \times 10^{-2}$ N. To characterize shape changes, we measure both the evolution of the total frontal surface (four lobes, highlighted in blue) and that of the rigid fold (in red), both being normalized by their surface in the absence of flow, and plotted as a function of the incoming velocity in Fig6.25a.

Although both surfaces decrease with increasing flow velocity, the lobe with the stiffer fold closes less than the whole structure due to its higher stiffness. Some images of the deformation are shown in Fig6.25b: the presence of this fold generates an asymmetrical

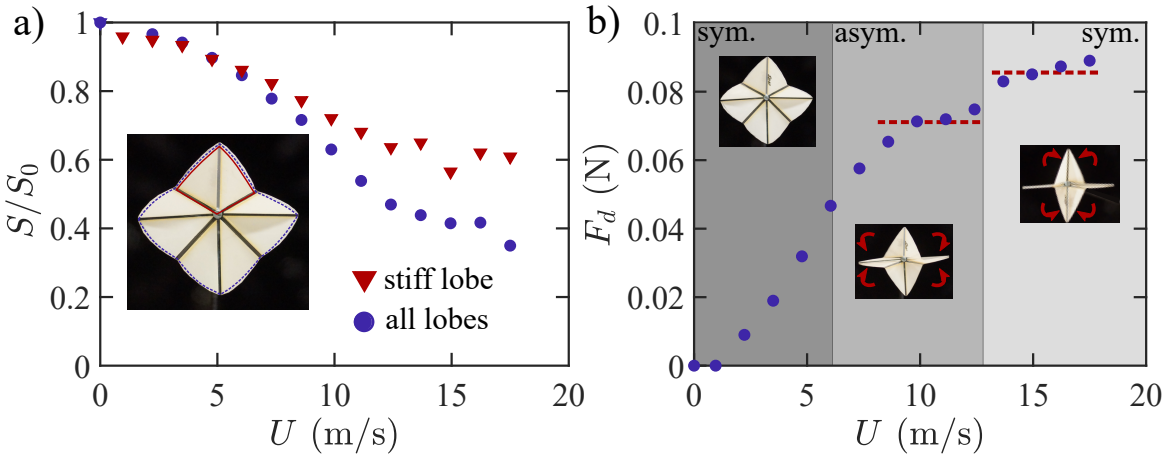

Figure 6.25: a) The frontal area of the whole origami units and the non-uniform lobes against fluid flow velocity, both normalized by their initial values.b) Evolution of the drag forces for a non-uniform waterbomb unit, the stiffer fold leads to a double drag plateau.

folding with two lobes closing while the stiffer lobe and the opposite one remain open. They then close at higher speeds, around 15 m/s. This kinematics leads to a different evolution of the drag force. The two-stage closure kinematics results in two stagnation regimes for the force illustrated by the dotted red lines in Fig6.25b. It should also be noted that the height of the two plateaus does not correspond to either of the two fold stiffness. Indeed, the elasticity parameter is not sufficient to explain the reconfiguration mechanism. It is necessary to take into account the new folding kinematics and the stiffness ratio between the two types of folds.

A further step would be to investigate the effect of the stiffness ratio between the two types of folds and change the number of folds. Indeed here the presence of four lobes induces an asymmetrical closure and impacts the lobe opposite to the stiffened one, but if the structure had three lobes ($N = 6$) we can suspect a different impact on the kinematics.

6.9 Conclusion

In this chapter, we show that origami articulated kinematics impacts the shape reconfiguration process induced by a flow. We focus on the specific geometry of the water-bomb cell: this elementary unit undergoes large shape changes, with its facets progressively aligning with the flow. This collapse of the frontal area enhances drag reduction, to the point that fluid loading no longer increases with flow speed in the regime of large deformation. Such cancellation of velocity dependence was rarely reported in the literature.

The Origami technique further allows us to easily change mechanical properties through the folds parameter, in order to tune the evolution of fluid forces with flow speed. In particular, our result shows that the upper limit set on drag can be varied by adjusting the fold stiffness or the initial rest configuration. Varying the number of folds otherwise led to unanticipated results. Within the range of crease patterns tested, it appears that details of the folding kinematics do not impact the early stages of the reconfiguration process. Specimens with a different number of lobes share similar global aerodynamics and mechanical load-deflection curves, thus producing similar responses. Some deviations are however observed for larger deformations, which implies that exploring the role of this parameter through the whole kinematics can provide another lever for force control or shape morphing. By comparing the experimental trend with the results reported from previous studies on flexible systems, we show that origami folding can then exacerbate the drag reduction process and reach a super reconfiguration state.

Our experimental approach was complemented by a theoretical model that couples aerodynamics and structural elasticity. We model our origami cell as a collection of rigid panels connected by elastic hinges, and the fluid forces are approximated through a simplified pressure formulation with no retroaction of the body on the fluid. To support this assumption, we implement a more rigorous potential flow model on a single 2D fold, more amenable to such derivations, and which can also take into account frictional forces. Through this simpler geometry, we both demonstrate that our formulation is enough to capture the underlying mechanism in the "super-reconfiguration process" and that skin drag is negligible in the velocity range reached by our wind tunnel setup. Despite our simplifying assumptions, the model is thus consistent with experimental observations and may be adapted to other folding geometries. It paves the way to study the flow-induced deformation of more complex origami specimens.

CONCLUSION

Contributions: another brick in the wall

In this thesis, we aimed to connect the field of fluid-structure interaction with the growing area of research on origami and kirigami. Prior studies on flow-induced deformation primarily concentrated on continuous flexible systems such as beams or plates, and revealed that the behavior can be altered through the object's geometry and mechanical properties. In this work, we extend these studies beyond the traditional framework and examine the impact of a cut and fold substructure on flow behavior. Specifically, we intended to determine if we could control the deformation and forces on a sheet through its cut and folded design.

Part 1 - Introducing cuts to control shapes in a flow

Chap. 1 : Uniform pattern The first chapter focuses on the deformation of a uniform kirigami sheet in a water flow. We start with a cutting pattern made up of parallel and staggered slits on a flat and thin Mylar sheet, which is simple enough for our extensive study and has intriguing features such as extreme stretchability and the creation of a three-dimensional mesotexture upon stretching. We examine the impact of the cuts and their spatial arrangement on the deformations induced by the surrounding fluid flow. A kirigami sheet acts as a poro-elastic system, where the cutting pattern influences both the **elastic properties** and the evolution of the pore shape and size, impacting **fluid loading**.

The mechanical behavior and elasticity of kirigami sheets are determined by an effective stiffness that is directly related to the cutting parameters, allowing for engineered elasticity. This enables us to control the sheet's elastic resistance to fluid forces and regulate its deformation under flow. The interplay between external fluid loads and internal elastic restoring force is captured by the Cauchy number.

We have observed a surprising effect on fluid dynamics due to the presence of cuts: an asymmetrical expansion of the deformation profiles, despite having a uniform cutting pattern. This unique deformation kinematics is due to the formation of a local meso-texture during the stretching of the kirigami sheet. The uncut parts of the sheet rotate out of the traction plane and behave like inclined blades in flow. It generates tangential fluid forces that break the global profile symmetry and causes the sheet to deviate towards one side, which is determined by the local direction of rotation (polarity).

This fluid-structure coupling is multi-scale and complex, with local interactions with the flow at the pore scale impacting the global deformation, which in turn affects the pore geometry. We rationalize our experimental results by developing a continuous model, which provides us with a better understanding of these complex fluid-structure interactions. Having determined the underlying mechanisms of this coupling, we explore ways to manipulate the two factors (stiffness and polarity) to influence the deformation under fluid loading in the next two chapters.

Chap. 2 : Bi-polar pattern In the previous chapter, the elementary cells rotated in the same direction along the sheet. In this chapter, our goal is to vary this direction spatially and explore the effects of a multipolar configuration (specimens with non-uniform polarity along the pattern). To start, we mainly studied bipolar cases, in which the kirigami sheets are divided into two parts, with each portion rotating in opposite directions designated by a sign: $\oplus$ or $\ominus$ based on the standard trigonometric direction.

By adjusting the transition position (the size of each section), the symmetry and amplitude of the resulting shapes can be altered. For instance, a symmetrical morphology can be achieved when the transition is in the center of the sheet, unlike the unipolar kirigami sheets

of Chapter 1. Furthermore, switching the polarity from a $\overline{(+-)}$ to a $\overline{(-+)}$ configuration results in different profiles that are no longer left-right mirror images as seen in the specimens of Chapter 1. For example, a parabolic shape transforms into a hemispherical one in the previously mentioned bipolar symmetrical scenario. Importantly, the direction of rotation is defined relative to the incoming flow. It means that the same kirigami would deform in different ways depending on the direction of the flow direction passing through it.

Controlling polarity provides an interesting lever to influence the symmetry of deformation lobes, motivating us to investigate more intricate arrangements such as tri- or quadri-polarity. However, configurations with excessive polarity changes result in the same symmetrical form as if tangential forces were counteracting each other resulting in a purely normal net force.

Chap. 3 : Bi-zonal pattern We explore a second lever by varying the cutting pattern, leading to a modulation of stiffness (as previously established in Chapter 1). Here again, we start with a simple configuration where the kirigami sheet is divided into two zones: a soft and stiff one whose respective size and relative stiffness are varied (the cutting pattern of the soft portion is kept constant, hence in practice only the stiff part is altered)

Like for the previous bi-polar configuration, the addition of non-uniformity in stiffness disrupts the symmetry of the pattern and provides a different deformation profile depending on the direction of the incoming flow. Thus, according to the polarity exposed to the flow, the fluid forces induce internal tensions that promote the extension of different portions of the pattern. Two distinct scenarios are therefore related: first if the flexible part is strained the resulting deformation profiles tend toward similar shapes regardless of the stiffness difference or size of the rigid part. While if the stiff part is under stress, new behaviors arise such as non-monotonic expansion kinematics characterized by a shift in the lobe trajectory, from the right to the left. Such deviations are still unobserved in the two last chapters for uniform or bi-polar specimens. For several bizonal patterns (rigid portion four times stiffer), we even note an abrupt transition from a symmetrical morphology in which both sides of the sheet is highly stretch to a more conventional asymmetric shape with only the stiff part extending.

This transition is characterized by a sudden decrease in amplitude near a critical velocities range, which is reminiscent of Schouveiler et al. (2013) [74], who studied the transition of a deformation in a continuously flexible disk subjected to a uniform flow. They found specific velocity ranges where distinct deformation modes emerge with sudden shifts between ranges. As such, slight changes in external fluid stimulus are likely to result in large shape variations.

The shift in symmetry during expansion is caused by the competition between two portions of the pattern. Due to the difference in stiffness, the pores open in a sequential manner - starting with the soft part and then the rigid one. This delay in the opening process leads to this non-monotonic expansion in flows that are significantly exacerbated by the gap in stiffness. These singular phenomena can be described using a simplified model or two extensible beams of different stiffness subjected to external fluid loading (whose expression comes from the previous chapters). This simplistic modeling is nevertheless able to capture the non-monotonic kinematics of expansion reported by the experiments and describe the balance between the tension involved by each beam and the external fluid loading.

Modifying the cutting pattern and playing on the stiffness is also an effective way to influence the deformations in flows. The two last chapters provide two levers to influence the kirigami shape, let us finish this first phase by establishing an inverse problem.

Chap. 4 : Shape morphing The two previous chapters pave the way to a wider variety of morphologies and behaviors in flows by introducing heterogeneities in the cutting

pattern. The logical outcome of our story is to reverse the approach and finally solve the shape-morphing problem: "given a desired shape and a specified flow speed, we will seek to determine the appropriate cutting pattern that will allow us to attain it." Thus in this short chapter, we give some insights and clues to address this objective.

Based on an extended version of our theoretical modeling, we propose a complete optimization algorithm to find the polarity and stiff distribution which fit the best with the targeted shapes. From this continuous result, we deduce the real pattern to manufacture through a discretization algorithm and finally test the kirigami sheet predicted. Our unsuccessful attempts indicate that the theoretical formulation must be improved to take into account the mechanical subtleties of non-uniform kirigami patterns.

Part 2 - Drag reduction of cut and folded structures

Chap. 5 : Kirigami sheet and drag force In the second part of the manuscript, we explored the effect of folds and cuts on the evolution of fluid forces acting on our textured structures, comparing them to flexible continuous deformable systems.

In line with the previous chapters, we began with the kirigami structures, whose large deformations significantly impact the evolution of drag $F_d(U)$, resulting in a smaller velocity dependence than the typical quadratic behavior of undeformable bluff-body bodies $F_d \propto U^2$. We first proceeded to drag measurements on uniform specimens of varying effective stiffness K_2 (as detailed in chapter 1). We then demonstrate how fluid forces can be re-scaled by introducing the Cauchy number and normalizing the forces by stiffness: $F_d/K_2(C_y)$.

In the previous section, we demonstrated that the fluid-elastic competition, as characterized by C_y, determines the deformation. We now extend this reasoning to include the drag forces, stiffer patterns will experience a weaker deformation and a stronger drag, leading to the rescaling of F_d with K_2. Hence, effective stiffness plays a crucial role in determining both the deformation state and fluid forces. For a given value of K_2, the resulting forces and shapes will be nearly identical, regardless of the local design of the pattern (i.e., iso-stiffness patterns).

Our prior theoretical modeling used to describe flow-induced deformation has been employed again to estimate the global fluid force, obtained by integrating along the whole deformation profile, the projection of local forces. The results of the model indicate a complex relationship between drag and shape, including a lower blockage and frontal area facing the flow, as well as an increasing streamlining effect. Comparison between theoretical predictions and experiments shows good agreement, suggesting that our simplified modeling captures essential physical aspects (at least for uniform configurations).

We extend our approach to the non-uniform patterns of chapters 2 and 3. We previously showed that the presence of heterogeneities resulted in two different solution forms based on the polarity relative to the incoming flow direction. Similarly, a non-uniform pattern (in terms of polarity or stiffens distribution) experiences two distinct drag laws. This testifies once again to the close link between deformation and fluid forces.

Chap. 6 : Origami unit and reconfiguration In this final chapter, we shift our focus from cuts to folds and explore the world of origami. Compared to the kirigami we can distinguish two key differences: the way it deforms, its elasticity being localized only along folds (rigid face approximation), and its interaction with the surrounding flow, which occurs around the structure instead of through it. Despite these differences, both kiri- and ori-gami methods allow for significant shape changes and engineered elasticity through the local tessellation.

For our experiment, we selected a cell origami pattern, which has symmetrical folding and unfolding kinematics and only one degree of freedom. The pattern, known as the waterbomb unit, is composed of alternating mountain and valley folds radiating from a common vertex. This base is renowned for its bistable properties, but for our purposes, we will focus primarily on its high compaction capacity which leads to modifications of the frontal surface.

Simultaneous measurement of drag and frontal surface evolution reveals unusual behavior. The fluid flow impacting the waterbomb facets leads to the symmetrical compaction of the whole cell, it induces a significant decrease in frontal surface and a marked reduction in drag. This results in the force reaching a plateau where it no longer increases with velocity, indicating an upper limit in the drag evolution.

By varying the parameters of the origami cell: size R, fold stiffness κ, number of folds N and initial equilibrium position θ_0, we notice that these influence both the deformation and forces under flow. The latter result of the comparison between fluid force and elastic response captured by the Cauchy number $C_y = \rho U^2 R^2/\kappa$. Note that for an origami pattern, the structural rigidity is characterized by the crease rigidity κ. Here again, by normalizing the drag force with the fold stiffness, we report the collapse of the trends, meaning that the upper limit of drag is notably controlled by the latter.

Our approach is completed by the derivation of a theoretical model based on the minimization of the balance between an elastic potential energy term that models the folding pattern as a network of torsional springs (acting as hinges between two rigid facets) and the work of the fluid pressure forces depending of the folded state. This theoretical model is able to describe the experimental results and identifies the influence of subtle parameters, such as initial angle and number of folds, on the deformation and drag reduction process.

Finally, despite the dissimilarity in deformation kinematics between origami articulated systems and continuously flexible materials, they both exhibit similar reconfiguration scenarios: at low speeds, drag follows the bluff body law in U^2, but beyond a certain critical Cauchy range, a significant change in the shapes occurs with a marked decrease in forces. The presence of folds enables higher levels of deformation and results in a super reconfiguration state with a more pronounced reduction of drag than the continuous flexible systems.

How large is the wall?

Our study illustrates the potential of folded and cut structures to gain control of shapes and force evolution within a fluid environment. By modifying the local patterns, we influence the internal structural stiffness that counterbalances the external fluid loading that provides a complex and rich interplay between the sub-structure and the surrounding flow. By making the bridge between flow-induced deformation problems and architectured design we, therefore, pave the way if a new type of fluid-structure interaction problem.

Perspectives: Some stones to mark the trail

The work presented in this manuscript mainly focused on a single type of cutting and folding pattern, as a starting point of this novel approach. We selected patterns simple enough to allow for representative parametric studies, and complex enough to produce new behaviors compared to traditional continuous flexible systems.

Nevertheless, as illustrated throughout the different chapters, other tessellations exist and have already been investigated in the literature, whether for mechanical or purely geometrical studies. The coupling with a fluid flow is expected to depend on the type of network, with a new pattern constituting a new problem. To this end, we have already explored some leads that we will present as a perspective for future work. Most of the following points have been investigated in the context of research internships that I co-supervised, and the name of the person (whom I thank again) is indicated in the title.

Other cutting patterns - E. Forestier

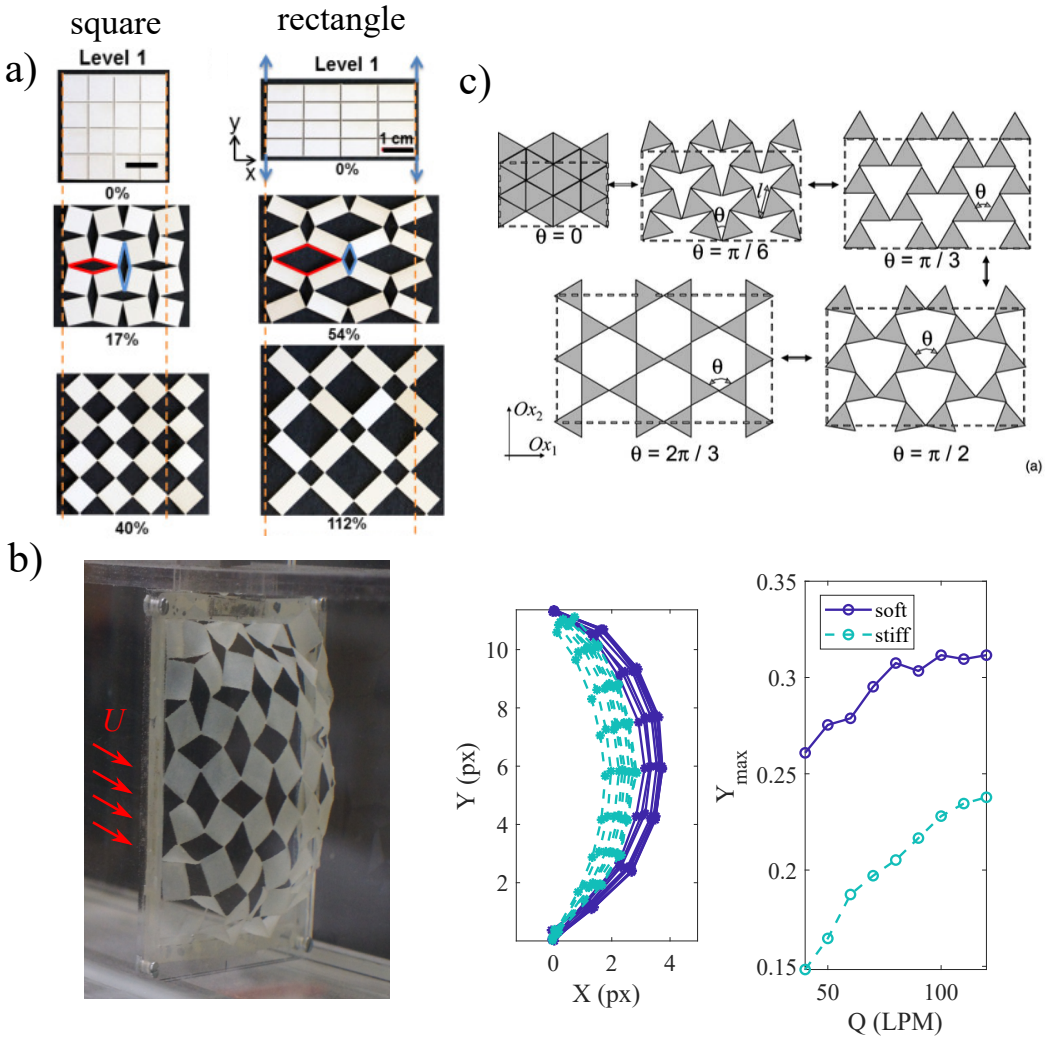

Figure 6.26: a) Cuts divide the sheet into a collection of squares or rectangles, which provide different stretching capacities and porosity-strain law, from [72] b) typical 3D shape reached by a kirigami sheet with a square pattern, the deformation profiles are extracted from a side view for two patterns with different rigidities (different slits lengths).c) Changing the shape and connectivity of the pattern has an impact on the kinematics of the pore opening, here the uncut parts form a network of the triangle that exhibits a large porosity, from [118].

Another popular kirigami pattern is an array of perpendicular slits as shown in Fig6.26a,

which allows the sheet to open up and stretch through a rotation in the plane of the uncut material. Cuts divide the sheet into a collection of squares, which are connected at their vertex by slender flexible ligaments that act as hinges. To avoid any plasticity effects in the latter, we worked with rubber materials. Upon stretching, coordinated rotation of the rigid tiles results in the bi-axial expansion of the sheet.

Those kirigami sheets were clamped at their four edges and subjected to a water cross-flow. Fig6.26b shows the shape profiles of two specimens with different slits lengths. Here again, varying the cutting parameters impacts the effective stiffness, which affects the amplitude of the deformation (amplitudes deformation profiles reported in Fig6.26b).

A new lever is to play on the shape and size of the pores by modifying the pattern layout. One can for example introduce an aspect ratio and use rectangles instead of squares (see Fig6.26a), which will modify both the porosity-elongation law and the bi-axial extension capacity [72]. Or even use triangles or other polygons whose connectivity can be tuned to enlarge the deformation domain [118], and reach a new type of 3D morphologies (see Fig6.26c).

Passive flow controller

In this manuscript, we often neglected the retroaction of the structure on the fluid flow, which was modeled with an undisturbed uniform velocity. An exception is the blockage effect for kirigami sheets, which was accounted for by a velocity correction factor depending on the local porosity. While this simplified description of the fluid captured reasonably well experimental behaviors, it would be interesting to look at the flow structures generated by our sheets.

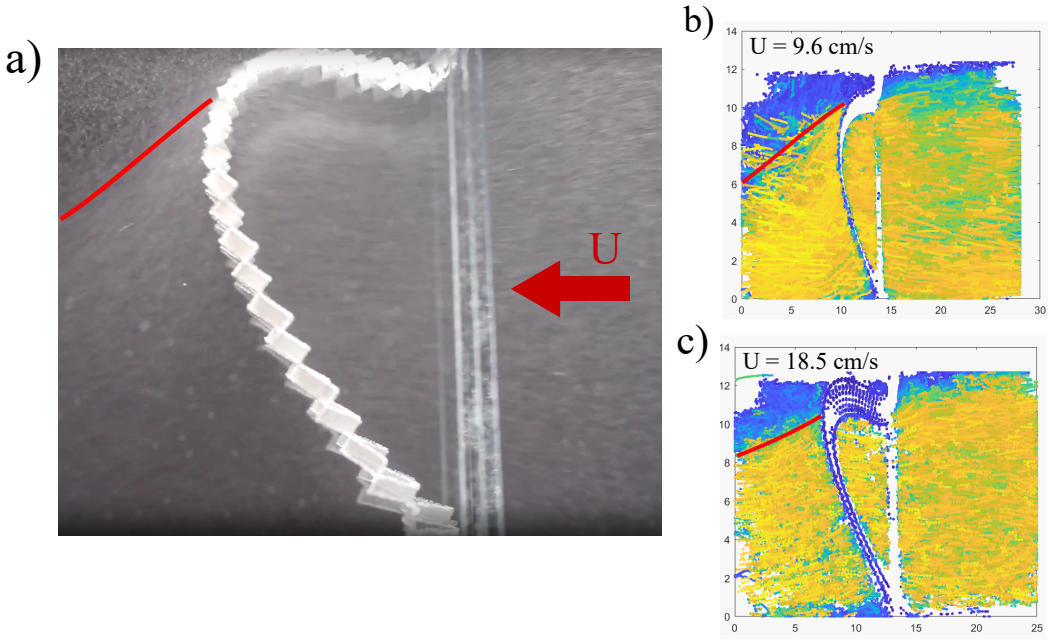

Figure 6.27: a) Snapshot of the PTV measurement, the beads pass through the deformed kirigami sheet, by tracking the beads we aim to find the velocity field. At a first glance, we report the mapping of the average velocity of each bead along its trajectory, two flow speed is reported b) $U = 9.6cm/s$,c) $U = 18.5cm/s$. The deformation impacts the downstream flow.

We carried out coarse preliminary measurements of the velocity field of the flow through a uniform kirigami sheet with Particle Tracking Velocimetry. Namely, we seeded the water channel with iso-dense particles, illuminated a plane crossing the kirigami sheet in the middle of the channel, and tracked the motion of the particles with a high-speed camera

(see Fig6.27a). The trajectory of each particle is reported in Fig6.27b-c, and color-coded with the corresponding average speed (from blue to yellow for increasing speeds). Upstream of the kirigami sheet, the flow is fairly uniform and parallel to the channel walls. However, the kirigami seems to reorient it to one side in its wake, and we also notice a recirculation zone with lower speeds behind the lobe (in blue, and delineated by a red line). Modeling those flow features does not seem crucial to capture experimental behaviors here. However, such large-scale fluid structures could play a more significant role in other configurations and lead to interesting behaviors. In this case, we would have to resolve the dynamics of the fluid as well to model the fluid-structure interaction.

Alternatively, instead of focusing on the sheet itself, one could use it as a way to influence fluid flow. We could then test other morphologies (symmetrical for example) to change the wake and influence the surrounding flow.

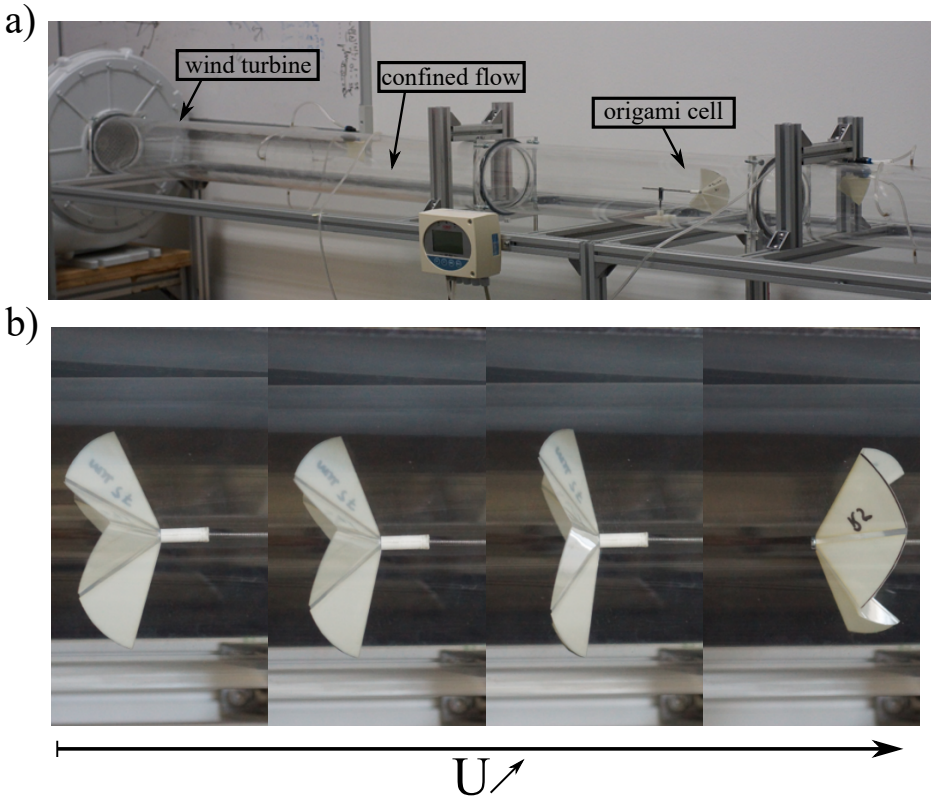

Figure 6.28: a) Experimental set-up of a passive valve, with a waterbomb unit regulating the air flow in a tube. b) The origami gradually opens and obstructs the flow before snapping to its second equilibrium state.

Passive smart sail and Drag forces control - S. Van Heiningen

In the manuscript, we talked about designing kirigami sheets to reach a targeted shape in a flow. We could extend this approach to fluid forces, and find the cutting pattern that produces a desired drag in a given flow or tune its evolution with the flow speed. For that, we would need to further investigate the relationship between flow-induced deformations and the resultant drag.

Such poro-elastic mechanisms are interesting to reduce the fluid load on porous sails or nets for example and protect them in strong winds or currents. If we control the evolution of forces with flow speed, we could also have a system that is operational in a given range of flow speeds (as a lifting surface for a sail for example), while preventing breakage in extreme conditions.

We have also pointed out that shapes and drag can depend on the direction of the flow that is passing through the porous sheet. This unusual property may be interesting for applications such as filtration or fog capture where the direction of the incident flow can play a role (fishing net, fog net,...). We could also imagine new sails or soft windmills which behave differently depending on the flow direction.

Let us now discuss another research topic (the ultimate one !) related to origami folded structures.

Foldable valve - R. Nain

The origami project can be investigated further along several axes. Before discussing new patterns and the non-uniformity of folds, let us envision a possible application of the water-bomb unit as a passive valve / hydro-breaker.

As discussed in chapter 6, this elementary origami cell is bistable (although we have not exploited it in our current studies). In his PhD, Rishabh Nain uses this property to implement a valve that opens and closes passively in an airflow inside a pipe (see its experimental set up in Fig6.28a). As the flow speed increases, the cell (that is placed with its concave side facing the flow) progressively opens and obstructs the conduct, as reported by the snapshots in Fig6.28b. Upon reaching a flat configuration, it then snaps to its second equilibrium state, clearing the way for the flow. One can change the critical flow speed at which it snaps through the structural parameter of the origami, and tune the relationship between the pressure drop across the origami valve and the flow rate.

The end

These perspectives are examples of research avenues that build on the two elementary bricks that we have laid. For my part, the journey ends here =(, but I think that the view of the landscape is beautiful from here.

Appendix: Substantial Summary

Advertisement, this substantial summary has been written in French but the whole manuscript is in English.

Les structures minces et flexibles se déforment et adaptent leurs morphologies face aux sollicitations externes de leurs environnements. Dans le monde végétal les systèmes biologiques utilisent leurs déformabilités pour réduire l'intensité des forces fluides agissant sur elles. Cette capacité leur confère une résistance accrue face à des écoulements fluctuants grâce au processus de réduction de traînée. Les déformations passives induites par le mouvement du fluide peuvent également jouer un rôle fonctionnel en améliorant les performances aérodynamiques ou en étant utilisées comme moyen de contrôle de l'écoulement. Toutefois, pour remplir ces fonctions, il est nécessaire de pouvoir programmer la réponse mécanique de la structure et anticiper les formes qu'elle peut adopter. Jusqu'à présent, les recherches scientifiques se sont principalement concentrées sur l'interaction entre des structures élancées se déformant par flexion, en modifiant leur rigidité et leur géométrie. Dans le cadre de cette thèse, nous explorons une autre approche, inspirée de l'art du pliage origami et de la découpe kirigami, qui permet de créer des formes programmables et modulables.

L'introduction de plis et de coupures sur une feuille mince permet d'obtenir des changements de formes complexes en trois dimensions et altère ses propriétés mécaniques, ce qui influence son comportement lorsqu'elle est soumise à un écoulement. Dans notre étude, nous examinons expérimentalement l'effet de l'ajout d'une telle sous-structure sur la déformation et les forces exercées par le fluide, en variant systématiquement les motifs des fentes et des plis. Ces études empiriques sont complétées par le développement de modèles théoriques qui contribuent à une meilleure compréhension des mécanismes sous-jacents. La première partie de la thèse est dédiée aux structures coupées kirigami et leurs déformations sous chargement hydrodynamique. A l'aide d'une étude paramétrique sur le schéma de fente locale (en quinconce et en parallèle) nous montrons son rôle sur le comportement mécanique intrinsèque de la structure globale. En modifiant le schéma de fente il est alors possible de moduler la rigidité et la capacité de déformabilité de nos systèmes. Une fois sous écoulement, nous mettons en avant que l'équilibre des efforts fluides externes et la réponse élastique interne est à l'origine des formes obtenues. A l'aide de modèles théoriques et expériences sur des systèmes rigides de géométrie analogue nous avons également mis en lumière le rôle de la porosité. Les fentes lors de la déformation s'ouvrent et laissent passer l'écoulement au travers de la structure, modifiant le champ de vitesse et les forces fluides locales (chapitre 1).

Cette première étude sur des schémas de découpe uniforme (identique sur toute la surface de la structure) pose les bases du couplage hydro-élastique. Nous investiguons par la suite des dispositions de fentes plus complexes, avec l'ajout d'encoches à proximité des fentes venant modifier la cinématique d'ouverture de la structure et impacter l'orientation locale des forces fluides. Ce nouveau levier permet de contrôler la symétrie des déformations à un chargement fluide donné en modulant la polarité locale du pattern (chapitre 2). Nous regardons également de plus près le cas de schémas hétérogènes, pour lesquels les découpes sont reparties de manière non-uniforme sur la surface de la feuille. L'ajout d'une portion plus rigide modifie le comportement de la structure sous écoulement selon que la direction de l'écoulement induisant l'ouverture de la partie souple ou rigide respectivement. Cette dysmétrie selon l'environnement fluide est alors investiguée avec une étude paramétrique sur des configurations bizones dont la rigidité de chaque bloc est modifiée (chapitre 3). A l'aide de ces deux nouveaux leviers nous formulons un problème

inverse qui cherchent à partir d'une forme cible à décrire le schéma de découpe nécessaire à son obtention (chapitre 4).

La seconde partie de nos travaux se centre principalement sur l'étude des forces de trainée (chargement fluide colinéaire à la direction de l'écoulement) s'exerçant sur ces meta-structures. Nous avons en particulier montré que la rigidité encodée par les fentes des kirigamis modulait l'intensité du chargement fluide (chapitre 5). Ces expériences indiquent donc que des structures elasto-poreuses kirigamis sont le siège de lois d'évolution de trainée non-usuelle avec une forte réduction des efforts liés. Nous décrivons par la suite la réponse sous écoulement d'un système pliable origami. Le pattern à l'étude (waterbomb) est composé d'un nombre pair de plis rayonnant depuis un vertex central avec une alternation de montagne et vallée, permettant ainsi de grande variation de surface frontale. Une fois sous écoulement la force de trainée correspondante est fortement impactée par cette réduction d'aire et nous mettons en évidence la présence d'un plateau de force : la trainée ne dépendant plus de la vitesse d'écoulement après un certain niveau de déformation. Ces origamis sont fabriqués à l'aide de la superposition de deux feuilles de thermoplastique d'épaisseur différentes ; une fine pour les plis et une épaisse pour les faces, prévenant ainsi la flexion des faces et localisant la déformation le long des plis. En jouant sur l'épaisseurs des feuillets utilisés, nous effectuons une étude paramétrique de la trainée sur la taille et la rigidité des cellules origamis. Nous avons mis en évidence que la taille des origamis ne modifiait pas l'émergence du régime de plateau mais que la raideur des plis modulait l'amplitude de ce dernier. En jouant ensuite sur le dégrée d'ouverture initiale (modifiable par la thermoformabilité) et la géométrie (nombre de plis), nous montrons également que ces deux leviers peuvent être utiliser pour influer sur l'évolution des forces fluides et le degré de pliage structurel. L'ensemble de ces campagnes expérimentales est complétée par un approche théorique simplifiée qui capture les tendances observées. Notre modèle tenant compte de la réduction de surface liée à la déformabilité et l'augmentation de l'effet de profilage, nous sommes en mesure de faire apparaitre théoriquement ce régime de non-dépendance de vitesse propre à la présence de plis dans la structure.

En résumé nos résultats démontrent que la déformation résulte d'une interaction complexe entre la charge exercée par le fluide (qui évolue avec la déformation) et la rigidité structurelle déterminée par l'arrangement des plis et des coupures. En modulant spatialement ces motifs, il devient possible de contrôler les formes adoptées par la structure ainsi que les forces générées par l'écoulement. Cette approche offre donc une voie novatrice et riche en possibilités pour le contrôle passif et actif du couplage structure dans un environnement fluide via l'architecture locale.

Bibliography

[1] Chuan-Ping Shao, Ye-Jun Chen, and Jian-Zhong Lin. Wind induced deformation and vibration of a platanus acerifolia leaf. *Acta Mechanica Sinica*, 28(3):583–594, 2012. **Cited in page 15**

[2] Steven Vogel. When leaves save the tree. *Natural History*, 102(9):58–63, 1993. **Cited in page 15**

[3] S. Vogel. Drag and flexibility in sessile organisms. *Am. Zool.*, 24(1):37–44, 1984. **Cited in pages 15 and 127**

[4] S. Vogel. Drag and reconfiguration of broad leaves in high winds. *J. Exp. Bot.*, 40(8):941–948, 1989. **Cited in pages 15 and 16**

[5] Deane L Harder, Olga Speck, Catriona L Hurd, and Thomas Speck. Reconfiguration as a prerequisite for survival in highly unstable flow-dominated habitats. *Journal of Plant Growth Regulation*, 23(2):98–107, 2004. **Cited in page 15**

[6] Stephan Vollsinger, Stephen J Mitchell, Kenneth E Byrne, Michael D Novak, and Mark Rudnicki. Wind tunnel measurements of crown streamlining and drag relationships for several hardwood species. *Canadian Journal of Forest Research*, 35(5):1238–1249, 2005. **Cited in page 15**

[7] Juan de Dios Rivera. Aerodynamic collection efficiency of fog water collectors. *Atmospheric Research*, 102(3):335–342, 2011. **Cited in pages 15, 123, 127, and 140**

[8] Karl J Niklas. Differences between acer saccharum leaves from open and wind-protected sites. *Annals of Botany*, 78(1):61–66, 1996. **Cited in page 16**

[9] M. Gomez, D. E. Moulton, and D. Vella. Passive control of viscous flow via elastic snap-through. *Phys. Rev. Lett.*, 119(14):144502, 2017. **Cited in pages 16 and 17**

[10] M. Brandenbourger, A. Dangremont, R. Sprik, and C. Coulais. Tunable flow asymmetry and flow rectification with bio-inspired soft leaflets. *Phys. Rev. Fluids*, 5(8):084102, 2020. **Cited in pages 16 and 17**

[11] S. Ramananarivo, R. Godoy-Diana, and B. Thiria. Rather than resonance, flapping wing flyers may play on aerodynamics to improve performance. *Proc. Natl. Acad. Sci.*, 108(15):5964–5969, 2011. **Cited in page 17**

[12] Guillaume O Antoine, Emmanuel de Langre, and Sébastien Michelin. Optimal energy harvesting from vortex-induced vibrations of cables. *Proceedings of the Royal Society A: Mathematical, Physical and Engineering Sciences*, 472(2195):20160583, 2016. **Cited in page 17**

[13] S. Alben, M. Shelley, and J. Zhang. Drag reduction through self-similar bending of a flexible body. *Nature*, 420(6915):479–481, 2002. **Cited in pages 17, 20, 21, 50, 51, and 166**

[14] S. Alben, M. Shelley, and J. Zhang. How flexibility induces streamlining in a two-dimensional flow. *Phys. Fluids*, 16(5):1694–1713, 2004. **Cited in page 17**

[15] Lionel Schouveiler and Arezki Boudaoud. The rolling up of sheets in a steady flow. *Journal of Fluid Mechanics*, 563:71–80, 2006. **Cited in pages 17, 18, 21, 51, 126, 151, 164, 166, and 167**

[16] Frédérick Gosselin, Emmanuel De Langre, and Bruno A Machado-Almeida. Drag reduction of flexible plates by reconfiguration. *Journal of Fluid Mechanics*, 650:319–341, 2010. **Cited in pages 17, 18, 19, 20, 21, 50, 51, 126, 127, 140, 151, 164, 166, and 167**

[17] L. Schouveiler and C. Eloy. Flow-induced draping. *Phys. Rev. Lett.*, 111(6):064301, 2013. **Cited in pages 18, 50, 51, and 151**

[18] Douglas P Holmes. Elasticity and stability of shape-shifting structures. *Current opinion in colloid & interface science*, 40:118–137, 2019. **Cited in page 18**

[19] Jean-Jacques Marigo. Mécanique des milieux continus i. 2014. **Cited in pages 19, 57, and 67**

[20] Lev Davidovich Landau, Evgenij M Lifšic, Evegnii Mikhailovich Lifshitz, Arnold Markovich Kosevich, and Lev Petrovich Pitaevskii. *Theory of elasticity: volume 7*, volume 7. Elsevier, 1986. **Cited in pages 19, 38, and 67**

[21] Frédérick Gosselin. *Mécanismes d'interactions fluide-structure entre écoulements et végétation.* PhD thesis, Ecole Polytechnique (Palaiseau, France), 2009. **Cited in pages 19, 20, and 21**

[22] Sebastien JP Callens and Amir A Zadpoor. From flat sheets to curved geometries: Origami and kirigami approaches. *Materials Today*, 21(3):241–264, 2018. **Cited in page 23**

[23] L. H. Dudte, E. Vouga, T. Tachi, and L. Mahadevan. Programming curvature using origami tessellations. *Nat. Mater.*, 15(5):583–588, 2016. **Cited in page 23**

[24] Thomas Hull. On the mathematics of flat origamis. *Congressus numerantium*, pages 215–224, 1994. **Cited in pages 23 and 141**

[25] Ning An, August G Domel, Jinxiong Zhou, Ahmad Rafsanjani, and Katia Bertoldi. Programmable hierarchical kirigami. *Advanced Functional Materials*, 30(6):1906711, 2020. **Cited in pages 24, 26, 27, 89, and 117**

[26] Gary Choi, Levi H Dudte, and L Mahadevan. Programming shape using kirigami tessellations. *Nature materials*, 18(9):999–1004, 2019. **Cited in pages 24, 25, and 108**

[27] Aaron Lamoureux, Kyusang Lee, Matthew Shlian, Stephen R Forrest, and Max Shtein. Dynamic kirigami structures for integrated solar tracking. *Nature communications*, 6(1):1–6, 2015. **Cited in pages 24 and 43**

[28] Ruike Zhao, Shaoting Lin, Hyunwoo Yuk, and Xuanhe Zhao. Kirigami enhances film adhesion. *Soft Matter*, 14(13):2515–2525, 2018. **Cited in page 24**

[29] J. T. Bruton, T. G. Nelson, T. K. Zimmerman, J. D. Fernelius, S. P. Magleby, and L. L. Howell. Packing and deploying soft origami to and from cylindrical volumes with application to automotive airbags. *R. Soc. Open Sci.*, 3(9):160429, 2016. **Cited in pages 23 and 25**

[30] K. Miura. Method of packaging and deployment of large membranes in space. *The Institute of Space and Astronautical Science report*, (618):1–9, 1985. **Cited in pages 23 and 25**

[31] Sahab Babaee, Simo Pajovic, Ahmad Rafsanjani, Yichao Shi, Katia Bertoldi, and Giovanni Traverso. Bioinspired kirigami metasurfaces as assistive shoe grips. *Nature Biomedical Engineering*, 4(8):778–786, 2020. **Cited in page 24**

[32] Ahmad Rafsanjani, Yuerou Zhang, Bangyuan Liu, Shmuel M Rubinstein, and Katia Bertoldi. Kirigami skins make a simple soft actuator crawl. *Science Robotics*, 3(15):eaar7555, 2018. **Cited in page 24**

[33] Kento Yamagishi, Takenori Nakanishi, Sho Mihara, Masaru Azuma, Shinji Takeoka, Kazuyuki Kanosue, Tomoyuki Nagami, and Toshinori Fujie. Elastic kirigami patch for electromyographic analysis of the palm muscle during baseball pitching. *NPG Asia Materials*, 11(1):1–13, 2019. **Cited in page 25**

[34] Yigil Cho, Joong-Ho Shin, Avelino Costa, Tae Ann Kim, Valentin Kunin, Ju Li, Su Yeon Lee, Shu Yang, Heung Nam Han, In-Suk Choi, et al. Engineering the shape and structure of materials by fractal cut. *Proceedings of the National Academy of Sciences*, 111(49):17390–17395, 2014. **Cited in page 25**

[35] Xiao Shang, Lu Liu, Ahmad Rafsanjani, and Damiano Pasini. Durable bistable auxetics made of rigid solids. *Journal of Materials Research*, 33(3):300–308, 2018. **Cited in pages 25 and 26**

[36] Mark Schenk and Simon D Guest. Geometry of miura-folded metamaterials. *Proceedings of the National Academy of Sciences*, 110(9):3276–3281, 2013. **Cited in page 26**

[37] Dae-Young Lee, Ji-Suk Kim, Sa-Reum Kim, Je-Sung Koh, and Kyu-Jin Cho. The deformable wheel robot using magic-ball origami structure. In *International Design Engineering Technical Conferences and Computers and Information in Engineering Conference*, volume 55942, page V06BT07A040. American Society of Mechanical Engineers, 2013. **Cited in page 26**

[38] V Brunck, F Lechenault, A Reid, and M Adda-Bedia. Elastic theory of origami-based metamaterials. *Physical Review E*, 93(3):033005, 2016. **Cited in pages 26, 155, 157, and 162**

[39] Ke Liu, Tomohiro Tachi, and Glaucio H Paulino. Invariant and smooth limit of discrete geometry folded from bistable origami leading to multistable metasurfaces. *Nature communications*, 10(1):1–10, 2019. **Cited in page 26**

[40] Scott Waitukaitis, Rémi Menaut, Bryan Gin-ge Chen, and Martin Van Hecke. Origami multistability: From single vertices to metasheets. *Physical review letters*, 114(5):055503, 2015. **Cited in page 26**

[41] Kaori Kuribayashi, Koichi Tsuchiya, Zhong You, Dacian Tomus, Minoru Umemoto, Takahiro Ito, and Masahiro Sasaki. Self-deployable origami stent grafts as a biomedical application of ni-rich tini shape memory alloy foil. *Materials Science and Engineering: A*, 419(1-2):131–137, 2006. **Cited in pages 26, 27, and 28**

[42] Ying-Shi Guan, Zhuolei Zhang, Yichao Tang, Jie Yin, and Shenqiang Ren. Kirigami-inspired nanoconfined polymer conducting nanosheets with 2000% stretchability. *Advanced Materials*, 30(20):1706390, 2018. **Cited in pages 26 and 27**

[43] Midori Isobe and Ko Okumura. Initial rigid response and softening transition of highly stretchable kirigami sheet materials. *Scientific reports*, 6(1):1–6, 2016. **Cited in pages 27, 38, 39, 41, 42, 61, 62, 66, 67, and 88**

[44] Ahmad Rafsanjani and Katia Bertoldi. Buckling-induced kirigami. *Physical review letters*, 118(8):084301, 2017. **Cited in pages 27, 38, and 67**

[45] Doh-Gyu Hwang and Michael D Bartlett. Tunable mechanical metamaterials through hybrid kirigami structures. *Scientific reports*, 8(1):1–8, 2018. **Cited in pages 27, 36, 38, 39, 41, 42, 60, 61, 62, 66, and 88**

[46] Hiroki Taniyama and Eiji Iwase. Design of rigidity and breaking strain for a kirigami structure with non-uniform deformed regions. *Micromachines*, 10(6):395, 2019. **Cited in pages 27 and 116**

[47] Paolo Celli, Connor McMahan, Brian Ramirez, Anton Bauhofer, Christina Naify, Douglas Hofmann, Basile Audoly, and Chiara Daraio. Shape-morphing architected sheets with non-periodic cut patterns. *Soft matter*, 14(48):9744–9749, 2018. **Cited in pages 27 and 88**

[48] Ning An, Meie Li, and Jinxiong Zhou. Modeling sma-enabled soft deployable structures for kirigami/origami reflectors. *International Journal of Mechanical Sciences*, 180:105753, 2020. **Cited in pages 27 and 28**

[49] Lishuai Jin, Antonio Elia Forte, Bolei Deng, Ahmad Rafsanjani, and Katia Bertoldi. Kirigami-inspired inflatables with programmable shapes. *Advanced Materials*, 32(33):2001863, 2020. **Cited in pages 28, 108, and 113**

[50] S Li, H Fang, and KW Wang. Recoverable and programmable collapse from folding pressurized origami cellular solids. *Physical review letters*, 117(11):114301, 2016. **Cited in page 28**

[51] Jing Li, Ranjiangshang Ran, Haihuan Wang, Yuchen Wang, You Chen, Shichao Niu, Paulo E Arratia, and Shu Yang. Aerodynamics-assisted, efficient and scalable kirigami fog collectors. *Nature communications*, 12(1):1–8, 2021. **Cited in pages 28 and 29**

[52] Lawren Gamble, Aaron Lamoureux, and Max Shtein. Multifunctional composite kirigami skins for aerodynamic control. *Applied Physics Letters*, 117(25):254105, 2020. **Cited in page 29**

[53] Ji Zhang, Tiane Li, Changguo Wang, and Xiangqiao Yan. Aerodynamic drag characteristics of miura-ori composite structure. *Journal of Aerospace Engineering*, 34(4):06021004, 2021. **Cited in pages 29 and 30**

[54] Mircea Cozmei, Tristan Hasseler, Everett Kinyon, Ryan Wallace, Antonio Alessandro Deleo, and Marco Salviato. Aerogami: Composite origami structures as active aerodynamic ccontrol. *Composites Part B: Engineering*, 184:107719, 2020. **Cited in pages 29 and 30**

[55] Yi Yang, Marcelo A Dias, and Douglas P Holmes. Multistable kirigami for tunable architected materials. *Physical Review Materials*, 2(11):110601, 2018. **Cited in pages 36, 37, 38, 67, 68, and 113**

[56] Yichao Tang, Gaojian Lin, Shu Yang, Yun Kyu Yi, Randall D Kamien, and Jie Yin. Programmable kiri-kirigami metamaterials. *Advanced Materials*, 29(10):1604262, 2017. **Cited in pages 38, 39, 67, 68, 69, 71, and 81**

[57] Midori Isobe and Ko Okumura. Continuity and discontinuity of kirigami's high-extensibility transition: A statistical-physics viewpoint. *Physical Review Research*, 1(2):022001, 2019. **Cited in pages 39, 41, 67, and 88**

[58] Terry C Shyu, Pablo F Damasceno, Paul M Dodd, Aaron Lamoureux, Lizhi Xu, Matthew Shlian, Max Shtein, Sharon C Glotzer, and Nicholas A Kotov. A kirigami approach to engineering elasticity in nanocomposites through patterned defects. *Nature materials*, 14(8):785–789, 2015. **Cited in pages 39, 41, 42, 60, 66, and 88**

[59] Basile Audoly and Yves Pomeau. Elasticity and geometry. In *Peyresq Lectures on Nonlinear Phenomena*, pages 1–35. World Scientific, 2000. **Cited in pages 41 and 141**

[60] M Guttag, Hussain H Karimi, C Falcón, and Pedro Miguel Reis. Aeroelastic deformation of a perforated strip. *Physical Review Fluids*, 3(1):014003, 2018. **Cited in pages 50, 51, 56, 123, and 151**

[61] Yaqing Jin, Jin-Tae Kim, Shyuan Cheng, Oumar Barry, and Leonardo P Chamorro. On the distinct drag, reconfiguration and wake of perforated structures. *Journal of Fluid Mechanics*, 890, 2020. **Cited in pages 50, 51, 56, 123, 128, and 151**

[62] Harald Tronstad. Nonlinear hydroelastic analysis and design of cable net structures like fishing gear based on the finite element method. *NTNU Trondheim, Norwegian University of Science and Technology, Department of Marine Structures, Faculty of Marine Technology, Report MTA 2000-139, Doctorts Thesis*, 2000. **Cited in pages 51 and 128**

[63] Hui Cheng, Lin Li, Karl Gunnar Aarsæther, and Muk Chen Ong. Typical hydrodynamic models for aquaculture nets: A comparative study under pure current conditions. *Aquacultural Engineering*, 90:102070, 2020. **Cited in pages 51 and 128**

[64] Geir Løland. Current forces on, and water flow through and around, floating fish farms. *Aquaculture International*, 1(1):72–89, 1993. **Cited in pages 51 and 128**

[65] Etienne Guyon, Jean-Pierre Hulin, Luc Petit, and Pierre Gilles de Gennes. *Hydrodynamique physique*. EDP sciences Les Ulis, 2001. **Cited in pages 54 and 152**

[66] Sighard F Hoerner. Fluid-dynamic drag. *Hoerner fluid dynamics*, 1965. **Cited in page 55**

[67] Tianshu Liu. Evolutionary understanding of airfoil lift. *Advances in Aerodynamics*, 3(1):1–24, 2021. **Cited in page 55**

[68] Charles N Eastlake. An aerodynamicist's view of lift, bernoulli, and newton. *The Physics Teacher*, 40(3):166–173, 2002. **Cited in page 55**

[69] Doug McLean. *Understanding aerodynamics: arguing from the real physics*. John Wiley & Sons, 2012. **Cited in page 55**

[70] DR Merritt and F Weinhaus. The pressure curve for a rubber balloon. *American Journal of Physics*, 46(10):976–977, 1978. **Cited in page 66**

[71] Peter Buchak, Christophe Eloy, and Pedro M Reis. The clapping book: wind-driven oscillations in a stack of elastic sheets. *Physical review letters*, 105(19):194301, 2010. **Cited in page 66**

[72] Yichao Tang and Jie Yin. Design of cut unit geometry in hierarchical kirigami-based auxetic metamaterials for high stretchability and compressibility. *Extreme Mechanics Letters*, 12:77–85, 2017. **Cited in pages 88, 179, and 180**

[73] Hiroki Taniyama and Eiji Iwase. Design of a kirigami structure with a large uniform deformation region. *Micromachines*, 12(1):76, 2021. **Cited in pages 88 and 116**

[74] Lionel Schouveiler and Christophe Eloy. Flow-induced draping. *Physical Review Letters*, 111(6):064301, 2013. **Cited in pages 100 and 176**

[75] Rafic M Ajaj, Christopher S Beaverstock, and Michael I Friswell. Morphing aircraft: The need for a new design philosophy. *Aerospace Science and Technology*, 49:154–166, 2016. **Cited in page 108**

[76] Benjamin KS Woods and Michael I Friswell. Multi-objective geometry optimization of the fish bone active camber morphing airfoil. *Journal of Intelligent Material Systems and Structures*, 27(6):808–819, 2016. **Cited in page 108**

[77] Robert F Shepherd, Filip Ilievski, Wonjae Choi, Stephen A Morin, Adam A Stokes, Aaron D Mazzeo, Xin Chen, Michael Wang, and George M Whitesides. Multigait soft robot. *Proceedings of the national academy of sciences*, 108(51):20400–20403, 2011. **Cited in page 108**

[78] Hyun Kim, Suk-kyun Ahn, David M Mackie, Jinhyeong Kwon, Shi Hyeong Kim, Changsoon Choi, Young Hoon Moon, Ha Beom Lee, and Seung Hwan Ko. Shape morphing smart 3d actuator materials for micro soft robot. *Materials Today*, 41:243–269, 2020. **Cited in page 108**

[79] Mina Konaković-Luković, Julian Panetta, Keenan Crane, and Mark Pauly. Rapid deployment of curved surfaces via programmable auxetics. *ACM Transactions on Graphics (TOG)*, 37(4):1–13, 2018. **Cited in page 108**

[80] Jacques Hadamard. Sur les problèmes aux dérivées partielles et leur signification physique. *Princeton university bulletin*, pages 49–52, 1902. **Cited in page 110**

[81] John D'Errico. fminsearchbnd, fminsearchcon. matlab central file exchange, 2021. *URL https://www. mathworks. com/matlabcentral/fileexchange/8277-fminsearchbnd-fminsearchcon (AccessedonMarch1, 2020)*. **Cited in page 113**

[82] Johan Hastad, Bettina Just, Jeffery C Lagarias, and Claus-Peter Schnorr. Polynomial time algorithms for finding integer relations among real numbers. *SIAM Journal on Computing*, 18(5):859–881, 1989. **Cited in page 114**

[83] Jannik Schottler, Nico Reinke, Agnieszka Hölling, Jonathan Whale, Joachim Peinke, and Michael Hölling. On the impact of non-gaussian wind statistics on wind turbines–an experimental approach. *Wind Energy Science*, 2(1):1–13, 2017. **Cited in pages 122 and 123**

[84] Adele Moncuquet, Alexander Mitranescu, Olivier C Marchand, Sophie Ramananarivo, and Camille Duprat. Collecting fog with vertical fibres: Combined laboratory and in-situ study. *Atmospheric Research*, 277:106312, 2022. **Cited in page 123**

[85] Hakki Ergun Cekli and Willem van de Water. Tailoring turbulence with an active grid. *Experiments in fluids*, 49(2):409–416, 2010. **Cited in page 123**

[86] JR Morison, JW Johnson, and SA Schaaf. The force exerted by surface waves on piles. *Journal of Petroleum Technology*, 2(05):149–154, 1950. **Cited in page 128**

[87] Hao Chen and Erik Damgaard Christensen. Investigations on the porous resistance coefficients for fishing net structures. *Journal of Fluids and Structures*, 65:76–107, 2016. **Cited in page 128**

[88] B. H. Hanna, J. M. Lund, R. J. Lang, S. P. Magleby, and L. L. Howell. Waterbomb base: a symmetric single-vertex bistable origami mechanism. *Smart Mater. Struct.*, 23(9):094009, 2014. **Cited in pages 140, 141, 145, 146, 155, and 157**

[89] V. Brunck, F. Lechenault, A. Reid, and M. Adda-Bedia. Elastic theory of origami-based metamaterials. *Phys. Rev. E*, 93(3):033005, 2016. **Cited in pages 141, 142, 156, 158, 167, and 168**

[90] S. J. P. Callens and A. A. Zadpoor. From flat sheets to curved geometries: Origami and kirigami approaches. *Mater. Today*, 21(3):241–264, 2018. **Cited in page 141**

[91] S. Dutta and M. D. Graham. Dynamics of miura-patterned foldable sheets in shear flow. *Soft matter*, 13(14):2620–2633, 2017. **Cited in page 141**

[92] K. S. Silmore, M. S. Strano, and J. W. Swan. Buckling, crumpling, and tumbling of semiflexible sheets in simple shear flow. *Soft Matter*, 17(18):4707–4718, 2021. **Cited in page 141**

[93] G. V. Rodrigues, L. M. Fonseca, M. A. Savi, and A. Paiva. Nonlinear dynamics of an adaptive origami-stent system. *Int. J. Mech. Sci.*, 133:303–318, 2017. **Cited in page 141**

[94] Jiayao Ma, Huijuan Feng, Yan Chen, Degao Hou, and Zhong You. Folding of tubular waterbomb. *Research*, 2020, 2020. **Cited in page 141**

[95] B. H. Hanna, S. P. Magleby, R. J. Lang, and L. L. Howell. Force–deflection modeling for generalized origami waterbomb-base mechanisms. *J. Appl. Mech.*, 82(8), 2015. **Cited in pages 141, 145, 146, 155, and 157**

[96] Frederic Lechenault, Benjamin Thiria, and Mokhtar Adda-Bedia. Mechanical response of a creased sheet. *Physical review letters*, 112(24):244301, 2014. **Cited in pages 141, 142, 143, 144, 145, and 146**

[97] Y. Ben Amar, M .and Pomeau. Crumpled paper. *Proc. R. Soc. A: Math. Phys. Eng. Sci.*, 453(1959):729–755, 1997. **Cited in page 141**

[98] A. Lobkovsky, S. Gentges, H. Li, D. Morse, and T. A. Witten. Scaling properties of stretching ridges in a crumpled elastic sheet. *Science*, 270(5241):1482–1485, 1995. **Cited in page 141**

[99] Eric Sultan and Arezki Boudaoud. Statistics of crumpled paper. *Physical review letters*, 96(13):136103, 2006. **Cited in page 142**

[100] Daniel L Blair and Arshad Kudrolli. Geometry of crumpled paper. *Physical review letters*, 94(16):166107, 2005. **Cited in page 142**

[101] Théo Jules, Frédéric Lechenault, and Mohktar Adda-Bedia. Local mechanical description of an elastic fold. *Soft matter*, 15(7):1619–1626, 2019. **Cited in page 142**

[102] F. Lechenault, B. Thiria, and M. Adda-Bedia. Mechanical response of a creased sheet. *Phys. Rev. Lett.*, 112(24):244301, 2014. **Cited in page 143**

[103] J. T. B. Overvelde, T. A. De Jong, Y. Shevchenko, S. A. Becerra, G. M. Whitesides, J. C. Weaver, C. Hoberman, and K. Bertoldi. A three-dimensional actuated origami-inspired transformable metamaterial with multiple degrees of freedom. *Nat. Commun.*, 7(1):1–8, 2016. **Cited in page 143**

[104] T. Jules, F. Lechenault, and M. Adda-Bedia. Local mechanical description of an elastic fold. *Soft matter*, 15(7):1619–1626, 2019. **Cited in page 143**

[105] S. Deboeuf, E. Katzav, A. Boudaoud, D. Bonn, and M. Adda-Bedia. Comparative study of crumpling and folding of thin sheets. *Phys. Rev. Lett.*, 110(10):104301, 2013. **Cited in pages 145 and 146**

[106] T. Barois and E. de Langre. Flexible body with drag independent of the flow velocity. *J. Fluid Mech.*, 735(1):R2, 2013. **Cited in page 148**

[107] K Takeda and M Kato. Wind tunnel blockage effects on drag coefficient and wind-induced vibration. *Journal of Wind Engineering and Industrial Aerodynamics*, 42(1-3):897–908, 1992. **Cited in page 150**

[108] EC Maskell. A theory of the blockage effects on bluff bodies and stalled wings in a closed wind tunnel. Technical report, Aeronautical Research Council London (United Kingdom), 1963. **Cited in page 150**

[109] J Anthoine, D Olivari, and D Portugaels. Drag coefficient determination of bluff bodies–analysis of blockage effect. In *COST Action C*, volume 14, pages 5–7, 2009. **Cited in page 150**

[110] V.M. Falkner and S.W. Skan. Solutions of the boundary layer equations. *Philos. Mag.*, 12:865–896, 1931. **Cited in pages 152 and 154**

[111] Anuar Ishak, Roslinda Nazar, and Ioan Pop. Falkner-skan equation for flow past a moving wedge with suction or injection. *J. Appl. Math. Comput.*, 25(1):67–83, 2007. **Cited in pages 152 and 154**

[112] Lev Davidovich Landau and Evgenii Mikhailovich Lifshitz. *Fluid Mechanics: Landau and Lifshitz: Course of Theoretical Physics, Volume 6*, volume 6. Elsevier, 2013. **Cited in page 152**

[113] Hermann Schlichting and Joseph Kestin. *Boundary layer theory*, volume 121. Springer, 1961. **Cited in page 154**

[114] S. F. Hoerner. Fluid-dynamic drag. *Bakersfield, CA: Hoerner Fluid Dynamics*, 1993. **Cited in page 165**

[115] D. Melancon, B. Gorissen, C. J. García-Mora, C. Hoberman, and K. Bertoldi. Multistable inflatable origami structures at the metre scale. *Nature*, 592(7855):545–550, 2021. **Cited in page 168**

[116] H. Kobayashi, B. Kresling, and J. F. V. Vincent. The geometry of unfolding tree leaves. *Proc. R. Soc. B: Biol. Sci.*, 265(1391):147–154, 1998. **Cited in page 169**

[117] B. Kresling. Coupled mechanisms in biological deployable structures. In *IUTAM-IASS Symposium on Deployable Structures: Theory and Applications*, pages 229–238. Springer, 2000. **Cited in page 169**

[118] Joseph N Grima and Kenneth E Evans. Auxetic behavior from rotating triangles. *Journal of materials science*, 41(10):3193–3196, 2006. **Cited in pages 179 and 180**

ECOLE
DOCTORALE

Titre : Flow-gamis : Interaction de structures pliées et coupées avec un écoulement

Mots clés : Interactions fluide-structure, Elasticité, Origami, Kirigami, Reconfiguration, Réduction de trainée

Résumé : Une structure souple et élancée se déforme dans un écoulement fluide, adaptant sa morphologie à son environnement. Cela lui confère une meilleure résistance dans un écoulement fluctuant, via le processus de réduction de traînée. Les déformations passives induites par le fluide en mouvement peuvent également jouer un rôle fonctionnel, pour améliorer les performances aérodynamiques ou comme levier dans des problématiques de contrôle d'écoulement. Pour remplir ce rôle, il faut néanmoins être capable de programmer la réponse mécanique et prévoir les formes atteintes. Jusqu'à présent, la littérature s'est principalement concentrée sur l'interaction avec l'écoulement de structures élancées se déformant en flexion, en faisant varier leur rigidité et leur géométrie. Dans cette thèse, nous tirons parti d'une autre technique de changement de forme programmable inspirée de l'art du pliage origami et de la découpe kirigami.

L'introduction de plis et de coupures sur une feuille mince permet des changements de forme 3D complexes et modifie ses propriétés mécaniques, ce qui affecte son comportement dans un écoulement. Nous étudions expérimentalement l'effet de l'ajout d'une telle sous-structure sur la déformation et les forces fluides, en faisant varier systématiquement le motif des fentes ou des plis. Ces études expérimentales sont combinées avec le développement de modèles théoriques qui permettent une meilleure compréhension des mécanismes sous-jacents. Nous montrons que la déformation résulte d'une compétition entre la charge fluide (qui évolue avec la déformation) et la rigidité structurelle qui est conditionnée par l'arrangement des plis/coupures. En variant spatialement ces motifs, il est ainsi possible de moduler les formes et les forces induites par un écoulement, offrant ainsi un moyen de contrôle riche et inédit

Title : Flow-gamis: Interaction of folds and cuts with a flow

Keywords : Fluid-structure interaction, Elasticity, Origami, Kirigami, Reconfiguration, Drag reduction

Abstract : A flexible and slender structure deforms in a fluid flow, adapting its morphology to its environment. This gives it better resistance in a fluctuating flow, in particular by reducing its drag. These passive deformations can also play a functional role, to improve aerodynamic performance. To fulfill this role, one must nevertheless be able to program its mechanical response. So far, the literature has mainly focused on the interaction with the flow of slender structures deforming in bending, varying their stiffness and geometry. In this PhD, we take advantage of another programmable morphing technique inspired by origami folding art and kirigami cutting art.

The introduction of folds and cuts on a thin plate allows complex 3D shape changes and modifies its mechanical properties, which will affect its behavior in a flow. We study experimentally the effect of such a substructure on the deformation and the fluid forces, by systematically varying the pattern of cuts or folds. These experimental studies are combined with the development of theoretical models that allow a better understanding of the underlying mechanisms. We show that the deformation results from a competition between the fluid loading (which evolves with the deformation) and the structural rigidity which is conditioned by the crease/cut arrangement. By spatially varying these patterns, it is thus possible to modulate the shapes and forces generated by a flow, thus offering a rich control lever

Institut Polytechnique de Paris
91120 Palaiseau, France